

Human Brain Networks: Consensus, Reproducibility, Inter-Modal Comparison and Epilepsy Pathology

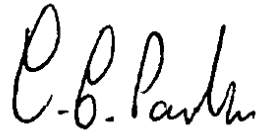
Christopher S. Parker

Doctor of Philosophy
Centre for Medical Image Computing
Department of Computer Science
UCL

August 2016

Dedicated to my father, Timothy Charles Parker (1948 - 2016).

I, Christopher S. Parker, confirm that the work presented in this thesis is my own. Where information has been derived from other sources, I confirm that this has been indicated in the work.

A handwritten signature in black ink, reading "C.S. Parker". The signature is written in a cursive style, with the first letters of each name being capitalized and prominent.

Abstract

Classical and contemporary research in neuroscience postulates that connectivity is a fundamental component of human brain function. Recently, advances in computational neuroimaging have enabled reconstruction of macroscopic human brain structural connectivity *in vivo* using diffusion MRI. Studies show that the structural network topology may discriminate between neurological phenotypes or relate to individual brain function.

To investigate disease effectively, it is necessary to determine the network methodological and biological variability. Reproducibility was calculated for two state-of-the-art reconstruction pipelines in healthy subjects. High reproducibility of connection weights was observed, which increased with connection strength. A high agreement between pipelines was found across network density thresholds. In addition, a robust core network was identified coinciding with a peak in similarity across thresholds, and replicated with alternative atlases. This study demonstrates the utility of applying multiple structural network pipelines to diffusion data in order to identify the most important connections.

Focal epilepsy is characterised by seizures that can spread to contiguous and non-contiguous sites. Diffusion MRI and cortico-cortical evoked potentials were acquired in focal epilepsy patients to reconstruct and correlate their structural and effective brain networks and examine connectivity of the ictal-onset zone and propagative regions. Automated methods are described to reconstruct comparable large-scale structural and effective networks. A high overlap and low correlation was observed between network modalities. Low correlation may be due to imperfections in methodology, such as difficulty tracing U-fibers using tractography. Effective

connectivity amplitude, baseline fluctuation, and outward connectivity tended to be higher at ictal-onset regions, while higher structural connectivity between ictal-onset regions was observed. Furthermore, a high prevalence of structural and effective connections to sites of non-contiguous seizure spread was found. These results support the concept of highly excitable cortex underlying ictal-onset regions which promotes non-contiguous seizure spread via high outward connectivity.

Acknowledgements

I would sincerely like to thank my supervisors Prof. Sebastien Ourselin and Dr. Jonathan Clayden, who have provided much support and guidance throughout my PhD, as well as the materials needed to undertake the studies in this thesis. Both have both provided timely suggestions when needed. In particular, I would like to thank Jonathan for the many helpful and inspiring (and often humorous) discussions of research ideas, for providing feedback on my work, and at times troubleshooting software issues. These interactions have helped me form a good internal dialogue which I can now use independently to perform high quality research.

While working at the Centre for Medical Image Computing and Developmental Imaging and Biophysics Section, I've met a number of people who deserve credit. Many thanks to Dr. M. Jorge Cardoso, who has been an ever-willing source of enthusiastic and innovative ideas and, together with Dr. Marc Modat, has also developed and given support in using key software. Dr. Pankaj Daga also developed software and participated in useful discussions relating to processing the MRI data.

Thanks to Dr. Kiran Seunarine for support with bash and R programming in the early stages of the project, and for generally lightening the atmosphere wherever possible. I would also like to thank Dr. Fani Deligianni for the many friendly discussions about my work and in coordinating to develop several R programming scripts used for data processing. Furthermore, thanks to Prof. Chris Clark and Dr. Michael Dayan for acquiring the healthy subject data used in this thesis.

I would also like to extend my gratitude to Dr. Beate Diehl from the National Hospital for Neurology and Neurosurgery, who has kindly provided the epilepsy data used in this thesis. Her thoughts and advice have been invaluable for interpret-

ing the results from a more applied and clinical perspective. Thanks to Ms. Catherine Scott, who helped arrange and set-up the *in vitro* experiment. I am also thankful to Dr. Roman Rodionov, who has participated in helpful discussions regarding the epilepsy MRI data. Thanks to Mr. Gareth Bahlke and Mr. Nathan Toms who gave their time to engage in objective discussions about interpreting evoked potentials from an engineering perspective and about designing the *in vitro* experiment.

Finally, thanks to my family who have been encouraging and supportive of me throughout this time. This thesis is dedicated to my father who achieved many things and instilled in me a good motivation and work ethic.

Contents

1	Introduction	21
2	Introduction to Imaging and Electrophysiology	25
2.1	Magnetic Resonance Imaging	25
2.1.1	Nuclear Magnetic Resonance	25
2.1.2	Free Induction Decay	27
2.1.3	Signal Echoes	30
2.1.4	Spatial Encoding	31
2.2	Diffusion Magnetic Resonance Imaging	34
2.2.1	Brownian Motion	34
2.2.2	Diffusion-Weighted Images	35
2.2.3	Diffusion in Biological Tissue	37
2.2.4	Artefacts in Diffusion-Weighted Spin-Echo EPI	40
2.2.5	Tractography	40
2.2.6	Advanced Diffusion-Weighted Imaging Acquisitions	42
2.2.7	Complex Fiber Models	45
2.3	Computed Tomography	46
2.3.1	X-Ray Production	46
2.3.2	X-Ray Interactions	47
2.3.3	CT Scanners	49
2.3.4	CT Artefacts	50
2.4	Intracranial EEG, SPES and CCEPs	51
2.4.1	Intracranial EEG Measuring System	51

2.4.2	Biophysical Basis of Single Pulse Electrical Stimulation . . .	53
2.4.3	Biophysical Basis of CCEP Waveforms	56
2.5	Summary	58
3	Micro- and Macro- scopic Structural Brain Connectivity	59
3.1	Microscopic Brain Connectivity	60
3.1.1	Columnar Cortical Connectivity	60
3.1.2	Lateral Cortical Connectivity	64
3.2	Macroscopic Brain Connectivity	68
3.2.1	Major White Matter Fiber Systems	68
3.2.2	Higher Order Brain Function and Disconnection Syndromes	70
3.2.3	Contributions of Diffusion MRI Tractography	72
3.2.4	Large-Scale Brain Networks and Graph Theory	75
3.3	Summary	82
4	Consensus and Reproducibility in Structural Networks	83
4.1	Introduction	83
4.2	Methods	86
4.2.1	Subjects and Images	88
4.2.2	Image Pre-processing	88
4.2.3	Cortical Parcellation	88
4.2.4	Native and Common Node Scale Parcellations	89
4.2.5	Registration of Cortical Parcels to Diffusion Space	90
4.2.6	Fiber Orientations	91
4.2.7	Probabilistic Fiber Tractography	92
4.2.8	Network Construction	92
4.2.9	Consensus between Reconstruction Pipelines	93
4.2.10	Network Properties of Consensus Networks	94
4.2.11	Reproducibility of Structural Networks	94
4.3	Results	95
4.3.1	Consensus Between Reconstruction Pipelines	95

4.3.2	Network Properties of Consensus Networks	98
4.3.3	Reproducibility of Structural Networks	102
4.4	Discussion	105
4.4.1	Consensus Between Reconstruction Pipelines	106
4.4.2	Reproducibility of Structural Networks	112
4.5	Summary	117
5	Reconstructing Large-Scale Structural and Effective Brain Networks	119
5.1	Introduction	120
5.2	Methods	122
5.2.1	Subjects and Electrode Implantation	123
5.2.2	Reconstructing Effective Networks	125
5.2.3	Reconstructing Structural Networks	131
5.3	Results	134
5.3.1	CCEPs	134
5.3.2	Diffusion Tractography	143
5.4	Discussion	146
5.4.1	Epochs	146
5.4.2	Stimulation Artefact	147
5.4.3	CCEPs	149
5.4.4	Electrode-Electrode Networks	150
5.4.5	Electrode Localisation	151
5.4.6	Electrode ROIs	152
5.4.7	Tractography	153
5.5	Summary	154
6	Structural and Effective Networks: Inter-Modal Comparison, Ictal-Onset Connectivity and Seizure Spread	155
6.1	Introduction	156
6.2	Methods	161
6.2.1	Structural and Effective Networks	161

6.2.2	Binary Network Analysis	162
6.2.3	Structural and Effective Network Comparison	162
6.2.4	Ictal-Onset Connectivity	163
6.2.5	Non-Contiguous Seizure Spread	163
6.3	Results	165
6.3.1	Structural and Effective Networks	165
6.3.2	Structural and Effective Network Comparison	165
6.3.3	Ictal-Onset Connectivity	165
6.3.4	Non-Contiguous Seizure Spread	169
6.4	Discussion	172
6.4.1	Structural and Effective Network Comparison	172
6.4.2	Ictal-Onset Connectivity	174
6.4.3	Non-Contiguous Seizure Spread	175
6.4.4	Methodological Considerations	177
6.5	Summary	179
7	Conclusions	181
7.1	Reproducibility and Consensus in Structural Brain Networks	181
7.2	Reconstructing Structural and Effective Networks	183
7.3	Inter-Modal Comparison and Connectivity in Epilepsy	185
7.4	Summary of Conclusions	187
	Appendices	189
A	Abbreviations	189
B	Electrolyte <i>In Vitro</i> Stimulation Experiment	191
B.1	Introduction	191
B.2	Methods	191
B.3	Results	193
B.4	Discussion	193
C	Summary of Publications	199

Bibliography

List of Figures

2.1	Free induction decay following a 90° RF pulse.	30
2.2	Spin-echo pulse sequence diagram.	34
2.3	PFG spin-echo pulse sequence diagram.	37
2.4	PFG spin-echo pulse sequence with EPI spatial encoding gradients diagram.	38
2.5	Diffusion tensor in isotropic and anisotropic tissue.	39
2.6	FA and colour-coded FA maps.	41
2.7	Streamline tractography schematic.	42
3.1	Schematic diagram of a neuron.	61
3.2	Vertical and lateral cortical connections in macaque primary visual cortex.	63
3.3	Lateral cortical connections in macaque dorsolateral prefrontal cortex.	65
3.4	Cortico-cortical association tracts delineated using dissection. . . .	69
3.5	Cortico-cortical association tracts delineated using diffusion trac- tography.	74
3.6	Seven Bridges of Königsberg graph theory problem.	76
3.7	Network representation of whole-brain connectivity.	79
4.1	Summary of network reconstruction pipelines.	87
4.2	Merging cortical parcels.	90
4.3	Representative cortical parcellations for P1 and P2 pipelines.	91
4.4	Normalised dice similarity coefficient between pipelines shown across density thresholds.	96

4.5	Similarity between P1 and P2 networks across density thresholds. . .	97
4.6	P1 fibers underlying convergent connections in a representative sub- ject.	98
4.7	Prevalence of convergent connections across subjects.	99
4.8	Reproducibility of P1 and P2 pipelines over network density.	103
4.9	Median reproducibility metrics for P1 and P2 connections.	104
4.10	Reproducibility of peak convergence connections.	105
5.1	Overview of methods used to reconstruct diffusion tractography and CCEP networks.	123
5.2	Raw CCEP data.	125
5.3	CCEP artefacts excluded by visual inspection.	129
5.4	Summary of CCEP epoching.	135
5.5	Electrode amplitude with respect to polarity of nearest stimulation electrode; IC signals in responses estimated by ICA.	137
5.6	Example of artefacts and suspected CCEP responses.	138
5.7	Example of artefact-corrected CCEP data.	139
5.8	Grand mean amplitudes in electrodes nearest the anode and cathode, before and after artefact correction.	140
5.9	Peak detection algorithm.	141
5.10	Peaks in uncorrected and artefact-corrected CCEP data.	141
5.11	Histogram of peak amplitudes and latencies of first peaks.	142
5.12	CCEP network.	142
5.13	Electrodes in CT and diffusion space.	143
5.14	Electrodes in diffusion space in relation to the brain surface.	144
5.15	Streamlines connecting electrodes in subject 1.	145
5.16	Diffusion tractography network for subject 1.	145
6.1	Ictal-onset and seizure propagation connection categories.	164
6.2	Weighted structural and effective networks and the union and inter- section of the binary structural and effective networks.	166

6.3	Similarity between binary structural and effective networks.	168
6.4	Ictal-onset effective and structural network connectivity measures pooled across all subjects.	169
6.5	Nodal graph theoretical properties at ictal-onset and non ictal-onset electrodes.	170
6.6	Prevalence of non-contiguous seizure spread effective and structural network connections.	171
6.7	Connectivity measures of non-contiguous seizure spread connec- tions across all subjects.	171
6.8	Examples of non-contiguous seizure spread networks.	172
6.9	Marginal density histogram of CCEP amplitude and latency in sub- ject 1.	178
B.1	Photograph of <i>in vitro</i> stimulation experiment	192
B.2	<i>in vitro</i> experiment signal filtering.	194
B.3	<i>in vitro</i> experiment mean responses.	195
B.4	Relation between electrode distance and maximum amplitude in early periods following stimulation.	196
B.5	Experiment artefacts and corrections Table	197

List of Tables

- 4.1 Graph theoretical characteristics of consensus networks. 101
- 5.1 Epilepsy subject details. 126
- 5.2 Summary of CCEP stimulations and recordings. 130
- 5.3 Prevalence of evoked potentials by number of peaks. 143
- 5.4 Tractography summary. 144
- 6.1 Subject structural and effective network properties. 167

Chapter 1

Introduction

Studying human brain anatomy has traditionally only been possible during brain surgery or in individuals post-mortem- using gross dissection or by viewing slices under a microscope. Observations on human brain anatomy were therefore limited in number and could not be performed longitudinally. Neuroimaging methods, such as Magnetic Resonance Imaging (MRI), allow non-invasive observation of human brain anatomy *in vivo*, and have therefore permitted observations in living individuals over time and in large numbers. Neuroimaging and associated computational post-processing methods have become increasingly sophisticated since their introduction and accordingly, there has been a rise in the popularity of neuroimaging methods to study brain anatomy and function. In particular, advances in diffusion MRI tractography, high resolution structural brain imaging, and whole-brain parcellation algorithms have enabled the study of the entire complement of brain regions and their inter-connections. This research field is known as *connectomics*. Omics fields are concerned with the analysis of pools of quantitative biological information relating to structural and functional organisation, the first example of which was genomics.

The broad motivation of this thesis is to learn more about brain connectivity in health and disease. Large-scale brain connectivity networks provide a rich source of anatomical information which may be used to understand healthy brain anatomy and its normal deviation, and therefore determine alteration of brain connectivity in disease states. Disruptions in brain connectivity have been previously implicated

in a number of neurological disorders, such as epilepsy and Alzheimer's disease, and the so-called *disconnection syndromes*, such as conduction aphasia. Connectomics information may uncover potential biomarkers which may be used to predict disease onset, diagnose disease, and monitor disease progression. On the other hand, the compliment of brain connections may be unique to the individual and provide a connectivity fingerprint, which may correlate to aspects of human behaviour, physiology and cognition. There is therefore a prospect of developing both personalised and population-based models of brain connectivity with benefits in the medical arena and beyond.

The motivations behind this thesis naturally evolved over time. Upon starting my PhD, connectomics was a new research field- there had only been a handful of publications in the area in late 2012. Before partaking in any clinical study using structural brain networks, it is important to assess reproducibility. It is essential to know whether brain networks are consistent over repeated acquisitions, or whether the variability due to acquisition and computer processing artefacts outweighs the natural underlying variation in brain networks between individuals. Having demonstrated reasonable reproducibility, the next consideration was whether the choice of contemporary computational methods used to build networks from many competing alternatives was influential, or whether they actually provide similar connectivity information. Having established that the reconstruction method is reproducible within and between subjects and comparable across contemporary reconstruction methods, the next challenge was to test the value of structural brain networks in a clinical context. One appropriate clinical question was whether structural brain networks could be combined with effective brain networks in order to improve localisation of the ictal-onset zone in drug-resistant epilepsy patients undergoing pre-surgical evaluation. This clinical application required development of computational pipelines to reconstruct large-scale effective networks, which required overcoming a number of caveats in the raw data.

The aims of this thesis were therefore to firstly assess the intra-subject and inter-subject reproducibility of whole-brain structural connectivity networks de-

rived from diffusion-weighted images. The second aim was to assess the similarity in structural brain networks obtained from completely independent pipelines employing contemporary methods of equal capability. The third aim was to evaluate and apply pipelines to reconstruct comparable effective and structural networks in a cohort of drug-resistant focal epilepsy patients. The final aim was to correlate and compare effective and structural networks, examine ictal-onset connectivity using each modality, and to investigate mechanisms of non-contiguous seizure spread using structural and effective networks.

The thesis structure is as follows. This chapter describes the motivation, aims and content overview of the thesis. Chapter 2 describes the imaging and electrophysiological methods used as a basis for network reconstruction. Chapter 3 describes aspects of microscopic and macroscopic structural brain connectivity useful for interpreting structural and effective brain networks. Chapter 4 investigates the reproducibility of structural brain networks and the consensus between different pipelines. Chapter 5 describes and quantitatively and qualitatively evaluates the methods used to reconstruct structural and effective networks in frontal lobe and parietal lobe epilepsy patients. Chapter 6 investigates the structural and effective network overlap and correlation, ictal-onset connectivity, and mechanisms of non-contiguous seizure spread. The final chapter summarises the conclusions, their implications and future prospects of research trends and studies arising from this thesis.

This thesis finds high reproducibility of contemporary state-of-the-art structural network reconstruction pipelines and quantifies this reproducibility among different cortical atlases and across network densities. Convergence between independent reconstruction pipelines was found to be very high. Consensus networks, corresponding to the strongest connections that have maximum overlap between pipelines, are demonstrated and their reproducibility is quantified. Methods to generate comparable structural and effective networks in focal epilepsy patients are described and evaluated in detail. Finally, correlation between structural and effective networks is quantified and the potential utility for identifying connectivity

abnormalities of the ictal-onset zone is reported. Results show that while structural networks are highly reproducible in cortical atlases at the macroscopic scale, effective connectivity markers may be particularly useful for identifying ictal-onset zone, while both modalities provide evidence of connections supporting seizure spread between distant areas.

Chapter 2

Introduction to Imaging and Electrophysiology

This chapter introduces the principles behind the MRI, Computed Tomography (CT) and Single Pulse Electrical Stimulation (SPES) modalities used to observe brain anatomy and function of subject cohorts in this thesis. Firstly, the phenomenon of Nuclear Magnetic Resonance (NMR), Free Induction Decay (FID) and spin echoes and how these can be used to generate images is described. Secondly, the process of Brownian motion and diffusion-weighted imaging and how this can be used to examine brain connectivity is explained. Next, the physical basis of X-rays and CT are briefly described. Finally, the biophysical principles underlying SPES and local field potentials are explained.

2.1 Magnetic Resonance Imaging

MRI uses strong magnetic fields to polarise nuclei within a specimen and radiofrequency (RF) coils to excite the nuclei and record their relaxation properties [194]. The relaxation properties depend on the local molecular environment, enabling exploration of contrast between different tissues within the specimen.

2.1.1 Nuclear Magnetic Resonance

All elementary particles possess the quantum mechanical property known as spin. Nuclei with a non-zero (integer or half integer) integral spin (those with an odd number of protons, neutrons, or both), are candidates for NMR, as they possess a

net magnetic moment and are therefore able to possess two stable energy states in the presence of a static magnetic field. Hydrogen has a spin of 1/2 and has a high signal in the MRI scanner due to its high abundance in living organisms- it is the main component of water and tissue; and is the most commonly imaged nuclei in MRI.

The rotating charge caused by spin means that nuclei act as dipoles or bar magnets. In the absence of a magnetic field, all the nuclei spins point in random directions, resulting in no net magnetisation.

When placed in a static magnetic field, the spin axis aligns to the magnetic field, and the interaction of the magnetic field with the nuclei spin causes them to experience a torque, which causes them to precess around their spin axis at a fixed frequency ω , termed the Larmour frequency. The Larmour frequency $\omega = \gamma B_0$, where B_0 is the strength of a static magnetic field (in Tesla, T) and γ is the gyromagnetic ratio. The static magnetic field is part of the MRI scanner, while the gyromagnetic ratio is a constant property of nuclei and quantifies the ratio of the magnetic dipole moment to the angular momentum. Higher magnetic fields result in a higher precessional frequency.

In a static magnetic field, nuclei may adopt one of two energy states- *spin-up* or *spin-down*, becoming aligned either in a parallel (with the magnetic field) or anti-parallel (against the magnetic field) orientation, respectively, in relation to the direction of the magnetic field. It takes slightly less energy to align in a parallel rather than anti-parallel orientation. The difference in energy between the spin-up and spin-down states is $\Delta E = \hbar\gamma B_0 = \hbar\omega$, where \hbar is the reduced Planck's constant. The energy difference therefore depends on the strength of the magnetic field.

Due to this energy difference there are slightly more nuclei aligned in the lower energy spin-up orientation. The relative proportion of spins that are in spin-up (N_-) compared to spin-down (N_+) state is given by

$$\frac{N_+}{N_-} = e^{-\frac{\Delta E}{kT}}$$

where k is the Boltzmann's constant, T is temperature and ΔE is the difference in

energy between the spin-up and spin-down states. This ratio of spin-up to spin-down nuclei is directly proportional to the MRI signal. Since the energy difference linearly depends on the magnetic field strength, stronger MRI magnets produce a higher signal. Likewise, lower temperatures also result in a higher signal, although it is not feasible to control the temperature of a living specimen. Hydrogen (^1H) has the highest gyromagnetic ratio of all nuclei and therefore gives the highest signal per unit mass. It is also very highly abundant in the human body, particularly in water and fat. For a magnetic field of 1.5 T at room temperature, the relative proportion of spin-up compared to spin-down protons is approximately 1 in 100,000. Thus, the NMR signal is based on a small proportion of nuclei.

2.1.2 Free Induction Decay

In the presence of a magnetic field, the small difference in the number of protons in the spin-up compared to spin-down state results in a net magnetisation, which has longitudinal and transverse components. The longitudinal component is the net magnetisation in the direction of the main magnetic field of the scanner (z-direction), while the transverse magnetisation is the magnetisation in the perpendicular direction to the main magnetic field (xy-plane). A net longitudinal magnetisation is created, while the net transverse magnetisation is zero as the spins phases are randomly distributed.

RF coils surrounding the MRI machine can impart energy to the precessing nuclei by emitting radiowaves in a direction orthogonal to the applied magnetic field. In order for energy to be transmitted, the radiowaves must be emitted at the Larmour frequency- the resonant frequency of the nuclei of interest. Emission of such radiowaves excites the spins and is referred to as an excitation pulse. Absorption of RF wave energy has two effects on the spins. The number of spin-down nuclei increases since sufficient energy is imparted to some nuclei to switch them from spin-up to spin-down state. Decreasing the number of spin-up protons decreases the net longitudinal magnetisation as there is now a smaller ratio of spin-up compared to spin-down nuclei. Secondly, the phases of precessing nuclei become synchronised. This phase coherence means the magnetic vectors of the spins are

aligned, creating a net transverse magnetisation in the xy-plane that rotates at the Larmour frequency.

After an RF excitation pulse, net longitudinal magnetisation has been reduced and transverse magnetisation created. Following this, the spin states of the protons are free to return to their equilibrium state in the presence of the static magnetic field (Fig. 2.1). Therefore, the number of spin-down protons, as well the phase coherence, slowly diminishes. This causes the net longitudinal magnetisation to grow back towards its equilibrium value and the net transverse magnetisation to decrease towards zero. This process of relaxation is termed FID and occurs due to two processes: spin-lattice relaxation and spin-spin relaxation. These two processes are explained below.

In a molecular lattice such as biological tissue, dipoles nearby to one another continuously interact, resulting in exchange and loss of energy from the spins to the lattice, hence the term spin-lattice relaxation. Dipoles that had gained energy and flipped to a spin-down state may lose sufficient energy to return to spin-up orientation. Over time, the net longitudinal magnetisation recovers to its equilibrium value due to energy being given up to the lattice. The longitudinal magnetisation recovers exponentially with a time constant T_1 . T_1 refers to the length of time for 63% (or $1 - \frac{1}{e}$) of the longitudinal magnetisation signal to recover. The time constant T_1 depends on the local environment of the dipoles and is therefore tissue dependent.

The T_1 of tissues varies in the range of hundreds of milliseconds to a few seconds. Large, slow moving molecules in the lattice are most effective at removing energy from the spins. For this reason, fat has a relatively short T_1 . Small, lightweight faster moving molecules are least effective at removing energy from the spins and so regions with a greater proportion of free water, such as cerebrospinal fluid (CSF), have a long T_1 . Atoms in rigid structures or macromolecules are least effective at removing energy and therefore compact bone, teeth and metallic objects have a very long T_1 .

The precession of spins is in phase following injection of an RF pulse. Following this, the precessions gradually dephase as some precess more slowly than

others, and energy is imparted and exchanged, resulting in further desynchronisation. This occurs as neighbouring dipoles exert additional small magnetic fields on one another, which alter each other's spin, hence the term spin-spin relaxation. There is also the effect of nearby magnetic molecules which add or subtract from the primary magnetic field, causing local variation in the magnetic field and further dephasing away from the Larmour frequency of the main magnetic field. The length of time for the signal to decrease to 37% (or $\frac{1}{e}$) of its original value is termed T_2 , and depends on the tissue composition.

The T_2 relaxation time is shorter than T_1 and is usually in the order of hundreds of milliseconds. In liquids molecules are rapidly moving so that the magnetic field experienced by individual spins is cancelled out on the time scale of the MRI scan, leading to long T_2 values for liquids. In solids, there is less movement of molecules and therefore less averaging of magnetic fields experienced by individual spins (i.e. a greater degree of magnetic field inhomogeneity), leading to shorter T_2 values. Water bound to macromolecules (e.g. proteins), which move slowly, has a shorter T_2 than free water. T_2^* recovery time refers to the recovery time observed in an imperfect magnetic field which contains field inhomogeneities which artificially shorten the true T_2 of the tissue.

In 1946 Felix Bloch carried out a famous study on nuclear induction using a continuous wave NMR experiment [29]. The experiment kept the RF field constant while varying the magnetic field. The transient NMR signal observed was theorised to represent the summation of magnetisation vectors in the sample, and the decay caused by interactions between the individual spins. Bloch equations were subsequently formulated to describe the behaviour of macroscopic magnetisation. The Bloch equations describe the growth of the longitudinal magnetisation and decay of transverse magnetisation in relation to the T_1 and T_2 of the tissues, the strength of the applied magnetic field and the Larmour frequency of the nuclei. Derivations of the Bloch equations for a 90° RF pulse show that recovery of net longitudinal magnetisation over time is given by $M_z(t) = M(1 - e^{-\frac{t}{T_1}})$, whereas the decay of transverse magnetisation is given by $M_{xy}(t) = Me^{-\frac{t}{T_2}}$, where M is the magnetisa-

tion immediately following the RF pulse.

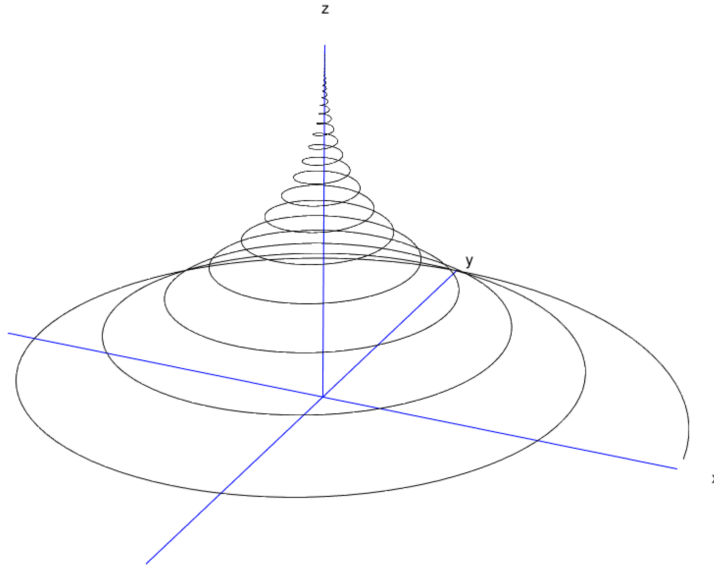


Figure 2.1: FID of the net magnetisation vector following a 90° excitation pulse. The net magnetisation vector rotates in the xy-plane at the Larmour frequency. The transverse component (xy-plane) diminishes due to T_2 relaxation whereas the longitudinal component (z-axis) recovers due to T_1 relaxation.

Following initial excitation, inhomogeneity in the main magnetic field, as well as the presence of additional magnetic field gradients (for spatial encoding, for example) causes differences in the frequency of individual nuclei precessions away from the expected Larmour frequency of the main magnetic field, causing rapid decay of the MRI signal. Therefore, instead of measuring the FID directly, a signal echo may be produced and measured using a gradient-echo or spin-echo pulse sequence.

2.1.3 Signal Echoes

Two concurrent gradients of opposite polarity can be applied following the RF excitation pulse in order to produce a signal echo, termed *gradient echo*. At the gradient echo time (TE), the spins precessing at higher frequency during the application of the first gradient will experience a lower frequency after application of the second opposite polarity gradient (and *vice versa*) and therefore all spins will be perfectly in phase at the end of the second gradient, creating a gradient echo. However, due to magnet inhomogeneities the strength of the signal decayed by the T_2^* process.

Another method to produce an echo is to apply a 180° RF pulse at some time following the initial 90° pulse (Fig. 2.2). In a spin-echo sequence, a 180° RF pulse is emitted at time $TE/2$, which causes all precessions to flip 180° in the zy -plane. This flip adds a phase to each spin which reverses the order of the spin vectors such that the higher frequency spins are now ‘catching up’ (i.e. rephasing) with the lower frequency spins. Dephasing that occurred due to magnetic field inhomogeneity up until time $TE/2$ is exactly reversed at time TE since the rephasing has been applied for the same period of time. At this timepoint, all precessions are in phase and a signal echo is formed. In contrast to a gradient echo, the spin-echo cancels the effects of T_2^* relaxation and produces a stronger signal. The amplitude of the echo signal in a spin-echo sequence is determined by T_2 relaxation.

2.1.4 Spatial Encoding

In addition to the main magnetic field of the MRI scanner bore, additional smaller magnetic field gradients are added across the imaged specimen in order to encode spatial location. The magnetic field gradient causes spins to rotate at different frequencies depending on their spatial location along the magnetic gradient. Three orthogonal gradient components are required for spatial encoding: slice selection, frequency encoding and phase encoding. Slice selection gradients are applied during an RF pulse, while frequency and phase encoding gradients are applied following an RF pulse.

To select the imaging slice, a z -field gradient is applied in conjunction with the RF pulse. Because the RF pulse has a limited range of frequency components, only the nuclei that are resonating within the bandwidth of the RF pulse (those within a certain range along z), corresponding to a slice in the z -direction, are excited. All other spins remain aligned with B_0 . The RF pulse is modulated in amplitude as a function of time to form a sinc shape in order to achieve the desired bandwidth. The slice selection gradient requires a following refocussing gradient of equal negative amplitude but half the duration. This offsets any phase differences to the Larmour frequency acquired during the initial slice select gradient and ensures that all the precession signals are in-phase across the selected slice.

The signal echoes obtained by exciting the slice are encoded by frequency and phase (described below) and sampled on a grid of locations in k-space. K-space is a domain representing the signal acquired for different frequency and phase-encoding acquisitions. Each phase encoding step corresponds to a different row (phase) of the k-space matrix, while each column corresponds to frequency. Each point in k-space consists of the MR signal from all points in the image slice under the corresponding gradient fields. Therefore, each element of k-space encodes the properties (amplitude, frequency, phase) of a sine wave function which acts across the entire image. This is because the sampled echo represents the signal from the entire excited slice. The image is reconstructed by taking the 2D Fourier transform of the k-space matrix [39].

To encode spatial location within the slice, a preparatory frequency encoding gradient is applied immediately following the initial RF excitation pulse but before the signal echo is formed. The nuclei also experience a single phase encoding gradient coincident with the preparatory frequency encoding gradient. When the signal echo is sampled, a further frequency encoding gradient (also called a readout gradient) of opposite polarity is applied. The integral of the gradient acquired by each spin is therefore changing throughout the acquisition of the signal echo. The integral of the frequency encoding gradient experienced by the signal at a point in time along the echo gives the point in k-space (x-axis for frequency encoding and y-axis for phase encoding) that the signal refers to. Therefore, the time-sampled echo corresponds to a line in k-space, as the phase encoding gradient has remained constant but the frequency encoding gradient is changing from negative, through zero (the centre of k-space), to positive. This process can be repeated for each row of k-space if the corresponding phase-encoding gradients are increased for each repetition.

Fig. 2.2 shows an example of one repetition of a standard spin-echo sequence with spatial encoding gradients. Initially, a slice select gradient is applied along the z-direction simultaneously with a 90° RF excitation pulse. The slice selection gradient is immediately followed by a short refocussing gradient. Frequency and phase encoding gradients are then applied in the x and y direction, respectively, to

label the precessions with their spatial location. Next, a 180° RF pulse is applied in conjunction with a slice select gradient in order to flip the excited precessions (and hence reverse any dephasing effects caused by T_2^*). Note that the refocussing pulse accompanying this second slice select gradient is the same polarity because the directions of spin precessions has been reversed. At time TE, a readout gradient (frequency encoding) is applied during sampling of the spin-echo. The readout gradient applies an increasing positive gradient to the precessions, such that the integral of the magnetic field experienced by the precessions increases from negative to positive by the end of the echo. The phase encoding gradient however has been applied previously and the phase offset remains constant throughout the echo, meaning that the echo signal corresponds to one phase (i.e. one row in k-space).

At each repetition of the sequence, the slice selection process and generation of spin-echoes is repeated with different phase encoding gradients. When k-space has been completely sampled, a 2D Fourier transform can be performed to map the frequency domain signal acquired from the MRI scanner into the spatial domain of the specimen for each slice. Slices are then stacked to produce a three-dimensional volume.

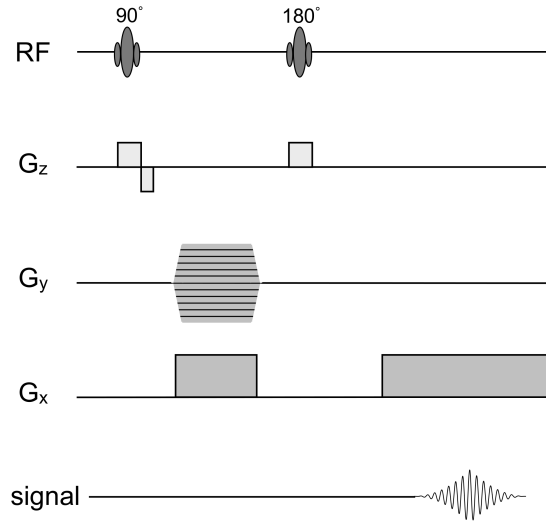


Figure 2.2: Spin-echo pulse sequence with slice selection and spatial encoding gradients. G_x , G_y and G_z refer to gradients in the x, y and z direction, respectively. RF refers to the radiofrequency pulse. Phase encoding gradients are incrementally decreased in each repetition, as indicated by the horizontal lines, until the full range of phase-encoding gradients have been applied.

2.2 Diffusion Magnetic Resonance Imaging

Diffusion MRI allows the *in vivo*, non-invasive mapping of the diffusion of water molecules. The first diffusion map of the human brain was made in 1986 [196]. In brief, magnetic field gradients are applied to label the spins of diffusing molecules and a projection of their displacement is measured by the MRI scanner. The diffusion along different displacement directions contains useful information about the underlying cellular structure and geometry, which relates to tissue properties such as osmotic homeostasis and nerve fiber orientations [195]. Such information can be used to infer connectivity and microstructural properties of the brain which further our understanding of brain anatomy and function.

2.2.1 Brownian Motion

Molecules in fluids undergo random thermal motion, also known as Brownian motion. The process is driven by thermal energy and at the macroscopic scale leads to displacement of diffusing molecules, as characterised by the diffusion coefficient, D . Diffusion can be described by the mean-squared distance travelled by molecules

in a given time interval, as given by Einstein's equation $\langle X \rangle^2 = 6Dt$ [110], where $\langle X \rangle^2$ is the mean-squared diffusion distance in three dimensions, D is the diffusion coefficient of the molecule and t is the diffusion time.

The diffusion coefficient can be measured directly by measuring the concentration of diffusing molecules over time and applying Fick's first Law [173]. Fick's first law states that the flux is proportional to the concentration gradient, where the coefficient of proportionality is the diffusion coefficient. The diffusion distance of free water ($D = 2 \times 10^{-3} \text{ mm}^2/\text{s}$) over the course of a typical MRI experiment ($t = 100 \text{ ms}$) is $\sim 35 \text{ } \mu\text{m}$, which is the same order of magnitude as the size of cellular compartments ($\sim 100 \text{ } \mu\text{m}$). Probing the diffusion of water in biological material using MRI therefore gives valuable insight into the cellular compartmental structure at that location. Because the presence of cellular compartments causes the diffusion to be reduced compared to free water, diffusion-weighted imaging measures the Apparent diffusion coefficient (ADC) instead of the diffusion coefficient itself.

2.2.2 Diffusion-Weighted Images

In order to produce diffusion-weighted images, magnetic field gradient pulses can be added to a spin-echo pulse sequence. Diffusion of magnetically labelled spins in between applications of opposite polarity magnetic field gradients attenuates the MRI signal in proportion to the exponent of the amount of diffusion occurring in parallel to the gradient orientation.

This is because in the presence of diffusion-sensitising gradients, the angular frequency of spins depends on their position along the direction of the applied gradient. In a spin-echo sequence the diffusion-sensitising gradients are applied for two equal periods of time either side of the 180° refocussing pulse. For a stationary spin, the phase acquired by the spins due to the diffusion-sensitising gradient is equal and opposite on either side of the 180° refocussing pulse, resulting in a spin-echo reflecting the T_2 of the tissue. In the presence of diffusion in parallel with the direction of the diffusion-sensitising gradients, the phase acquired during the first period is not cancelled out by the second, and therefore the diffusing spins have acquired a certain phase difference compared to stationary spins. This causes

attenuation of the spin-echo signal. Greater diffusion causes more dephasing and further attenuation of the signal.

The signal attenuation for diffusion-weighted imaging can be described by $S = S_0 e^{-bD}$, where S is the observed MRI signal in the presence of diffusion-sensitising gradients, S_0 is the signal obtained with no diffusion-weighting gradients, b is the b-factor and D is the diffusion coefficient. The b-factor is a summary metric describing the total amount of diffusion weighting in a diffusion-sensitising pulse sequence. The b-factor is calculated as:

$$b = \gamma^2 G_{\text{diff}}^2 \delta^2 \left(\Delta - \frac{\delta}{3} \right)$$

where G_{diff} is a vector representing the diffusion-weighting gradients orientation and magnitude, δ is the period of time each gradient polarity is applied for, and Δ is the time between leading edges of diffusion gradients of opposite polarity. Increasing the b-factor (by increasing diffusion-sensitising gradient G_{diff} , δ , or Δ) increases the amount of diffusion-weighting. The b-factor was initially developed to overcome the difficulties in calculating the signal attenuation in the presence of cross-terms between the imaging and diffusion gradient pulses.

The diffusion coefficient can be calculated given an observed MRI signal in the presence and absence of diffusion-sensitising gradients. In a diffusion MRI pulse sequence, one non-diffusion-weighted image is normally acquired and further diffusion-weighted images are acquired with diffusion-sensitising gradients in multiple three-dimensional orientations in order to determine the three-dimensional diffusion characteristics of each voxel [79].

The majority of diffusion-sensitising pulse sequences are based on the work of Stejskal and Tanner, who introduced the pulsed field gradient (PFG) method [292] (Fig. 2.3).

Large gradients are needed to produce detectable diffusion-weighting in the image and therefore gradients of a significant time duration compared to the repetition time are used in the PFG sequence. The highest diffusion-sensitivity in a pulsed field gradient echo is obtained by placing gradient pulses simultaneously on

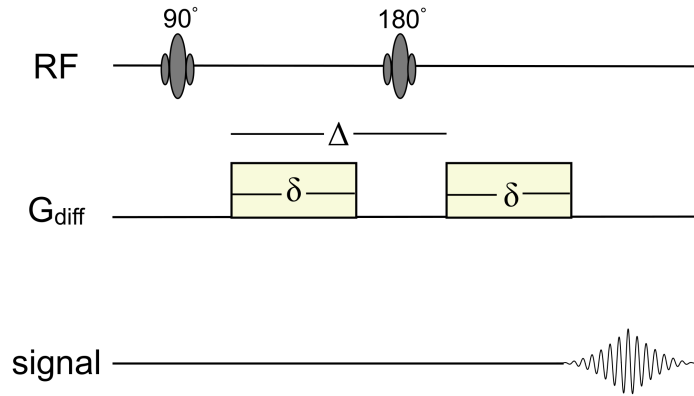


Figure 2.3: PFG spin-echo pulse sequence diagram. Diffusion-sensitising gradients are applied either side of the 180° RF pulse. The length of time the gradient is applied in each case is δ and the time between leading edges of the gradients is Δ . In the presence of diffusion the spin-echo signal observed at time TE is attenuated.

the three axes (thus creating a three-dimensional diffusion-encoding gradient) and giving as much time as possible to the diffusion-sensitising gradients within the spin echo sequence [79].

Diffusion-weighted imaging is particularly susceptible to motion since diffusion occurs on the scale of μm . Therefore, although diffusion-sensitising gradients can be added to a standard spin-echo echo-planar imaging (EPI) sequence [217, 315], in practice, a single-shot spin-echo EPI is used to avoid motion artefacts while collecting a large number of images with different diffusion gradient directions within an acceptable scan time (Fig. 2.4). Echo-planar imaging uses a train of inverted frequency-encoding gradients and blipped phase-encoding gradients following the 180° pulse to acquire the image in a single shot. The use of echo-planar imaging makes it feasible to use diffusion MRI in a clinical setting as it is fast and less susceptible to motion artefacts than PFG spin-echo.

2.2.3 Diffusion in Biological Tissue

The diffusion coefficient is useful for describing diffusion in an isotropic medium, where water is unrestricted and diffuses equally in all directions. In some materials, such as muscle and brain white matter, diffusion occurs to a greater extent in one orientation than others, which is termed diffusion anisotropy [76, 81, 70, 315]. In

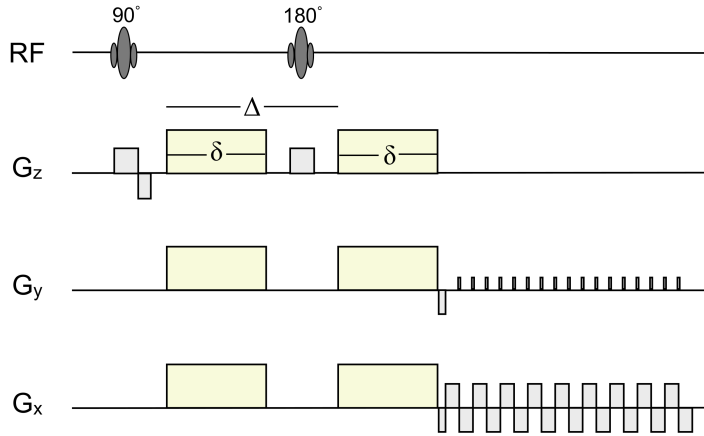


Figure 2.4: PFG spin-echo pulse sequence with EPI spatial encoding gradients. Diffusion-sensitising gradients (yellow) are applied along a particular direction. Frequency encoding gradients are applied in a train of alternate polarity gradients in order to fill k-space in a single shot. A negative phase-encoding gradient is initially applied followed by positive blips at each frequency encoding gradient polarity crossover. The process is repeated for each slice and for each diffusion gradient direction.

a diffusion-weighted image diffusion anisotropy manifests with the observation of greater diffusion in some gradient orientations than others. In this case, the diffusion profile may be better characterised using a diffusion tensor [173, 197]. The diffusion tensor describes the relative diffusion along the x, y and z axes of the tissue.

$$\mathbf{D} = \begin{bmatrix} D_{xx} & D_{xy} & D_{xz} \\ D_{yx} & D_{yy} & D_{yz} \\ D_{zx} & D_{zy} & D_{zz} \end{bmatrix} \quad (2.1)$$

The diffusion tensor describes the covariance of the diffusion between the x, y and z directions per unit time. The diagonal elements D_{xx} , D_{yy} and D_{zz} are the variances along the x, y and z direction of the MRI co-ordinate axis while the off-diagonal terms are the covariances of the diffusion along the axes.

The diffusion tensor may be used to obtain summary metrics about the amount of diffusion and the degree of anisotropy (Fig. 2.5). The diffusion tensor may be represented by its principal eigenvalues (λ_1 , λ_2 , λ_3) and eigenvectors (ϵ_1 , ϵ_2 , ϵ_3), describing the magnitudes and directions of greatest diffusion, respectively. The amount of diffusion (as an average along the three axes) is described by the

mean diffusivity and is the mean of the eigenvalues of the diffusion tensor: $MD = (\lambda_1 + \lambda_2 + \lambda_3)/3$. The fractional anisotropy (FA) describes the degree of anisotropy (the ratio of the magnitudes of the anisotropic and isotropic parts of the diffusion tensor) of the diffusion and is calculated from the eigenvalues of the tensor:

$$FA = \sqrt{\frac{3}{2} \frac{\sum_{i=1,2,3} (\lambda_i - \bar{\lambda})^2}{\sum_{i=1,2,3} \lambda_i^2}}$$

where $\bar{\lambda}$ is the mean eigenvalue.

The signal attenuation in the presence of anisotropic diffusion then becomes $S = S_0 e^{-\mathbf{bD}}$, where \mathbf{b} is the b-matrix and \mathbf{D} is the diffusion tensor. The b-matrix is the same size as the diffusion tensor and quantifies the amount of diffusion-weighting while taking into account cross-terms created by interactions between different gradient components [226]. To measure the full diffusion tensor a minimum of six noncollinear diffusion encoding directions are required.

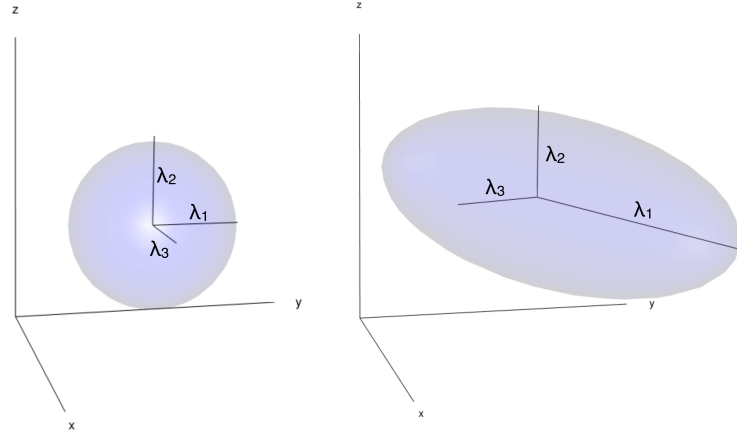


Figure 2.5: Diffusion tensor appearance in isotropic (left) and anisotropic (right) tissue. In isotropic tissue diffusion is equal in all directions and the diffusion tensor appears perfectly spherical, with each eigenvector having equal eigenvalues. In anisotropic tissue there is greater diffusion in one or more directions, leading to a cylindrically shaped diffusion tensor with eigenvectors having different eigenvalues. The eigenvector with the greatest eigenvalue is the dominant diffusion direction and presumed fiber orientation in the case of simple fiber geometry.

2.2.4 Artefacts in Diffusion-Weighted Spin-Echo EPI

Although single-shot EPI is the most common acquisition method for DWI, there are some artefacts induced as a result of the acquisition procedure, including eddy-current distortions and susceptibility artefacts.

Diffusion-weighted images obtained using EPI are susceptible to eddy-current distortions due to rapid gradient switching. Rapid switching induces currents in the conductive components of the MRI machine, such as the cryostat and RF coils, which leads to contribution of erroneous magnetic field gradients to the MRI signal. Eddy-current distortions lead to deformations in the diffusion-weighted image, which impairs comparison between the diffusion-weighted image and another undistorted image. Reducing the amount of diffusion weighting reduces the effect of eddy-current distortions, but decreases the contrast of interest. One option is to use smoother gradient changes (e.g. a sinusoidal gradient pulse). However, such oscillating gradients result in poorer diffusion sensitivity. Another solution is to use an actively shielded gradient coil, which has no fringe fields and so does not generate eddy-currents.

Susceptibility artefacts occur in diffusion-weighted images due to local changes in the magnetic field at tissue boundaries. This causes slight differences in the resonant frequency of nuclei, which leads to spatial distortions as the positions of the signal are mapped onto the image by frequency. These artefacts appear as non-rigid spatial distortions, occurring primarily near tissue boundaries, such as those near the brainstem and frontal lobes. The artefact particularly affects the air-tissue interface around sinuses as the air has a very different magnetic susceptibility to tissue. These artefacts are a particular problem for EPI acquisitions because of the low band-width in the phase-encoding direction.

2.2.5 Tractography

In brain white matter, neurons are grouped into fiber bundles. In these fiber bundles there is greater diffusion in parallel to the axonal orientations within the bundle and restricted diffusion in the perpendicular direction, giving rise to anisotropic diffusion. Anisotropy in diffusion tensors across the brain is commonly displayed as an

FA map, which shows the greyscale FA value in each voxel of the brain, highlighting the areas traversed by fiber paths (Fig. 2.6). Directional information may also be viewed as a colour-coded FA map, where the colour denotes the predominant orientation of diffusion in the x (red), y (green) and z (blue) directions. These RGB maps allow visual identification and discrimination of major white matter tracts and their connectivity (Fig. 2.6).

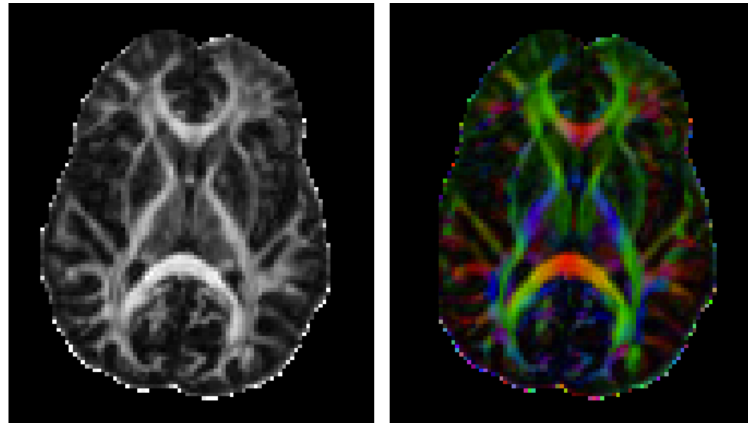


Figure 2.6: FA map (left) and colour-coded FA map (right). The FA map shows the degree of anisotropy in the diffusion tensor, ranging from 0 to 1, as a greyscale image. The colour-coded FA map shows the orientation of the dominant eigenvector of the diffusion tensor as either red (left-right), green (anterior-posterior) and blue (superior-inferior) and the brightness by the FA value.

White matter anisotropic diffusion may be exploited to reconstruct the spatial trajectories of nerve fibers in the brain, a process termed diffusion tractography. Many tractography algorithms exist which may use local or global information.

In local tractography, spatial trajectories (streamlines) are reconstructed by choosing a seeding location, and iteratively propagating the streamline along the fiber orientations. Streamlines continue to propagate until stopping criteria are reached which infers there is no further connection. Stopping criteria may include low FA (indicating absence of nerve fibers) or high curvature (indicating an unrealistic fiber path). A simple example of a local tractography algorithm applied to fiber orientations is shown in Fig. 2.7. The streamline is seeded at the base of the grid and follows the dominant fiber direction at each step. Local tractography algorithms may propagate deterministically, where the peak of the fiber orientation is

followed at each iteration [239], or probabilistically, where the direction followed is sampled from a distribution of the fiber orientation [22]. Probabilistic tractography algorithms generate many streamlines in order to obtain an estimate of connection probability between brain areas [252].

Global tractography algorithms firstly estimate a measure of connectivity on a fine scale (e.g. voxel to voxel) and then reconstructs the most plausible streamlines—those that best explain the underlying diffusion data, while discarding streamlines that are inconsistent with the data. This helps to overcome difficulties in local tractography algorithms which can prematurely terminate streamlines that encounter small amounts of noise along a true fiber path.

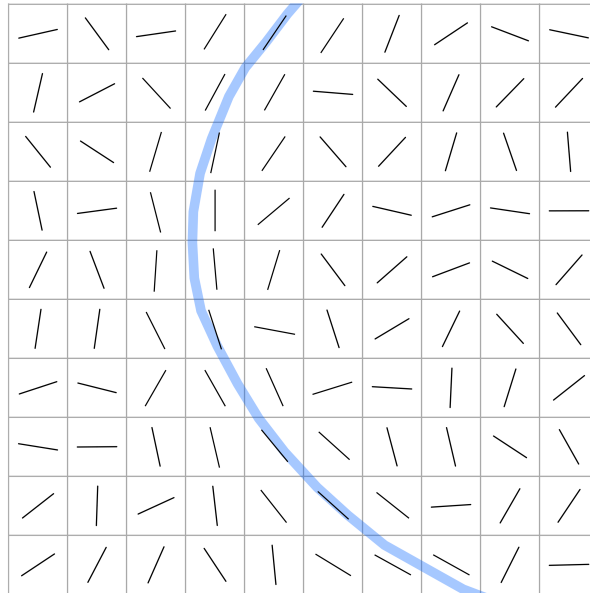


Figure 2.7: Streamline tractography. The dominant orientation in each voxel is given by the orientation of the line segment. Connectivity between voxels may be inferred by seeding a streamline and following the dominant fiber orientation in successive steps. In this two-dimensional schematic representation, the blue line, representing the streamline, has inferred a connection between the voxels it has traversed.

2.2.6 Advanced Diffusion-Weighted Imaging Acquisitions

Due to partial volume effects within a diffusion-weighted MRI voxel, the fiber structure may not always be adequately described by a simple diffusion tensor. Single fibers may disperse and bend, while multiple fibers may converge, cross and kiss, leading to diffusion profiles with multiple lobes, each having their own unique dis-

persion and bending properties. The use of a diffusion tensor in such cases leads to erroneous estimation of the fiber orientations and their anisotropy properties. During tractography, such errors contribute to false positive and false negative connections. For example, in a voxel containing crossing fibers, the diffusion tensor appears isotropic in the crossing plane, leading to both low FA and higher uncertainty in the maximum eigenvector, which may lead to premature termination or erroneous propagation of the streamline.

To address errors caused by complex fiber configurations, significant research effort has been made to improve the spatial and angular resolution of diffusion-weighted images. Advanced acquisition techniques such as High Angular Resolution Diffusion Imaging (HARDI), Diffusion Spectrum Imaging (DSI) and q-ball imaging provide more direct ways of estimating the diffusion profile than standard spin-echo EPI sequence.

The HARDI method is an umbrella term for acquiring diffusion-weighted images with a high number of diffusion gradient orientations, in recognition that complex fiber arrangements may otherwise be under-represented. Increasing the number of directions allows for better fitting of complex fiber models. HARDI is frequently accompanied by higher b-values in order to achieve a greater diffusion weighting concurrently with higher angular resolution [128].

Both DSI and q-ball imaging are HARDI techniques which are based on the concept of q-space [14]. The q refers to the gradient wave vector (a vector in three-dimensional space specified by the diffusion gradients) in the case where δ is infinitely small. The q-space imaging sequence uses the basic Stejskal and Tanner PFG spin-echo sequence with very short δ (narrow pulse approximation) and $\delta \ll \Delta$. With the narrow gradient pulse, the dephasing becomes proportional to the scalar product between the relative spin displacement and the gradient wave vector. q-space is analogous to k-space and is a two-dimensional domain of frequency space indexed by the applied diffusion gradients (as opposed to the frequency encoding gradients in k-space).

DSI, also known as q-space imaging, acquires many samples of q-space in

order to estimate the diffusion Probability Density Function (PDF) [337]. The PDF represents the density of diffusion vectors along displacement vectors. A Cartesian sampling of q-space may be transformed to the diffusion PDF by Fourier transform. This is a direct estimate of the diffusion profile in comparison to standard diffusion-weighted spin-echo EPI which models the diffusion process using a small number of parameters. The Orientation Distribution Function (ODF) can be estimated by projecting the PDF onto a spherical surface. Fiber orientations can then be inferred by finding local peaks of the ODF. The DSI technique suffers from some practical weaknesses. A high number of diffusion-weighted images are required in order to produce a complete Cartesian sampling of q-space. The technique is therefore time-intensive and not practical for clinical use. Further, DSI requires large PFG's to satisfy the Nyquist condition for diffusion in nerve tissue [313]. In addition, there are difficulties in accurately estimating the ODF from a Cartesian sampling due to non-uniform sampling of the spherical surface. Furthermore, Cartesian sampling of q-space is not an efficient way to sample the ODF as some of the data may be redundant.

To address the sampling burden of DSI, an alternative approach has been proposed termed q-ball imaging, which is based on sampling a spherical shell (or combination of shells) in diffusion wavevector space [313]. It is more efficient to measure the diffusion ODF by directly sampling the diffusion signal on a spherical shell as it requires a lower number of samples. Reconstructing the ODF directly using spherical sampling and reconstruction has a number of advantages. First, both the sampling and the reconstruction are both performed on the sphere so the reconstruction is immune to Cartesian reconstruction bias. With a spherical sampling scheme, there is also a natural framework for calculating the angular resolution, whereas it is not clear how to define the angular resolution for a Cartesian scheme. Last, the acquisition can be targeted to specific spatial frequency bands of interest by specifying the radius of the sampling shell.

2.2.7 Complex Fiber Models

Another way to account for complex fiber configurations is to apply a more robust representation of the fiber orientations to standard diffusion-weighted acquisitions. Multi-compartment fiber orientation models have been developed which can represent multiple fiber populations with different orientations, in addition to the extra-cellular and intra-cellular spaces [250]. These models assume that the diffusion-weighted signal is a sum of exponential functions arising from different compartments within a voxel. For example, the ‘ball-and-sticks’ multi-compartment model fits a ball (a sphere representing the extra-cellular isotropic diffusion) and variable number of sticks (infinitely thin cylinders representing varying number of fiber orientations) to the diffusion-weighted signal [22, 23]. Some multi-compartment models have been developed which utilise additional information about the diffusion profile obtained by acquiring diffusion images with different b-values, known as multi-shell acquisitions. For example, the Neurite Orientation and Dispersion Distribution Imaging (NODDI) technique acquires multiple shells in order to fit an estimate of the dispersion of fibers within a voxel [363]. Recently, a model-free approach to estimating multiple fiber orientations has been developed termed Constrained Spherical Deconvolution (CSD) [310]. This method assumes that the observed diffusion attenuations are a convolution of the fiber orientations and the signal response function (the signal response to fiber orientation). By assuming a certain signal response function the fiber orientations may be obtained by deconvolving the observed diffusion signal with the signal response function. The technique performs well in crossing fiber regions and can estimate up to eight orientations using spin-echo diffusion-weighted images with sixty directions or more.

2.3 Computed Tomography

Computed Tomography (CT) uses x-rays to reconstruct three-dimensional images of a specimen. A series of transaxial slices are acquired by rotating the x-ray machine around the patient and applying complex reconstruction algorithms to reconstruct the two-dimensional slices from one-dimensional projections [4]. CT images display the linear attenuation coefficient of tissue and have good soft tissue contrast, being previously used for medical imaging diagnosis in a range of disorders in the brain (e.g. stroke, haemorrhage, tumours) and body (e.g. emphysema, pulmonary embolism). CT is also routinely used for locating intracranial electrodes in drug-resistant epilepsy patients undergoing presurgical evaluation. The following paragraphs will give a brief summary of how x-rays are produced, how they interact with tissue, the components of the CT machine, image acquisition and reconstruction technique, and common artefacts. The source for this section is Allisy-Roberts and Williams [4].

2.3.1 X-Ray Production

X-rays are produced inside an x-ray tube by stopping fast moving electrons on a metal target. The x-ray tube is a vacuum containing a positively charged electrode (anode), negatively charged electrode (cathode), filament, and target. To produce fast moving electrons, the metal filament is heated to a very high temperature so that electrons escape from its surface through thermionic emission. As they escape into the vacuum the electrons are repelled from the cathode towards the anode. They travel at very high speeds (\sim half the speed of light) before crashing into a metal target material of high atomic number, such as Tungsten, with an energy equal to that of the voltage difference between the anode and cathode.

In the target material two types of interaction occur which give rise to characteristic and continuous components of the x-ray energy spectrum. Bombarding electrons may collide and displace an atomic electron in the K or L shell of an atom in the target material. Following this collision, the displaced electron is replaced by another atomic electron residing in a higher energy shell, resulting in emission of an x-ray. The energy of the x-ray photon that is released following this interaction

is equal to the difference in electron binding energies of the shells. This interaction contributes to the characteristic component of the x-ray spectrum, and is so named as the energies of these x-rays are predictable, being dependent on the difference in binding energies of the electron shells of the target material.

Bremsstrahlung effects also occur which contribute to the continuous portion of the x-ray spectrum. This interaction occurs if a bombarding electron penetrates the K-shell of an atom in the target material and is deflected. An x-ray is emitted with an energy equal to the energy lost through deflection. The highest energy photon emitted by x-ray tubes occurs when a Bremsstrahlung interaction completely stops an electron and an x-ray is produced with the energy of the bombarding electron.

X-ray tubes therefore produce a spectrum of photons with different energies. The spectrum contains a smooth, continuous component, and a characteristic component containing spikes of energy bands. X-rays leave the target material at right angles to the incident electron beam and are subsequently filtered by the x-ray production components and purpose built filters. This removes low energy photons which would unnecessarily contribute to patient dose and not the image.

2.3.2 X-Ray Interactions

Photons with a spectrum of energies are emitted from the detector onto the imaged specimen. As the x-ray beam passes through the patient it is either transmitted or attenuated. Attenuated photons are either absorbed or scattered. Attenuation occurs due to two types of interactions- Compton and photoelectric. The amount of attenuation reflects the energy spectrum of the photon beam, the atomic number Z of the tissue, and the density ρ of the tissue. CT attempts to recover the linear attenuation coefficient μ of the tissues with respect to water. The linear attenuation coefficient is the probability that a photon interacts (is attenuated) per unit length of the path it travels.

In a Compton interaction, an x-ray photon bounces off a free (loosely bound) atomic electron in the tissue. The X-ray is now scattered and has a lower energy. The probability of the Compton interaction is proportional to the physical density of

the material (it is actually proportional to the electron density, but this varies only by 10% between elements of tissues). The interaction contributes the Compton linear attenuation coefficient λ to the total linear attenuation coefficient μ . λ is proportional to $\frac{\rho}{E}$ (where ρ is the density of the tissue and E is the energy of the photon) and is independent of Z . However, there is only a very small decrease in Compton interactions over the energy range used in medical imaging.

In a photoelectric interaction, the photon interacts with a bound inner shell electron in the K-shell or L-shell of the atom, on the condition that the energy of the photon is above (but nearby) the binding energy of that electron. This displaces the electron from the atom. Another electron drops into the position of the displaced electron, emitting a characteristic x-ray of energy equal to the energy difference between the two shells binding energy states (tissue will largely be transparent to this characteristic x-ray radiation as it is normally lower than the binding energy of the shells). The photon disappears since all photon energy is lost. This interaction contributes the photoelectric attenuation coefficient τ , which is proportional to $\frac{\rho Z^3}{E^3}$.

Another less important interaction leading to attenuation of the x-ray beam is elastic (Rayleigh) scatter, whereby the x-ray bounces off a bound electron. This effect only occurs at low photon energies since the energy of the photon must be less than the binding energy of the bound electron.

In biological tissues, which contain a mixture of elements, the occurrence of Compton and photoelectric effects depend on the effective atomic number. Photoelectric effects are dependent on Z^3 , while Compton interactions are independent of Z . Photoelectric effects are proportional to $\frac{1}{E^3}$ while Compton effects have a low dependence on E . Therefore, at low photon energies and high Z , photoelectric interactions are the dominant effect. While at high photon energies and low Z , Compton interactions are the predominant effect. In soft tissue, water and air (low Z), the Compton effects predominates the attenuation of the x-ray beam, while photoelectric absorption predominates for contrast media and bone (both high Z).

2.3.3 CT Scanners

The CT machine consists of an x-ray tube, collimator and detector array mounted on a rotating gantry. The rotating gantry is heavy (~ 500 kg), but can rotate at \sim two revolutions per second or faster. The patient lies on a motorised table top that moves along the axis of rotation of the gantry and images are acquired in transaxial slices.

Modern CT scanners have so-called third generation geometry and are multi-slice scanners, capable of truly three-dimensional acquisition. Third generation scanners are equipped with detectors that cover the full cross-section of the patient, which allows collection of data through a 360° gantry rotation. Multi-slice refers to multiple banks of detectors which are required to produce three-dimensional CT images.

The fundamental unit of an x-ray image is a projection of the attenuation of the x-ray beam. Approximately 1000 such projections are acquired in a single rotation of the gantry. In order to construct two-dimensional slices, advanced image reconstruction algorithms are used, the most common algorithm being filtered back projection. The principle of back projection is to reconstruct a two-dimensional image by adding together the attenuation projections at each rotation. To increase the accuracy of this approach, filtered back-projection algorithms use additional data from neighbouring attenuation projections which either add or subtract to the image depending on the distance between the projections, with the closest projections having the greatest effect. Different filtered back-projection algorithms are available depending on the image task (e.g. for bone imaging or soft tissue contrast). The reconstructed two-dimensional images are then stacked to form a three-dimensional volume.

Modern CT images are of 512×512 resolution, although 256×256 or 1024×1024 imaging grids are also common. The slice thickness is determined by the thickness of the detector. The number in each voxel is referred to as the CT number (also known as Hounsfield number), and represents the average linear attenuation coefficient of the tissue (μ_t) with respect to the linear attenuation coefficient of water (μ_w) across the voxel. It is given by $CT = 1000 \times \frac{\mu_t - \mu_w}{\mu_w}$. The CT number is

therefore calibrated to water, although the attenuation values of tissues and water depend on the x-ray tube kV and filtration of the x-ray beam. CT numbers are typically from -1024 to 3071.

2.3.4 CT Artefacts

CT images may contain artefacts which affect image quality. Beam hardening occurs as the low energy photons of the x-ray beam are preferentially attenuated while passing through the patient. These hardened beams are attenuated less by the tissue, which results in structures towards the center of the patient having lower attenuation coefficient. This can be corrected using a beam-hardening correction algorithm or a bow tie filter which progressively filters the outer rays of the x-ray beam. Another artefact to consider is streak artefacts caused by high attenuation objects such as metal implants. Streak artefacts appear as dark and light lines emanating from the high attenuation object. Most modern scanners have metal correction algorithms which remove this artefact. Another artefact is partial volume effect. The CT number is an average across all tissues in the voxel, meaning objects that are small compared to the voxel size, but with a large attenuation coefficient, may be seen. Other artefacts which are sometimes present in CT images include motion artefacts, photon starvation, ring artefacts and cone beam artefact.

Intracranial electrodes are made of platinum, which has a Z of 78, making it a very highly attenuating material. The electrodes are more attenuating than bone, and are therefore easily visible on a CT image. Streak artefacts are frequently visible surrounding the electrodes, although these do not commonly present a problem for localisation of electrodes.

2.4 Intracranial EEG, SPES and CCEPs

This section describes the intracranial EEG measuring system and the biophysical basis of SPES and local field potentials generated following SPES.

2.4.1 Intracranial EEG Measuring System

The following paragraphs will describe the materials, implantation, measurement and artefacts in intracranial EEG.

The intracranial EEG measuring system includes a set of platinum electrodes and their wires embedded in a flexible plastic sheath. Wires carry the signal to the amplifier which measures and amplifies the voltage before sending it to the computer recording system. Electrodes placed on the brain cortical surface are called grid (or sub-dural) electrodes, while those in deeper brain structures are referred to as depth electrodes. Grid electrodes consist of rectangular electrode arrays, where each electrode is described by their diameter, depth, and spacing. Grid electrode arrays normally contain six electrodes per row, and electrodes typically have a diameter of 4 mm, exposed depth of 2.3 mm and spacing of 10 mm. Depth electrodes consist of a set of cylindrical electrodes arranged adjacently along a flexible wire, and are described by their diameter, length and spacing. There are normally six electrodes per wire and these typically have a diameter of 1.12 mm, length of 2.41 mm and spacing of 10 mm.

The electrode implantation process consists of choosing a suitable implantation location, implanting the electrodes, and closing the skull. The choice of implantation location is based on clinical grounds, where the aim is to identify the ictal-onset zone (the cortical area generating seizures) and propagative regions, and any eloquent cortical areas. The ictal-onset zone and propagative regions are considered for resection while eloquent areas are spared. The decision is based on previous ictal and non-ictal scalp EEG monitoring, seizure semiology and the location of potential pathologies such as cortical dysplasia or lesions.

The implantation method is performed under general anaesthesia. Structural MRI is used to guide the location of the skull opening. If grid electrodes are used, a craniotomy and durotomy is needed. Craniotomy and durotomy refer to incision

and removal of part of the skull or dura mater, respectively. Grid electrodes are placed on the surface of the cortex and held in place by adhesive paste. If only depth electrodes or grid electrode strips (a single row of grid electrodes) are required, a burr hole, created by drilling or scraping a hole in the skull, may be used to provide access to the brain. Grid electrode strips may then slide through the burr hole whereas depth electrodes penetrate into the brain itself. In the case of depth electrodes, a stereotaxic frame is used during surgery with reference to a stereotaxic structural MRI in order to determine the correct implantation location. Following implantation, the skull is surgically closed and bandaged and the electrodes remain in place for around five days while the patient is monitored in a hospital room. During this time inter-ictal and ictal intracranial EEG recordings are made and high frequency stimulation may be used for functional mapping of eloquent cortical areas. A cortico-cortical evoked potential (CCEP) study may also be performed.

Intracranial EEG measures differences in electrical potential, in the microvolt range, of each implanted electrode with respect to some reference electrode. The reference electrode is normally located in a relatively inactive part of the brain. Electrodes discretely sample the continuous voltage field generated by sources of electrical activity in the brain. Volume conduction effects occur which distort the voltage field as the current passes through brain tissue, across the cortical-electrode interface to the surface of the electrode. However, this effect is lower for intracranial EEG than scalp EEG as the electrodes lie underneath the skull and scalp layers. The spatial resolution of intracranial EEG is approximately 1 cm, meaning a source of brain electrical activity may spread up to but not exceeding 1 cm distance [191].

A number of electrical and biophysical artefacts should be considered when interpreting intracranial EEG. Power line noise may arise from the alternating current of any electrical cables passing near to the conductive components of the measuring system. This manifests as a fixed 50 Hz background noise in the EEG signal and is avoided by performing measurements in an electrically shielded room. The signal is contaminated by small amounts of intrinsic thermal noise due to the random thermal motion of electrons in conducting materials. The electrode-electrolyte interface can

also cause artefacts. Firstly, although the electrodes are initially fixed to the brain tissue, they may move following surgery. This may result in an unknown quantity of CSF at the electrode-electrolyte interface. This affects the volume conduction of electrical activity to the electrode, as the low impedance of CSF contributes to shunting of current, which may appear as rapid current spread through the CSF from relatively distant sources. Electrodes may become dislodged, leading to a triangular-shaped ‘pop’ artefact response to signals caused by very low impedance at the electrode-electrolyte interface. Furthermore, the electrode-electrolyte interface is an electrically complex system which has both impedance and capacitive properties which may spread the signal in time [129].

2.4.2 Biophysical Basis of Single Pulse Electrical Stimulation

The aim of SPES is to activate local neuronal pathways in order to observe effective cortical connectivity while preventing tissue damage. To deliver the stimulus, a constant-current pulse is applied between two implanted electrodes and the electroencephalogram is recorded from all other electrodes. The effectiveness of SPES depends on the amplitude, width, frequency, phase and polarity of the stimulation pulse, as well as the underlying tissue morphology. The influence of these factors upon neuronal activation is discussed below.

Effective electrical stimulation generates an action potential in a neuron, axon, or dendrite. In order to generate an action potential, the neuronal membrane potential (the voltage difference between intra- and extra-cellular compartments) must pass beyond the depolarisation threshold (-55 mV for pyramidal cells). The excitability of a neuronal structure is described by the *rheobase*- the minimum extra-cellular current necessary to induce a response in a system; and the *chronaxie*- the minimum pulse duration for inducing a certain response at a current strength of twice the rheobase. Axons and axon initial segments have lower chronaxies than cell bodies or dendrites, due to the higher density of sodium current channels in axons and axons hillocks compared to cell bodies and dendrites, while the nodes of Ranvier have the shortest chronaxie [247]. Larger diameter myelinated fibers will therefore likely be the first activated elements following electrical stimulation. The

the base of pyramidal cell axons is in the order of $1 \mu\text{A}$, while the chronaxie is approximately $200 \mu\text{s}$. The current strength and pulse duration used in SPES often exceeds threshold values of several neuronal elements and there is little selectivity of stimulation.

Cortical stimulation generates extra-cellular current flow, as the current outside the cell flows freely whilst it is more restricted when passing through the highly resistive membranes of neuronal compartments. The current density, J , at a given distance from a monopolar electrode in a homogeneous isotropic volume conductor is given by $J = I/4\pi r^2$, where I (unit, A) is the current intensity of the electrode and r is the distance (unit, m) from the electrode [184, 53]. The current density is therefore inversely proportional to the square of the distance from the source. Multiple current sources combine linearly by the superposition principle of electric fields. However, behaviour of electric fields in brain stimulation is complex due to differing resistivity of tissues and the irregular geometry of the brain. Estimation of current density in complex inhomogeneous mediums such as the brain is possible under quasi-static conditions and requires application of the finite element model. Nathan et al. [242] used finite element modelling to determine that the current density below a pair of stimulation electrodes is inversely proportional to the square of the distance from the cortical surface [242]. With a stimulation current amplitude of 4 mA , the current density directly beneath the electrodes is 0.02 A/cm^2 whereas it decays to 0.008 A/cm^2 5 mm away.

Studies of cortical and corticospinal neurons in rodents, cats and primates showed that the current needed to activate a neuron is proportional to the square of the distance between the neuron and the electrode tip [247, 6, 294]. A review by Ranck Jr [264], which calculated the current to maximal activation distance for monopolar intracortical stimulation of pulse width $200 \mu\text{s}$, found that the maximal distance at which intracortical stimulation may be effective is proportional to the inverse square of the current- stimulation of amplitude 4 or 1 mA will activate neurons at a maximal distance of 3 or 2 mm , respectively. Bipolar stimulation produces a more focused electric field and it has been estimated a sphere of radius 2 mm around

the electrodes are activated [277]. Since the electric field experienced along a nerve fiber determines the effectiveness of the stimulation, it is also important to consider the arrangement of the electrode with respect to the targeted neuronal elements. Neuronal elements in parallel to the electric field (those orientated tangentially to the cortical surface) are easier to excite than those perpendicular [264].

Regarding pulse width, some have observed that a lower stimulation current are required for increasing pulse widths up to 500 μs [206], while others have suggested a pulse width of 100 μs or less is suitable to minimise the applied charge [12]. Therefore, a pulse width between 100-500 μs may be considered optimal [234].

A monopolar or bipolar stimulation may be applied. A monopolar stimulation refers to stimulating electrode pairs which are some distance apart (one with variable position designed to produce the effect), whereas bipolar stimulation refers to adjacent stimulating electrodes. Finite element modelling of the current density in monopolar and bipolar stimulation showed that the current density decreases much less rapidly with depth and stimulates a wider region in monopolar than bipolar stimulation. Bipolar stimulation has therefore been used in CCEP studies as it results in a more focused electric field [242].

Monophasic or biphasic pulses may be used. In a monophasic pulse, the voltage difference between the stimulation electrodes is applied and removed, whereas in a biphasic pulse, the anode and cathode electrodes are immediately swapped around after one cycle. It is thought that a biphasic pulse produces a more balanced electrical charge at the electrodes [208], since different mechanisms of charge generation (which are not necessarily reversible) occur at the anode and cathode [230]. This charge imbalance may also be mitigated by performing an alternating monophasic stimulation, whereby the polarity of the electrodes is switched around after each pulse.

It should be noted that neuron activation also depends on the electrode type, with depth electrodes requiring a lower current to elicit neuronal activation than surface electrodes [294]. The current threshold to elicit a neuronal response also depends upon the physiological state of the system under investigation [94].

2.4.3 Biophysical Basis of CCEP Waveforms

The following paragraphs describe the relation between neuron orientation and observed voltage, and introduce the concepts of local field potentials and cortico-cortical evoked potentials.

Post-synaptic terminals of activated neurons generate dipolar voltage fields where the voltage decreases with the square of the distance from the source of the electrical activity. The electrode voltage therefore depends on the location of the electrode with respect to the active brain region and the orientation of the dipoles in this active region- the voltage field of a dipole decreases with the square of the distance and the voltage field is largest in the direction parallel to the orientation of the dipolar field. Therefore, active brain regions that are nearby and composed of parallel orientated dipoles will have the largest impact on the electrode voltage. The cortex contains a large number of synapses which mostly connect to pyramidal neurons orientated perpendicularly to the cortical surface. The major component of the electrode signal is therefore from synapses in the cortex. Signals from sulci are expected to be lower than gyri because the orientation of neurons is parallel to the cortical surface and they are a further distance from the electrode. In addition, facing sulci contain oppositely orientated dipoles whose field may cancel if simultaneously activate.

Local field potentials are recorded using intracranial electrodes and represent the superposition of extra-cellular voltages arising from cellular processes within the brain, with respect to some reference. The local field potential is therefore a spatial average of multiple sources and scales with the inverse of the distance between the source and the electrode. The shape of the local field potential depends on the synchrony and orientation of current sources and represents primarily active pyramidal neurons since these are aligned, have high synchrony and are the major output targets of the cortex. Non-synaptic events such as calcium spikes, intrinsic currents and resonances, spike afterhyperpolarisations and down states may also contribute to the local field potential [53].

CCEPs are local field potentials elicited by SPES, and have been observed at

local and distant recording sites. They consist of an early ($\sim 0 - 100$ ms) and late response ($\sim 100 - 500$ ms) [344, 324, 221, 116, 178], most widely described by the N1 and N2 negative potentials [221, 223, 185, 188, 350]. A recent review on CCEPs by Keller et al. [179] summarised evidence which suggests that the N1 represents excitatory depolarisation of pyramidal cells in deep cortical layers [179]. Current source density analysis of sensory stimulation showed that the earliest sensory responses are depolarisation of the middle cortical layers (III and IV), resulting in a surface negative potential lasting 10-30 ms and of 10-40 Hz frequency [236, 281]. Another study found that the early N1 response of the CCEP is accompanied by a burst of action potentials at the recording site [2]. This earlier response, thought to represent the N1 potential, is followed by patterns of excitatory and inhibitory post-synaptic potentials across all cortical layers of longer duration and lower frequency (1-4 Hz), which is similar to the N2 potential. In support of this, early studies on the effects of epicortical stimulation on the firing rate of single cells showed an early excitatory response in the time frame of the N1, followed by a longer lasting, slower inhibition that occurred in the N2 time frame [82].

Keller et al. [179] described three mechanisms of activation at the stimulation site which lead to generation of N1 and N2 responses. Firstly, depolarisation of the dendritic trees of pyramidal cells in cortical layers II, III, IV and VI may increase the chance of an action potential. Secondly, current depolarising layer II or III inhibitory interneurons synapsing to adjacent pyramidal cells [42] leads to an indirect decrease in pyramidal cell firing. Lastly, depolarisation of long range axons traversing the region of stimulation generates action potentials propagating orthodromically (to local and distant pyramidal synapses) as well as antidromically (propagating backwards to depolarise the pyramidal cell soma and dendrites). However, Matsumoto et al. [221] note that orthodromic discharges are more likely due to the easier excitability of large axons and initial segments than smaller structures such as presynaptic terminals [182].

Variability in the shape of evoked responses has been observed. In fact, even the most widely used N1 and N2 peaks have not been observed in all subjects

[324, 168] and do not necessarily co-occur [319]. This has lead to some CCEP studies employing alternative connectivity measures, such as A1 and A2, which measure the peak of the absolute magnitude of the response in the early and late time periods [116, 178]. The rationale for using these measures is that variability in polarity and latency has been observed- negative deflections are often followed by positive deflections and *vice versa*. In support of the validity of alternative polarity measures, a previous study demonstrates a similar spatial correlation between CCEP and resting fMRI when using the N1 or P1 response [177]. However, there is little biological theory underpinning the use of other connectivity measures, and in practice the evoked response may vary with subject, anatomical location, and underlying connection.

2.5 Summary

In this chapter, the basic physical principles of NMR and MRI image formation were described. The process of diffusion and how diffusion-weighted gradients can be added to a spin-echo MRI EPI sequence to produce contrast related to white matter fiber orientation was then explained. Use of diffusion MRI tractography for tracing fiber connections, advanced diffusion-weighted acquisitions and post-processing methods were discussed. Next, the principles of x-ray production and interactions, and how these are used to create CT images were briefly explained. Finally, the technical aspects of the intracranial EEG measuring system were introduced, and the biophysical basis of SPES and evoked local field potentials (CCEPs) were reviewed. Artefacts were also described for each modality.

Chapter 3

Micro- and Macro- scopic Structural Brain Connectivity

Current understanding of brain structural connectivity at the microscopic and macroscopic scales has evolved over many years of research and used many different observational techniques. Some important discoveries were made as long ago as 400 BC, although most advances have been in the last few centuries. The primary methods for observing structural connectivity have been blunt dissection, microscopy, degeneration, tract tracing and recently diffusion MRI tractography.

This chapter will describe aspects of microscopic and macroscopic cortical structural connectivity in the human brain important to the interpretation and understanding of the information derived from diffusion MRI tractography and CCEPs presented in this thesis. Both diffusion MRI tractography and CCEPs estimate structural connectivity on the macroscopic scale- that is, between sites separated by distances of millimetres to centimetres. However, an understanding of the microscopic connectivity is beneficial to interpretation of CCEPs as lateral cortical connections are thought to contribute a major component to the evoked potential. Therefore, this chapter will describe both microscopic and macroscopic cortical connectivity. Furthermore, network connectivity may be estimated by grouping ensembles of macroscopic connections and this chapter will therefore conclude by describing the macroscopic network aspects of cortical structural connectivity.

3.1 Microscopic Brain Connectivity

The human brain is non-homogeneous mass of cells. There are approximately 8.6×10^{10} neurons [7] in the average individual, with $1 - 2 \times 10^{10}$ located in the cerebral cortex [40], each of which has around 10,000 connections. There are four main components of the brain: neocortical grey matter, white matter, sub-cortical grey matter and CSF. The organisation and morphology of neurons varies throughout the brain, being most heterogeneous in the neocortex. The notion that neurons (see Fig. 3.1) form a contiguous network of physically separated cells [348] that communicate via chemical synapses [150] and propagate messages via electrical action potentials, are important concepts of brain function. Key principles of cortical structure include the presence of cortical layers connected perpendicularly to the cortical surface, lateral connections orientated tangentially to the surface, and emergence of long range cortico-cortical connections traversing the white matter. The following paragraphs will describe the vertical and lateral components of microscopic cortical connectivity.

3.1.1 Columnar Cortical Connectivity

Advances in tissue preparation, staining, microscopy, histology, degeneration and tract tracing have all enabled better understanding of cortical organisation at the cellular level. Degeneration and tract tracing studies are labelling techniques which have provided most insight into the vertical connectional organisation, while microscopy has enabled characterisation of the distribution of cell bodies.

The human cortex is $\sim 2-4$ mm thick. Six inter-connected cortical layers have been described which run parallel to the cortical surface [100, 44] (Fig. 3.2). They are labelled I to VI, with lower numbers being located nearer the cortical surface. Layer I is referred to as the molecular layer and is sparsely populated, containing some cell bodies and extensions of apical dendrites. Layer II, named the external granular layer contains pyramidal neurons (neurons with a triangular-shaped soma and large apical dendrite) and stellate neurons (neurons with a star-shape formed by dendritic processes radiating from the cell body). Layer III, the external pyramidal layer contains mainly small and medium-sized pyramidal neurons. Layer IV is re-

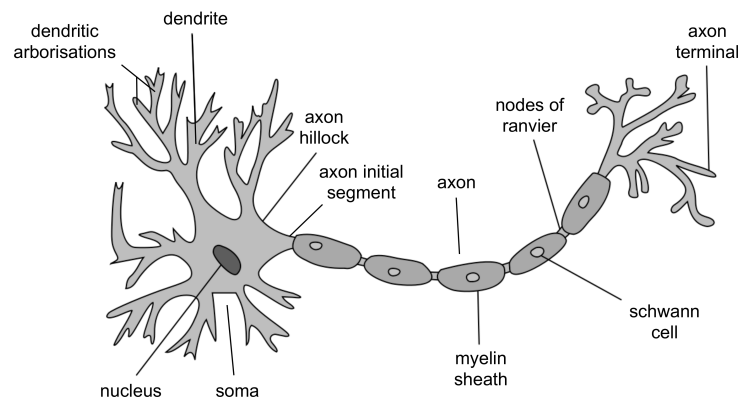


Figure 3.1: Schematic diagram of a neuron. Dendrites are neuronal processes arising from the cell body (soma), which receive synaptic inputs from other neuron axon terminals. Dendrites typically form branches of dendritic arborisations. The axon hillock is a specialised part of the cell soma that connects to the axon, whereas the axon initial segment is a highly excitable and unmyelinated part of the axon which arises from the soma. Synaptic inputs to dendrites, soma, axon hillocks and initial segments are summated and if the excitation passes beyond a given threshold an action potential is generated. Action potentials propagate along the axon of the neuron towards the axon terminal. The myelin sheath, formed by Schwann cells, and nodes of Ranvier, increase the speed and efficiency of the action potential propagation. Axon terminals form synapses onto dendrites of other neurons and permit the action potential signal to propagate between neurons.

ferred to as the internal granular layer and contains stellate and pyramidal neurons. Layer V is the internal pyramidal layer and contains large pyramidal axons. Layer VI is the polymorphic layer, containing a sparse population of large pyramidal neurons and small spindle-like pyramidal neurons [43].

The presence of cortical layers composed of different cell types, density and connection architecture, was demonstrated by Flechsig in the late 19th century [126]. The exact composition and density of each layer, as well as the number of layers (the cytoarchitectonic structure), varies across the cortex on the scale of centimeters [44, 332]. Although the classification of the cortical zones varies depending on the staining method, which is used to depict different aspects of cell morphology (e.g. Nissl staining for neuron cell bodies and myelin staining for neuron axons), comprehensive maps of the cortical zones, as determined by their vertical composition and arrangement of neurons, have estimated that up to around 100 cytoarchitectonic areas exist in the human brain [57, 44, 92, 332, 298]. For example, Economo and Koskinas defined 107 cortical areas using myeloarchitecture

[332], whereas Campbell defined 17 areas based on cytoarchitecture and function [57]. The most commonly used atlas of cortical zones is that of Brodmann's, which defines 52 areas based on cytoarchitecture and histology and was published in 1909 [43]. The definition of what comprises a cortical area, and how to define the boundaries between these areas remains incompletely defined due to inter-individual heterogeneity, inter-zone heterogeneity, variable distinctiveness in the borders between prescribed zones and variable definition relating morphology to function.

Nevertheless, some basic structural and functional principles of the vertical organisation of the cortex are broadly applicable. Vertical connections arise from pyramidal axons and axon collateral terminal synapses, and are more numerous than lateral connections [348, 214, 249]. Vertical connections link neurons within a single cortical column [213, 124, 356], where cortical columns contain neurons with similar functional properties [132]. A cortical column contains ~ 100 neurons, is $\sim 35\text{--}60\ \mu\text{m}$ across [52], and is the smallest level of vertical organisation in the cortex. Cortical columns (also known as minicolumns) are organised into macrocolumns, which contain ~ 50 minicolumns [119], linked by lateral cortical connections.

A cortical column contains predominantly intrinsic vertical fiber connections, of which four types of connection have been described [52]. Neuron collaterals-dendrites, axons and axon collaterals form excitatory connections which traverse the vertical space of the cortical column between layers I and VI. Double bouquet cell axons form inhibitory connections from layer II to layer III [90]. Axons arising from soma in layer VI are excitatory and tend to connect to layer IV [255]. Layer IV stellate cell axons are also excitatory and connect to layer II. Layer V apical dendrites receive connections from layer II. Areas in between predefined cytoarchitectonic zones- the 'peripheral neuropil space', are characterised by a sparse population of cell bodies, but are rich in unmyelinated axon fibers, dendritic arborizations and synapses [170, 297].

Afferent cortical connections arise from the thalamus (a six-centimetre-long bulb-shaped grey matter structure located near the centre of the brain), corpus cal-

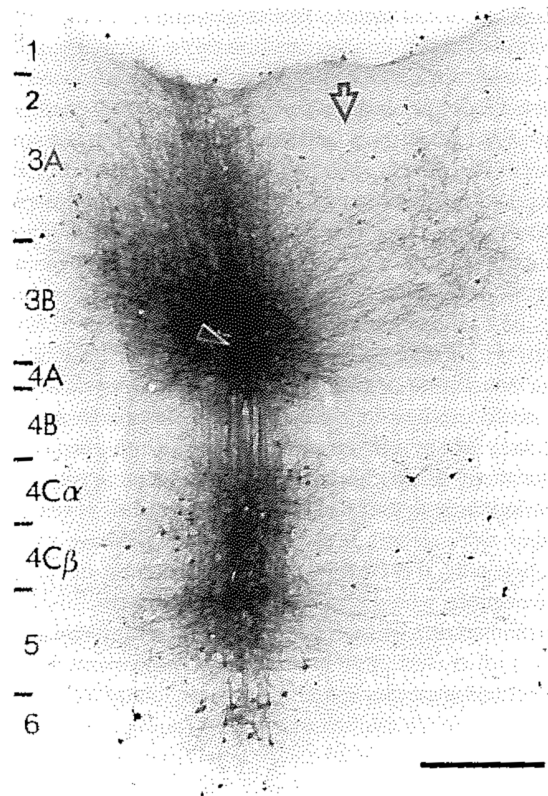


Figure 3.2: Vertical and lateral connections in the macaque primary visual cortex labelled with tract tracer biocytin. The dark arrow indicates the injection site and light arrow indicates path of lateral connections to a terminal projection cluster. Scale bar is 200 μm . Image was taken from Schüz and Miller [282], originally published in Levitt et al. [200].

losum (a large horse-shoe shaped fiber system connecting the cortex of left and right hemispheres) and ipsilateral cortico-cortical sources. Thalamic connections arrive in layer IV (a small number of connections go to later IIIb and V). The callosal input arrives in layer IV, IIIb, III and II [240, 157]. Cortico-cortical fibers also arrive in layer IV, IIIb, III and II. Therefore, the thalamic input connects to deeper layers than callosal and cortico-cortical connections. Efferent cortical connections arise from pyramidal neurons located in multiple cortical layers. One study stratified the output structures of connections from various cortical layers in monkey cortex. Efferent connections from layer VI target the thalamic nuclei, claustrum and other cortical regions [172]. Layer V has axons projecting to the spinal cord, pons, medulla, tectum, thalamus, red nucleus and striatum. Layer III neurons send efferent signals to ipsilateral cortex and the corpus callosum and layer II are cortico-

cortical only. Lateral connections between cortical columns arise mainly from layer III [55, 349]. Cortico-cortical connections arise from myelinated axon efferents originating from layer III and form bundles which traverse the white matter.

The majority of cortical neurons are excitatory pyramidal neurons and therefore the dominant functional network architecture is excitatory. However, a smaller fraction of inhibitory connections play a role in regulating the network function, although the mechanisms of how this is achieved are not well understood. Two types of inhibitory action occur: perisomatic- where inhibitory synapses (from basket and chandelier cells) are made onto cell soma, initial segments and axon hillocks, having a large negative influence on the generation of an action potential [89, 90]; and synaptic integration- where inhibitory connections (from double bouquet cells) are made onto branches and distal segments of dendrites, having a weaker integrative effect on the generation of action potentials on the target cell [52]. The mechanism of balance of excitation and inhibitory circuits within a cortical column and how this relates to overall brain function are not well understood.

3.1.2 Lateral Cortical Connectivity

It was suggested in Schüz and Miller [282] that lateral cortical connections are a fundamental component of neocortical connections, as superficial pyramidal neuron projections were found in the primary visual cortex of the marsupial quokka [316], which diverged from humans 135 million years ago. Lateral cortical connections were initially demonstrated using the Golgi staining method [227]. Degeneration and tract tracing studies have since provided insight into their spatial extent, laminar specificity, input and output, and function.

Lateral monosynaptic connections span several millimeters [274, 275, 137, 138], as demonstrated in cat, treeshrew and monkey, with the vast majority within a couple of millimeters from a given locus (Fig. 3.3). Lateral connections primarily connect cortical columns within a single cortical area, although can cross cortical area borders. For example, a projection patch can cross borders between Brodmann cortical areas 9 and 46, which are both dorsolateral prefrontal cortex [200, 260]. The spatial distribution of neurons connecting to or from a given locus was found to

be anisotropic, and this was demonstrated using both optical imaging [3] and tract tracing [220], with a greater length of connection most commonly in the anterior-posterior direction. The width of the small and large axis of the anisotropic connection was estimated to be ~ 1.5 mm and ~ 3.5 mm, respectively, in cat cortex [220]. Furthermore, lateral connections arising from a cortical locus are mostly reciprocal [123].

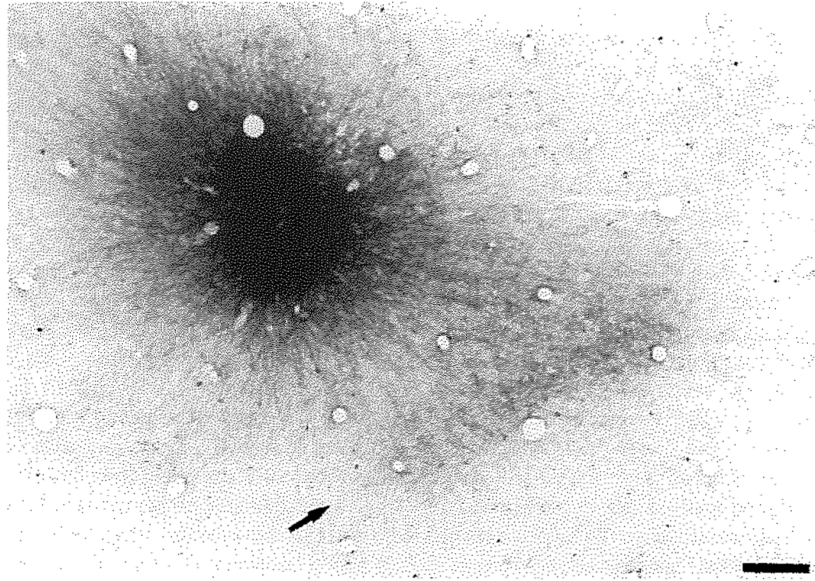


Figure 3.3: Tangential view of lateral cortical connections in macaque dorsolateral prefrontal cortex labelled with tract tracer biocytin. The arrow indicates the elongated patch of terminal projections. Scale bar is $200\ \mu\text{m}$. Image was taken from Schüz and Miller [282], originally published in Levitt et al. [200].

In addition to the anisotropic connection field, distant lateral connections were commonly associated with multiple (typically four to eight) anisotropic sub-millimetre patches, referred to as projections. These were found in the spatial distribution of cells providing input to a given cortical area as well as those receiving output. Patches were approximately $200\text{--}300\ \mu\text{m}$ diameter, spread $350\text{--}600\ \mu\text{m}$ apart, and exhibited similar anisotropic shapes to the primary connection locus. This phenomenon has been observed in all cortical areas studied- for example in V1 of cat [138], human [51], and rodent [50]; in somatosensory cortex of macaque [171] and ferret [175]; and in motor cortex of macaque [171]. Size and spacing of terminal patches differs between areas but seems to scale with the diameter of the

basal dendritic field of pyramidal neurons in each area. The connections between a cortical locus and its patch were also highly reciprocal.

In 1975 a detailed study on the striate cortex using degeneration techniques showed that the majority of lateral connections were in layers II and III and only sparsely found in layer IV. These findings have been reproduced in the primary visual cortex of cat [137, 218, 134], macaque [28, 356] and human [51] using tract tracing.

Degeneration studies have shown that the vast majority of cells providing lateral input to a given cortical area are excitatory pyramidal neurons and their targets are other pyramidal neurons [123, 273, 228, 229]. Inhibitory connections are more rare but have been demonstrated [176, 187]. The type of cells receiving input from a cortical location are essentially determined by the composition of cell types in the projection patch and there is little selectivity of cell connection [228].

Excitatory post-synaptic potentials generated by lateral connections have been demonstrated following electrical stimulation [158, 146]. However, their strength depended on the stimulation parameters. One feature of lateral cortical connections is that they are weaker and more variable compared to larger thalamo-cortical or cortico-cortical connections. However, it is estimated that they still provide a significant proportion of excitation to cortical cells *in vivo* [305].

There is some consistency across studies which show that the conduction velocity of signals through lateral connections is quite slow, being between 0.1-0.2 m/s. This has been demonstrated using a range of techniques in a range of species [299, 3]. Conduction velocity of 0.1-0.2 m/s corresponds to taking 10-20 ms to travel 2-3 mm laterally. However, it is unclear why propagation is this slow given diameters of connecting neurons are thought to be in the order of 1-3 μm .

The anisotropy of lateral connections has been strongly linked with functional maps in visual, auditory and somatosensory cortex, in that neurons with similar sensory preferences tend to be laterally connected. In visual cortex, tract tracing studies show that neurons with similar orientation preference (those neurons activated in response to visual stimuli at similar orientations in the field of view) tend

to be connected [139]. This has also been demonstrated using optical imaging in the primary visual cortex of cat [181, 180] and macaque [215]. Cross-correlations between single cell activities within 4.2 mm of a cortical site showed that neurons with similar orientation preferences had high correlation [312]. Similar functional preference of lateral connections has been observed in the auditory cortex, where cells with similar frequency preference in the tonotopic map are connected [266]. In the somatosensory cortex tracer injection studies by Juliano et al. [174] showed that areas activated following a particular somatosensory stimulation corresponded highly with the tracer that was injected into the suspected cortical area corresponding to the somatosensory area targeted by the stimulation. Interestingly however, anisotropy of lateral connections has been observed in the absence of a clearly defined functional map [200]. For example, sensorimotor cortex corresponding to forelimb digits and shoulder representations were found to be preferentially connected [162]. In addition, some nearby connections are thought to bear little relation to functional maps, as the functional connection preference is higher for longer distance connections [306, 37]. It is estimated that approximately one third of distant lateral projections connect to neurons with similar orientation preferences [306, 37]. A further complication to consider is the definition of the functional preference of a neuron given that neurons can have multiple functional preferences. For example, visual stimulation orientation and ocular dominance both describe the function of a neuron in the visual cortex.

3.2 Macroscopic Brain Connectivity

Understanding of macroscopic brain connectivity was enabled through techniques such as blunt dissection, myelin staining, and tract tracing. Diffusion MRI tractography helped confirm and refine our understanding of brain macroscopic connectivity, as well as adding new information that had been previously unobtainable. The following paragraphs will provide an account of the macroscopic organisation of cortical connectivity gained using classical techniques, before describing key advances in understanding brain structure using diffusion MRI tractography. An account of the relationship between macroscopic connectivity and brain function in health and disease will be provided. Finally, the use of diffusion MRI tractography in understanding macroscopic network organisation will be introduced.

3.2.1 Major White Matter Fiber Systems

Post-mortem dissection led to important discoveries such as the difference between white and grey matter. Piccolomini distinguished between white and grey matter in terms of colour, consistency and location. White matter was described as white compared to the “ashen-color” of the grey matter. In consistency the white matter was described as softer compared to the “harder and more compact” grey matter. In location, the grey matter encapsulated the white matter which “commenced everywhere” within the convolutions of the grey matter [256].

Although the white matter appeared homogeneous to the naked eye, post-mortem dissection led to recognition of white matter fibers and their trajectories [293], where fibers following the same path stick together in sheets or fascicles (Fig. 3.4). The cortical origin of white matter fibers [216], and the importance of white matter fibers to motor and higher order cognition [343], was also recognised. Willis used sections of brainstem to differentiate between ascending and descending fibers and to speculate on possible associated motor and sensory functions [248], thus forming the first description of the major white matter fibers that would later become classified as projection fibers.

Categorisation of the major fibers into projection, association, and commissural tracts resulted from detailed post-mortem studies of white matter trajectories during

the 19th century [49, 268, 269]. These studies showed that projection fibers connected the motor and sensorimotor cortex to muscles and sensing organs of the body via the spinal cord. Callosal fibers formed connections between the left and right brain hemispheres [93]. Association tracts were found to connect cortical regions within the same hemisphere. Association fibers were located deep in the white matter, whereas superficial fibers, referred to as the U-fiber system, were located nearer the cortical surface and connected cortical regions in close proximity. Dissection studies based on soaking the brain in alcohol, performed by Christian Reil, demonstrated most of the major individual association tracts [267]. The latin terminology adopted for most of the associative bundle names came from Karl Burdach in 1822 [49], who also confirmed Reil's findings. Examples of major association tracts include the inferior longitudinal fasciculus, which connects the occipital and temporal lobes; and the arcuate fasciculus, which connects inferior parietal to inferior frontal lobe.

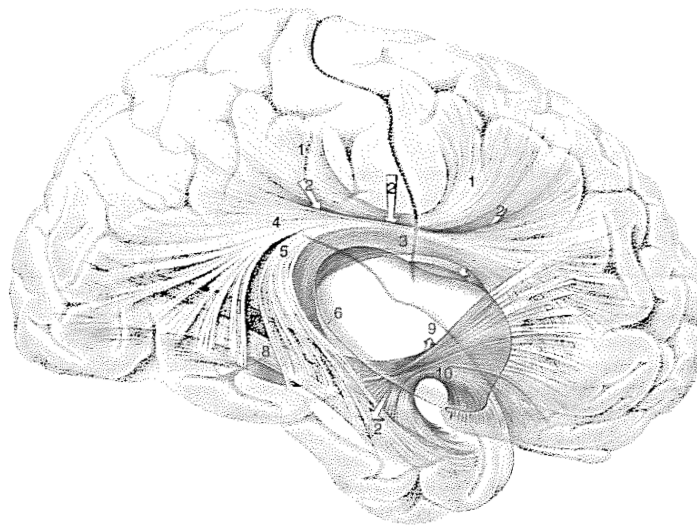


Figure 3.4: Overview of long range cortico-cortical association tracts delineated using dissection. 1. Superior occipital fasciculi, 2. Corona radiata, 3-5. Superior longitudinal fasciculi, 6. Outline of the insula, 7. Inferior occipitofrontal fasciculi, 8. Inferior longitudinal fasciculi, 9. Location of the anterior commissure, 10. Uncinate fascicle. Image was taken from Schüz and Miller [282], originally published in Nieuwenhuys et al. [245].

In the 1960s tract tracing methods were developed which allowed a detailed report of the organisation of cellular systems at the circuit level, refining models

of local neuronal circuits to contain feedback and feedforward, hierarchical and parallel organisation [120, 233]. This provided a good foundation for computational approaches to studying brain connectivity.

3.2.2 Higher Order Brain Function and Disconnection Syndromes

So-called associationist theories of brain structural organisation have dominated modern understanding of higher order cognitive brain function, and this theory of brain function led to the classification of a number of disconnection syndromes [66].

Wernicke's associationist theory, based on post-mortem dissections of human brains and their neuropathology, was introduced in 1874 and stated that higher brain functions were the product of associative connections between cortical areas storing motor and sensory images. Therefore, disorders of higher function resulted from a disconnecting breakdown of associative connections through white matter lesions [341]. This theory helped explain some classical disconnection syndromes, such as conduction aphasia, agnosia, and the apraxias [66].

Not long afterwards, Dejerine [91] described pure alexia syndromes using case reports and proposed a visual verbal center for storing visual images of words in left angular gyrus. This proposal broke Wernicke's associationist rule in that (i) higher brain functions could be located in a particular cortical area, and that (ii) the visual verbal center was located outside visual cortex which was against Wernicke's model of alexia. For this reason, Wernicke wrote a critique of Dejerine's view [45]. However, these views of cortical specialisation, that higher brain function arose from specialised cortical areas, grew more popular and were further strengthened by Campbell's and Brodmann's division of the cortex into discrete cytoarchitectonic regions [57, 44]. In the 20th century, these localisationist and associationist views were criticised and alternative models, described as holistic, anti-localisationist, or anti-associationist [135], dominated until Gechwind's time saw a revival of the associationist school of thought.

In the 1950s Myers and Sperry provided strong evidence for hemispheric lateralisation of brain function by examining the effects of callosal sections in animals

and then in patients with epilepsy. This motivated Geschwind to consider older literature and re-examine his patients with higher brain dysfunctions [136]. His publication became the manifesto of the neo-associationist school. His published theory added two new components to the classical view: Flechsig's rule, and a phylogenic perspective to the development of associations. Flechsig's rule found that in humans no connections existed between early myelinated areas, the primary sensory cortices. Instead they were indirectly connected via association fibers and association cortices. The phylogeny of Flechsig's rule suggests that in lower mammals inter-sensory connections exist, but in more phylogenically advanced animals connections are made with newly developed regions of association cortex which become interspersed with older zones. The limbic system was a key component of lower phylogenic animals, and evolution of association cortex in humans underly evolution of higher brain function. Geschwind's hypothesis was that the key development in humans was a higher-order association area in the parietal lobe- the inferior parietal lobule, which represented an association area of association areas, acting to free humans from the dominant pattern of sensory-limbic associations and permitting cross-modal associations involving non-limbic modalities [136].

This phylogenic perspective employs connectional models involving rabbit (having inter-connected sensory cortices all connected to the limbic system), monkey (having inter-connected patches of sensory cortex and association cortex, all connected to the limbic system via the association portion of each patch) and human (patches are now connected to a tertiary association cortex in the parietal lobe, with no limbic connection). Geschwind proposed that the tertiary association area found in humans allowed associations between two non-limbic stimuli, which was essential for learning higher order cognitive functions such as language.

Wernicke school of disconnection was particularly about white matter lesions to association tracts, whereas Geschwind's model used phylogenic principles and focused on lesions to association areas and the white matter pathways arising from them. Geschwind re-evaluated disorders of higher functions and provided detailed accounts of higher function disorders due to disconnection (sensory-limbic dis-

connections, sensory-Wernicke disconnections, sensory-motor disconnections and hemisphere disconnection).

Current understanding of higher brain function has been refined based on new assessments of cortical function and cortico-cortical connectivity. Specific functional roles for association cortex were found by Damasio and Mesulam in both monkey and human brains [86, 232]. This was confirmed through functional imaging [362]. The roles of association cortex are more complex than originally thought in localisationist theories- with brain function being distributed over networks whose cortical elements have similar yet different roles depending on the brain function. Geschwind assumed a feed-forward serial nature of information transfer. Currently, we have more evidence for feed-backward and parallel pathways. The presence of parallel bidirectional distributed processing for higher functions has recently been confirmed in humans [221, 27].

The contemporary framework of higher order brain function consists of a network of multiple specialised cortical areas, grouped into territories, and connected through parallel, bidirectional pathways. Higher function deficits can therefore arise due to both loss of specialised cortical function and damage to connecting pathways, which may therefore include hyperconnectivity and hyperfunction. Clinico-pathological correlations not meeting expectations due to lesion location may be hypothetically explained in terms of altered connections. In view of the contributions of diffusion MRI tractography in understanding higher brain function, Catani et al. [66] recently introduced a framework for explaining clinicopathological correlations, which accounts for localised cortical damage, connection dysfunction (hyper and hypoconnectivity) and so-called hodotopic dysfunction (overall dysfunction caused by both localised and connectional dysfunction) [66].

3.2.3 Contributions of Diffusion MRI Tractography

Diffusion MRI tractography is a non-invasive and much shorter procedure than traditional tract tracing techniques, and furthermore obtains *in vivo* estimates of structural connectivity (Fig. 3.5). This enables a high participation and throughput of connectivity information for an entire brain at once, which in turn has had many

benefits for studying structural connectivity. This section will describe the major areas of contribution of diffusion MRI tractography to our understanding of macroscopic connectivity.

Diffusion MRI tractography studies have given insight into human macroscopic structural connectivity not possible using classical techniques, in some cases identifying new tracts [64], modifying our understanding of existing pathways [127, 354], and allowing large-scale connectivity analyses [259].

The arcuate fasciculus was classically understood as a single pathway. However, deterministic tractography performed in a diffusion dataset averaged across individuals demonstrated that there is also a previously undescribed indirect pathway. This model of two parallel pathways helps explain the diverse clinical presentations of conduction aphasia [64].

Tractography in a large cohort of healthy individuals has helped clarify the number and location of fronto-occipital connections in humans. Whereas previous post-mortem dissections and other diffusion tractography studies suggested the existence of a bilateral ventral pathway directly connecting frontal and occipital lobes (the inferior fronto-occipital fasciculus), this study also demonstrates a dorsal pathway running through the outer corona radiata which does not correspond to the superior longitudinal fasciculus and which has not been previously described in animals. This may therefore represent a newly discovered tract unique to humans. However, the authors comment that this finding awaits confirmation using tract tracing and myelin staining, to validate whether it is a unique tract in humans or part of the existing superior longitudinal fasciculus system [127].

The vertical occipital fasciculus connects the ventral and dorsal occipital, parietal and temporal lobe although its existence was controversial since its discovery by Wernicke in 1881 [340]. Diffusion MRI tractography studies in a large group of individuals allowed confirmation of its existence and further characterised its path in humans [354].

One benefit of high throughput diffusion MRI tractography is that it enables the relatively rapid creation of average atlases of human macroscopic connectiv-

ity. A tractography atlas of the human brain was recently published by Catani and De Schotten [61] using diffusion tensor tractography and is a comprehensive expansion of their previous atlas [63]. In this study, the diffusion-weighted images from twelve healthy male subjects were averaged to build a representative diffusion-weighted dataset. Tractography was then performed from regions of interest, defined from previously published post-mortem dissections, and mapped to a common reference space for practical referral.

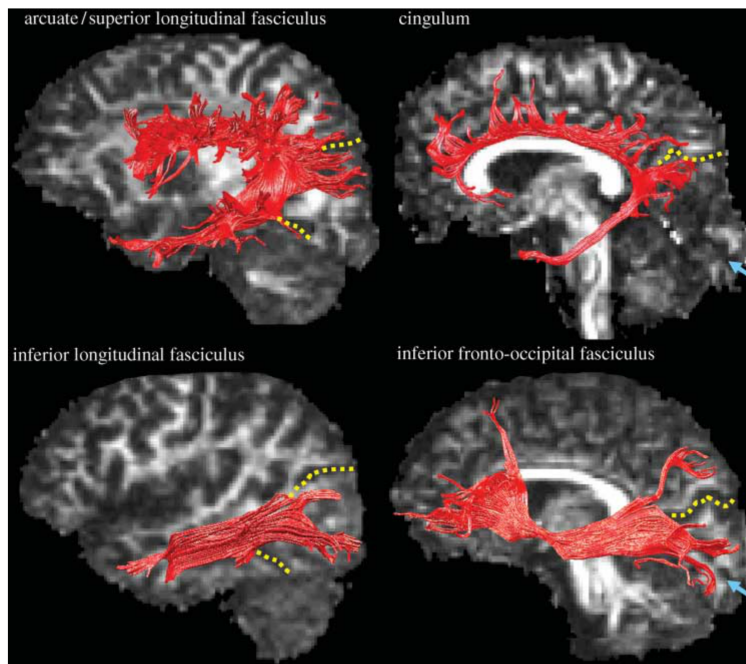


Figure 3.5: Long range cortico-cortical association tracts delineated using diffusion tractography. Tractography was performed in the left hemisphere of a single individual. Tracts are overlaid on sagittal and parasagittal MRI slices through the opposite hemisphere to the displayed tract. Image is taken from Catani et al. [65].

Scanning in large numbers not only allows characterisation of typical connection patterns, but also enables assessment of individual variability. Various studies have characterised the intra- and inter-subject reproducibility of macroscopic structural brain connectivity [16, 71]. The Human Connectome Project is a \$30 million NIH-funded study which aims to acquire high resolution diffusion and functional MRI datasets for 1200 individuals and apply state-of-the-art methodology to reconstruct maps of structural and functional connections *in vivo* and quantify the variability within and across individuals [259].

One clear benefit of obtaining structural information *in vivo* is the ability to correlate macroscopic structural connectivity to clinical phenotype [66]. Since diffusion MRI tractography was introduced, a large number of publications have reported changes in connectivity in diseases such as Alzheimer's disease, schizophrenia, Huntington's disease, autism and dyslexia. This has been hailed as somewhat of a revolution in the clinico-anatomical correlation method of studying brain diseases [66].

3.2.4 Large-Scale Brain Networks and Graph Theory

Graph theory provides a mathematical framework for the study of interacting elements composing a system, and was first introduced by Leonhard Euler in 1736. Euler conceived the Seven Bridges of Königsburg graph problem [26], which seeks to find a mathematical proof of the sequence of bridges traversed in order to visit every bridge once and only once in the town of Königsburg (now Kaliningrad), Russia (Fig. 3.6). Euler formed an abstract representation of the problem as a graph, where land masses were represented as nodes and bridges were represented as edges. Euler showed that such a path is possible if the graph is fully connected and there are exactly zero or two nodes with an odd node degree, meaning that the Seven Bridges of Königsburg graph problem has no solution. Thus, the concept of a graph was formally introduced.

A graph is defined as a mathematical representation of pairwise interactions between units. The fundamental units of a graph are the nodes (also known as vertices) and edges (also known as links, or connections). Nodes are units of the graph that receive and send information, whereas edges represent the information that is transferred between nodes.

Many other real world systems can be represented by graphs. For example, the transport system is a network of locations (nodes) joined by roads (edges). The shortest route between two locations is equivalent to finding the shortest path in the graph. Physiological metabolism can be represented as a graph where metabolic processes link different molecules. Similarly, the internet is a system of computers connected by cables. Humans are social beings and one of the largest application of

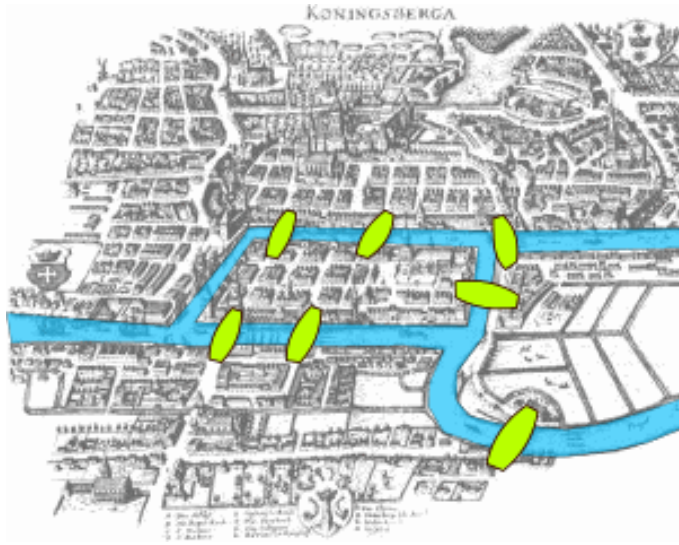


Figure 3.6: Map of Königsberg taken from the time Leonard Euler’s Seven Bridges of Königsberg problem was conceived, showing the four land masses and seven bridges (green) between them. The problem was to devise a walk through the city which traverses each bridge once and only once. Euler formulated the problem in abstract terms using graphs and determined that there was no solution. This was the first formal representation and analysis of graphs in a mathematical context. Image was taken from Wikipedia [283].

graph theory is in the study of social interactions.

Many fundamental graph theory metrics have been developed in the field of social networks. Graph theory metrics quantify the topological organisation of a network at the single node (local metrics) and network (global metrics) levels. Some commonly used local and global graph theoretical metrics are described below.

The clustering coefficient of a node measures the extent to which the connections from a particular node are themselves inter-connected, i.e. clustered [335]. The local clustering coefficient is calculated as the number of connections existing between the nearest neighbours of a node divided by the total number of possible connections. This formulation is equivalent to the fraction of triangles around a given node [279]. The global clustering coefficient is calculated as the mean clustering coefficient over all nodes, which is equivalent to the ratio of the number of connected triangles to possible triangles across the network.

The pathlength describes how close nodes are in terms of network topology [335]. A path exists between two nodes that can be connected by some combination of edge traversal. The pathlength between two nodes is calculated as the

minimum total number of edges traversed to travel through the network from one node to another. The local pathlength of a node is the average of path lengths that connect this node to all other nodes. The global pathlength is the mean of all local pathlengths in a network. The global pathlength therefore gives a general indication of the number of paths travelled to connect any two nodes in the network.

Betweenness centrality (referred to hereafter as centrality), is a measure of how frequently a given node acts as an intermediate node when considering all minimum paths between other nodes in the network [130]. It is the cumulative number of shortest paths between all other nodes in the network that pass through the given node, divided by the total number of connections in the network. Nodes with high centrality, defined as those having centrality two standard deviations above the mean across nodes, are considered as hubs, as they are particularly important in mediating communication between other nodes.

The small world phenomenon is a commonly reported characteristic in complex networks and signifies a network topology which is somewhere between a random network and a regular lattice [161]. A random network will have a relatively short global pathlength and low global clustering coefficient compared to a regular lattice, which will exhibit higher mean path length and higher clustering. A small-world network has either a shorter global pathlength than a random network, higher global clustering, or both. The small-worldness of a network can be calculated as the ratio of global clustering coefficient to global pathlength after both measures have been normalised by their equivalent values found in randomly generated networks. To make this calculation, networks of the same number of nodes and connection density, but a random combination of connections, are generated and their global pathlength and global clustering coefficient calculated. A small-worldness, or small-world index (SWI), greater than 1 indicates that the network has small-world properties.

Brains are networks of neurons connected by synapses. Recently, there has been huge rise in the popularity of connectomics approaches to studying brain connectivity [48]. Conceptually, the connectome refers to the representation of the

brains complete physiological wiring- including all neurons and connections. Observing and understanding this wiring is therefore the ultimate aim of connectomics. Currently, obtaining wiring diagrams of brain networks at the single neuronal level is possible only for a relatively small numbers of neurons, since individual neurons are mapped using serial sections. For instance, the complete connectome of the nematode worm *Caenorhabditis elegans*, which contains 302 neurons, was recently mapped in its entirety using electron micrographs of serial sections [342]. The human brain contains approximately 8.6×10^{10} neurons [7] which makes reconstruction of the human brain connectome at the single neuronal level currently infeasible. However, recent advances in image acquisition and post-processing methods in diffusion-weighted imaging have permitted the study of the complete ensemble of macroscopic brain connections *in vivo* using diffusion MRI tractography.

At the macroscopic scale, the cerebral cortex may be thought of as a network of hierarchically organised areas, that perform different sensory, cognitive or motor functions [120, 179]. In this context network nodes are grey matter regions with distinct function, such as those defined in Brodmann's or Campbell's maps [43, 57]. Edges of macroscopic brain networks are the long range association and callosal tracts connecting grey matter regions through the white matter. However, the definition of a functional unit of cortex is not established and differs depending on the cytoarchitectonic, myeloarchitectonic, connectional or other functional criteria used. In addition, since fiber bundles form physical connections that subserve directed functional interaction, edges in brain networks can be categorised as either structural, functional, or effective. Structural connectivity refers to representation of direct axonal connections between neurons or cortical areas. Functional connectivity refers to the statistical dependence between the physiological dynamics of brain regions, and effective connectivity refers to the directed influence that one region has over another.

Structural brain networks reconstructed using diffusion MRI tractography have been studied from both the methodological and applied perspective. Studies concerning methodological influences on structural brain networks include the effect

of acquisition and post-acquisition reconstruction methods on the intra- and inter-subject reproducibility of edge weights and graph theory metrics [320, 16, 56, 71, 72, 25, 47, 108, 36, 367], the effect of reconstruction methods on anatomical accuracy compared to tract tracing techniques [203, 17, 202, 329, 69], similarity between reconstruction methods [368, 251], the effect of node scale on graph theory metrics [359], the relation between structural and functional networks [159], and those concerning how to statistically analyse brain networks [357, 231, 288, 131, 330, 289, 361, 75]. Applied studies have characterised graph theory metrics in healthy populations (Fig. 3.7) [151, 166, 291, 143, 272, 167] with respect to development [155, 263, 353, 351, 317, 97, 265], ageing [144, 339, 121, 35, 254], gender [144, 105, 352, 164] and intelligence [204, 121], and across a range of neurological diseases such as Alzheimer's disease [211, 338, 284, 258], stroke [83, 189, 46], multiple sclerosis [287], epilepsy [320, 366, 199], schizophrenia [334, 360, 285, 364], autism spectrum disorder [201], early blindness [286] and many other diseases [18, 10, 54].

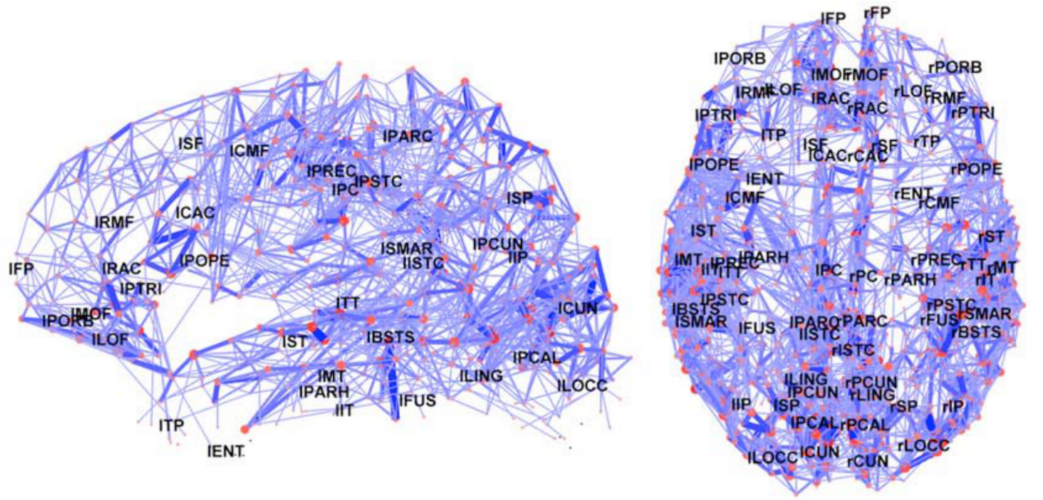


Figure 3.7: Network representation of brain connectivity for a single subject shown in lateral and dorsal views. Nodes (red) are cortical ROIs and edges (blue) are tracts connecting cortical ROIs. Shown is the backbone network derived from minimal spanning tree of the original network, which was constructed by performing tractography between the 998 ROIs. Node radii are scaled by the connection strength and edge width is scaled by streamline density. Image taken from Hagmann et al. [153].

Previous studies have shown that, like many other naturally occurring com-

plex systems, such as the internet and transport network, the structural network has a small-world topology [48, 335, 152]. Such networks are characterised by a similar global pathlength and a higher global clustering coefficient than equivalent measures found in randomly generated networks with the same node degree distributions. This organisation enables efficient information transfer between any two elements of the system and simultaneously a high degree of local communication [335], supporting the concept of segregation (highly interconnected sub-groups of brain regions, e.g. retinotopic maps) and integration (connections between sub-groups e.g. language systems) of information transfer in the human brain. The structural network contains hubs; regions that are highly connected or highly central to network communication [143, 153, 286, 246]. Occipital and parietal cortical regions are frequently highly connected and contain hub regions such as the left and right precentral cortical gyri and precuneus. In addition, networks have been split into communities of nodes, also known as modules, defined as sets of nodes which have relatively higher connectivity within than between communities. Modules are found hierarchically, with the left and right hemispheres forming the lowest level of modularity, where modularity is defined as the degree to which the networks components can be separated and recombined. Temporal, parietal, occipital and frontal lobes form the next level in the hierarchy and these are further sub-divided into smaller communities of highly connected nodes depending on the brain parcellation scheme. A recently described phenomenon of structural brain networks is the rich club node community. The rich club is a set of nodes that are both highly central and highly inter-connected, therefore sharing aspects of hubness and modular community. Regions such as the precuneus, superior parietal and superior frontal regions were designated as rich-club nodes in the original study [327], with their speculated function in improving integration of information transfer and providing robustness to network damage.

Many studies have demonstrated altered brain network topology in disease groups compared to controls at both the local and global level. For example, Xu et al. [346] used diffusion tensor tractography to investigate the topological prop-

erties of structural networks in a group of medial temporal lobe epilepsy patients compared to controls [346]. They found that both groups had a balance between integration and segregation of network topology, as indicated by their small-worldness properties. However, an increase in global pathlength of medial temporal lobe epilepsy patients and a decrease in efficiency and nodal degree of some regions (such as the left superior temporal gyrus, left hippocampus, the right occipital and right temporal cortices) was observed. Liu et al. [210] examined the white matter network in a cohort of patients with left temporal lobe epilepsy and mesial temporal sclerosis compared to healthy controls [210]. By analysing deterministic tractography networks using graph theory they found decreases of global and local efficiencies and widespread reduction of regional efficiency in ipsilateral temporal, bilateral frontal, and bilateral parietal areas. This study supports of widespread structural network alterations in medial temporal epilepsy with hippocampal sclerosis. Vaessen et al. [323] examined large-scale structural and functional networks in childhood frontal lobe epilepsy [323]. The broad scale of affected cognitive domains suggests a widespread network pathology which may extend beyond the frontal lobe. They also found increased clustering and pathlength in functional but not structural networks, suggesting that childhood frontal lobe epilepsy may involve a decoupling between structural and functional networks.

A major challenge in applying network analysis in disease groups is the specificity of findings of altered connectivity. Many studies have demonstrated increased global pathlength in disease groups, indicating loss of efficient network connectivity. Another challenge concerns the reproducibility of findings across different individuals, sites and methodological pipelines. A reproducible finding indicates that the measure depicts real biological information, but high reproducibility is difficult to achieve due to imperfect reproducibility of the diffusion-weighted images [320] and the unknown impact on reconstructed networks when applying a variety of methodological tools that are combined [251, 368]. Other challenges include determining the anatomical validity of reconstructed networks [203], the choice of connection strength threshold [330, 104, 88], normalisation of network measures

by their null network equivalents [289, 131] and how to separate effects of different network measures on one another [289].

3.3 Summary

In this chapter the micro- and macroscopic aspects of brain structural connectivity, as learnt through classical and contemporary fiber tracing techniques, were described. Organisation of neurons into a cortical column, their lateral connections, and how morphology and connectivity of the cortex define cortical function were summarised. Next, discovery and characterisation of the major white matter fibers and the current and contemporary theories about how these relate to brain function in health and disease were outlined. Finally, the major contributions of diffusion MRI tractography to contemporary knowledge on human brain connectivity and the emergence and use of connectomics research was explained.

Chapter 4

Consensus and Reproducibility in Structural Networks

Structural brain network reconstruction is complex and yields large amounts of quantitative information relating to inter-region connectivity. Such information may be used to discover new biomarkers for neurological disease and therefore it is essential to determine the intra- and inter-subject reproducibility as well as the agreement across different post-acquisition reconstruction pipelines. This chapter describes the variation in methods used for reconstructing network nodes and edges. Methods are described to quantify reproducibility and consensus in connection weights between independent yet contemporary state-of-the-art reconstruction pipelines with a variety of different cortical atlases. It is shown that both reproducibility and consensus are high across all atlases and density thresholds. The significance of these findings are discussed with respect to the broader literature relating to reproducibility, inter-pipeline agreement and atlas node scale. The parts of this chapter concerning consensus between pipelines was recently published [251].

4.1 Introduction

Studying brain structural networks using diffusion MRI tractography has recently become a popular research topic in neuroscience [48]. In this field the research aim is to quantify connectivity between grey matter regions via white matter pathways *in vivo*, on a global scale, in order to understand the topological organisation of brain

structure and to relate this to aspects of neurological health and disease. The structural topology may be analysed by characterising the brain as a graph, whereby sets of network nodes, representing grey matter regions, transfer information between one another via network edges, representing connecting axonal pathways.

It has been suggested that the organisation of the structural network may reflect neurological phenotype. For example, network metrics such as clustering coefficient and pathlength have been related to the effect of age [106], gender [144] and IQ [204]. In addition, network alterations have been observed in neurological diseases such as Alzheimer's disease [211, 284], epilepsy [322, 365] and schizophrenia [328, 360, 334], meaning such metrics may become useful as topological biomarkers of brain integrity or pathology. However, reconstructing brain network nodes and edges is both a conceptual and practical challenge and there is little agreement between studies of how exactly these should be defined.

Nodes of the brain network, which represent spatially distinct regions of grey matter, may be defined using different parcellation schemes and scales. A common parcellation technique has been to warp the structural image to an anatomical template, such as the AAL atlas [318], where the grey matter regions have been manually labelled in a single representative subject [143, 204, 328, 334]. Alternative warping strategies have been applied; for example, those utilising cortical shape and curvature information [339], or multiple template propagations [272]. In addition, different templates may be used to generate different parcellation schemes. Most parcellations used in whole-brain structural network studies have been relatively coarse, with around 100 brain regions. Because of the uncertainty concerning where to place region boundaries, some studies have divided parcellated regions into smaller pseudorandom patches [151, 317], or performed network analysis across a range of parcellation scales [153, 154, 109]. Regions defined in structural space must then be accurately warped to diffusion space in order to estimate the inter-regional connectivity, and a number of registration schemes are available.

Edges of the structural brain network, which represent white matter tracts between two grey matter regions, are frequently quantified based on the number

of connecting fibers. As such, the issue of which fiber model, initialisation and tracking technique to use arises. The diffusion tensor model [15], combined with deterministic tracking, is a common technique for reconstructing network edges [286, 339, 155, 9]. Multiple fibers may be represented using multiple diffusion tensors, the orientation distribution function (ODF) [336], multi-compartment models [22] and the fiber orientation distribution (FOD) [308]. The ball and sticks multi-compartment model is one example of a popular fiber model employed to track through multiple fiber populations in structural network studies [144, 105]. In contrast to multi-compartment models, the FOD representation assumes an identical signal response for each fiber population and does not employ model fitting. Deterministic tracking determines inter-regional connectivity by following the dominant fiber orientation whereas probabilistic tracking samples directions from a distribution of orientations to produce a connectivity distribution.

In networks obtained using probabilistic tractography, a continuous measure of connectivity is generated which reflects, to some degree, the probability of connection between all pairs of brain regions. A probability threshold may then be applied to produce a binary network, where connections are either absent or present [320]. However, assigning importance to connections is a challenge and the choice of threshold affects the occurrence of false positive and negative connections, resulting in a trade-off between sensitivity and specificity of the connections [88, 203]. Thresholding also has an intrinsic impact on the network topological measures [330].

Given the complexity and number of steps involved in network reconstruction from the raw diffusion MRI images, it is important to provide an assessment of consensus in networks obtained from alternative reconstruction pipelines which vary not in just one or two components but in the entire reconstruction pipeline (i.e. the parcellation, registration and fiber model). This would also enable some assessment of the potential impact in swapping and substituting individual components of the reconstruction.

Furthermore, pipelines may vary in reproducibility of structural network con-

nection weights or derived graph theoretical measures. A number of recent publications have assessed the impact of methodological choice on reproducibility of structural brain networks [320, 16, 71, 56]. Reproducibility has been investigated, using repeated diffusion-weighted scanning, with respect to both diffusion signal acquisition scheme [320, 16], parcellation scheme and scale [16, 56] and connectivity weighting scheme [71]. Vaessen et al. [320] reported high reproducibility for some network metrics and found that the diffusion encoding scheme had little effect on their reproducibility [320]. Bassett et al. [16] averaged reproducibility over different parcellation schemes and scales in diffusion tensor and diffusion spectrum acquisitions [16]. They found that reproducibility was higher using diffusion tensor acquisitions and that topological network properties, such as small-worldness and modularity were preserved across different parcellation schemes and scales. Cammoun et al. [56] examined reproducibility across multiple node scales by manually merging regions in a small group of subjects. They found that connection reproducibility was dependent on node scale, as higher node scale networks had lower reproducibility [56].

In this study, we assessed the consensus and reproducibility of structural connectivity networks obtained from two alternative pipelines across a range of network density thresholds, by merging alternative parcellations to a common and equivalent node scale. This allowed us to investigate similarity between independent network reconstructions on a connection-wise basis and to identify the underlying brain connections occurring most robustly in both pipelines. Our results suggest it may be useful to apply multiple pipelines to obtain structural brain networks from diffusion data and to employ the comparison framework described here to identify the most important connections.

4.2 Methods

A summary of the structural network reconstruction pipeline is shown in Fig. 4.1.

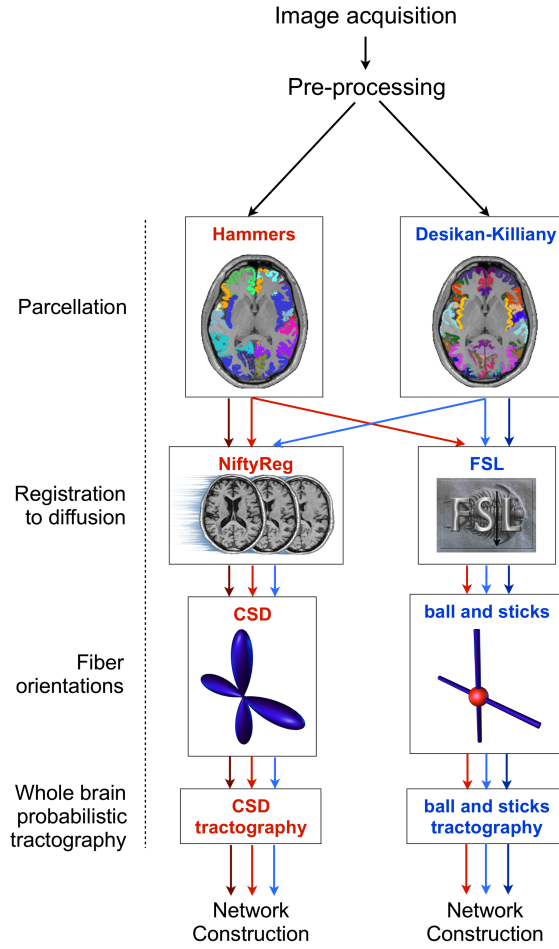


Figure 4.1: Summary of network reconstruction stages applied to structural and diffusion images for P1 and P2. The pipeline stages are shown on the left and the alternative implementations of the methods are shown inside the boxes. Arrows indicate the passage of merged (dark arrows) and native (light arrows) atlases through the pipeline stages (red and blue refer to Hammers and Desikan-Killiany atlases, respectively). Nodes were defined by registration of the cortical parcels to diffusion space. Edges were defined by performing tractography from the parcel boundary through the fiber orientations. Note that the whole-brain probabilistic tractography methods differed only in relation to the recommended settings for the software used to track through the fiber orientations. The network construction stage calculated the connecting fiber density between all cortical parcel pairs across the entire cerebral cortex and was identical for both pipelines. Applying these stages to the merged and native atlases resulted in comparisons between pipelines at three node scales; the merged atlas scale (34 nodes, dark arrows), Hammers atlas scale (44 nodes, light red arrows) and Desikan-Killiany scale (68 nodes, light blue arrows). We also applied the registration and whole-brain tractography pipelines to the AAL atlas (not shown).

4.2.1 Subjects and Images

Twenty-eight young healthy adult subjects (16 male, mean age \pm SD 28.5 ± 3.9 years) participated in this study. Subjects had no brain abnormalities at the time of scanning, as determined by examination of their structural scan by an expert radiologist. Two T1-weighted images of $1 \times 1 \times 1$ mm resolution were acquired sequentially with a 3D Fast Low-Angle Shot (FLASH) sequence (176 contiguous sagittal slices, 256 x 224 mm FOV, TR=11 ms, TE=4.94 ms and $\alpha=15^\circ$) on a 1.5 T Siemens Avanto MRI scanner at Great Ormond Street Hospital, London. A diffusion-weighted echo planar sequence (TR = 7300 ms, TE = 81 ms) with 60 non-collinear diffusion directions ($b = 1000\text{s/mm}^2$) was used to acquire diffusion-weighted images of $2.5 \times 2.5 \times 2.5$ mm and three un-weighted images ($b=0$ images). The diffusion-weighted sequence was repeated three times for each subject in a single scanning session.

4.2.2 Image Pre-processing

DICOM images were converted into NIfTI format using TractoR [74] and the brain was extracted from all images using FSL's brain extraction tool [290]. In order to increase the signal to noise ratio of the structural image, the two acquired T1-weighted images were registered and averaged in Freesurfer v5.1.0 [270]. The diffusion-weighted volumes were corrected for eddy-current induced distortions by affine registration to an unweighted reference image using the diffusion-specific FSL FDT algorithm [169].

We chose to compare two alternative state-of-the-art reconstruction pipelines (these two pipelines will hereafter be referred to as P1 and P2, Fig 1). Both reconstructions had similar capabilities but varied with respect to the details of the cortical parcellation, registration and probabilistic fiber model method.

4.2.3 Cortical Parcellation

To define network nodes, the cortical grey matter of the averaged T1-weighted image was parcellated into regions using automated software. **P1.** NiftySeg was used to parcellate the structural image into 44 cortical regions (22 per hemisphere), as

defined by the Hammers Atlas [156]. The parcellation algorithm first labels brain regions by propagating a set of manually labelled T1-weighted images to the structural image [59, 237]. The LoAd tissue segmentation algorithm was then applied to the structural image to obtain the cortical grey matter of the parcellated regions [60]. **P2.** Freesurfer was used to parcellate the structural image into 68 cortical regions (34 per hemisphere), as defined by the Desikan-Killiany Atlas [99]. The parcellation algorithm assigns a neuroanatomical label to each location on a cortical surface model of the image, based on probabilistic information from a manually labelled training set [122].

4.2.4 Native and Common Node Scale Parcellations

The pipelines employed atlases with a different number of brain regions, preventing a direct connection-wise comparison between them. Therefore, parcels in the native atlases were merged to a common node scale (Fig. 4.2). The number of merges was the minimum required to give correspondence between the atlases and resulted in 34 brain regions (17 per hemisphere). Parcels in the Desikan-Killiany atlas (P2) were merged across the entire cortex based on anatomical correspondence to their equivalent Hammers atlas (P1) parcels. For example, the pars opercularis, pars orbitalis and pars triangularis parcels in the native Desikan-Killiany atlas corresponded to the inferior frontal gyrus parcel in the native Hammers atlas and therefore in both of the merged atlases. The Desikan-Killiany and Hammers atlases differed fundamentally in temporal lobe regions, meaning an equivalent merging of parcels could not be found. Therefore, the temporal lobe is itself considered as a single node in both merged parcellations (Fig. 4.2 and 4.3). The merging process did not result in identical parcellations. The remaining differences in common scale parcellations were due to alternative border criteria as well as alternative parcellation algorithms. Therefore, in addition to the native Desikan-Killiany and Hammers atlases, we also obtained the two merged 34 node scale versions of each atlas for each subject (Fig. 4.3).

Each common scale parcellation was registered to diffusion space (as described below) using the registration implementation for the corresponding pipeline (e.g.

following the P1 registration-tractography for the merged P1 parcellation). We also applied the paired registration-tractography implementation from each pipeline to both of the native atlases. We further tested the robustness of our results by applying each registration-tractography implementation to the Automated Anatomical Labelling (AAL) Atlas parcellation, which had 78 cortical regions [318].

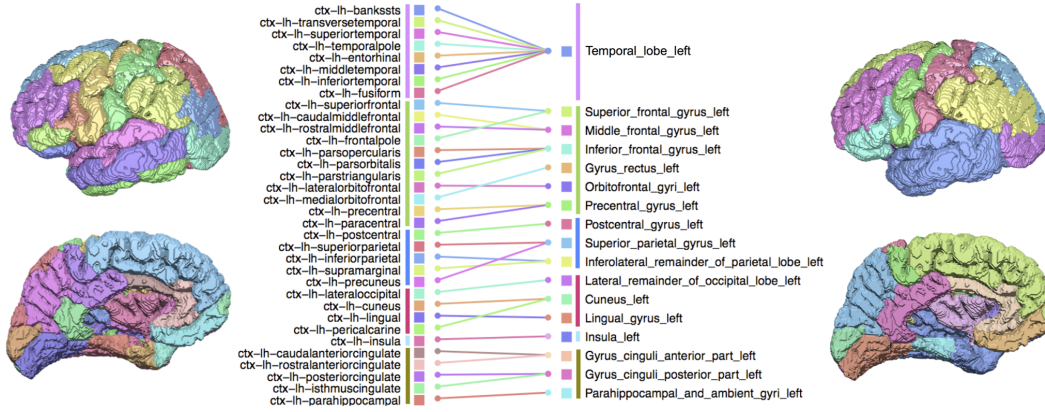


Figure 4.2: Merging cortical parcels of P2 parcellations. The native scale P2 parcellation (68 parcels) is shown on the left and the merged P2 parcellation (34 parcels) is shown on the right. The merging pattern was identical for both hemispheres and therefore only the left hemisphere is shown. The colour scheme of brain regions is as in Fig. 4.3. Lines represent merging of native scale parcels (left) to their equivalent common scale parcels (right). Coloured vertical lines correspond to regions in the temporal (purple), frontal (green), parietal (blue), occipital (red), insula (light-blue) or limbic (yellow) lobes. Native scale P1 parcellations (44 nodes) were merged to the common scale parcellation by merging all temporal lobe parcels.

4.2.5 Registration of Cortical Parcels to Diffusion Space

The structural and diffusion-weighted images were co-registered in order to define the cortical parcels of interest in diffusion space. The registration field was determined as follows. An affine registration was used to register the first $b=0$ image to the averaged T1-weighted image. The T1-weighted image was then non-linearly registered to the $b=0$ image using the inverse of the transformation acquired in the previous stage as a starting transformation. The transformation field was retained and applied to the cortical parcellation to transform parcels to diffusion space. The categorical nature of the labels was preserved through a nearest neighbour resampling scheme. **P1.** NiftyReg was used to perform the linear and non-linear registrations using the default settings [280, 237]. NiftyReg used normalised mutual

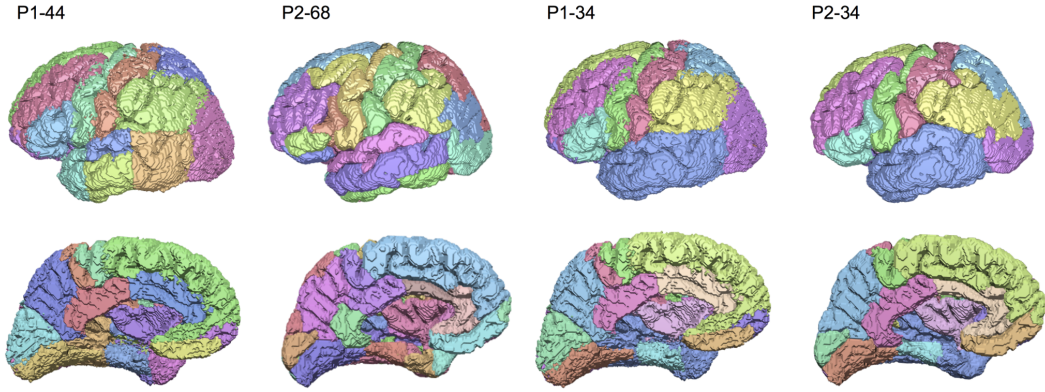


Figure 4.3: Representative cortical parcellations of P1 and P2 at the native and common node scale. Temporal lobe regions in P1 native scale parcellations (P1-44, far left) were merged, resulting in a lower scale parcellation (P1-34, middle right). Selected regions across the entire cerebral cortex in P2 native scale parcellations (P2-68, middle left) were merged (P2-34, see Fig. 4.1). This resulted in a common and anatomically equivalent parcellation scale of 34 nodes for both P1 and P2 networks.

information to calculate image similarity and a bending energy regularisation with cubic B-spline parameterisation for the non-linear warping. **P2.** The linear and non-linear registration was performed by FSL FLIRT and FNIRT, respectively [169]. Normalised cross correlation and sum-of-squared difference was used to calculate image similarity for the linear and non-linear warping stages, respectively. The membrane energy was used to regulate the non-linear warp field which was parameterised as a cubic B-spline scheme.

4.2.6 Fiber Orientations

The orientations of fiber bundles at each voxel were inferred using one of two methods. **P1.** CSD was applied to estimate the underlying FOD in each voxel, using MRTrix [309]. CSD assumes that the observed diffusion signal is a convolution of fiber orientations and a diffusion signal response function, meaning the fiber orientations may be extracted by spherical deconvolution of the diffusion signal. The maximum spherical harmonic order for the deconvolution was set to 8. **P2.** A ball and two sticks multi-compartment fiber model was fitted to the diffusion data, using the Bayesian Estimation of Diffusion Parameters Obtained using Sampling Techniques (BEDPOSTX) algorithm in FSL. The BEDPOSTX algorithm uses Markov chain Monte Carlo sampling to estimate the uncertainty in fiber orientations [23].

4.2.7 Probabilistic Fiber Tractography

The paths of fiber trajectories in the brain were reconstructed by seeding 100 probabilistic fibers from the interior boundary voxels of each cortical parcel. The interior boundary voxels were the intersection of the dilated binary cortical parcellation with the fiber propagation mask (defined for each pipeline below). **P1.** Fibers were propagated using the default settings in MRTrix [307]. The sampling interval was 0.2 mm, maximum curvature threshold was 60° and minimum FOD amplitude threshold for tracking through a voxel was 0.1. The propagation mask was defined as the union of white matter, sub-cortical grey matter and ventricle regions from the LoAd tissue segmentation provided by NiftySeg. **P2.** The default settings in FSL ProbTrack algorithm were used to determine the fiber trajectories [22]. The sampling interval was 0.5 mm and stopping criteria meant that fibers terminate if they curve by more than 80° . The propagation mask was defined as the white matter segmentation provided as part of the Freesurfer output, and included white matter, sub-cortical and ventricular regions.

Note that P1 initiates fibers by uniform sampling of boundary voxels with a FOD amplitude greater or equal to 0.2, whereas P2 initiates fibers from the centre of each boundary voxel. Also, P1 terminates fibers if the FOD amplitude is below 0.1. For both pipeline tracking schemes, fibers were terminated immediately after leaving the propagation mask so that their cortical parcel connections could be recorded.

4.2.8 Network Construction

Network construction and analysis was performed using the R programming language [301]. Cortical parcels were represented as network nodes and the fiber connections between them as edges. Fibers connected node pairs if their end-point coordinates terminated within two distinct cortical parcels. The connection weight between two cortical nodes was defined as the density of connecting fibers (as in [72]), calculated as the sum of connecting fibers divided by the mean volume of the seed (boundary) voxels adjacent to the two parcels (boundary voxels were assigned to the nearest parcel by Euclidean distance). Performing this calculation for all

fibers produces an N -by- N undirected matrix of connection weights, where N is the number of nodes in the parcellation (either 34, 44, 68 or 78). The weighted cortical connection matrix was calculated for the repeat diffusion scans of all subjects. The subject mean weighted connection matrices (across the three repeat diffusion scans) were calculated for all subjects by averaging each weight across all scans.

4.2.9 Consensus between Reconstruction Pipelines

Convergence between alternative pipelines was investigated in binary networks of equal density. Binary networks were generated by thresholding the subject weighted networks and convergence was quantified for all possible densities in the range $[0,1]$, by selecting the x highest ranked connections in the weighted matrix, for $x = 1 : c$, where c is the total number of possible connections (calculated as $(N^2 - N)/2$). Connections of equal weight (predominantly weights of value 0), were randomly assigned a rank, meaning connections were chosen randomly if the network density threshold intersected connections of equal weight. Convergence was quantified between the pair-wise subject binary networks using the Dice Similarity Coefficient (DC). DC was defined as the proportion of intersecting connections relative to the total number of connections at that density. This measure is identical to the percentage convergence measure of network similarity used in [145] for networks of equal density.

Our investigation was interested in similarity between pipelines independent of network density effects (denser networks have a higher DC by chance). Therefore, at each network density, we computed a one sample t-statistic between the observed DC across all subjects to the expected DC value, using a two-tailed t-test. The expected DC value was equal to the network density, d , as the number of connections expected to agree in two random binary networks ($d.d.c$) was divided by the total number of connections ($d.c$). Our null hypothesis was that similarity between pipelines was equal to that by chance, given the density. The p-value computed from this t-statistic was our estimate of the significance of the similarity. To estimate the dependency of the significance on our sample population, we bootstrapped the subjects 1000 times at each network density. As lower p-values

represented higher similarity, we inspected the negative logarithm of the p-value to obtain a global maximum significance and corresponding network density where the binary network similarity was most reliably different from random.

4.2.10 Network Properties of Consensus Networks

The binary networks corresponding to the peak convergence threshold will hereafter be referred to as ‘consensus networks’ for convenience. The graph theoretical properties of the consensus networks were calculated for all subjects using the *igraph* package [84] in the R programming language. The global properties of characteristic pathlength [335] and global efficiency [193], and the local properties of local efficiency [193], clustering coefficient [244] and assortativity [243], were calculated as described in [279].

4.2.11 Reproducibility of Structural Networks

Variance of connection weights in each atlas and each pipeline were calculated using a random effects model [73]. This is a linear model which assumes that there are two levels of variance (intra and inter-subject) that explain the observed data with respect to an overall population mean. The connection weight for the j th scan of the i th subject, a_{ij} , can be described as $a_{ij} = \mu + \delta_i + \varepsilon_{ij}$, where $\delta \sim N(0, \sigma_b^2)$ and $\varepsilon \sim N(0, \sigma_w^2)$.

The intra- and inter-subject variances (σ_w^2 and σ_b^2 , respectively) and overall population mean (μ) were fitted using a restricted maximum likelihood estimation, implemented using the ‘lmer’ function of the ‘lme4’ package in the R programming language [19].

Reproducibility of entries in the cortical weighted matrix was quantified using the intra-subject and inter-subject Coefficient of Variation (CV, σ_w^2/μ and σ_b^2/μ , respectively) and the Intra-class Correlation Coefficient (ICC, $\sigma_b^2/(\sigma_b^2 + \sigma_w^2)$). The CV measures the standard deviation as a fraction of the mean, while the ICC measures the ratio of between subject variance to total variance (defined as the intra-subject plus inter-subject variance). An ICC above 0.5 indicates good intra-subject reproducibility, as the inter-subject variance is greater than the intra-subject vari-

ance. Reproducibility was assessed in the common scale pipelines and native pipelines. Reproducibility was examined across density thresholds by selecting those supra-threshold connections in the subject grand mean weighted matrix.

4.3 Results

4.3.1 Consensus Between Reconstruction Pipelines

The raw weights matrix represents the connecting fiber density between cortical region pairs across the entire cerebral cortex. The connecting fiber density was highly correlated between subject mean networks obtained from alternative reconstructions in terms of both rank and weight (34 nodes: Spearman $\rho = 0.675 \pm 0.06$, Pearson $r = 0.630 \pm 0.061$, 44 nodes: Spearman $\rho = 0.677 \pm 0.076$, Pearson $r = 0.702 \pm 0.085$, 68 nodes: Spearman $\rho = 0.586 \pm 0.095$, Pearson $r = 0.632 \pm 0.085$), confirming that these pipelines had yielded similar networks.

A general trend of decreasing DC with decreasing network density was observed. The grand mean DC across all subjects and densities was 0.741 ± 0.165 , 0.759 ± 0.132 and 0.724 ± 0.135 for the 34, 44 and 68 atlas scales, respectively. At a network density of 1 the DC was 1 as all connections existed in both pipelines. Clearly, the DC should be interpreted in the context of the expected similarity of random networks at the same density (Fig. 4.4).

The networks were significantly more similar between pipelines than by chance across all density thresholds (Fig. 4.5). Similarity increased approximately linearly with increasing threshold (corresponding to a decreasing network density), until very high thresholds were reached, where a peak similarity was observed (at network densities between 0.1 - 0.2, depending on the atlas), after which similarity decreased sharply towards 0. The peak similarity threshold resulted in binary networks that were most highly similar between the pipelines whilst accounting for the expected similarity at this density by chance. The most highly significant similarity was found at densities of 0.196, 0.161 and 0.106 (110, 152 and 242 connections) for node scales of 34, 44 and 68, respectively. The magnitude of the significance was similar between atlases of different scales ($-\log p \approx 75$) at the peak similarity

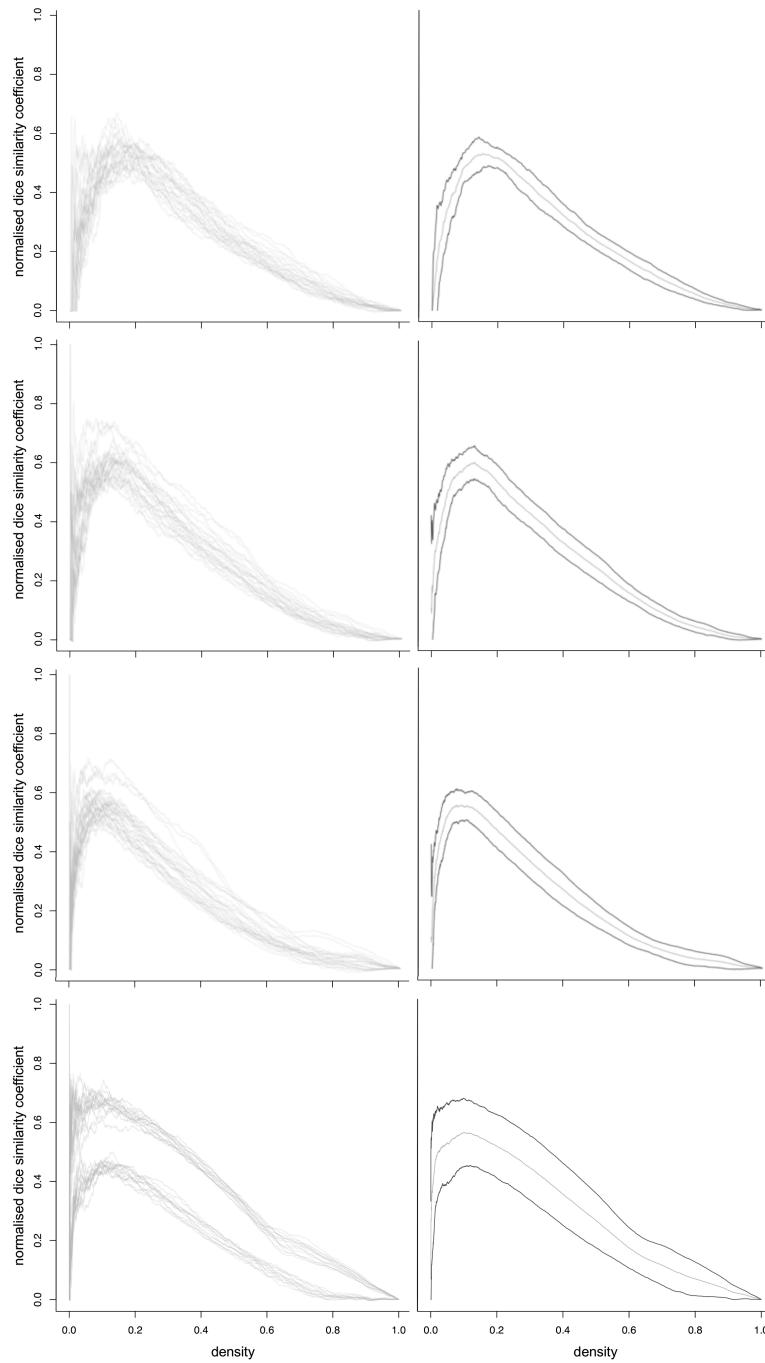


Figure 4.4: Normalised dice similarity coefficient between pipelines across density thresholds for all subjects. The normalised similarity coefficient was calculated by subtracting the expected from the observed dice coefficient at each density. Shown are the the subject normalised dice coefficients (left) and the mean normalised dice coefficient \pm standard deviation (right) for pipelines using the Common (top), Hammers (middle-top), Desikan-Killiany (middle-lower) and AAL (lower) atlases. A peak normalised dice coefficient is observed for densities in the region of 0.05-0.20 for all atlases.

threshold.

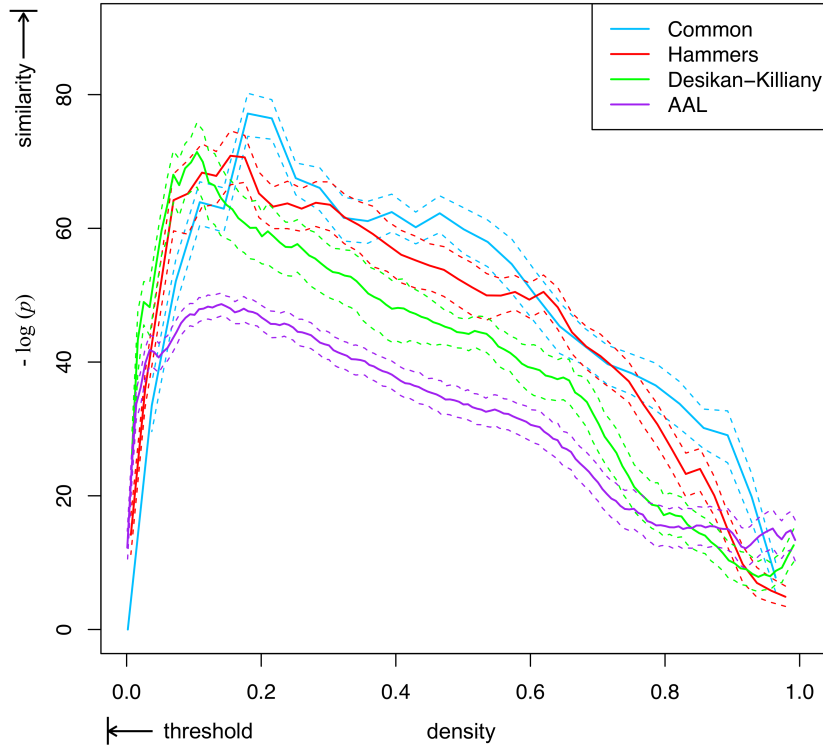


Figure 4.5: Similarity between P1 and P2 networks across density thresholds using atlases at three node scales. Significance of similarity was calculated by comparing the distribution of within-subject DC to the expected DC by chance, given the density of the networks. Shown is the mean negative log p -value of the DC between binary networks thresholded at a given density. The within-subject DC's were bootstrapped to obtain a standard error on the mean (dashed lines). A global peak similarity was found at a density of 0.196, 0.161, 0.106 and 0.142 for the Common (34 nodes), Hammers (44 nodes), Desikan-Killiany (68 nodes) and AAL (78 nodes) atlases, respectively.

Similar results were obtained using the AAL atlas. The weighted networks were highly correlated between pipelines in terms of rank and weight (Spearman $\rho = 0.703 \pm 0.161$, Pearson $r = 0.692 \pm 0.162$) and the grand mean DC was 0.701 ± 0.114 (Fig. 4.4). The peak similarity was observed at a density of 0.142 (427 connections), where $-\log p$ was 48.9 (Fig. 4.5).

The paths of fibers underlying peak convergent connections are shown in Fig. 4.6. Fibers representing the inter-lobe connections, intra-lobe connections and inter-hemispheric connections are shown for a representative subject reconstructed through the P1 pipeline. By visual inspection, it can be appreciated that the spatial

distribution of fibers corresponds with known major anatomical tracts according to previous literature [62]. Major white matter tracts, such as the inferior longitudinal fasciculus, superior longitudinal fasciculus, cingulum and arcuate, were represented by fibers underlying inter-lobe connections. On the other hand, fibers representing intra-lobe connections appeared to be mostly cortical U-fibers.

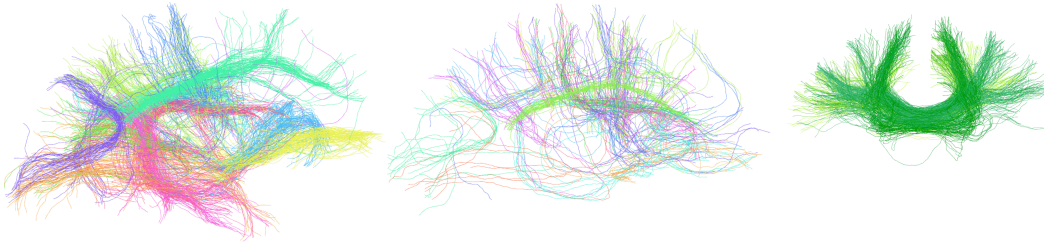


Figure 4.6: P1 fibers underlying convergent connections in the left hemisphere of a representative subject. Fibers are coloured by their network connection. (a) Inter-lobe fibers viewed from the medial aspect. (b) Intra-lobe fibers viewed from the medial aspect. (c) Inter-hemispheric fibers shown from the coronal aspect. The paths of fibers underlying convergent inter-lobe connections agrees with that of major anatomical tracts, such as the ILF (orange) and cingulum (green). Convergent intra-lobular connections were mostly represented by short-range cortical U-fibers. Convergent inter-hemispheric fibers travel via the corpus callosum and connected homotopic cortical regions, such as the superior, middle and inferior frontal gyri (green). For visual clarity, a maximum of 200, 50 and 100 fibers from the subset of whole-brain tractography fibers are shown per connection for (a), (b) and (c), respectively. Also, only fibers greater than 7 cm are shown for (a) and (b) and greater than 10 cm for (c).

4.3.2 Network Properties of Consensus Networks

The convergent connections of the consensus networks are summarised in Fig. 4.7. The connections that agreed between pipelines tended to be similar across subjects. The convergent connections, which had high hemispheric symmetry, were primarily between ipsilateral intra-lobe regions and between bilateral homotopic regions. The left and right insula gyri were the most highly connected nodes in the consensus network.

The density of the consensus networks decreased when comparing lower to higher node scales atlases, whereas the number of connections increased. The graph theoretical metrics of global pathlength, clustering coefficient, global efficiency, local efficiency and assortativity, which were calculated for all consensus networks,

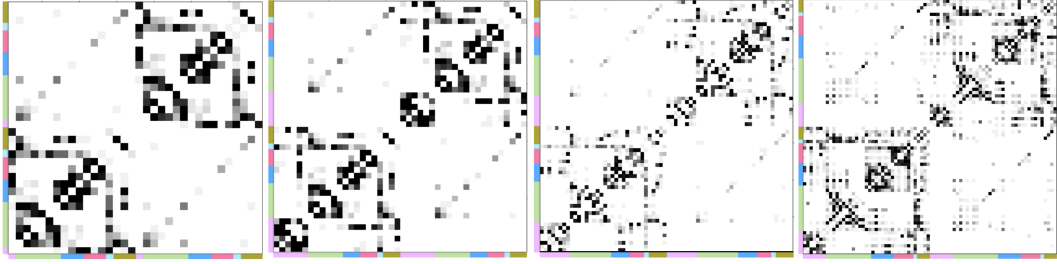


Figure 4.7: Prevalence of convergent connections across subjects at the peak convergence density. The prevalence is shown for the common (left), Hammers (middle-left), Desikan-Killiany (right-left) and AAL (right) atlases. Convergent connections were defined as the intersection of subject networks thresholded at the peak convergence density obtained from our bootstrap statistical analysis. The node lobe memberships are indicated by the adjacent colour bars, as in Figure 2. Colours represent the temporal (purple), frontal (green), parietal (blue), occipital (red), insula (turquoise) and cingulate (brown) lobes.

are shown in Table 4.1. Graph theoretical properties of the consensus networks were similar between pipelines employing atlases at the same node scale, whereas some differences were found in graph theoretical properties between atlases of different node scales. The global pathlength and clustering were not significantly different between pipelines at the same scale but tended to increase and decrease in higher node scale atlases, whereas global efficiency tended to decrease. Assortativity was less stable between pipelines and showed no clear trend with node scale. The AAL atlas consensus networks had a relatively high density considering the number of network nodes in the parcellation, compared to other atlases.

Atlas (nodes)	DC	Connections	Density	PL	CC	G.Eff	L.Eff	AS
Common (34)	0.71±0.03	110	0.196					
P1				2.39±0.08	0.47±0.02	0.42±0.01	0.71±0.04	0.12±0.09
P2				2.42±0.17	0.47±0.05	0.42±0.03	0.72±0.05	0.04±0.08
Hammers (44)	0.74±0.05	152	0.161					
P1				2.69±0.11	0.48±0.02	0.37±0.02	0.74±0.03	0.10±0.10
P2				2.61±0.11	0.48±0.04	0.38±0.02	0.71±0.03	0.06±0.06
Freesurfer (68)	0.66±0.05	242	0.106					
P1				2.93±0.14	0.41±0.03	0.34±0.02	0.67±0.05	0.12±0.06
P2				2.94±0.18	0.43±0.04	0.34±0.02	0.71±0.04	0.02±0.05
AAL (78)	0.70±0.11	427	0.142					
P1				2.40±0.09	0.45±0.03	0.42±0.02	0.42±0.01	0.11±0.07
P2				2.43±0.04	0.47±0.01	0.41±0.01	0.42±0.01	0.07±0.06

Table 4.1: Graph theoretical characteristics of consensus network (subject binary networks thresholded at the peak convergence density). Shown are the mean \pm standard deviation of the graph theoretical properties of Pathlength (PL), Clustering Coefficient (CC), Global Efficiency (G. Eff), Local Efficiency (L. Eff) and Assortativity (AS), across subjects.

4.3.3 Reproducibility of Structural Networks

The distribution of reproducibility metrics for all cortical associations was not significantly different between common and native scale networks or between alternative reconstruction pipelines (Fig. 4.8, density = 1). However, there was a trend of increasing reproducibility (higher ICC and lower intra- and inter-subject CV) when the density of the network decreased (i.e. weaker associations were removed), with lower vs. higher scale networks, and for P1 vs. P2 networks.

We examined reproducibility metrics across a range of density thresholds of the group networks for both common and native node scales. For both P1 and P2 pipelines, reproducibility metrics improved approximately linearly with decreasing density. A trend for higher reproducibility for P1 vs. P2 networks and common scale vs. native scale connections was observed when comparing results across equivalent densities.

At the common node scale, the median ICC increased from 0.74 to 0.91 for P1 connections and from 0.64 to 0.73 for P2 connections. Intra-subject CV decreased from 0.56 to 0.07 for P1 networks and from 0.97 to 0.21 for P2 networks, while inter-subject CV also decreased from 0.93 to 0.25 for P1 networks and from 1.26 to 0.28 for P2 networks as density decreased. Using the Hammers Atlas, the median ICC increased from 0.72 to 0.89 for P1 connections and from 0.61 to 0.74 for P2 connections as density decreased. Intra-subject CV decreased from 0.66 to 0.12 for P1 networks and from 1.08 to 0.18 for P2 networks, while inter-subject CV also decreased from 1.06 to 0.35 for P1 networks and from 1.28 to 0.35 for P2 networks as density decreased. With the Freesurfer Atlas, the median ICC increased from 0.65 to 0.88 for P1 connections and from 0.55 to 0.77 for P2 connections as density decreased. Intra-subject CV decreased from 0.93 to 0.16 for P1 networks and from 1.43 to 0.27 for P2 networks, while inter-subject CV also decreased from 1.21 to 0.49 for P1 networks and from 1.45 to 0.48 for P2 networks as density decreased. Using the AAL Atlas, the median ICC increased from 0.64 to 0.86 for P1 connections and from 0.51 to 0.77 for P2 connections as density decreased. Intra-subject CV decreased from 0.95 to 0.18 for P1 networks and from 1.54 to

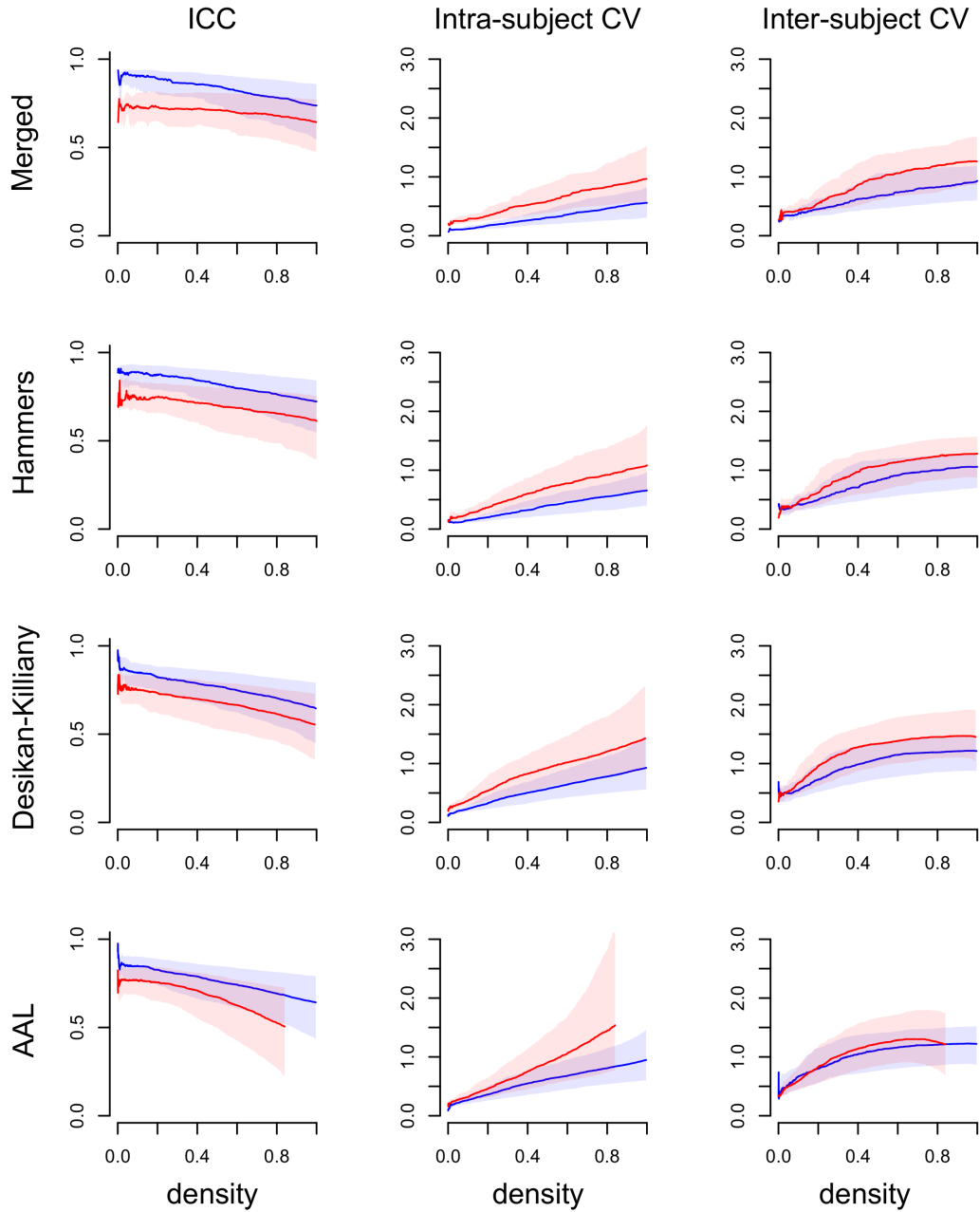


Figure 4.8: Reproducibility metrics for P1 (blue) and P2 (red) connections over a range of network densities of the group networks. (Left) ICC. (Middle) Intra-subject CV. (Right) Inter-subject CV. Lines and shaded area show the median and interquartile range of the metric for all supra-threshold associations for the Merged (top), Hammers (middle-top), Desikan-Killiany (middle-lower) and AAL (lower) Atlases. Reproducibility increased with decreasing density for both pipelines in all atlases. Reproducibility was high across the range of densities for both pipelines and all atlases, as shown by ICCs generally above 0.6.

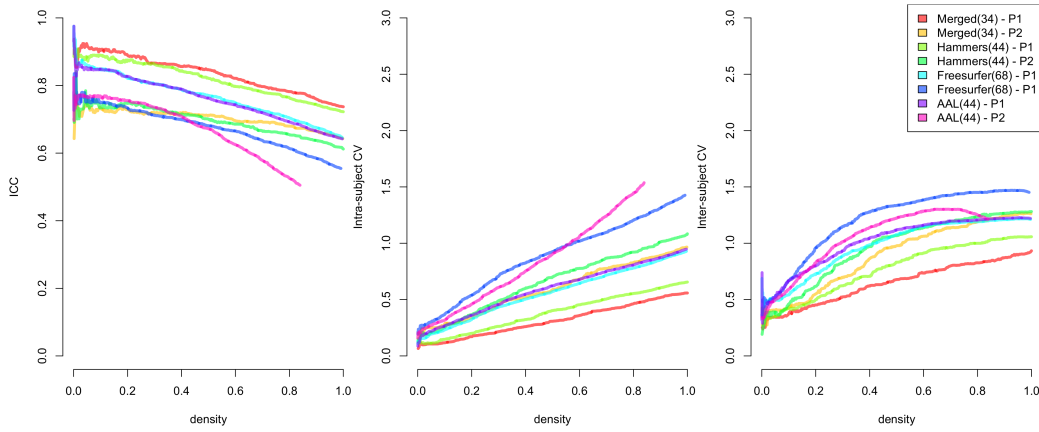


Figure 4.9: Median reproducibility metrics for P1 and P2 connections for all atlases over a range of network densities of the group networks. (Left) ICC. (Middle) Intra-subject CV. (Right) Inter-subject CV.

0.24 for P2 networks, while inter-subject CV also decreased from 1.22 to 0.45 for P1 networks and from 1.21 to 0.42 for P2 networks as density decreased.

Although the reproducibility metrics varied approximately linearly with changing density, some trend of instability in the median reproducibility value was observed at very low densities. This effect was observed at densities of below approximately 0.05 for the four atlases (Fig. 4.9).

It is interesting to compare the reproducibility of consensus network connections in the four atlases, as these represent the set of most highly connected and highly convergent network connections between the alternative reconstructions (Fig. 4.10). In particular, the common node scale allowed us to directly compare connections and their reproducibility across different pipelines whilst controlling for the effect of node scale. At the local peak convergence density, reproducibility of convergent connections was high for both P1 and P2 networks across all atlases. With the merged atlas, the median ICC was 0.89 and 0.73 for P1 and P2 networks, respectively. The median intra-subject CV was 0.17 and 0.34 for P1 and P2 networks, whereas the median inter-subject CV was 0.45 and 0.54 for P1 and P2 networks, respectively. In the Hammers atlas, the median ICC was 0.87 and 0.74 for P1 and P2 networks, respectively. The median intra-subject CV was 0.18 and 0.32 for P1 and P2 networks, whereas the median inter-subject CV was 0.45 and 0.57 for P1 and P2 networks, respectively. In the Freesurfer atlas, the median ICC was 0.85 and 0.72 for P1 and P2 networks, respectively. The median intra-subject CV was 0.19 and 0.33 for P1 and P2 networks, whereas the median inter-subject CV was 0.46 and 0.56 for P1 and P2 networks, respectively. In the AAL atlas, the median ICC was 0.83 and 0.71 for P1 and P2 networks, respectively. The median intra-subject CV was 0.20 and 0.35 for P1 and P2 networks, whereas the median inter-subject CV was 0.47 and 0.58 for P1 and P2 networks, respectively.

P1 and P2 networks, respectively. Using the Freesurfer atlas, the median ICC was 0.85 and 0.75 for P1 and P2 networks, respectively. The median intra-subject CV was 0.24 and 0.38 for P1 and P2 networks, whereas the median inter-subject CV was 0.57 and 0.68 for P1 and P2 networks, respectively. With the AAL atlas, the median ICC was 0.84 and 0.76 for P1 and P2 networks, respectively. The median intra-subject CV was 0.31 and 0.39 for P1 and P2 networks, whereas the median inter-subject CV was 0.73 and 0.7 for P1 and P2 networks, respectively.

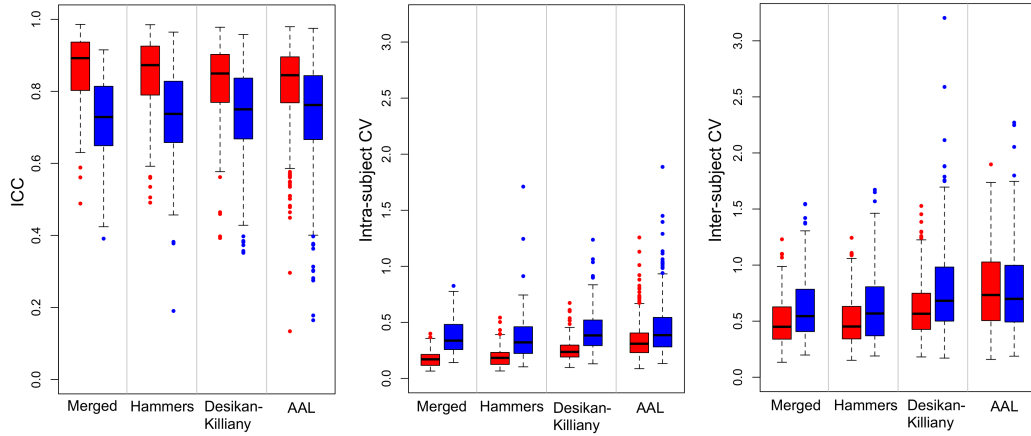


Figure 4.10: Reproducibility metrics for peak convergence connections. The median and interquartile range of ICC, intra-subject CV and inter-subject CV for all peak convergence connections in P1 (red) and P2 (blue) networks are shown for the Merged, Hammers, Freesurfer and AAL Atlases. There was a trend for increasing reproducibility (higher ICC, lower intra- and inter-subject CV) for P1 networks. Whiskers extend to the most extreme data point which is no more than 1.5 times the interquartile range from the box.

4.4 Discussion

In this study, we quantified the convergence between probabilistic structural networks obtained using two independent state-of-the-art reconstruction pipelines over a range of network density thresholds, by merging alternative parcellation schemes to an anatomically equivalent and common node scale. We also replicated our experiment using both the native parcellations and an alternative (AAL) parcellation scheme. In addition, the reproducibility of all pipelines was quantified. Our results show there is high agreement between the two alternative reconstruction methods, as demonstrated in the merged and native atlases. We observed a global peak con-

vergence corresponding to the brain network that occurred most robustly between the two methods. The graph theoretical properties of these ‘consensus networks’ were highly similar between pipelines employing the same atlas but showed some variation across atlases at different node scales. Fibers representing these networks recovered the majority of major white matter tracts in all atlases, giving us confidence that the network has reasonably high anatomical validity. Reproducibility increased with decreasing network density, and there was a trend for greater reproducibility of P1 vs. P2 networks and when using atlases at lower node scales. The consensus network connections were also highly reproducible.

4.4.1 Consensus Between Reconstruction Pipelines

Individual components of the structural network reconstruction pipeline can impact on network anatomical accuracy or the network metrics, meaning the combinatorial choice of which complete reconstruction pipeline to employ is of great importance. Previous studies have found that graph theoretical properties of binary structural brain networks, such as hierarchical modularity and small-worldness, were similar across alternative acquisition and parcellation methods (at the same node scale) [16], as well as between alternative connection weighting schemes [203, 71]. However, the agreement between completely independent reconstruction methods of similar capability has not been previously addressed. We found that the mean DC across all subjects and densities was significantly higher than by chance for all atlases, meaning that alternative reconstructions yielded connection weights that were ranked similarly across the entire rank profile. We therefore observed a highly significant agreement between structural networks obtained from two independent state-of-the-art reconstruction pipelines for the first time. This is an important finding since it demonstrates agreement between individual network connections as opposed to network topological measures, which may have resulted from a wider array of connection configurations. Furthermore, we can have some confidence that the networks are robust to swapping individual stages between the pipelines to some degree.

A high similarity may be expected given the similar capabilities of the

pipelines. High correlation in connection rank profiles is an intrinsic property of probabilistic tractography studies, whereby probabilistic fibers tend to disperse from the true anatomical tracts as they encounter complex fiber architectures or noise in the diffusion data. This leads to densely populated network weights where the connectivity profile of neighbouring nodes is highly correlated. This may be the primary reason for such a high convergence across the entire density range, even at very low density thresholds (Fig. 4.5). Although highly significant relative to random networks, the similarity of AAL atlas pipelines was lower than the other atlases. This was due to a number of subjects' weighted networks having a relatively high number of non-connected (and therefore randomly ranked) region pairs, leading to a lower convergence across thresholds (Fig. 4.5).

A global maximum convergence across thresholds was identified and this corresponded to a sparse network with approximately 100-300 connections (network densities of 0.1 -0.2), depending on the atlas. We propose that the connections in the consensus network correspond highly with the underlying anatomical substrate compared to other thresholds. Therefore, for studies employing similar network reconstruction methods, we speculate that this is an appropriate threshold to apply to the weighted networks for balancing sensitivity and specificity to true brain connections.

The convergence decreased sharply towards zero when the network density was below the peak convergent density. This may be explained by factors such as the relatively large impact of rank mismatches in connections between pipelines (due to differences in their respective sensitivity) when the number of connections is low, or a homogeneous weight distribution of the highest ranking connections leading to effectively random ranking and lower convergence.

de Reus and van den Heuvel [88] recently assessed the impact of threshold on the sensitivity and specificity of brain network connections [88]. Using the Desikan-Killiany atlas with 68 nodes, they estimated the number of true positive connections as 420.7 (corresponding to a network density of 18.5%), which is slightly higher than our study. This difference could be explained by their use of a different ex-

perimental design, whereby a model of the true positive distribution was fitted to the prevalence distribution calculated across subject binary networks obtained from deterministic tractography. It is interesting to note that while de Reus and van den Heuvel [88] and our study used different pipelines and analysis methods, the estimate of the number of brain connections is of a similar magnitude. The number of connections in the consensus networks was 110, 152 and 242 (corresponding to network densities of 0.196, 0.161 and 0.106) for atlas of node scale 34, 44 and 68, respectively. This trend of an increasing number of connections occurring consistently between pipelines at higher node scales may be expected given the increase in possible region pairs. Similarly, de Reus and van den Heuvel [88] found that the estimated number of true positive connections increased in the Harvard-Oxford atlas, which has 96 nodes.

Other studies have investigated the effect of threshold on anatomical validity of structural networks, by utilising a ground truth for particular sub-components of the network. Li et al. [203] investigated the effect of threshold on the sensitivity and specificity of structural network connections, using connectivity data derived from post-mortem tract tracing techniques in the macaque brain as a ground truth. The performance of several tractography strategies was assessed by analysing the area under the receiver operating characteristic curve. However, their study was limited to a subset of brain regions due to limited availability of tract tracing data in macaque brain and an optimal threshold for performing network analysis was not reported. Bastiani et al. [17] used a network ‘quality control’ technique to analyse the sensitivity and specificity of brain network connections across thresholds for deterministic tractography reconstruction techniques [17]. However, their sensitivity and specificity metrics measured connectivity between sets of regions known to be connected according to *a priori* information and therefore may have had limited applicability to other connections across the network. In contrast to these works, our study utilised information across all brain region pairs and compared two independent pipelines as opposed to performing a more focussed study on individual fiber tractography reconstruction stages.

We found high similarity in graph theoretical properties of the consensus networks when comparing those derived from the same node scale atlas. This may be expected, given the convergence of connections at the peak convergence density was above 65%, and that the networks had the same connection density, which is known to significantly impact upon the graph theoretical metrics [330]. Despite high similarity across alternative pipelines at the same node scale, some graph theoretical properties were significantly different across node scales. Most notably, the number of connections in the consensus network increased and density of the network decreased in atlases at higher node scales. This could be due to division of connections between multiple parcels at higher node scales due to an increase in the number of possible regional pairs.

We found that the peak convergence density using the AAL atlas was similar to that of the Desikan-Killiany atlas, despite the AAL atlas having a higher node scale. This may be because the AAL atlas uses a fundamentally different type of parcellation scheme and algorithm. While the Desikan-Killiany atlas contains only the grey matter region of the cortex, the AAL atlas represents larger regions which include both grey and white matter. This may have increased the number of robustly occurring cortical connections, as some streamlines, which may otherwise have become truncated before reaching the grey matter of the cortex (due to noise and tissue partial volume effects), intersect these parcels. Furthermore, the AAL segmentation algorithm uses an affine registration between the subject brain and a standard brain from MNI space, meaning subject differences in brain morphology are not considered. Larger parcels and limited ability to account for individual brain variation may have meant single connections became distributed across multiple parcels in the network, leading to a high peak convergence network density compared to the Hammers and Desikan-Killiany atlases (Fig. 4.5).

With the exception of the AAL atlas, the pathlength and global efficiency tended to increase and decrease, respectively, in consensus networks with increasing node scale atlases. This may be due to the lower consensus network densities at higher node scales, resulting in a decrease in the ratio of edges to nodes. Also,

clustering coefficient and local efficiency decreased when comparing the consensus networks obtained from the Hammers (44 nodes) to the Desikan-Killiany atlas (68 nodes). Zalesky et al. [358] examined the effect of node scale on the pathlength and clustering coefficient of networks generated using deterministic tractography and found that an increase and decrease in the pathlength and clustering coefficient metrics, respectively [358]. Their study examined a wide range of node scales (from 82 to 4000 in steps of 500) whereas our study re-affirms these findings at finer node scale increments. However, clustering and local efficiency showed no clear trend with node scale when comparing the Common (34 nodes) and Hammers atlases (44 nodes).

It should be noted that although the observed correspondence of connection fiber paths with known white matter tracts does suggest some degree of anatomical truth to the underlying connections in the consensus networks (Fig. 4.6), spurious network weights may be included in the consensus networks due to a common bias in the tractography methods. Therefore, although the reconstructed tracts are sensible, they are unlikely to be exhaustive. For example, local tractography techniques may produce shorter fibers than found *in vivo*, as fibers are deflected from the true path due to noise and limited angular resolution. This may have meant connection weights between distant regions were lower than expected. Some network reconstruction methods have accounted for this by penalising the weighting of shorter inter-regional distances [203]. In addition to the weighting scheme, many other alternative pipelines are available which may result in different convergence results. Therefore, it should be emphasised that we demonstrated agreement between two pipelines out of a large number of possibilities and that our results may not apply to pipelines which employ different parcellation, registration or tractography methods. Finally, the peak convergent threshold described here was derived from a population of healthy individuals and may not represent an appropriate threshold for other clinical populations where connections may have become altered or absent.

Some relevant publications have recently been released concerning agreement between different reconstruction methods [368], and thresholding structural brain

networks in the presence of false positive connections[104].

Zhong et al. [368] investigated the convergence and divergence of different construction methods in terms of their assessment of individual differences in structural brain networks. The study employed different network resolutions, and different tractography and connection quantification techniques. Individual differences were assessed in terms of edge weights, node efficiency, and global and local efficiency [368], in a group of 57 subjects and summarised as a subject-subject correlation matrix per method. Their analysis of the convergence between patterns of individual difference (subject-subject correlation matrix of network properties) showed that subsets of construction methods show convergent patterns of individual differences while others were divergent. Some network properties showed convergent patterns of individual differences among specific sets of construction methods, indicating that the method convergence depended on the network measures of interest. This study gives insight into convergence and divergence between a subset of methods for particular connectational aspects (edge weight, nodal efficiency, global and local efficiency), which provides useful insights into potential discrepancies found between studies employing different network construction methods.

Convergence and divergence among construction methods, as found in Zhong et al. [368] may be expected in the presence of fundamental differences in the pipeline methods (e.g. high resolution vs. low resolution, probabilistic vs. deterministic tractography). This contrasts with our study which found a high similarity between independent pipelines of equivalent capability.

Drakesmith et al. [104] recently examined the impact of false positives in the value and bias in graph metrics across thresholds and in identifying group differences [104]. They generated a model network by manually pruning a tractography dataset from a single individual and added the removed streamlines as false positives to structural networks from a group of 248 subjects. They then undertook a range of experiments to determine the effect of false positives on graph theory metrics across thresholds, the effect of thresholding itself on graph theory metrics and the stability of statistical inferences (with and without group differences). The study

found that network metrics were highly susceptible to false positives- and although thresholding reduces the effect of false positives, it also biases the graph metrics, and creates instability in statistical inference in these metrics. In addition, the range at which an effect is observed varies with the graph metric meaning a true effect may only be observed in a limited range of thresholds. While we suggest that the consensus networks correspond highly with the true positive network connections, it should also be considered that the consensus networks described here would also contain false positive connections if they appeared in both P1 and P2 pipelines. Drakesmith's work indicates that a small number of false positive connections can have a significant impact on graph metrics and their statistical analysis and therefore although the consensus network may have high anatomical accuracy it is likely still not free from bias.

4.4.2 Reproducibility of Structural Networks

A particular advantage of our approach to comparing reproducibility across pipelines is that the effect of node scale was removed by merging parcellations to a common and equivalent node scale. The ICC was high for connection weights in both pipelines, suggesting high reproducibility. However, this study found high intra-subject and inter-subject CVs of unthresholded cortical associations for both reconstructions. A previous study has also reported high CVs of raw cortical associations up to 100% using probabilistic tractography [320]. Despite high variance of unthresholded cortical associations, it was shown that the derived graph theoretical properties of thresholded networks, such as node degree, clustering coefficient and pathlength, have higher reproducibility [320, 16, 71]. The trend of increasing reproducibility (higher ICC and lower CV) of supra-thresholded associations with decreasing density found in this study (Fig. 4.8) may explain these findings. The effect of increasing reproducibility for sparser networks (i.e. higher mean associations) may be explained by a pruning of weaker, noisier connections, which are more likely to be false positive or true negative connections. This may act additively with the effect that whole-brain metrics are less affected by noise compared to single connections which result from a smaller amount of the total network data.

Since performing this reproducibility study, there have been a number of publications concerning the effect of threshold on reproducibility of structural networks [108, 367, 36].

Duda et al. [108] recently found that the reproducibility (ICC) of graph metrics derived from thresholded graphs was moderate (~ 0.5) and in some cases decreased with decreasing network density [108]. This was demonstrated using the Mindboggle and AAL atlases (62 and 78 nodes, respectively). Large variability in the reproducibility of graph metrics was found at densities below approximately 15%, which is in agreement with our study which found greater variability in reproducibility of edge weights below 10%. However, they did not report the reproducibility of raw edge weights in relation to decreasing density, as reported here.

In agreement with our findings of higher reproducibility of edge weights with lower density, Zhao et al. [367] found that hubs or rich club nodes had higher reproducibility of node strength and edge weights than the non-hub or non-rich club nodes. These findings agree with our results as hub and rich-club nodes are frequently those with higher connection weights which would tend to have higher reproducibility. Zhao et al. [367] also found that regions with higher strength also tended to have higher ICCs, which is also in agreement with findings in this study.

Bonilha et al. [36] found high reproducibility of graph metrics derived from thresholded weighted association matrices. When examining the relationship between edge weight and reproducibility, they found a higher edge weight was correlated significantly to higher reproducibility in deterministic tractography datasets, but not in probabilistic tractography datasets. Interestingly, for both probabilistic and deterministic methods, the study found that links with higher inter-subject variability in number of streamlines were associated with a lower ICC, leading the authors to suggest that those connections more consistently tracked across subjects are also more reproducible.

A trend observed in this study was that of higher reproducibility for lower node scale networks for both alternative reconstructions (Fig. 4.9). This agrees with previous studies that have shown lower intra-subject correlation in associations with

higher node scale [56]. This node scale effect may be explained by a decrease in correspondence between parcel boundaries (across repeat scans) at higher node scales due to registration error, meaning that the proportion of mismatch with relation to parcel size increases. In Cammoun et al. [56], reproducibility significantly decreased with scales of 83, 150 and 258 nodes. Our study demonstrates a trend for decreasing reproducibility at finer node scale increments, possibly at a scale difference as low as 10 nodes. Interestingly, the relationship of increasing reproducibility with decreasing density was less stable at very high densities (Fig. 4.9).

A number of publications have been recently released concerning the effect of node scale on reproducibility of structural networks [36, 367, 108, 25].

Bonilha et al. [36] found that edge weights connecting larger ROI within an atlas had higher reproducibility. This agrees with our findings of higher reproducibility in lower node scale atlases as these will have larger ROIs. Their study also found that edge weights connecting ROIs that were closer together tended to have higher reproducibility, which is expected since the path traversed by connecting streamlines is shorter meaning streamlines will encounter less noise in the diffusion image.

Zhao et al. [367] investigated reproducibility of graph metrics derived from surface and volume representations of the AAL atlas at low (80 nodes) and high resolution (1024 nodes). Interestingly, they found that the global binary network metrics had higher reproducibility in higher resolution than lower resolution atlases. On the other hand, local metrics had higher reproducibility in lower resolution than higher resolution atlases. This may be due to lower resolution atlases having larger ROI sizes, leading to more stable local metrics, while higher resolution atlases have smaller ROI sizes but a more homogeneous edge weight distribution.

Promisingly, a method to generate high resolution structural networks with high reproducibility has been reported. Besson et al. [25] examined reproducibility in the node strength of high-resolution connectomes (500,000 nodes intra-, 50,000 nodes inter-acquisition) in a single subject undergoing 10 repeat diffusion-weighted and anatomical T1 acquisitions [25]. By defining network nodes as the vertices of

cortical and sub-cortical surface mesh triangles, they found that by seeding a large number of streamlines, good to excellent intra-acquisition reproducibility of node strengths could be obtained. The intra-acquisition correlation in edge weights was also reasonably high, as was the inter-acquisition correlation in both edge weights and node strengths. Although their method relied on some processing steps such as surface smoothing, common space registration and downsampling, the integrated methodological framework for creating a high resolution connectome as originally proposed by Glasser et al. [141] and now extended by Besson et al. [25] is a promising tool for creating high resolution networks that are highly reproducible.

Lastly, it could be argued that there was a trend for higher connection reproducibility distributions in P1 than P2 networks when both node scale and density were fixed. Although we have no prior reason to expect different reproducibility between pipelines, it is possible that this trend may be explained by the relative suitability of applying the reconstruction to this particular preprocessed data. We could have performed a more extensive search of the parameter space for each of our reconstruction stages in order to optimise the convergence or reproducibility effect. However, this was not the point of the study. We sought to answer whether the choice of pipeline matters in a general sense. To answer this, we chose alternative state-of-the-art methods which have similar capabilities but vary with respect to the details of their implementations. Given the insignificant difference in ICC distributions between pipelines, we suggest that reproducibility and pattern of anatomic connection will be comparable between other studies that utilise reconstructions of a similar capability and node scale.

Importantly, the local peak convergent connections had high reproducibility for both reconstructions, with the lower quartile ICC above 0.80 and 0.65 for P1 and P2 respectively (Fig. 4.10). This suggests that the core group network consensus connections was highly reproducible in both reconstructions.

Methodological Considerations

Some methodological aspects should be considered when interpreting these results. As previously mentioned, although the observed correspondence of convergent fiber

paths with known white matter tracts does suggest some degree of anatomical truth to the underlying connectivity measures, high convergence or reproducibility between pipelines cannot be interpreted as a guarantee for anatomical accuracy. In fact, alternative reconstruction techniques are available which may result in different reproducibility of convergence results.

An advantage of using an atlas-based parcellation is that parcel border criteria has been well defined in the literature and has high inter-subject correspondence, which may have resulted in higher reproducibility compared to other parcellation strategies, such as those based on functional or structural criteria. However, the use of anatomical criteria to define parcel borders means that parcels are imperfectly correlated with the true structural or functional connectivity patterns. Despite having performed the initial structural parcellations on high signal to noise ratio images, there remains some degree of error in the label assignments due to residual noise and partial volume effects. In addition to this, the parcellation scale used may not reflect the true macroscopic connection scale. These effects may have led to some degree of blurring of spatially separate structural connections between two or more regions. In our data, the occipito-parietal tract (Fig. 4.6) is an example of a single spatially distinct tract that connects three parcels. A connectivity-based parcellation approach, such as hierarchical clustering, may be useful for refining anatomical parcel borders to closer match the connectivity structure [77]. It should also be noted that the merging process assigned the temporal lobe as single node in both common scale parcellations, meaning the contribution of intra-temporal connections to the convergence or reproducibility results were omitted. This may have been avoided by splitting the temporal lobes parcels in an equivalent manner for both reconstructions.

Due to magnetic susceptibility artefacts and phase inhomogeneity in diffusion MRI data, the non-linear registration strategy used here may have provided a closer alignment of the parcels with the true grey matter in diffusion space than a linear registration. However, as with all studies of this type, imperfect registration between structural and diffusion space and large voxel sizes lead to incorrect assignment of

some grey matter parcel voxels in diffusion space. This mis-registration may lead to under or over-estimation of the true connectivity. An example of this in our study may be the over-estimation of insula connectivity, as some insula fibers appear to represent the corona radiata (Fig. 4.6), suggesting a mis-registration of some insula voxels into the internal capsule. The overlap between parcels and white matter may be decreased by excluding white matter voxels with high FA from the parcellation or by using FA to guide the registration. However, there is likely to be some residual misalignment due to the lower resolution of diffusion images and partial volume effects at the grey matter boundary.

Probabilistic tractography utilising multiple fiber directions accounts for the complex nature of fiber configurations and produces a dispersion of fibers, to some degree, reflecting connectivity throughout the entire brain. However, the voxel fiber distributions reflect uncertainty due to noise and limited diffusion-encoding directions, leading to a tendency for shorter fibers than that found in the real brain as fibers are deflected from the true tract path. This fiber length bias may have decreased the cortical association between distant regions. Some network reconstruction methods have accounted for this by penalizing the association value of shorter fiber distances [203]. Furthermore, the influence of noise on the fiber propagation means that both network reconstruction methods contain some degree of false positive and false negative association values, as fibers may connect parcels in the absence of (or may not connect parcels in the presence of) a true anatomical connection. An example of a false positive connection are the inter-hemispheric cingulum connections that do not travel via the corpus callosum. Other tractography algorithms, such as global tractography, may be more resilient to noise and therefore produce networks with a reduced number of false positive or false negative connections [202].

4.5 Summary

High convergence between two independent state-of-the-art structural network reconstruction pipelines was observed on a connection-wise basis for all density

thresholds. Reproducibility of connections weights increased with decreasing density for all atlases and pipelines. A sparse ‘consensus network’, which occurred most robustly between the pipelines, was identified in four atlases, and had a density of between 10% and 20% (100-250 connections). We propose that these connections have high anatomical validity compared to other thresholds, which is useful given the inherent difficulty in defining thresholds for brain network studies. The pipeline had relatively little effect on the network properties of the consensus networks, although some relationship with atlas node scale was observed, in agreement with previous studies. When performing structural network analysis, it may be useful to apply multiple pipelines to diffusion-weighted data and to use the comparison framework described here to identify the most important connections.

Chapter 5

Reconstructing Large-Scale Structural and Effective Brain Networks

Having demonstrated reasonable reproducibility and inter-pipeline agreement in macroscopic structural networks in the previous chapter, we next sought to test the potential clinical utility of the method, in combination with effective networks reconstructed using CCEPs, in detecting pathological connectivity in a cohort of focal epilepsy patients. Reconstructing structural and effective connectivity networks between implanted intracranial electrodes is challenging due to a number of factors such as determining electrode positions in the presence of brain shift and handling artefacts in the CCEPs. For combined analyses, equivalent networks should be constructed despite the differing nature of the raw data in diffusion-weighted imaging and CCEPs. In this chapter, the basic process and challenges of reconstructing effective and structural networks are firstly described. The method for reconstructing structural networks was adapted from cortical atlases, as described in the previous chapter, to electrode locations. Effective networks were reconstructed while considering limitations in the raw CCEP data such as the absence of stimulation onset tags, jitter in the stimulus delivery, and stimulation artefacts. Results show that the reconstruction methods perform reasonably well and therefore permits inter-modal comparisons and clinical analysis. Techniques used to reconstruct networks are

discussed in relation to alternative methods previously reported in the literature.

5.1 Introduction

Pre-surgical evaluation of drug-resistant epilepsy patients requires acquisition and interpretation of information across multiple modalities including scalp EEG, intracranial EEG, structural MRI and other neuroimaging methods. CCEPs may be acquired to test their potential clinical use in explaining seizure onset and seizure spread and for the purpose of comparing and correlating connectivity information to other modalities. Diffusion MRI images may also be acquired for the purpose of identifying the trajectory of eloquent tracts which should not be resected, and to provide connectivity information that may be corroborated with other modalities. CCEPs indicate the presence of functioning tracts from the stimulation to recording site, and therefore measures effective connectivity. Diffusion tractography enables estimation of the structural axonal connectivity between brain regions. Both CCEPs and diffusion images are increasingly acquired during pre-surgical evaluation as part of standard care.

Combining connectivity information derived from CCEP with diffusion MRI tractography may identify functional tracts, their directionality, speed of information transfer, and connection strength, and therefore inform and refine models of brain connectivity networks. This may enable a better understanding of the relation between structural and effective brain connectivity, identify potential pathological connectivity in epilepsy and aid identification of the ictal-onset zone and propagative regions with greater accuracy, ultimately leading to improved seizure freedom following surgery. However, reconstructing CCEP and diffusion connectivity involves many complex methodological stages.

Measuring effective connectivity using CCEPs includes averaging the encephalogram on repeated stimulations, consideration of stimulation artefact, and estimating the significance of the evoked potential. Averaging the encephalogram on repeated stimulation trials increases the signal to noise ratio of the evoked potential. An accurate inter-stimulation alignment and estimation of stimulus delivery time

is therefore needed to correctly estimate the amplitude and latency of the evoked potential. Due to the capacitive properties of electrode-brain interface [129], the electric field generated by the stimulation pulse is visible on the encephalogram, despite the time duration of the stimulation pulse typically being shorter than the sampling interval. This contaminates the encephalogram, particularly at early latencies following stimulation as it adds to signals from local field potentials. The true amplitude of the evoked potential peaks relates to the number and synchrony of neurons activated at remote sites, due to their innervation by cortico-cortical pathways, and may therefore be used to estimate the magnitude of an effective connection between brain regions. Effective connectivity may be estimated on a large-scale by stimulating many electrodes and recording their evoked potentials [177, 87, 116, 178].

Estimating structural connectivity between brain regions underlying intracranial electrodes involves a series of processing stages [251], and has not been frequently reported among research studies [296, 78]. Defining electrode locations in diffusion space requires co-registration between post-implantation (e.g. CT image) and pre-implantation spaces (e.g. diffusion image) and this is difficult due to the brain shift occurring following electrode implantation. Electrode ROIs should be generated corresponding to the grey matter underneath the electrode receiving cortico-cortical connections. The electrode locations and their ROIs must be defined in diffusion space and tractography subsequently performed. Tractography requires estimation of fiber orientations in diffusion images and application of one of several tractography methods. The fiber orientations should depict the underlying anatomy faithfully. Representation of multiple fibers and uncertainty in fiber orientation is desirable, but this is challenging due to the limited number of diffusion gradient directions acquired in clinical diffusion imaging. For quantitative connection analysis, tractography can be used to generate an undirected measure of connection strength between the electrode ROIs by propagating streamlines through the white matter.

Two previous studies have combined CCEPs and diffusion tractography

[296, 78]. Swann et al. [296] found a high concordance in connectivity between pre-supplementary motor area (pre-SMA) and right inferior frontal gyrus (rIFG) using CCEPs, diffusion tractography and task-based functional MRI. Short latency CCEPs were elicited between the pre-SMR and rIFG sites which were also connected by tractography fibers [296]. However, the overlap or correlation between structural and effective networks was not quantified. Conner et al. [78] combined CCEPs and diffusion tensor tractography in a group of epilepsy subjects. In this study the amplitude of the N1 evoked potential was correlated to the number of connecting fibers in connections arising from Brocas area [78]. This was enabled by transforming electrode co-ordinates to standard MNI space and reporting the pairwise connectivity for stimulation electrodes lying within Brocas region. The study found a moderate but significant positive correlation between the modalities ($R^2 = 0.41$). There have been no studies examining the correlation between CCEPs and diffusion tractography on a large-scale across the cortex by using all stimulated electrodes.

In this chapter, we reconstructed large-scale structural and effective electrode-electrode brain networks using reconstruction methods that address the methodological challenges mentioned above. Methods are described in detail and their effectiveness quantitatively and qualitatively evaluated. In the discussion, the reconstruction method is evaluated and compared to those used in previous CCEP and diffusion studies.

5.2 Methods

A summary of methods used to generate CCEP and diffusion tractography networks is shown in Fig. 5.1. Reconstruction of structural connectivity networks required the pre-implantation diffusion and T1 images in conjunction with the post-implantation T1 and CT images. Reconstruction of CCEP networks required only the original CCEP data. Note that this study was a retrospective analysis of MRI images and SPES stimulations acquired as part of standard clinical care.

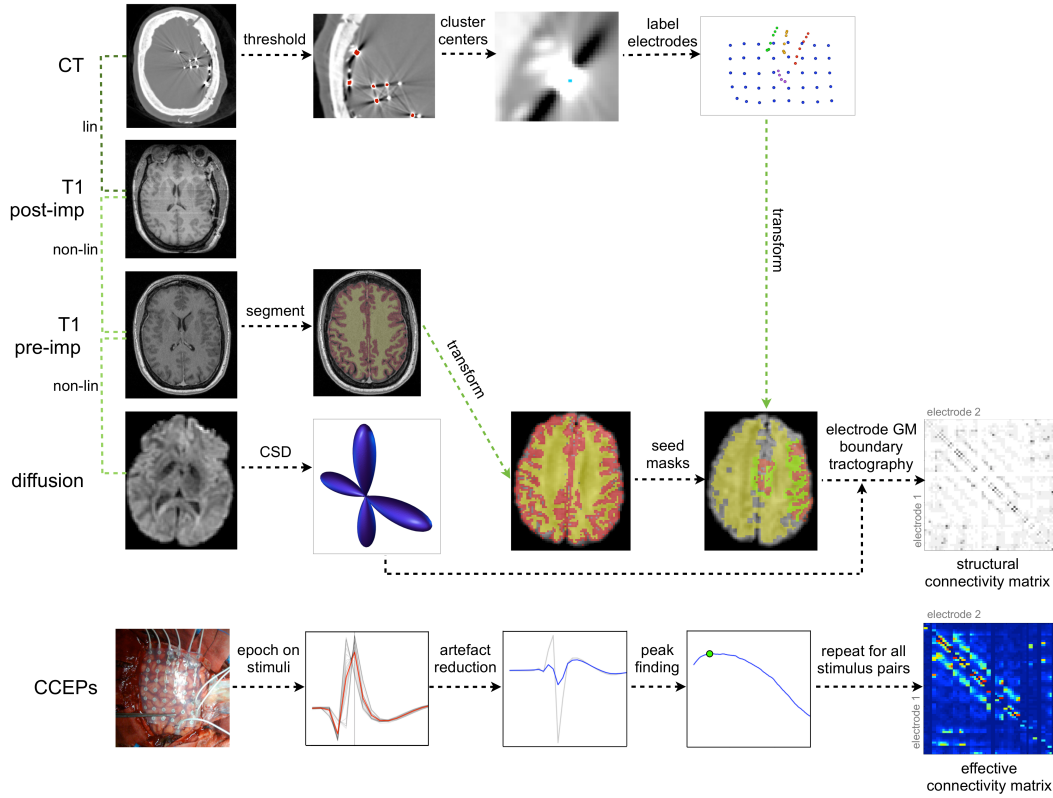


Figure 5.1: Overview of methods used to reconstruct diffusion tractography and CCEP networks. Structural networks were reconstructed using probabilistic diffusion tractography between electrodes mapped from the CT to diffusion image via the pre- and post-implantation T1 images. Effective connectivity networks were reconstructed using peak amplitudes of the CCEP.

5.2.1 Subjects and Electrode Implantation

Seven subjects (4 male, 3 female, mean age 34.6 years old, range 26-49 years old) were retrospectively selected from a larger cohort of drug-resistant epilepsy patients that had undergone invasive intracranial monitoring at the National Hospital for Neurology and Neurosurgery (NHNN), Queen's Square, UCL. The criteria for subject selection was the availability of pre-implantation T1-weighted MRI, pre-implantation diffusion-weighted MRI, post-implantation CT, post-implantation T1-weighted MRI, and SPES. Informed consent was obtained from the patients prior to the cortical stimulation procedures. Most subjects were diagnosed with frontal lobe epilepsy and had evidence of cortical dysplasia on their structural MRI (subject details are shown in Table 5.1). The decision to implant, the electrode targets, and the duration of implantation was made entirely on clinical grounds, without ref-

erence to this study. A total of 644 sub-dural electrodes (grids and strips) and 60 depth electrode contacts were implanted. Sub-dural electrodes had a diameter of 4 mm, exposed surface area of 2.3 mm and inter-electrode spacing of 10 mm. Some subjects had high density sub-dural grids with 5 mm spacing. Depth electrodes had a diameter of 1.12 mm and length 2.41 mm. Depth electrodes were spaced 10 mm apart, with a small number of depth electrodes spaced 5 mm apart. Subjects were implanted for 5 - 9 days, so that sufficient monitoring occurred to identify the seizure focus and functionally eloquent cortical areas.

5.2.2 Reconstructing Effective Networks

5.2.2.1 Stimulation Parameters

SPES was performed in an electronically shielded room. The NicoletTM Cortical Stimulator with C64-OR amplifiers and Nicolet Cortical Stimulator Control Unit (ISO 13485, ISO 9001; Nicolet Biomedical, Madison, US) was used to deliver a constant-current (AC), bipolar (i.e. between adjacent electrodes), biphasic (500 μ s per phase) stimulation pulse of 4 mA intensity at \sim 0.2 Hz using the Nicolet LTM system. If clinical signs or aftercharges were observed, the intensity was reduced to a minimum of 2 mA, in steps of 1 mA. Stimulations were performed using the majority of row-wise adjacent electrode pairs (344 stimulation pairs across all subjects). Each stimulation was repeated 10-40 times. Intracranial EEG was recorded using a 128-channel EEG machine (Nicolet Biomedical, Madison, US) with a sampling rate of 512 or 1024 Hz, depending on the number of electrode EEGs acquired (Table 5.1). An average of two intracranial electrode EEGs with minimal background activity were selected as the reference. These were usually electrodes on sub-dural strips implanted on the inferior surface of the frontal lobe.

5.2.2.2 Epoching

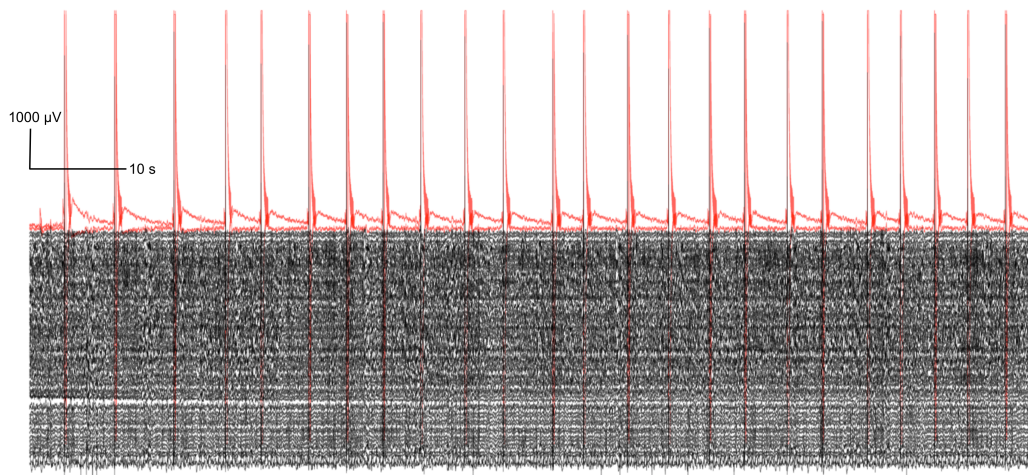


Figure 5.2: Raw CCEP data for a single stimulation electrode pair. Red and black lines indicate stimulation and recording channels, respectively. Stimulations were delivered approximately once every four seconds. Stimulation delivery times correspond approximately to voltage saturations of the stimulation channels.

Subject	Gender	Age (years)	Epilepsy	Implantation Duration (years)	Cortical Dysplasia	Num. Electrodes (analysed/implanted)	Num. Stim. Pairs	Samp. Freq. (Hz)	T1
1	F	49	L IF	5	L IF	62/92	45	1024	QS
2	F	34	L IF	9	L IF	99/104	46	512	C
3	M	26	R FC	8	None	118/128	63	512	C
4	M	39	L F	9	L IF	100/124	55	512	QS
5	F	27	L F	9	None	108/118	52	512	C
6	M	39	L P	7	L P	54/58	28	1024	C
7	M	28	R P	6	None	76/80	51	512	QS

Table 5.1: Epilepsy subject details. T1 refers to the pre-implantation T1 acquisition site (see 2.3.1 Image acquisition). Abbreviations: QS = Queen Square, C = Chalfont, L = Left, R = Right, IF = Inferior Frontal, FC = Frontocentral, P = Parietal, F = Frontal

Epochs were obtained on a stimulation-wise basis. Epoching involved three stages: identifying approximate stimulus delivery time, aligning the stimulus delivery time across stimulation trials, and offsetting the stimulus delivery time of the epoch to the origin.

CCEP data was firstly imported into MATLAB v2011b [219] using EEGLab [95]. MATLAB was used to identify the approximate stimulation onset time (see Identifying Stimulation Ramp-Up Time below). All subsequent CCEP analyses were performed in R v3.2.1 [261].

Identifying Stimulation Ramp-Up Time The anode stimulation channel was thresholded $>5000 \mu\text{V}$ and the first timepoint of each connected component was the initial approximation of the stimulus delivery time. These times correspond to the start of the ramp-up time of the stimulation electrode.

Aligning Epochs Across Stimulations Jitter was observed in the delivery of the stimulus across stimulation trials, with respect to the start of the ramp-up time of the stimulation electrode. This can be seen as a misalignment of the stimulation artefact between stimulation trials, as observed in the nearest recording electrode to the anode. To correct for this, recordings were aligned across stimulations using lagged cross-correlation to the first stimulation in the stimulation train, using a cross-correlation search window of $-15\text{:}+12$ ms. Each stimulation trial was adjusted by the time lag giving the highest correlation to the first stimulation trial.

Global Offset of Stimulus Delivery The stimulus delivery did not immediately follow the start of the voltage ramp-up of the stimulation channel (see Results, Fig. 5.4). Therefore, a global offset was applied to all recording channels for all stimulations. The global offset was calculated as the time until maximum amplitude of the mean signal following ramp-up start time within a window of $-15\text{:}+12$ ms following ramp-up at the nearest recording electrode. An epoch was generated for each stimulation and consisted of a three-dimensional array containing the amplitudes at timepoint indices for each recording electrode.

5.2.2.3 Artefact Correction

The signal amplitude in recording electrodes immediately following stimulation depended on the charge polarity of the nearest stimulation electrode (Fig. 5.5). Therefore, an ICA-based artefact reduction technique was implemented, whereby the data was re-projected following removal of the independent components (IC) of the signal representing the stimulation artefact. This is similar to previous artefact reduction techniques applied to scalp EEG [96] and transcranial magnetic stimulation (TMS).

ICA decomposes a set of observed signals into a selected number of source signals (the ICs) by maximising the non-Gaussianity of the joint distribution of the observed signals. A weighting matrix specifies the weighting of each IC for each of the original signals. The original signals may therefore be reconstructed using any combination of the ICs by removing these from the source signal matrix and reconstructing the original signals using the weighting matrix output by ICA.

ICA was performed for each stimulation trial separately using only the amplitudes of the recording electrodes. The fast-ICA algorithm was used to decompose the observed signals into five ICs within a time period of -40:+ 40 ms using the `fastICA` function in R [163]. The artefactual ICs were selected automatically, as those with absolute maximum above two standard deviations of the median of the absolute maximums across all ICs. The ICs representing artefact were removed from the source signal matrix and the signals were then reconstructed by projecting the remaining ICs in the signal matrix using the ICA mixing matrix.

Two artefactual ICs were most commonly designated as artefact. Increasing or decreasing the number of initial ICs had little effect on the number of ICs representing stimulation artefact.

5.2.2.4 Visually Excluding Other Artefacts

Following artefact correction, the mean signal of every recording electrode for every stimulation was visually examined to identify further artefacts. Epochs containing artefacts were excluded from all future analyses (Fig. 5.3). In total 673/30198 epochs were excluded due to artefacts. Artefacts were either (i) non-physiological

ramp-shaped response following stimulation (ii) large voltage surges (iii) visible 50 Hz power line noise in the average response, due to a combination of both 50 Hz power line noise contamination and a low number of stimulation trials (iv) slow exponential return to baseline following stimulation, indicating bad contacts. Examples of artefacts excluded by visual inspection are shown in Fig. 5.3.

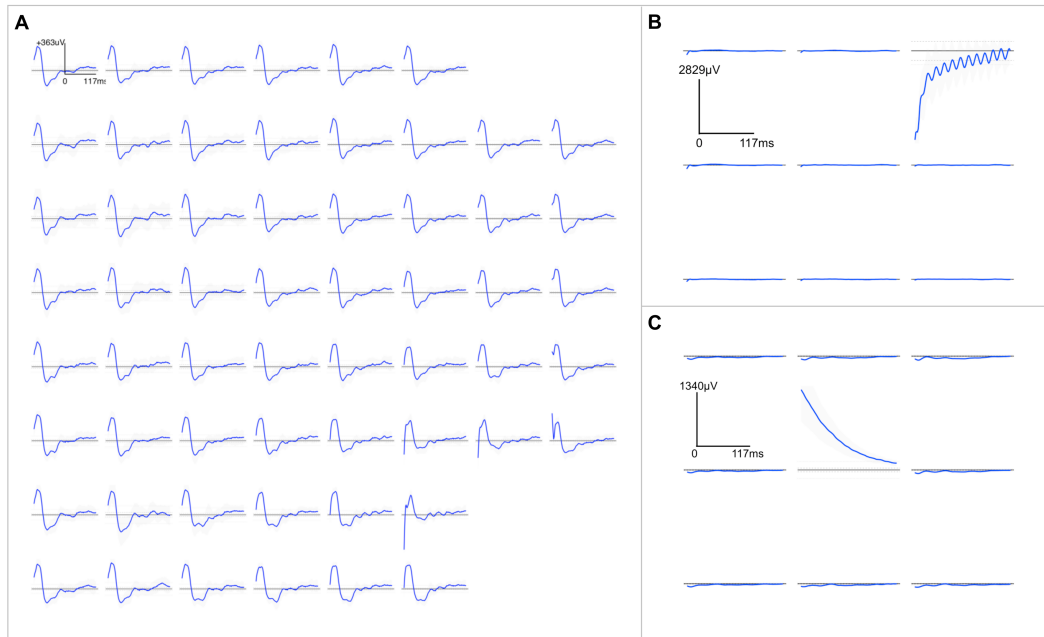


Figure 5.3: Examples of artefacts excluded by visual inspection. A: Non-physiological ramp-shaped artefact found in all recording channels when stimulating between electrodes GA09 and GA10 in subject 3. B: 50 Hz power line noise artefact visible in electrode GA24 following stimulation between electrodes GA19 and GA20 in subject 4. C: Slow voltage amplitude return to baseline in electrode G115 following stimulation between electrodes D101 and D102 in subject 7.

5.2.2.5 Evoked Potential Peaks

An in-house peak finding algorithm was implemented on the mean signal of each recording electrode to identify amplitudes and latency of evoked potentials. Firstly, amplitudes were low-pass filtered using a Butterworth filter with an order of 5 ms and a frequency of 110 Hz. The frequency of the filter was set to allow fast evoked potentials to pass whilst removing high frequency noise which may lead to false positive peak detection. Secondly, candidate peaks were identified by selecting those timepoints surrounded by positive and negative gradient. Next, candidate peaks were grouped by the connected components of the signal with low gradient

(mean gradient < 2 uV/ms within a 5 ms neighbourhood). The candidate peaks with maximum absolute amplitude in each connected component were selected. Finally, those selected candidate peaks with amplitude below twice the baseline standard deviation were excluded. In this calculation the standard deviation of the baseline was calculated using all timepoints across all stimulation trials in the time period of -500:-15 ms, whereas the amplitude searched for CCEPs was that of the mean evoked potential peak. Positive amplitude peaks with a prior negative gradient and negative amplitude peaks with a prior positive gradient were removed.

Subject	Stim.	Nodes	Rec.	Excluded	Analysed
1	46	62	2760	0	2760
2	46	99	4462	0	4462
3	59	118	6844	232	6612
4	55	100	5390	263	5127
5	52	108	5512	0	5512
6	28	54	1456	0	1456
7	51	76	3774	178	3596

Table 5.2: Summary of CCEP stimulations and recordings. The total number of stimulations performed, analysed electrodes, recorded responses, excluded responses (due to visually identified artefacts) and analysed responses are shown.

5.2.2.6 Effective Networks

An evoked waveform represents a connection between the stimulation electrode(s) and the recording electrode. The evoked potential may arise from a connection between the stimulation-electrode pair to the recording electrode, or from either stimulation electrode to the recording electrode. In consideration of these different methods to interpret evoked waveforms, peak features of interest were represented in two ways:- *stimpair* and *network*. The *stimpair* representation is the original format of the CCEP data: each observed peak represents a single data point corresponding to a connection between the stimulating electrode pair and the recording electrode. In the *network* representation, we reconstructed the electrode-electrode connectivity using the original (*stimpair*) CCEP data. In the *network* representation, each peak represents two connections in the electrode-electrode network; one from each stimulation electrode to the recording electrode. Note that in cases where responses had

multiple peaks, only the first peak was used. Peak features of stimulation-recording electrode pairs involved in multiple stimulations were averaged. The *network* representation therefore involves duplication and averaging of peak amplitudes. The network representation resulted in a directed electrode-electrode network of peak amplitudes and permitted large-scale network analysis and direct connection-wise comparison of connections between CCEP and diffusion networks in the native diffusion network space.

5.2.3 Reconstructing Structural Networks

5.2.3.1 Image Acquisition

Pre-implantation T1 and diffusion weighted images and post-implantation T1 and CT were acquired for routine clinical assessment. Pre-implantation diffusion weighted sequences were acquired using a single-shot spin-echo planar imaging sequence, cardiac gated with TE = 73 ms. Sets of 60 contiguous 2.4 mm thick axial slices were obtained, covering the whole brain, with diffusion-sensitising gradients applied in each of 52 non-collinear directions [maximum b-value of $1200 \text{ mm}^2 \text{ s}^{-1}$ ($\delta = 21 \text{ ms}$, $\Delta = 29 \text{ ms}$, using a gradient strength of 40 mT/m^{-1})] along with six non-diffusion-weighted ($b = 0$) scans. The gradient directions were calculated and ordered as described elsewhere [80]. The parallel imaging factor (SENSE) was 2. The field of view was 24 cm, and the acquisition matrix size was 96×96 , zero filled to 128×128 during reconstruction so that the reconstructed voxel size was $1.875 \times 1.875 \times 2.4 \text{ mm}$. The DTI acquisition time was $\sim 25 \text{ min}$, depending on subject heart rate.

One of two pre-implantation T1-weighted sequences (either ‘Queen Square’ or ‘Chalfont’,) were acquired for each subject, depending on the MRI centre attended at the time of evaluation (see Table 5.1). 3/7 subjects (1,4 and 7) had Gradient Recalled Inversion Recovery sequences at 1.5 T on a Siemens Avanto scanner at the Neuroradiology Department, NHNN, Queen square. These images were $0.488 \times 0.488 \times 1.500 \text{ mm}$ resolution, acquired with 144 axial orientated slices of 249.856 mm^2 using an acquisition matrix of 512×512 . The TR/ TE/ flip-angle was $2020 \text{ ms}/1.71 \text{ ms}/15^\circ$. 4/7 subjects (2,3,5 and 6) had Gradient Recalled sequence at 3T on

a GE Medical Systems scanner at the Chalfont MRI Unit, Epilepsy Society, Chalfont St. Peter. These images were 0.938 x 0.938 x 1.100 mm resolution, acquired with either (i) 170 coronal orientated slices (3/4 subjects) of 240 x 128 mm² using an acquisition matrix of 256 by 256, or (ii) 160 axial orientated slices (1/4 subjects), each of 240 x 128 x 242.004 mm, using an acquisition matrix of 256 by 258. The TR/TE/flip-angle was 7.96 ms/3.008 ms/20°.

Post-implantation T1-weighted images were acquired using a Gradient Recalled Inversion Recovery images sequence at 1.5T on a Siemens Avanto scanner at the Neuroradiology Department, NHNN. These images were of 1 x 1 x 1 mm resolution, acquired with 176 coronal-orientated slices of 192 by 192 voxels. The TR/TE/flip-angle was 1930 ms/ 3.37 ms/ 15°.

Post-implantation volumetric brain CT images of 0.43 x 0.43 x 1 mm resolution were acquired in axial orientation.

5.2.3.2 Electrode Localisation in Diffusion Space

Electrode voxel co-ordinates were calculated from the CT by plotting and manually labelling supra-threshold voxel clusters with reference to the patient implantation notes. A threshold of 2500 Hounsfield Units was used to identify very highly attenuating regions. Electrodes invisible on CT or absent intracranial recordings were not analysed (87/704 implanted).

Estimating structural connectivity between electrodes requires transformation of electrodes from CT to diffusion space and estimation of the underlying brain region. To account for substantial brain shift following electrode implantation, non-rigid co-registrations were applied between pre-implantation and post-implantation spaces. Firstly, a rigid registration was optimised between the post-implantation CT and post-implantation T1 image. A non-rigid registration was then optimised between the post-implantation T1 and pre-implantation T1 to correct for brain shift, and between pre-implantation T1 and diffusion (first b=0 image) images. The transformation field required to transform electrode co-ordinates from CT to diffusion space was composed using the following transformation fields: (i) post-implantation CT to post-implantation T1 (ii) post-implantation T1 to pre-

implantation T1 and (iii) pre-implantation T1 to pre-implantation diffusion. All registrations, compositions and transformations were implemented in NiftyReg (v1.3.9) using the default settings [237]. NiftyReg uses normalised mutual information to calculate image similarity and a bending energy regularisation with cubic B-spline parameterisation for the non-linear warping.

5.2.3.3 Diffusion Tractography

Pre-implantation T1 images were parcellated into cortical and sub-cortical grey matter, white matter and ventricles using the LoAd tissue segmentation algorithm implemented in NiftySeg [60]. Parcellations were transformed to diffusion space using the aforementioned non-rigid transformation obtained between the pre-implantation T1 and diffusion image (see Electrode Localisation in Diffusion Space). A nearest neighbour resampling scheme was used to preserve the categorical nature of parcellation labels.

The tissue parcellation was used to define seed, propagation, and termination masks for fiber tractography. These masks define the starting location, permitted tractography region, and termination regions for local fiber tractography. Firstly, cortical grey matter was assigned to the nearest electrode voxel within a maximum of 10 mm and depth electrodes voxels were dilated by 5 mm to create the electrode parcels. Any parcels that overlapped were assigned to the nearest electrode. The binary version of these cortical parcels was the termination mask. The intersection of the dilated termination mask and the white matter parcellation defined the seed mask. The propagation mask was the union of white matter, sub-cortical grey matter and ventricle regions from the parcellation. The termination mask was mutually exclusive from both the propagation and seed masks.

Next, fiber paths in the brain were reconstructed by seeding 100 probabilistic fibers from each seed voxel using MRTrix. Fibers were propagated using the default settings in MRTrix [307]. The sampling interval was 0.2 mm, maximum curvature threshold was 60° and minimum FOD amplitude threshold for tracking through a voxel was 0.1. Fiber propagation was stopped when exiting the propagation mask or entering the termination mask.

5.2.3.4 Structural Networks

Inter-electrode structural networks were obtained by representing electrodes as network nodes and the fiber connections between them as edges. Fibers connected node pairs if their end-point coordinates terminated within two distinct electrode cortical parcels. The connection weight between two cortical nodes was defined as the density of connecting fibers (as in [72]), calculated as the sum of connecting fibers divided by the mean volume of the seed (boundary) voxels adjacent to the two parcels (boundary voxels were assigned to the nearest parcel by Euclidean distance). This resulted in a N -by- N connectivity matrix of fiber densities between all N electrode parcels. We considered connections with streamline density above 0.1 in this report, for lack of a standardised thresholding method.

5.3 Results

5.3.1 CCEPs

5.3.1.1 Epochs

Identifying the start time of saturation of the anode recording channel was a sensitive method for obtaining an initial estimate of the stimulus onset time (Fig. 5.4). The saturation time corresponded to the start of the ramp-up time of the stimulator, whereas the stimulus delivery time is associated with the appearance of the stimulation artefact in the closest recording electrode to the anode.

Across stimulation trials, some variable amount of jitter was observed in the timing of the delivery of the stimulus with respect to the start of the ramp-up time of the stimulator (Fig. 5.4). This jitter typically appeared as either unimodal or bimodal distributions of the stimulation artefact waveform latency. This affected the morphology of the mean waveform post-stimulus, leading to incorrect estimation of both the artefact and the evoked potential waveforms. The auto-correlation method of aligning waveforms post-stimulus resulted in strongly aligned data across stimulations (Fig. 5.4) and resulted in an improvement in the estimation of the mean post-stimulus response. The average inter-stimulation alignment was 3.5 ± 0.8 ms. Improvement in the estimate of the mean is demonstrated by an increase in the

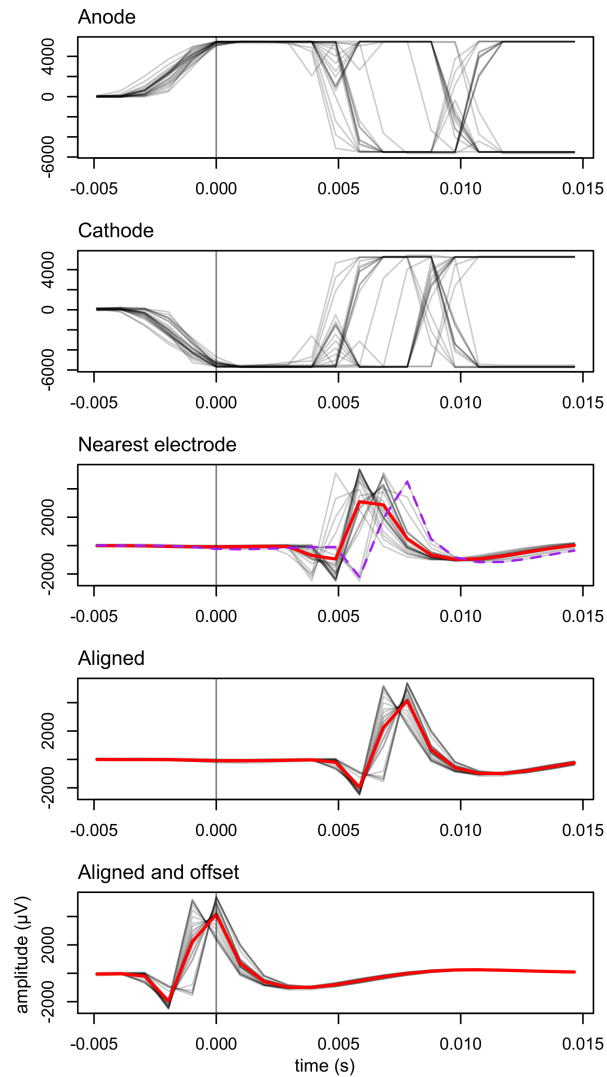


Figure 5.4: Summary of CCEP epoching. For each stimulation a current is generated between the anode and cathode electrodes, with the anode and cathode becoming positively and negatively charged, respectively (A,B). Saturation of the anode channel was used as an initial estimate of the stimulus delivery time (timepoint 0). The artefact was prominent on the nearby recording electrodes and was a better estimate of the stimulus delivery time. All stimulations were aligned to the first stimulation (purple line, C) using cross-correlation of the amplitude in the electrode nearest to the anode. The aligned data (C) was then offset to timepoint 0 using the maximum amplitude of the mean (red lines) of the electrode nearest the anode channel. This example stimulation is between two depth electrodes (DA01 and DA02) in subject 1. The nearest recording electrode was DA03.

maximum amplitude of the mean artefact when comparing data from the closest recording channel to the anode before and after alignment. The maximum amplitude in the anode-closest electrodes increased from 614.3 μV to 792.1 μV over the time period of -40:+40 ms for subject 1, indicating a better alignment. The maximum amplitude increased for all subjects apart from subject 3 which remained unchanged.

All epoched and aligned data was then offset by a variable latency to the actual delivery time. This resulted in variable offsets across stimulation pairs as it depended on the ramp-up time of the stimulator, which depends on the impedance of the material between the anode and cathode electrodes. The mean and standard deviation of offsets across all subjects was 5.4 ± 0.5 ms.

5.3.1.2 Artefact Correction

Epoching allowed estimation of the artefactual waveform across all stimulations for a given subject, which facilitated development of strategies to correct for artefactual waveforms. The artefact was examined by averaging the mean signals for all anode-closest and cathode-closest recording channels for a given subject. The anode-closest and cathode-closest waveforms had distinctive yet polar opposite shapes due to their location in the electric field (Fig. 5.5). In subject 1, the anode-closest artefact contained four peaks at latencies of -0.97, 0, 3.91 and 10.74 ms, with amplitudes of 441.9, -901.9, 159.16 and -50.12 μV , respectively. The cathode-closest artefact also consisted of four main peaks at latencies of -0.97, 0 and 3.91 and 10.74 ms with amplitudes of -433.1, 991.5 and -189.27 and 17.59 μV .

Artefactual waveforms affected time periods immediately following the stimulation, which is particularly problematic for examining evoked potential thought to reflect direct connections, as these occur at short latencies.

The automatic artefactual IC identification most commonly excluded two ICs representing artefact. In some instances, a single artefactual component was removed. Artefact correction resulted in a reduction in appearance of the artefact on recording channels whilst preserving evoked potentials (Fig. 5.6, 5.7 and 5.8). The overall effect of applying the artefact correction was a large attenuation of artefac-

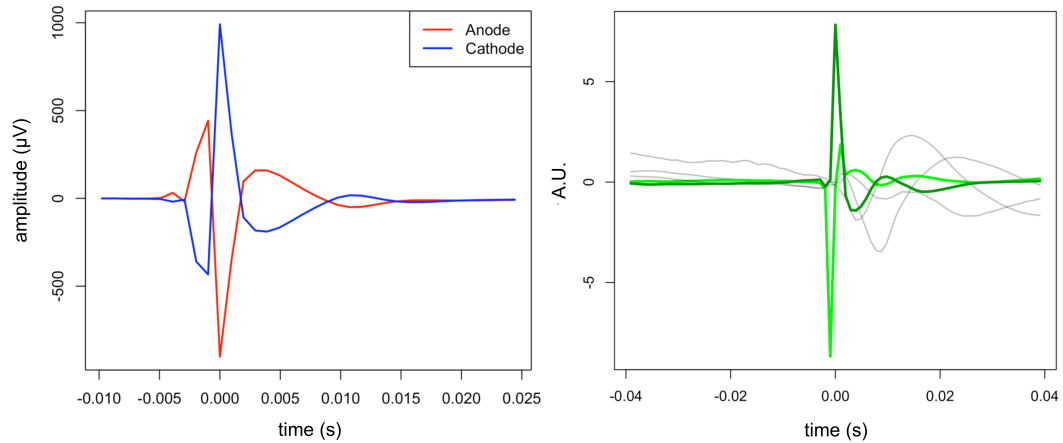


Figure 5.5: Left: Grand mean amplitudes across all stimulations in electrodes nearest the anode (red) and cathode (blue) in subject 1. The polarity of the stimulation artefact depended on the position of the recording electrode in the electric field and affected timepoints shortly after stimulation delivery. Right: IC signals estimated from an ICA of all recordings for a single stimulation. Artefactual ICs (green) were automatically identified and removed from the ICA source signal matrix before projection and reconstruction of artefact-corrected data. The stimulation was between two depth electrodes (DA05 and DA06) in subject 1.

tual peaks, shown by a decrease in the amplitudes of peaks in the average of mean responses (Fig. 5.8). In subject 1 the peaks amplitudes decreased from 441.87, -901.94, 159.16 and -50.12 μV in the recording channels nearest to the anode, to 144.05, -198.92, 138.21 and -9.45 μV in the artefact corrected data (at latencies of -0.97, 0, 3.91 and 10.74 ms).

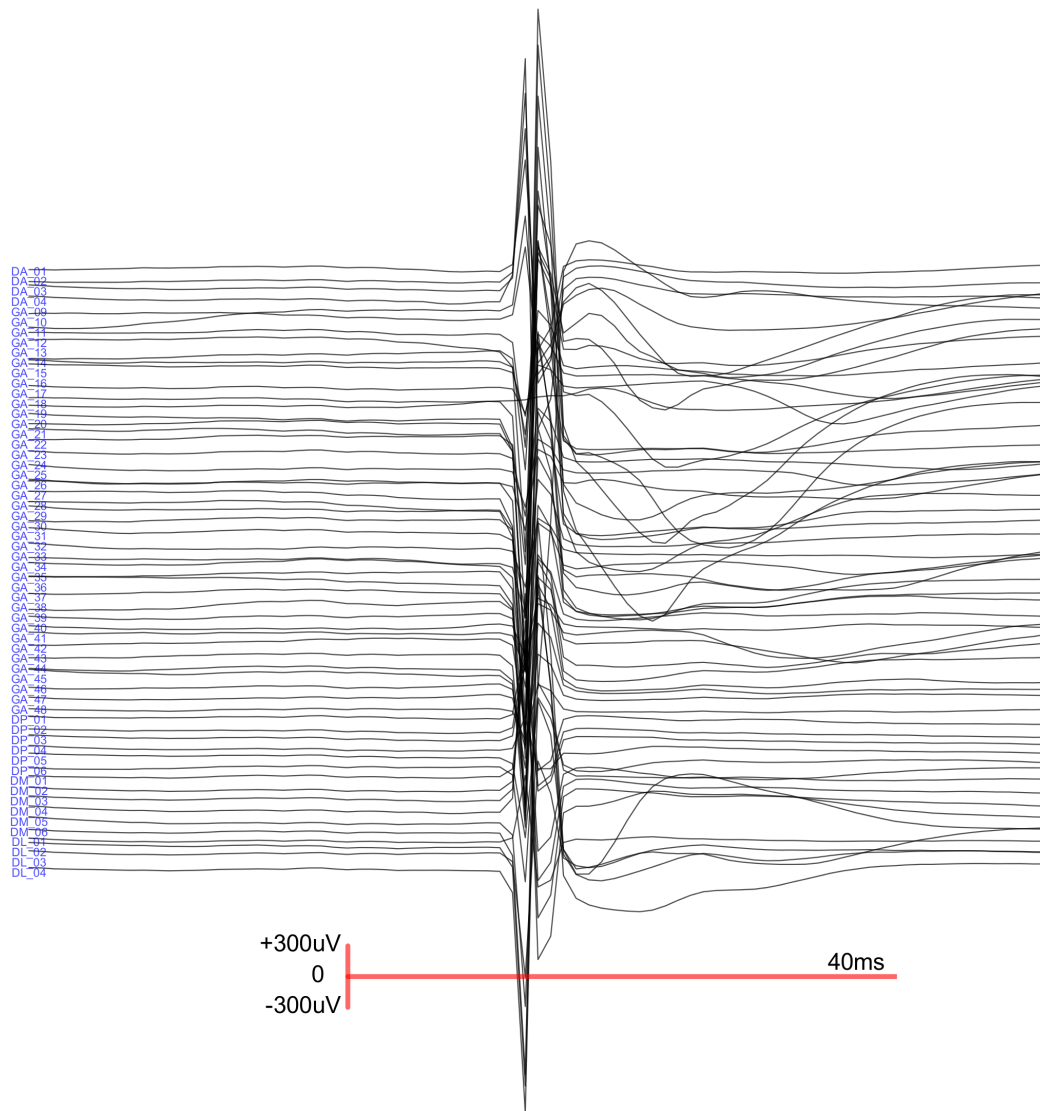


Figure 5.6: Amplitudes of epoched data for all recording electrodes after stimulation between two depth electrodes (DA05 and DA06) in subject 1. The large amplitudes at time-point 0 are artefacts while the slower waveforms found in some channels are evoked potentials.

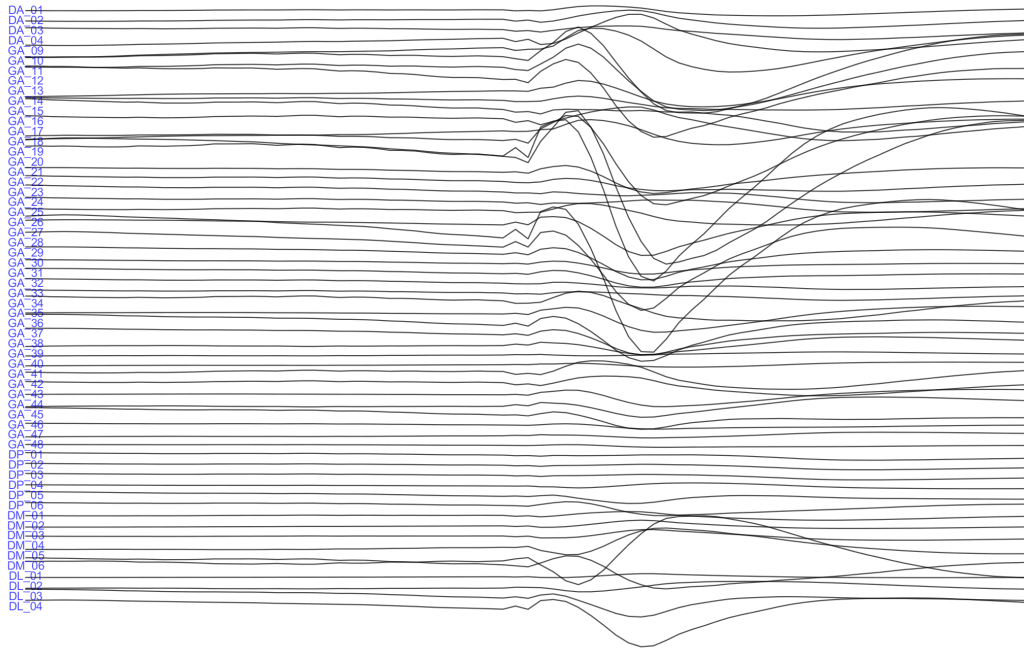


Figure 5.7: Artefact-corrected data in all recording electrodes after stimulation between two depth electrodes (DA05 and DA06) in subject 1. Amplitudes were corrected by performing an independent analysis on the signals shown in Fig. 5.6. The removed IC signals are shown in Fig. 5.5. The artefact features are greatly attenuated while evoked potentials are unaffected. Time and amplitude scale is as in Fig. 5.6.

The ICA approach appeared to result in a reduction of artefactual peaks when considering the appearance of the grand mean signal (Fig. 5.8). Other artefact correction approaches (such as template-weighted regression and weighted linear regression) also resulted in a some attenuation of artefactual peaks, but had unwanted effects (see Discussion).

5.3.1.3 Evoked Potential Peaks

The artefact correction did not perform perfectly for all stimulation pairs, as some artefactual peaks remained. Therefore, to reduce the number of false positive peaks, all peaks preceding 12 ms were excluded in the following analyses. This threshold was chosen visually to allow detection of early peaks and reduce detection of false positive artefactual peaks. Peaks occurring after 250 ms were excluded as evoked potentials representing direct connections were of primary interest in this study (see section 6.4 for a discussion of this choice of threshold).

The peak-finding algorithm detected evoked potential peaks whilst reducing

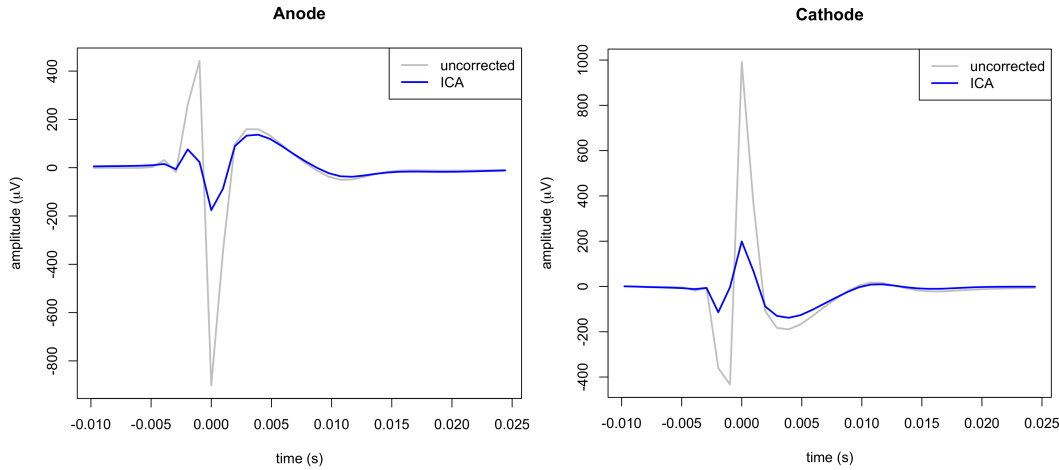


Figure 5.8: Grand mean amplitudes in electrodes nearest the anode (left) and cathode (right) in subject 1 before (grey line) and after artefact correction (blue line). Artefactual features are distinguished by their dependence on the polarity of the nearest stimulation electrode. The artefact correction resulted in attenuation of most artefact peaks.

the number of false positive peaks. False positive peaks were reduced by (i) excluding peaks prior to 12 ms (ii) low-pass filtering the data prior to peak-finding (iii) clustering peaks occurring within the same neighbourhood of small gradient, and (iv) excluding physiologically implausible peaks with high amplitude (those above $700\mu\text{V}$). Variation was observed in the amplitude, latency, and number of peaks found. Table 5.3 shows the prevalence of recording channels with one, two and three peaks across all stimulations. Evoked potentials most commonly had one peak. An example of the distribution of peak amplitudes and latencies for first peaks is shown in Fig. 5.11 for subject 1. The mean amplitude was $155.6\mu\text{V}$ and the mean latency was 75.6 ms. Only first peaks were used to construct CCEP connectivity networks (Fig. 5.12).

The figures below show examples of applying the peak detection algorithm to unfiltered and filtered responses (Fig. 5.9), and uncorrected and artefact-corrected responses (Fig. 5.10). Below that are figures showing the distribution of amplitudes and latencies of CCEP peaks used to reconstruct effective networks in subject 1 (Fig. 5.11). An example of a reconstructed effective network is shown in Fig. 5.12.

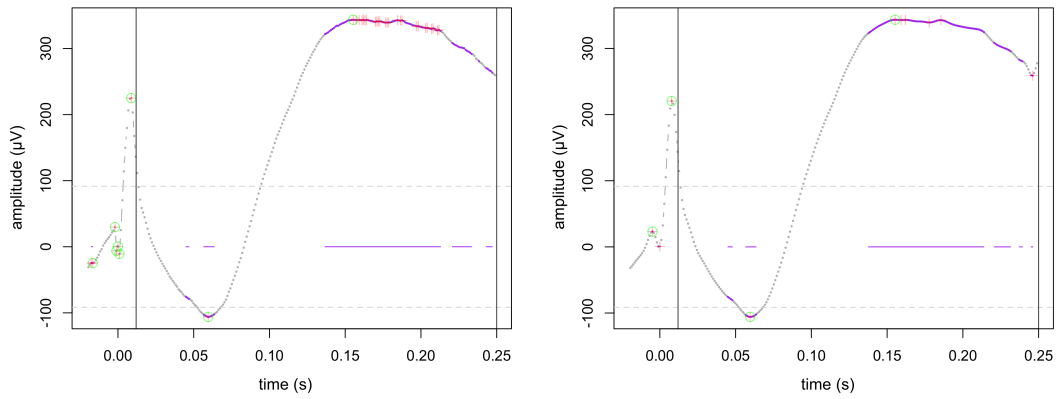


Figure 5.9: Peak detection algorithm. Left: Raw amplitudes Right: Low-passed amplitudes. Signals were low-passed filtered prior to peak detection to reduce the number of candidate peaks. Candidate peaks were those points surrounded by gradients of opposite polarity (red crosses). Evoked potentials were not removed by low-passing although the number of candidate peaks (red crosses) was greatly reduced. Candidate peaks were clustered by those residing in the same period of low gradient (purple points and line). Candidate peaks with the highest absolute amplitude (green circles) were then selected from each cluster. Selected peaks with amplitudes greater than two standard deviations of the baseline (dotted grey line) and which lie in the region of 12-250 ms were retained. All other peaks were discarded. Shown is a depth electrode (DA04) recording following stimulation between two depth electrodes (DA05 and DA06) in subject 1.

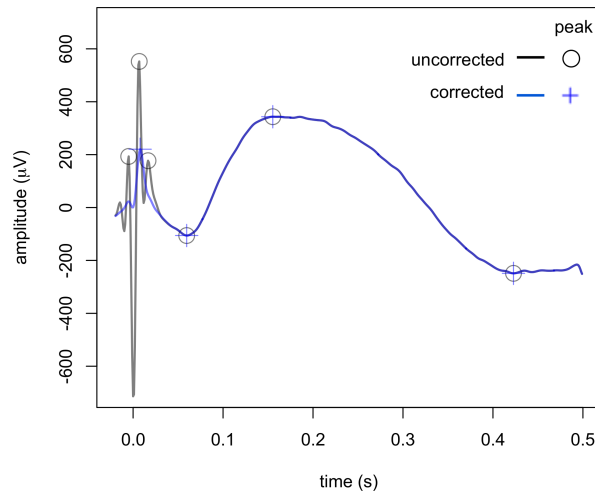


Figure 5.10: Peaks in uncorrected and artefact-corrected data. The artefact correction reduces the number of artefactual peaks whilst preserving evoked potential peaks. Shown is a depth electrode (DA04) recording following stimulation between two depth electrodes (DA05 and DA06) in subject 1.

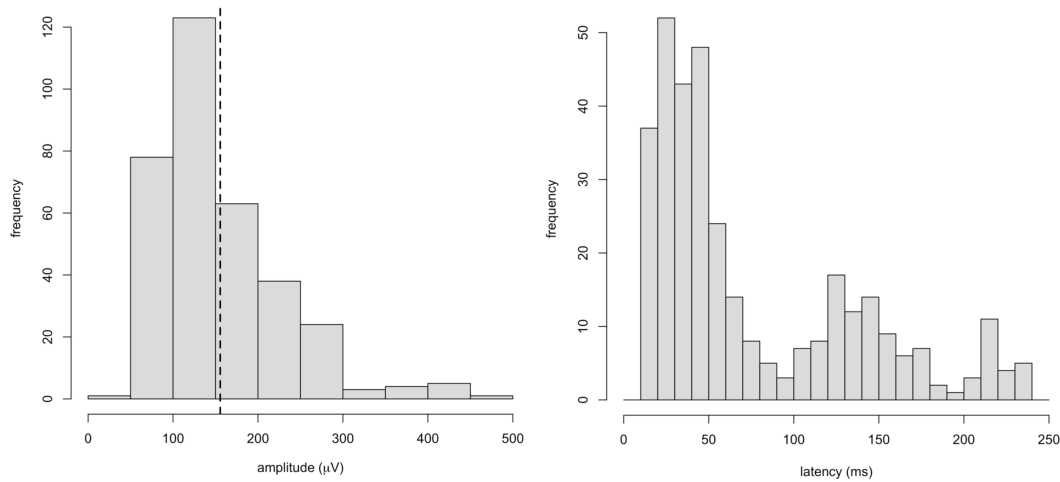


Figure 5.11: Histogram of all peak amplitudes and latencies of first peaks in subject 1. The mean peak amplitude was $155.6 \mu\text{V}$. Latencies were bi-modally distributed, with means of the two distributions at approximately 40 ms and 140 ms. The mean latency was 75.6 ms. These amplitudes were used to build large-scale electrode-electrode networks.

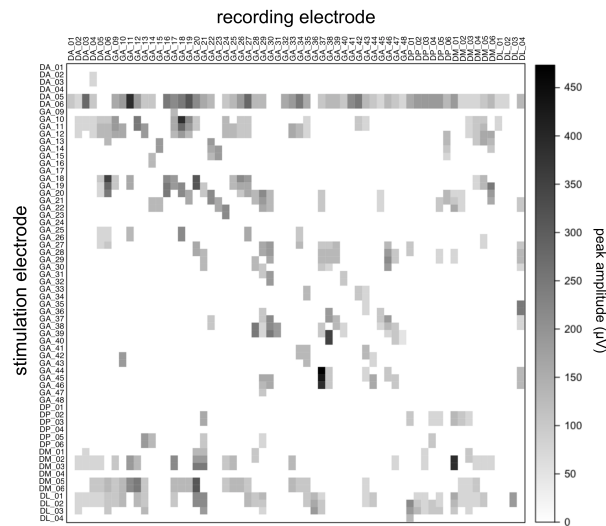


Figure 5.12: CCEP network for subject 1. Matrix entries show the peak amplitude between stimulation (row) and recording (column) electrodes. Observed peaks infer effective connection from both stimulation electrodes to the recording electrode. The network is not symmetrical indicating the directionality in the connection (towards the recording channel). Many connections are found between nearby electrodes.

Subject	0 peaks	1 peak	2 peaks	3 peaks	>3 peaks
1	87.7	7.1	4.1	0.9	0.2
2	95.9	2.8	1.1	0.2	0
3	92.6	3.6	2.4	0.9	0.5
4	83.0	8.2	5.5	2.3	1.0
5	89.8	6.6	2.0	0.8	0.8
6	89.0	7.8	2.4	0.7	0.1
7	40.4	25.3	17.9	8.3	8.1

Table 5.3: Prevalence of evoked potentials by number of peaks. The majority of evoked potentials had a single peak. Prevalence was calculated as a percentage given the total number of recordings analysed, as described in Table 5.2.

5.3.2 Diffusion Tractography

5.3.2.1 Electrodes and Electrode ROIs

The thresholding approach resulted in a reasonable electrode identification rate. Across all seven subjects, 11 implanted electrodes that had CCEPs recorded were not identified on the CT as their intensity either did not contrast sufficiently with neighbouring electrodes or the CT number was below the threshold. These electrodes were therefore not included in either the structural or effective networks. An example of identified electrodes for subject 1 is shown in Figures 5.13 and 5.14.

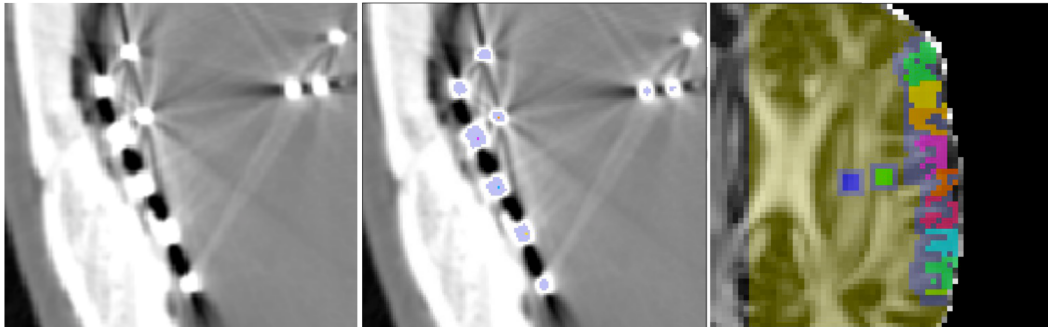


Figure 5.13: Raw CT image (left), Electrodes in CT images (middle) and electrode ROIs in the diffusion image of subject 1 (right). Middle: Blue regions are supra-threshold voxels. Coloured voxels are connected cluster centers representing the electrode locations. Right: Coloured regions indicate the grey matter ROI assigned to each electrode in diffusion space. Blue regions are the boundary voxels of the electrode ROIs. Yellow regions indicate the white matter propagation mask where streamlines propagated.

5.3.2.2 Diffusion Tractography

Electrodes were reasonably well localised to the cortical surface based on visual inspection (Fig. 5.14). An example of electrodes in diffusion space is shown in Fig. 5.13. Table 5.4 shows the mean grey matter volume assigned to each electrode, the number of seeded streamlines, and the number of streamlines intersecting electrode ROIs.

Subject	Mean ROI Volume (mm ³)	Seeds	Streamlines
1	549	521,000	98,375
2	925	966,400	234,833
3	676	1,076,100	296,867
4	415	751,700	99,694
5	681	1,109,000	256,559
6	564	461,300	90,080
7	577	612,600	161,237

Table 5.4: Tractography summary. The average volume of grey matter assigned to electrode ROIs was approximately 500 mm³, resulting in approximately half a million streamlines, of which approximately one quarter connected electrode ROI pairs.

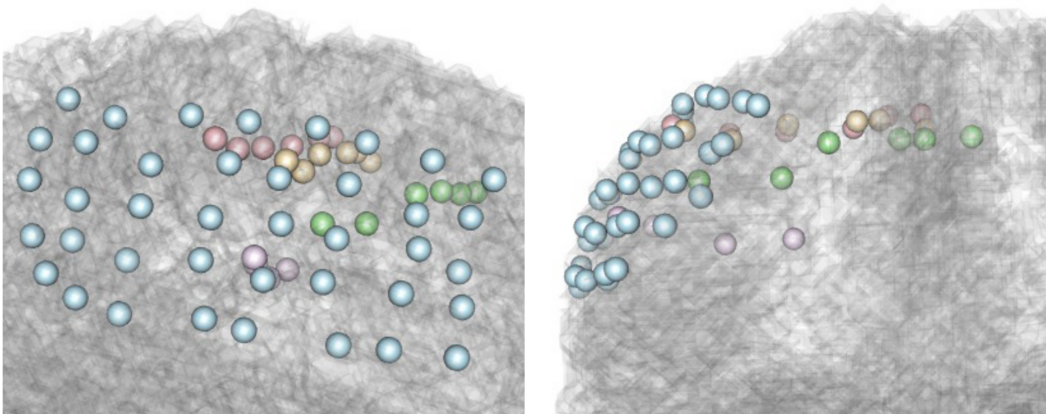


Figure 5.14: Electrodes in diffusion space in subject 1. Electrode voxels are shown as spheres and the grey matter tissue is shown as a semi-transparent volume. Grid electrodes (blue) are well localised to the cortical surface based on visual inspection. Depth electrodes (red, yellow and green) are located deeper in the brain volume.

Across all subjects reconstructed streamlines represented a mixture of short and longer range U-fibers, connecting nearby cortical regions within a lobe and sub-sections of association tract connecting cortical regions of different lobes. An

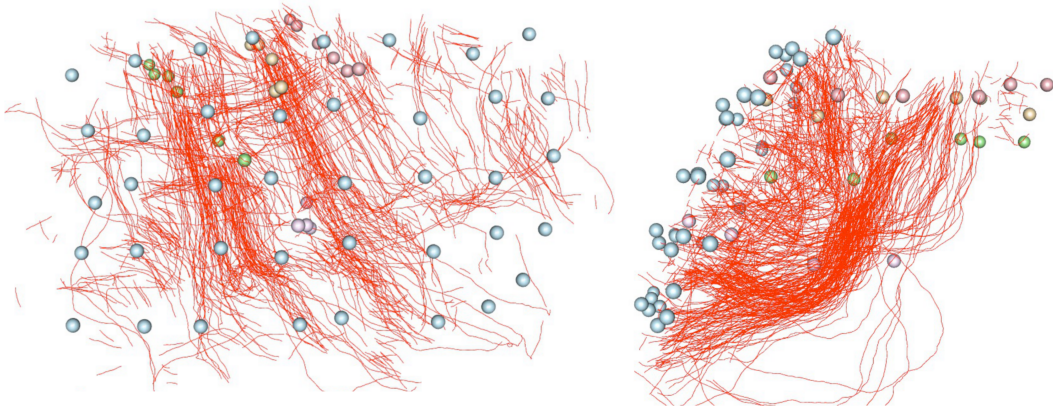


Figure 5.15: Streamlines connecting electrodes in diffusion space for subject 1. Grid electrodes are blue and depth electrodes are red, yellow and green. Streamlines appear to represent primarily short-range U-fibers. Prominent U-fibers were found between frontal lobe gyri.

example of streamlines is shown in Fig. 5.15. for subject 1. Dense superior-inferior tracts connecting frontal lobe gyri are visible which may represent sub-sections of the superior longitudinal fasciculus, while the majority of other streamlines appeared to represent short-range U-fibers. A structural network reconstructed using these streamlines is shown in Fig. 5.16.

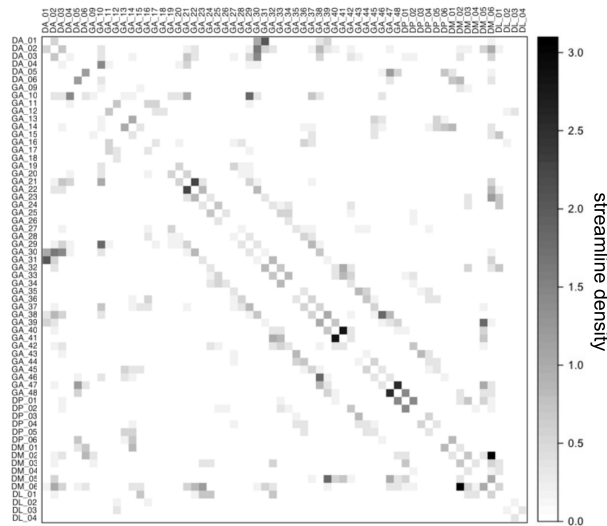


Figure 5.16: Diffusion tractography network. Matrix entries represent the streamline density (the number of connecting streamlines divided by the average grey matter volume assigned to each electrode) between electrodes (row and columns). The matrix is symmetrical as streamlines form undirected connections. Many connections are found between nearby electrodes.

5.4 Discussion

In this study, two pipelines were presented for reconstructing structural and effective connectivity networks from diffusion MRI and CCEP data. The pipelines are independent and designed to allow assessment of direct cortico-cortical connectivity and inter-modal comparison. Their combined use in estimating brain connectivity may aid identification of ictal onset areas and mechanisms of non-contiguous seizure spread.

5.4.1 Epochs

CCEP data may be epoched on stimulus delivery in order to estimate the mean waveform of evoked potentials across repeated stimulations. In this study, we described an automated three-step epoching procedure which involved initial estimation, alignment and offsetting the recordings to accurately estimate stimulus delivery time. In most previous CCEP studies the epoching process is not described [344, 178, 277, 32]. In some studies data is described as epoched using an electronic trigger which is time-locked to the stimulus delivery [221, 188, 223, 116]. Some CCEP systems therefore record the stimulus delivery time electronically, making the epoching process simple. However, as demonstrated in this study, care should be taken that the electronic trigger corresponds to the stimulus delivery time as opposed to the start of the ramp-up time of stimulation electrodes - the two differ due to the variable ramp-up time of the electrodes caused by different impedance properties of the tissue between different electrode stimulation pairs. In the absence of electronic stimulus triggers, as is the case with the CCEP system used in this study, an automated process such as that described may be used to epoch the data. This is useful as it enables analysis of data acquired on CCEP devices that do not have electronic tags, which may affect older generation CCEP systems. One previous study has used artefact template matching approach to estimate the stimulation delivery time [87]. However, an artefact template is difficult to create without an initial estimate of the stimulation onset time and requires assumptions about the appearance of the artefact.

5.4.2 Stimulation Artefact

Stimulation artefact and evoked potential signals are added together in the intracranial electroencephalogram, making delineation of early evoked potentials difficult. This is particularly problematic as the primary interest is direct connections which evoke short latency potentials. In this study we implemented an automated artefact reduction technique using ICA. In most previous studies an artefact reduction procedure has not been described. These studies have examined particular brain sub-networks where visual interpretation was used to identify waveforms which are clearly distinguishable from stimulation artefact [113, 304, 319, 67, 344]. Other studies have employed an exclusion window following stimulation of between 10 and 20 ms [178, 116, 188, 87]. Acquiring CCEPs using an alternating monophasic pulse is a common acquisition method which has the benefit of reducing the stimulation artefact [221, 304, 115]. In an alternating monophasic pulse the polarity of the artefact switches between positive and negative on each pulse, and the artefact waveform may therefore be reduced by averaging on repeated stimulations. In cases where the artefact persists, such as when using a biphasic [344, 222, 225, 178] or non-alternating monophasic pulse [183, 324], a post-acquisition artefact reduction method is desirable.

Artefact correction did not completely remove the artefact but allowed use of a shorter exclusion window than may have been needed prior to artefact correction, while reducing the effect of the artefact on non-excluded post-stimulus timepoints. The ICA method is well suited for reducing signal artefacts and has been used previously in scalp EEG [96]. Other artefact reduction methods were tested, notably including artefact template subtraction and weighted linear regression, but were found to be less reliable than the ICA approach. The artefact template subtraction method firstly created an artefact template for each stimulation by amplifying each recording signal by the square of distance to the nearest stimulation electrode, and adjusting the signal polarity based on the polarity of the nearest stimulation electrode. The artefact template was then created by averaging these signals. For each recording electrode the artefact template was transformed by the distance squared,

corrected for the appropriate polarity and subtracted from the signal. There are two main drawbacks to this artefact correction method. Firstly, it relies on assumptions that the voltage field of two monopolar sources decays inversely to the distance squared. This may not be true in inhomogeneous medium such as the brain, leading to errors in the amplification magnitude and in the polarity adjustment of the signal. Furthermore, recording channels large distances from the stimulation electrode will contribute little artefact signal to the template but large amounts of noise as the signal is amplified. These two effects lead to error in the creation of the artefact template and therefore errors in the artefact-corrected data. The weighted linear regression firstly created an artefact template, as above, and subsequently regressed the template from each recording signal using a weighted fitting. As this method also uses the same artefact template creation method, it suffers drawbacks of erroneous template signal and noise amplification. In addition, it relies strongly on the weighting function used in the regression, which may lead to very large or very small residuals at timepoints where the weighting is high or low.

It is possible that improvements to the selection of the number of ICs and the artefactual IC selection process may lead to a greater artefact reduction. Performing PCA prior to ICA was tested as a method to select the initial number of ICs. However, the number of PC's depends on an arbitrary variance threshold and the relationship between PCA and ICA was not sufficiently clear to select a definitive variance threshold for using PCA to select the number of ICs.

Recently, Trebault et al. [311] reported a more sophisticated template-based method for artefact correction. The method first matches the observed data to a library of artefact signals produced using a simple biophysical model, covering a range of possible stimulation parameters (monophasic and biphasic stimulation, and stimulation pulse duration). The closest matching model artefact is then regressed from the observed data. Results show that quantitative measures of artefact contamination are reduced. This is a promising technique for reducing stimulation artefact which permits robust analysis of earlier CCEPs. Their method is similar to the template-based regression and subtraction method tested on our data and described

above. Specifically, while our template creation method employed biophysical parameters of distance and polarity with respect to the stimulation electrode, Trebaul et al. [311] used biophysical parameters relating to a resistance-capacitance circuit model, and were further able to quantify artefact contamination by using simulated ground truth data. It would be interesting in future to compare the artefact reduction capabilities of ICA-based approach described here to the template-based technique detailed by Trebaul et al. [311].

A final consideration for reducing stimulation artefact is to obtain a better understanding of the artefact waveform with respect to the orientation (distance and electromagnetic field location) of the recording channel. This may enable generation of more accurate models of the stimulation artefact. We performed an *in vitro* stimulation experiment to enable better artefact waveform characterisation. However, a number of other experimental artefacts prevented useful analysis of this data (see Appendix).

5.4.3 CCEPs

In this study only evoked potentials prior to 250 ms were analysed, as short latency responses are thought to more faithfully represent direct axonal connections. Previous studies have examined the N1 and N2 negative evoked potentials [221, 350, 223, 185], occurring at approximately 100 and 150 ms, respectively. As with this study, most other CCEP studies have not observed predominantly negative peaks and have therefore analysed either the A1 and A2 evoked potentials (the absolute amplitude of the evoked potential), occurring at approximately the same latencies [188, 116, 178], or divided peaks into early and late time periods, corresponding to peaks occurring up to latencies of 100 and between 100-1000 ms, respectively [324, 326, 325, 125, 32]. There is no consensus in CCEP studies on the interpretation of early (e.g. N1, A1) and late evoked potentials (e.g. N2, A2). In a recently published CCEP review it has been suggested that both the N1 and N2 reflect direct connection although the N1 reflects early excitatory synaptic potentials whereas the N2 reflects later inhibitory post-synaptic potentials [179]. A recent large-scale study [116] examining A1 and A2 peaks commented that the N1 has

been reported to reflect direct connection whereas the N2 reflects indirect (cortico-cortico-cortical, cortico-subcortico-cortical etc.) connection [221]. However, as the authors mention, this contradicts earlier reports in cat visual cortex that suggests that afferent volleys can cause early and late responses within the time window of the A1/N1 and A2/N2 potentials [212]. In view of this ambiguity, this study analysed the first peaks of evoked responses and used latencies up to 250 ms to include all possible early evoked potentials.

5.4.4 Electrode-Electrode Networks

The CCEP evoked potential data consisted of a list of peaks and the corresponding stimulation electrodes and recording electrodes. In order to achieve correspondence between CCEP and diffusion networks, and therefore enable their comparison or combined application, peak amplitudes were represented in a electrode-electrode connection matrix. To do this, data was duplicated and sometimes averaged, and assumptions were made that evoked potentials corresponded to connectivity between both stimulation electrodes and the recording electrode. Similar assumptions have been made in previous large-scale CCEP studies. For example, Entz et al. [116] assigned a Brodmann area to each stimulation and recording site, resulting in one connection for each evoked potential, enabling study of large-scale connectivity between Brodmann areas. David et al. [87] only analysed stimulation electrodes which resided in the same Brodmann areas in order to build a large-scale representations of functional tracts from each brain region. Other smaller scale studies have analysed stimulation electrode pairs residing in the same cortical area in order to allow inferences to be made [223, 221, 67]. The previous study by Conner et al. [78] which compared CCEP and diffusion connectivity only analysed CCEP and diffusion connectivity arising from Broca's area [78]. This discarded information from all other stimulation pairs which did not have both stimulation electrodes located in Broca's area. Therefore, although the method of creating large-scale effective networks involved assumptions as well as data duplication and averaging, this is a similar concept to studying effective connectivity as in previous studies.

5.4.5 Electrode Localisation

Electrode anatomical localisation was used to interpret CCEP findings with respect to brain function. We used rigid and non-rigid registration to determine the locations of electrodes in structural T1 images, which provided an intermediate phase for registering electrodes to diffusion images. Previous studies have implanted electrodes using a stereotaxic frame, allowing extrapolation of coordinates to the Talairach [298] or MNI [118] anatomical reference spaces in order to identify brain regions underlying electrodes [344, 67, 87]. An alternative method has been to register the CT to a post-implantation T1 image where the anterior commissure to posterior commissure line has been defined, which also allows transformation of electrode coordinates to the Talairach reference space [277, 188]. Another method has been to identify the locations of electrode directly on the post-implantation structural T1 image using the signal void, and therefore determine the electrode locations using gross anatomical knowledge of locations of major brain regions [221, 223, 168, 224]. A further method has been to rigidly register the CT, post-implantation T1 and pre-implantation T1 image [113, 32, 225], which may be followed by projecting the electrodes towards the brain surface [178, 116, 185]. Finally, for visualisation purposes, some studies have represented electrode locations on a schematic diagrams, allowing an approximation of their anatomical location [222, 125, 304].

Registration of electrodes from CT space to post-implantation MRI space, followed by non-rigid registration to pre-implantation MRI space is expected to be a more accurate than surface projection following rigid registration of CT to pre-implantation MRI. This is because it uses contrast derived from anatomical information to directly drive the deformation, whereas in the case of projecting electrodes to the cortical surface, a uniformly radial direction of brain shift can not be assumed. Furthermore, use of stereotaxic co-ordinates or Talairach space makes large assumptions that the patient brain anatomy is similar to that of the atlas space, which may not be true due to individual variability in brain anatomy. A combination of rigid and non-rigid registration is expected to provide the most accurate

localisation of electrodes in structural T1 images, although frequently these images are not available and alternative methods such as those mentioned above can be performed. In the future, neuroimaging is likely to become more popular in pre-surgical evaluation and therefore post and pre-implantation T1 images will be more commonly available. A further method to consider for electrode localisation is that of using three dimensional modelling to represent the brain surface and electrode coordinates from intra-operative photographs and registering this model to the cortical surface of a pre-implantation structural T1 image.

5.4.6 Electrode ROIs

Defining electrode ROIs is needed to determine the connectivity of tractography streamlines. In this study the grid electrode ROIs were constrained within grey matter tissue defined in a tissue parcellation, whereas depth electrodes were simply dilated by 5 mm. Previous diffusion tractography studies in epilepsy have manually defined small ROIs propagated from MNI space in order to examine connectivity within particular brain sub-networks of interest, such as those relating to language function [209, 276, 111], or used ROIs in cortical atlases when performing large-scale cortical connectivity studies [241, 300, 365, 210]. However, in CCEP studies it is more difficult to define a brain ROI. It could correspond to the volume of activated neural tissue directly underneath the electrode following stimulation, or to the volume of tissue underneath the electrode which contributes to local field potentials observed at recording sites. The volume of activated neural tissue underneath each electrode is expected to be around 3 mm^3 , whereas the resolution of intracranial EEG measuring local field potentials is approximately 10 mm, meaning a source of brain electrical activity may spread up to but not exceeding 10 mm distance [191]. In fact, the volume of activated neural tissue is not identical for each stimulation, as the current density depends on the positions of the stimulated electrodes. This means that each electrode stimulation will activate a unique volume of tissue. One possible method to estimate the current density for each electrode stimulation pair would be to use finite element modeling [242], for which the tissue classes could be derived from a structural tissue parcellation. The current density may then be

thresholded according to the stimulation activation thresholds of neurons detailed in Ranck Jr [264]. It should however be noted that these thresholds refer to currents generated using a monopolar stimulation, whereas bipolar stimulation has been used in the majority of CCEP studies. In this study, electrode ROIs were expected to be approximately the same size as those contributing to local field potentials but larger than that expected to be activated during stimulation. Conner et al. [78] used virtual cuboidal ROIs of 20 x 20 x 20 mm around each electrode, and Swann et al. [296] used ROIs of 10 x 10 x 10 mm. This is expected to be a less specific method of defining electrode ROIs as the ROIs are not constrained to lie within the grey matter, and may therefore result in overestimation of their connectivity.

5.4.7 Tractography

The aim of diffusion tractography is to estimate the paths of axonal connections in the white matter. In this study, diffusion tractography was performed from the boundary voxels of electrode ROIs using probabilistic tractography. High reproducibility of connection weights was found when using this tractography method as part of a pipeline to construct whole-brain networks between ROIs in a cortical parcellation [251]. In addition, the tractography method was part of a pipeline which had high agreement to another state-of-the-art pipeline with similar capabilities (see section 4.3.1).

Diffusion tensor deterministic tractography is the most popular method for estimating structural connectivity in epilepsy [205, 365, 300, 347]. The ball-and-sticks multiple fiber population model coupled with probabilistic tractography has also been widely used [133, 241, 271]. The advantages of probabilistic tractography over deterministic tractography are the ability to estimate a continuous measure of connectivity which measures the likelihood of other minor axonal paths in addition to the single most likely path. In addition, the constrained spherical deconvolution approach is model-free and does not rely on a priori assumptions about the number of independent fiber populations in each voxel, whilst retaining wide flexibility in the number of fiber orientations it can represent. A more detailed description of diffusion tractography in structural networks is described in section 4.1. The trac-

tography results in this report suggests that probabilistic tractography may be more appropriate to reconstruct structural connectivity between intracranial electrodes as it recovers short range U-fibers in addition to other major white matter pathways.

The intersections of streamlines on electrode ROIs was used to build a large-scale inter-electrode structural connectivity networks, using a connection weighting scheme considering the volume of node areas, as used commonly in previous large-scale network studies using cortical atlases (see Chapter 3). This is the first such study to report construction of large-scale inter-electrode structural networks for the purpose of correlating structural and effective networks.

5.5 Summary

This is the first study to apply state-of-the-art reconstruction pipelines in both structural and effective connectivity networks for the purpose of inter-modal comparison and analysis of large-scale connectivity in epileptogenic networks. Contemporary state-of-the-art methods used for epoching, artefact reduction, peak-finding and large-scale network reconstruction of effective networks from CCEP data were described and compared with previous studies. Furthermore, structural networks were reconstructed using state-of-the-art pipelines demonstrated to have high reproducibility and agreement with other methods of equal capability in the previous thesis chapter. This chapter provides a reference for Chapter 6, which will correlate the structural and effective networks, examine potential connectivity abnormalities of the ictal-onset zone, and mechanisms of non-contiguous seizure spread.

Chapter 6

Structural and Effective Networks: Inter-Modal Comparison, Ictal-Onset Connectivity and Seizure Spread

In patients with drug-resistant focal epilepsy, seizure freedom following resective surgery relies on correct identification of cortical area generating seizures, known as the ictal-onset zone [278]. This is often challenging using current techniques which combine findings across multiple observational techniques such as intracranial EEG, scalp EEG, structural MRI, seizure semiology and patient history. It is possible that seizure freedom may be improved by using connectional information from diffusion MRI tractography and CCEPs. In this chapter, the challenges in identifying the ictal-onset zone in drug-resistant frontal lobe epilepsy are introduced. Connectional disturbances reported in epilepsy using diffusion MRI tractography and CCEPs are then described. The correlation and overlap between structural and effective networks is quantified, and the ability of the techniques to detect connectional abnormalities of the prescribed ictal-onset zone is examined. Structural and effective networks are then evaluated for evidence of macroscopic connections supporting non-contiguous seizure spread. Finally, findings regarding inter-modal agreement, seizure onset connectivity and non-contiguous seizure spread are discussed with respect to the wider literature.

6.1 Introduction

Epilepsy is a group of neurological disorders affecting approximately 1% of people and is characterised by recurring seizures associated with abnormal brain electrical activity. Focal seizures consist of localised areas of abnormal neuro-electrical activity which can subsequently spread to contiguous and non-contiguous brain areas. This is in contrast to generalised seizures which affect both hemispheres of the brain at onset. Frontal lobe epilepsy (FLE) is the second most common form of focal epilepsy, accounting for approximately 20-30% of all focal epilepsy cases [253]. Approximately 30% of focal epilepsy patients are resistant to anti-epileptic drugs and in these cases resective surgery is an option [148].

In drug-resistant epilepsy patients who undergo pre-surgical evaluation, localisation of the ictal-onset zone- the brain location where abnormal electrical activity starts; propagative regions- brain locations that abnormal electrical activity propagates to from the ictal-onset zone; and eloquent brain regions- brain regions required for essential processing tasks, such as language; are of primary importance. Localising the ictal-onset zone involves consideration of neurological findings across multiple modalities such as scalp EEG, intracranial EEG and neuroimaging such as structural and functional MRI, which are considered in context with seizure semiology (signs and symptoms of a seizure) and patient medical history.

It is difficult to localise the ictal-onset zone in FLE using seizure semiology due to inter-individual variation in frontal lobe function and anatomy and the incomplete understanding of how frontal lobe functional anatomy affects seizure semiology. Ictal and inter-ictal EEG are frequently non-localising due the difficulty in attributing sources to observed EEG abnormalities. It has been estimated that inter-ictal EEG can only localise the ictal-onset zone in about one third of FLE patients with ictal EEG changes [160]. Therefore, intracranial EEG is needed to define the extent of the ictal-onset zone in the majority of patients with frontal lobe epilepsy [160].

Improvements in seizure freedom in FLE following resective surgery have been partly attributed to advances in structural and functional neuroimaging [160]. This may be expected given that neuronal migration disorders such as cortical

dysplasia have been increasingly recognised as important causes of frontal lobe epilepsy- 50% of patients with frontal lobe epilepsy are MRI positive and there is a high correlation between an MRI identified lesion and the location of the epileptogenic zone [160]. Despite technical advances particularly in neuroimaging, seizure freedom rates are only 60-70% in temporal lobe epilepsies and 50% or less after extra-temporal resections [303], meaning accuracy in identifying the ictal-onset zone during pre-surgical evaluation in FLE may be improved.

Diffusion-weighted images and CCEPs are increasingly acquired during pre-surgical planning as part of standard care to provide complimentary information regarding connectivity of the prescribed ictal-onset zone. Combining connectivity information from diffusion imaging and CCEPs may allow a better estimation of epileptogenic networks and lead to improved accuracy in identifying the ictal-onset zone. The following paragraphs will summarise previous works demonstrating connective disturbances in epilepsy using diffusion imaging or CCEPs.

Diffusion tractography has been extensively used to study focal epilepsy outside of the frontal lobe. These studies have been undertaken with a variety of aims: to examine structural connectivity of particular tracts or brain regions relating to the epilepsy sub-type [238, 209, 276, 111, 296, 295, 11, 133, 190, 235, 271, 331], to examine large-scale structural connectivity [205, 365, 34, 103, 24, 98, 199, 210, 346, 347, 241, 300], and to investigate structural reorganisation with respect to epileptogenic [355, 345] or language networks [117] following surgery. Other studies have aimed to predict post-surgical from pre-surgical structural connectivity [241], to correlate tract measures to clinical outcome and EEG seizure propagation [102, 101], or large-scale structural connectivity to cognitive performance measures [321], and to better understand the relation between structural and functional connectivity in focal epilepsy outside of the frontal lobe [276, 205, 78, 365, 103, 24, 133].

Those studies examining particular tracts of interest in focal epilepsy originating outside of the frontal lobe have in some cases confirmed the presence of a structural link between regions of interest thought important in epilepsy pathol-

ogy [296]. On the other hand, other studies have found both ipsilateral decreases [11, 209] and contralateral increases [276] in microstructural indices (FA) in tracts closely associated with particular epilepsy types. Connectional changes have been correlated with cognitive function, as Diehl et al. [101] demonstrated correlation between microstructural indices (FA and ADC) and memory scores in the uncinate fasciculus of left temporal-lobe epilepsy patients. Large-scale cortical connectivity studies have demonstrated connectivity changes outside the ictal-onset lobe [346, 210, 205, 98, 365], with some evidence (correlation) for accompanying structural and functional changes [205]. Loss of efficient network topological organisation has been observed both functionally and structurally at the global level [365], and/or at the local level [365, 210, 346, 34]. Multiple reports have shown that structure-function coupling tends to decrease with disease severity [365, 24]. In addition, some global network metrics correlated closely with cognitive test scores [321].

A small number of studies have examined structural connectivity in FLE using diffusion tractography. These studies have investigated potential abnormal connectivity in particular tracts of interest [149, 333, 58], or across large-scale networks [323], examined the relationship between structural and functional connectivity [149, 186, 323], or assessed the ability of diffusion tractography to aid in planning of resective surgery [262].

Studies on tracts of interest in FLE epilepsy sub-types have shown disturbances [149, 58, 186] in structural connectivity of regions involved in epileptogenesis, although no alterations in supplementary motor area connectivity in FLE were found in one study [333]. Ipsilateral and contralateral changes in microstructural indices in tracts closely related to suspected epilepsy pathology has been observed [149, 58]. Studies on large-scale networks have shown changes in functional but not structural global topology in relation to childhood FLE [323]. Those studies examining the relationship between diffusion tractography and functional measures have demonstrated a decoupling between structure and function at a large-scale [323]. However, agreement between alterations in fMRI and diffusion tractography has been demon-

strated that helps explain seizure semiology and EEG recordings [186]. Finally, diffusion tractography has been shown to aid in resection planning by identifying eloquent tracts [262].

CCEPs have been previously used for mapping brain connections. Hypotheses regarding connectivity of particular brain networks such as the language [221, 78, 350], limbic [344, 67, 68, 188], motor [223, 114] and sensorimotor [114, 304] systems, or across broader brain networks such as the thalamus [277], parietal [224], frontal [224, 192] and temporal [344, 192, 319, 185] lobes has been investigated. For example, Matsumoto et al. [221] analysed the N1 and N2 component of CCEPs and found a bidirectional pattern of effective connections between a broader range of language areas than that suggested in the Wernicke-Gerschwind model of language. Umeoka et al. [319] analysed positive and negative peaks of the CCEP to demonstrate bilateral temporal connections thought responsible for seizure spread from one temporal lobe to the other.

To estimate effective connectivity on a larger scale, some studies have stimulated all possible electrode pairs and performed a group analysis by transforming electrodes to a standard space [177, 87, 116, 178]. In order to demonstrate the potential utility of this approach for mapping connectivity, David et al. [87] examined early responses to generate a group report of functional tractography between regions covered by electrodes. Their method allows summaries of the probability of recording a significant CCEP response and the latencies of these responses for a given brain region, and the concept is illustrated using CCEPs between the posterior superior temporal gyrus and the inferior frontal gyrus. More recently, Entz et al. [116] used a large-scale group approach to map the directionality of early and late responses across all stimulation pairs and identified the most reliable connections. Keller et al. [178] examined early and late responses across all stimulation pairs and probed the directionality of connections in order to define major cortical projectors and integrators of information.

A number of studies have examined effective connectivity of epileptogenic networks using responses to SPES [324, 326, 325, 125, 168, 183, 32]. Multiple studies

have demonstrated abnormal prevalence of delayed responses (which are distinguished from CCEPs in these studies, as described in [38]) in seizure onset regions [324, 326, 125]. It should be noted that studies demonstrating abnormal delayed responses [324, 326, 125] did not average the evoked response on repeated stimulations, as is common practice with CCEPs, but instead determined delayed responses visually by their repeated occurrence on single stimulations. For example, Valentin et al. [324] studied responses to single pulse electrical stimulation in a large group of 45 temporal lobe epilepsy patients [324]. Early CCEPs (0-100 ms post-stimulus) and late (100-1000ms post-stimulus) latency responses were observed during acquisition. The authors found that late responses, although only found in half of patients, were associated with regions where seizure onset occurred. This is in contrast to early response CCEPs, which were found in all patients and throughout the brain. Note that delayed responses were defined as slow wave and sharp spikes whereas early response CCEPs were defined as fast waves immediately following the stimulation. Another study has demonstrated higher amplitudes of the N1 CCEP component at ictal-onset electrodes compared to surrounding electrodes [168] and this effect was more pronounced in electrodes showing the repetitive spiking compared to paroxysmal fast patterns of seizure onset [112]. Some SPES studies have also demonstrated favourable surgical outcome in patients who had brain regions with abnormal responses to SPES resected [326, 125].

Despite significant advances in understanding connectivity of the ictal-onset zone, little is known about mechanisms of seizure propagation. Contiguous seizure spread, which is more commonly observed than non-contiguous seizure spread, is known to occur through cortical layer V [302]. However, intracranial EEG recordings also demonstrate spread of seizure activity between non-contiguous sites [107, 314], which may involve areas ipsilateral or contralateral to the ictal-onset zone [31, 21, 207]. For example, Baumgartner et al. [21] studied seizure propagation pathways in five patients with supplementary motor cortex seizures. The authors found epileptic discharges occurred synchronously in the supplementary motor area and the primary motor cortex and that the actively involved electrodes

were separated by silent electrodes, providing evidence for non-contiguous seizure spread. Blume et al. [31] studied the seizure propagation properties (direction and speed) of frontal lobe seizures using scalp and intracranial EEG. They found the most common route of seizure spread was to contiguous frontal lobe cortex, although intracranial EEG seizures also showed spread to opposite hemisphere cortex in the majority of cases. It is unknown whether this non-contiguous seizure spread may occur via direct cortico-cortical connection or indirectly via cortico-subcortico-cortical or cortico-cortico-cortical connection.

Diffusion tractography gives information relating to direct macroscopic inter-cortical connectivity, thus enabling the determination of the macroscopic white matter tracts arising from intracranial electrodes. Intracranial EEG enables the determination of the location of ictal-onset and non-contiguous seizure spread routes. CCEPs denote presence of functional tracts between implanted electrodes. Therefore, combining CCEPs, diffusion tractography and intracranial EEG seizure recordings may help elucidate the mechanisms of non-contiguous seizure spread.

There are three primary aims to this study: (i) to assess the correlation between structural and effective networks at a large-scale across the cortex; (ii) to assess the potential for diffusion tractography and CCEPs to identify structural and effective connectivity markers of the prescribed ictal-onset zone and (iii) to examine the mechanisms of non-contiguous seizure spread using structural and effective networks.

6.2 Methods

6.2.1 Structural and Effective Networks

Structural and effective networks were reconstructed for seven drug-resistant epilepsy subjects with either frontal or parietal lobe epilepsy, using the pipelines described in Chapter 5. Subject details can be found in Table 5.1, Chapter 5.

Inter-electrode effective connectivity was calculated as an average of the connectivity values from each stimulating electrode to the recording electrode, as described in the Chapter 5, Methods. This conversion of data representations from

stimpair to *network* allowed a direct connection-wise analysis of data points between the native diffusion structural network space and CCEP space.

Networks were reconstructed for multiple connection features. Effective networks were reconstructed for peak amplitude, latency and baseline standard deviation. Structural networks were reconstructed for streamline density and tract distance. Furthermore, the Euclidean distance network was also constructed using the coordinates of electrodes in CT images. Henceforth, peak amplitude networks will be referred to as effective networks and streamline density networks will be referred to as structural networks.

6.2.2 Binary Network Analysis

Graph theoretical analysis was applied to binarised structural and effective networks, in order to compare the nodal connection topography between ictal and non-ictal electrodes. Nodal graph theoretical measures calculated were indegree, outdegree, normalised indegree, normalised outdegree, clustering coefficient [244], centrality [41] and reciprocity. Indegree and outdegree refer to the number of outgoing and incoming connections of a node, respectively. Normalised indegree and outdegree refer to the indegree and outdegree of each node normalised by the maximum given the number of nodes in the network. Reciprocity was calculated as the number of bidirectional connections as a fraction of the outdegree. Indegree, outdegree, clustering coefficient and centrality were calculated using the *igraph* package in R [84]. Reciprocity was calculated using custom built scripts in R [301].

6.2.3 Structural and Effective Network Comparison

Two inter-modal comparison metrics were calculated:- the Jaccard Index, which measures the overlap in the binary structural and effective networks; and the Pearson correlation, which measures the correlation between structural and effective network connection weights. The Jaccard Index was calculated on a subject-wise basis as the size of the set of intersecting connections divided by the size of the set of union connections.

6.2.4 Ictal-Onset Connectivity

During pre-surgical evaluation, each subject underwent video telemetry (simultaneous video and EEG monitoring) to correlate EEG findings with seizure semiology. All subjects had multiple seizures during video telemetry. Of these seizures, a set of prototypical seizures was identified for each subject by an experienced neurophysiologist (Dr. Beate Diehl, NHNN).

Electrodes were then classified as either ictal-onset or not ictal-onset by analysing the first electrodes demonstrating seizure activity on the intracranial EEG of each prototypical seizure. Observations of seizure activity were made by an experienced physiologist (Ms. Catherine Scott, MPhil., NHNN). Seizure activity was defined as a clear ictal EEG pattern consisting of regular spikes, rhythmic sharp waves, spike-and-slow wave complexes, sharp-and-slow-wave complexes, rhythmic delta or theta activities, sharpened delta or theta activities, or low-amplitude high-frequency activity in the beta range, as in [1].

Network connections were classified as *in*- those entering an ictal-onset electrode; *out*- those leaving an ictal-onset electrode; *within*- those between ictal-onset electrodes; and *outside*- those between non ictal-onset electrodes, as shown in Fig. 6.1. The features of interest (peak amplitude, latency, baseline standard deviation and streamline density) were then examined across the four connection categories, on a pooled subject level for all effective network connections. The nodal graph theoretical properties of ictal-onset and non ictal-onset electrodes were also compared on a pooled subject level.

6.2.5 Non-Contiguous Seizure Spread

For each prototypical seizure, electrodes were classified by an experienced physiologist (Ms. Catherine Scott) as either ictal-onset- the electrode where seizure activity starts; early propagative - electrodes showing seizure activity within one second of seizure onset, and late propagative- electrodes showing seizure activity between one and two seconds. Seizure activity was defined as described above.

Possible non-contiguous seizure spread connections were then identified as all possible connections from onset to early propagative electrodes (O-E), onset to later

propagative electrodes (O-L), and early to later propagative electrodes (E-L). Non-contiguous connections were those between electrodes with distance greater than 11 mm, as determined using the electrode coordinates from the CT image. A distance of 11 mm was chosen as this includes the majority of row-wise adjacent grid and depth electrodes whilst allowing some small displacement due to brain shift. Three non-contiguous seizure spread connection categories were therefore defined (Fig. 6.1). The prevalence of structural or effective network connections in each of these three categories was then calculated using the binary networks. Prevalence was compared to the density of the original binary and non-contiguous binary networks, as this represents the prevalence expected by chance. The distribution of peak amplitudes and streamline density among non-contiguous seizure spread connection categories was also calculated and compared to the distribution in the original networks. Analyses were performed on a pooled subject level.

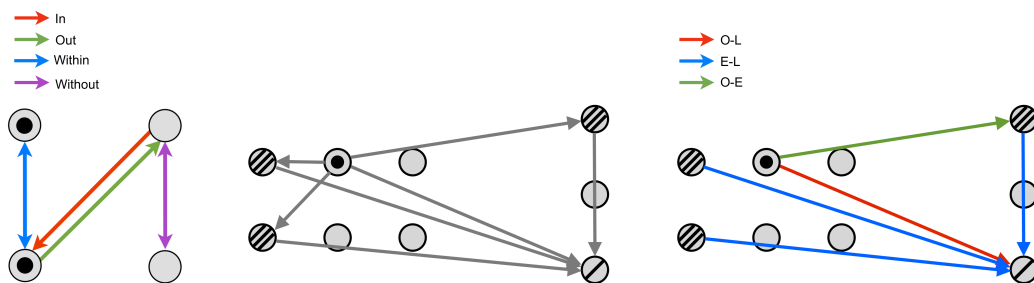


Figure 6.1: Illustrative examples of ictal-onset and seizure propagation connections used in the ictal-onset and non-contiguous seizure spread analyses. Left: Ictal-onset connection categories. Ictal-onset electrodes are filled circles. Connection categories are labeled by colour. Red, green, blue and purple colours correspond to connections *in*, *out*, *within* and *outside* ictal-onset electrodes. Middle: A network containing contiguous and non-contiguous connections (grey lines) between ictal-onset electrodes (filled circles), early propagative electrodes (triple-lined circles) and late propagative electrodes (single-lined circles). Right: Non-contiguous seizure spread connection categories. Contiguous connections were removed. Green, blue and red lines correspond to non-contiguous connections from onset to early, early to late, and onset to late electrodes, respectively.

6.3 Results

6.3.1 Structural and Effective Networks

Global network properties of structural and effective networks are shown in Table 6.1 for all subjects. The grand mean peak amplitude of weighted effective networks across all subjects was $163.8 \pm 45.84 \mu\text{V}$ whereas the grand mean streamline density of weighted structural networks was 0.56 ± 0.064 . The network density of binary networks was 0.169 ± 0.178 for effective networks and 0.109 ± 0.041 for structural networks. Global efficiency of effective networks (0.39 ± 0.18) was similar to structural networks (0.40 ± 0.08) for all subjects. Global clustering coefficient was also similar between effective networks (0.45 ± 0.20) and structural networks (0.47 ± 0.04). The mean global reciprocity of effective networks (0.34 ± 0.12) was less than 1 since they are undirected networks. The mean global reciprocity of structural networks was 1 since all connections are undirected.

6.3.2 Structural and Effective Network Comparison

The mean overlap between the binary structural and effective networks, as measured by the Jaccard Index, was 0.176 ± 0.024 . This was a higher overlap than expected by chance given the density of the networks (Fig. 6.2 and 6.3). However, the spearman correlation between the edge weights of CCEP and diffusion networks was low at $\rho=0.128 \pm 0.066$. (Table 6.1, Fig 2).

6.3.3 Ictal-Onset Connectivity

The number of ictal-onset electrodes for each subject is shown in Table 6.1. A total of 16 electrodes were classified as ictal-onset (mean 2.7 ± 1.8 across subjects). The subject with the lowest number of ictal-onset electrodes was subject 1 who had 1 ictal-onset electrode, while subject 4 had the most with 6. Note that subject 2 had diffuse seizure onset patterns and was therefore not included in ictal-onset connectivity analysis.

Ictal-onset connectivity category comparisons are presented for structural and effective connection features constrained along effective connections. Across all subjects, a trend for higher peak amplitude at ictal-onset electrodes was observed

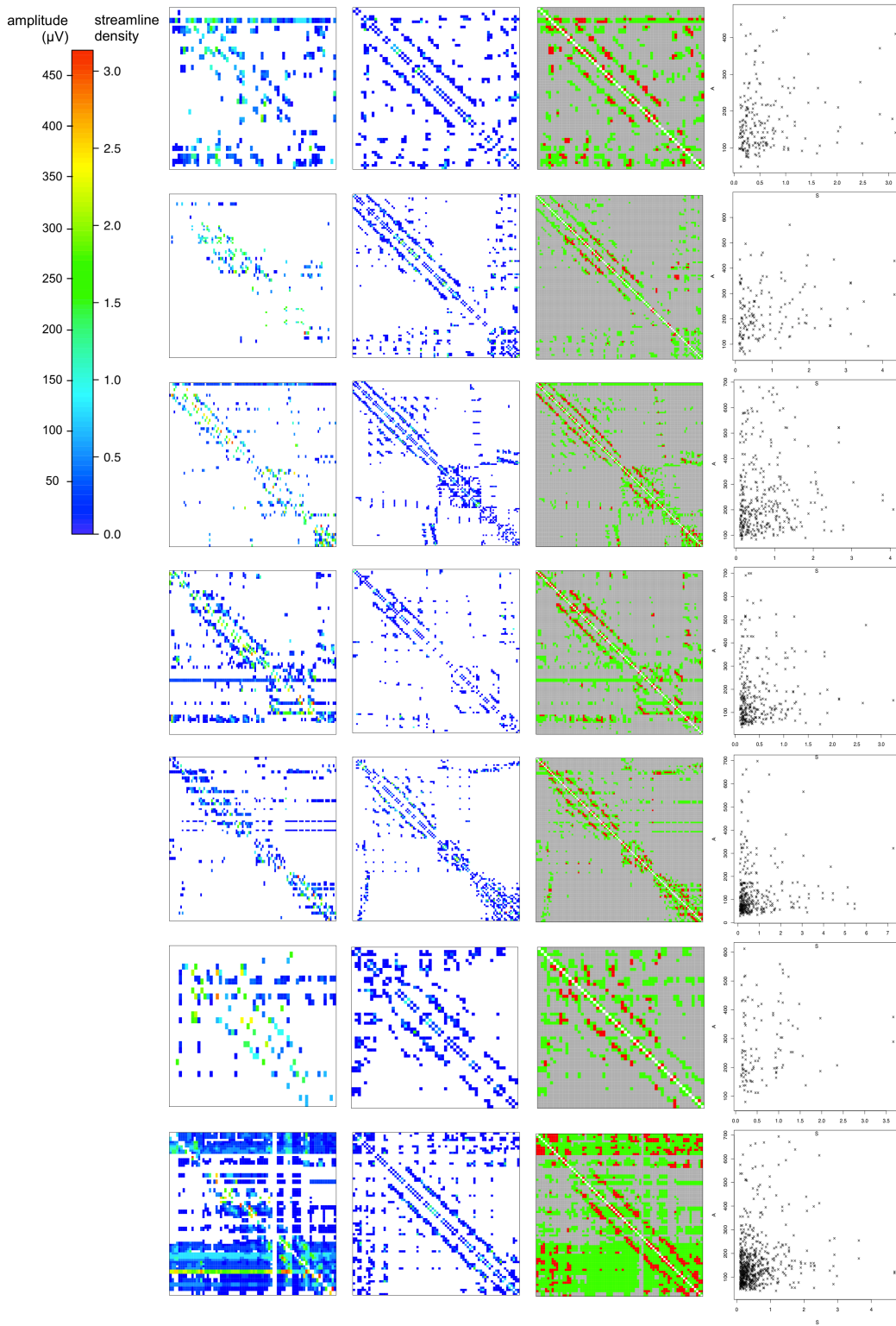


Figure 6.2: Effective and structural networks in all subjects. Left: Effective networks. Left-Middle: Structural networks. Right-Middle: Union (green) and intersection (red) of structural and effective networks. Right: Plot of effective network amplitude (A) and structural network streamline density (S). A high overlap but low correlation was observed between structural and effective networks.

Subject	C-Density	C-Peakamp (μV)	C-Lat (ms)	C-Clust	C-Eff	C-Recip	D-Density	D-Streamdens	D-Clust	D-Eff	Jrand	Jl	Cor	I	E	L
1	0.16	155.80 \pm 71.60	77.70 \pm 61.50	0.47	0.41	0.36	0.13	0.52 \pm 0.51	0.41	0.46	0.08	0.21	0.18	1	4	1
2	0.04	202.00 \pm 105.50	51.20 \pm 42.20	0.34	0.12	0.22	0.09	0.62 \pm 0.72	0.43	0.39	0.03	0.14	0.21			
3	0.07	214.20 \pm 131.50	48.60 \pm 37.20	0.28	0.34	0.27	0.09	0.58 \pm 0.58	0.50	0.39	0.04	0.17	0.05	2	4	12
4	0.15	134.20 \pm 114.00	41.60 \pm 29.20	0.44	0.44	0.44	0.06	0.50 \pm 0.50	0.46	0.27	0.04	0.16	0.07	6	6	6
5	0.09	97.30 \pm 85.20	42.30 \pm 41.40	0.37	0.36	0.33	0.07	0.67 \pm 0.89	0.49	0.32	0.04	0.20	0.06	2	10	4
6	0.11	211.00 \pm 126.90	33.50 \pm 22.20	0.38	0.34	0.22	0.15	0.50 \pm 0.50	0.50	0.45	0.07	0.17	0.15	3	10	2
7	0.56	131.90 \pm 104.30	31.80 \pm 23.70	0.87	0.71	0.56	0.17	0.55 \pm 0.59	0.50	0.50	0.15	0.18	0.17	2	4	2

Table 6.1: Summary of structural and effective network properties across subjects. Column abbreviations are as follows; Peakamp: mean peak amplitude. Lat: mean peak latency. Clust: global clustering coefficient. Eff: global efficiency. Recip: global reciprocity. Streamdens: mean streamline density. Jrand: expected Jaccard Index between binary structural and effective networks due to random chance alone given the density of the networks. Jl: observed Jaccard Index between binary structural and effective networks. Cor: Pearson correlation coefficient between weights of structural and effective networks. I: number of ictal-onset electrodes. E: number of early seizure spread electrodes. L: number of late seizure spread electrodes.

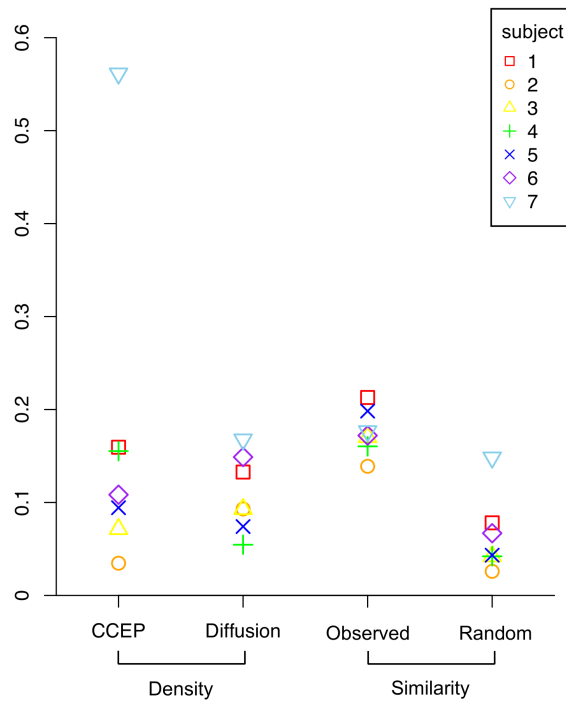


Figure 6.3: Similarity between binary effective (CCEP) and structural (diffusion) networks. The observed Jaccard index, measuring network similarity, was higher than expected given the density of the binary networks.

(Fig. 6.4). This was seen as a higher median peak amplitude for *in* and *within* ictal-onset connection categories, compared to CCEPs recorded for *out* and *outside* connection categories. Higher baseline standard deviation was observed at non ictal-onset electrodes connecting towards ictal-onset electrodes, as shown by higher baseline standard deviation for the *in* connection category. Across all subjects, a trend of altered structural connectivity was found in the streamline density of effective connections between ictal-onset electrodes, as shown by a higher median streamline density for the *within* connection category. No clear trends with latency were observed.

The distribution of nodal graph theoretical properties showed little variability between ictal-onset and non ictal-onset electrodes. However, outdegree and normalised outdegree of ictal-onset electrodes was higher (Fig. 6.5).

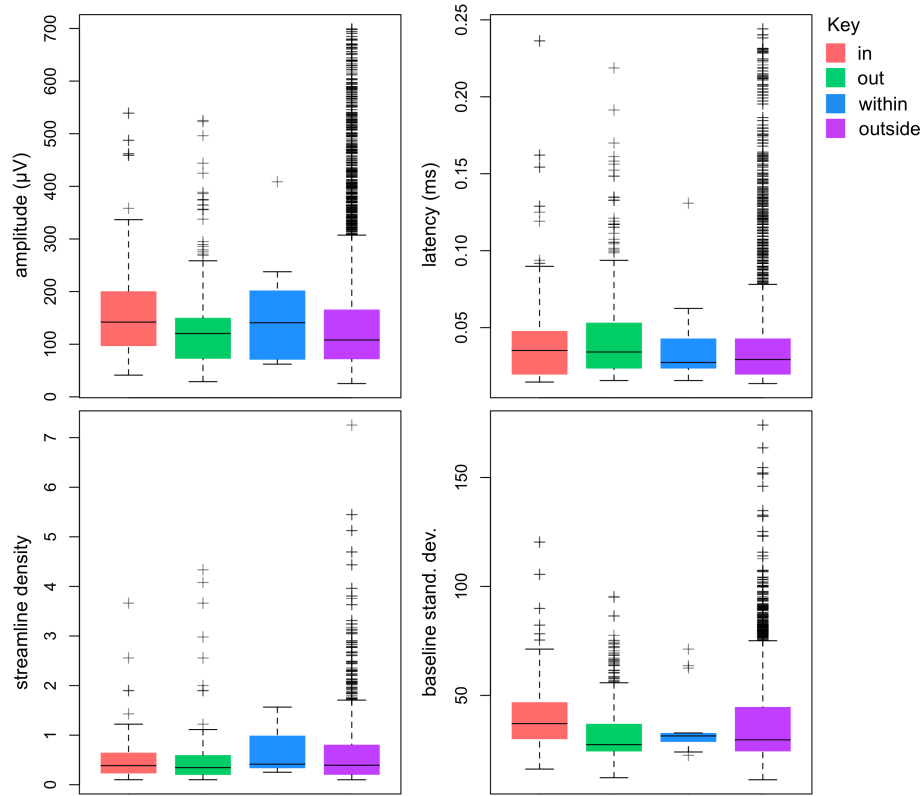


Figure 6.4: Ictal-onset effective and structural connectivity measures (CCEP network amplitude, latency and baseline standard deviation and diffusion network streamline density) pooled across all subjects. Shown are the median and interquartile range for four connection categories: *in* (connections towards ictal-onset electrodes), *out* (connections away from ictal-onset electrodes), *within* (connections between ictal-onset electrodes) and *outside* (connections not involving ictal-onset electrodes). Whiskers cover the range of data points no more than 1.5 times the interquartile range. A trend for higher distribution of CCEP amplitude and baseline standard deviation was observed for *in* connection categories, whereas a trend for higher distribution of CCEP amplitude and streamline density was found for *within* connections.

6.3.4 Non-Contiguous Seizure Spread

The number of electrodes classified as early and late seizure spread sites varied across subjects. The mean number of early seizure spread sites was 6.3 ± 2.9 , whereas the mean number of late seizure spread sites was 4.5 ± 4.1 (Table 6.1). As previously mentioned, subject 2 had diffuse seizure onset patterns and was therefore not included in the non-contiguous seizure spread analysis.

The prevalence of both structural and effective connections among all possible non-contiguous seizure spread connections was higher than expected by chance

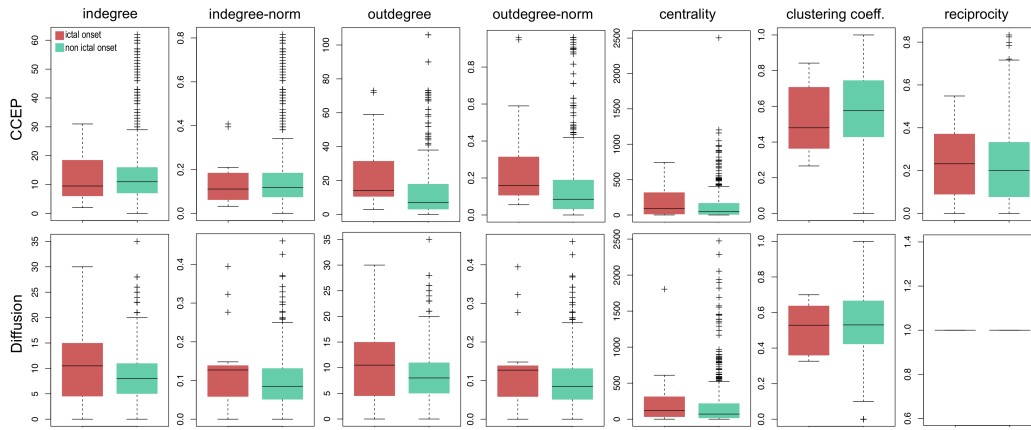


Figure 6.5: Nodal graph theoretical properties of indegree, normalised indegree, outdegree, normalised outdegree, clustering coefficient, centrality and reciprocity at ictal-onset compared to non ictal-onset electrodes. Nodal graph theoretical properties are shown for effective (upper) and structural (lower) networks across all subjects. Outdegree and normalised outdegree was higher at ictal-onset electrodes in effective networks.

for the O-E and O-L connection categories, whereas the prevalence of structural connections was also higher for the E-L category (Fig. 6.6). The chance prevalence was considered as the density of connections among all the possible non-contiguous connections, which was 0.176 ± 0.191 for effective networks and 0.076 ± 0.036 in structural networks.

Some trends in the weighted properties of non-contiguous seizure spread connections were observed in effective and structural networks. There was a trend for higher peak amplitude of O-E and E-L seizure spread connections in effective networks. The latency of O-E non-contiguous seizure spread connections was lower than the rest of the network and non-contiguous connections. Also, streamline density tended to be lower for O-L and E-L non-contiguous seizure spread connection categories. Examples of non-contiguous seizure spread networks for subjects 3, 6 and 7 are shown in Fig 6.8.

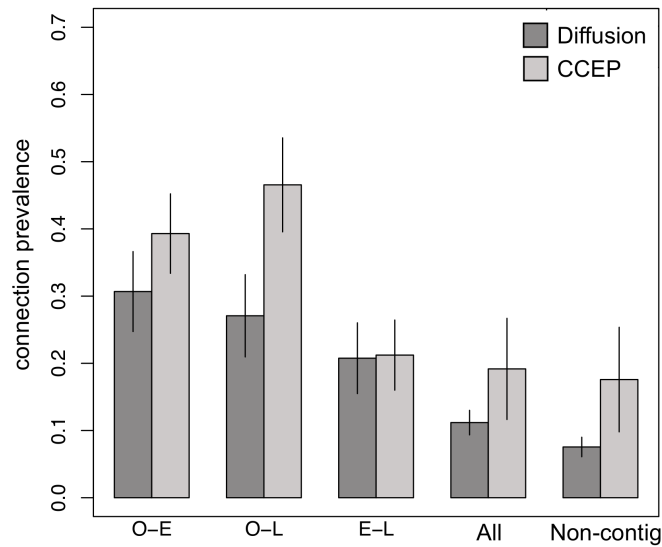


Figure 6.6: Prevalence (mean \pm standard error across subjects) of effective (CCEP) and structural (diffusion) network connections among all possible non-contiguous seizure spread connections (O-E: onset to early; O-L: onset to late; E-L: early to late). All structural non-contiguous seizure spread connection categories had a higher prevalence than expected compared to all network connections (All) and all non-contiguous connections (Non-contig). Effective networks had a higher prevalence of O-E and O-L connections, but not E-L connections.

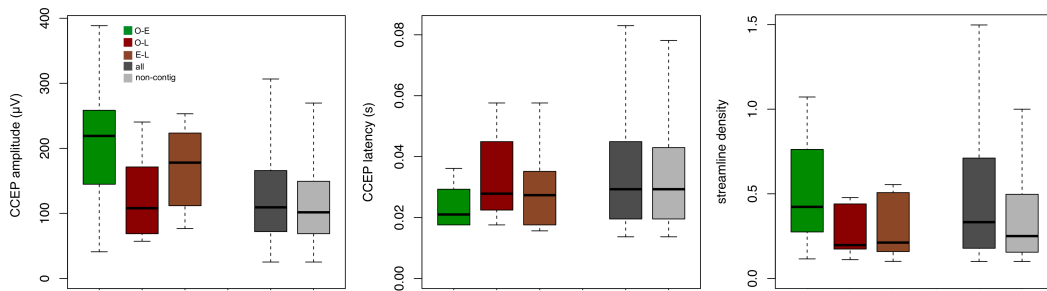


Figure 6.7: Connectivity measures (CCEP network amplitude and latency, diffusion network streamline density) of non-contiguous seizure spread connections across all subjects. Seizure spread connections (O-E: green, O-L: red and E-L: brown) are compared to the distribution of all connections (dark grey) and all non-contiguous connections (light grey). O-E connections had a higher CCEP amplitude and shorter latency. E-L connections had a higher CCEP amplitude.

Examples of non-contiguous seizure spread networks are shown in Fig 6.8.

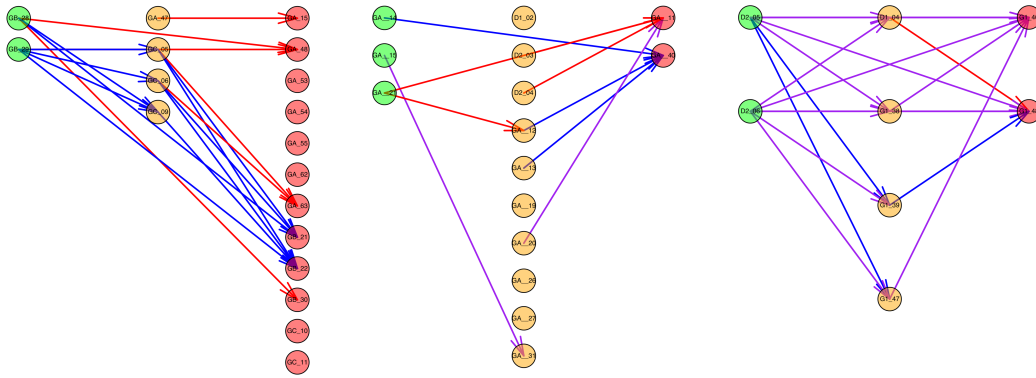


Figure 6.8: Examples of non-contiguous seizure spread networks in subject 3 (left), 6 (middle) and 7 (right). Plausible routes of seizure spread through ictal-onset (green), early propagative (orange) and late propagative (red) electrodes were observed when considering evidence of connectivity using either CCEPs (blue), diffusion tractography (red), or both (purple). Subject 3 had no non-contiguous seizure spread connections containing both effective and structural connection, although both modalities individually had connections from both onset to early and early to late propagative electrodes, indicating a possible mechanism for non-contiguous seizure spread through intermediate early propagative locations. Subject 6 had connections from onset to early and early to late electrodes when considering either or both modalities. Subject 7 had many connections containing both an effective and structural connection and many possible routes of seizure spread when considering either or both modalities.

6.4 Discussion

This was the first study to reconstruct both structural and effective networks at a large scale across the cortex. Combining these modalities enabled estimation of the agreement between structural and effective networks, the structural and effective connectivity of the ictal-onset zone and the connections underlying non-contiguous seizure spread. We found a high overlap between structural and effective networks, altered structural and effective connectivity of the ictal-onset zone, and evidence of structural and effective connections underlying non-contiguous seizure spread.

6.4.1 Structural and Effective Network Comparison

A high degree of overlap is expected between structural and effective networks as effective connections are constrained along structural connections- an axon is required to carry a neural signal between brain regions. Furthermore, some degree of correlation may be expected between structural and effective networks as the density of connecting fibers (the structural network connection weight) may cor-

respond to the number and synchrony of neurons activated at the remote site (the effective connection weight- peak amplitude is directly proportional to the number and synchrony of activated neurons).

This study found that structural and effective networks had a high degree of overlap in the binary connections, indicated by a high Jaccard Index. However, the correlation in the connection weights was low. Two other studies have reported agreement between CCEP and diffusion tractography connections [78, 296]. Swann et al. [296] found a high concordance in connectivity between pre-SMA and rIFG using CCEPs, diffusion tractography and task-based functional MRI. Short latency CCEPs were elicited between the pre-SMA and rIFG sites which were also connected by tractography fibers [296]. However, the overlap or correlation between structural and effective networks was not quantified. Conner et al. [78] examined the correlation between the number of streamlines and CCEP amplitude in connections arising from Broca's area. They found a small but significant correlation R^2 of 0.41. The higher correlation reported in Conner et al. [78] could be because the connection weights of CCEPs and tracts arising from a single cortical area with a well characterised connection were examined- Broca's area is known to play a key role in language processing with connections to Wernicke's area via the arcuate fasciculus. In contrast, this study examined the entire set of cortical connections covered by the intracranial EEG, which included grid and depth electrodes. This set of connections is likely to be more challenging to quantify through diffusion tractography or CCEPs than a single connection traversing a major white matter tract, and there may also be some false positive connections.

The low correlation between structural and effective networks found in this study could also be due to accumulation of inaccuracies in the estimation of the connection weights on a large scale across the cortex. Possible sources of error are discussed in detail in the previous Chapter. It should be noted that other measures of connection weight are available for both structural and effective networks which may give higher correlation. For example, structural networks may be weighted by tract volume [321], fractional anisotropy along the tract [209], or combinations of

these measures which can also penalise shorter distance connections [203]. Effective networks may additionally be weighted by the negative amplitude of the evoked potential [5] or the root-mean-squared ratio of the response to the baseline [198].

Loss of correlation between whole brain structural and functional networks has been previously reported in epilepsy. Zhang et al. [365] found a decrease in structure-function correlation with epilepsy duration in idiopathic generalised epilepsy. Besseling et al. [24] found lower structure-function correlation in rolandic epilepsy compared to controls, and Vaessen et al. [323] found an absence of increase in correlation between structural and functional networks with age in childhood frontal lobe epilepsy which was present in controls. These studies suggest that although structure-function correlation is typically present in epilepsy subjects, it is lower in some forms of epilepsy or with disease severity. The low correlation between structural and effective networks observed in this study may be due to a combined effect of disease-related loss of structure-function correlation, and imperfections in reconstructing structural and effective networks.

6.4.2 Ictal-Onset Connectivity

Previous studies have observed alterations in structural and effective connectivity of the ictal-onset zone [149, 58, 324, 326] in addition to regions outside of the ictal-onset zone [209, 365, 346]. In this study, a higher amplitude of CCEPs was found at the ictal-onset zone. Furthermore, a higher baseline standard deviation was observed at the ictal-onset zone in the intracranial EEG of epochs containing significant CCEP peaks when stimulating outside of the ictal-onset zone. Previous CCEP studies have demonstrated a higher prevalence of delayed responses [324, 326, 125] in addition to a higher amplitude of CCEPs at ictal-onset zones [168, 112]. Together these CCEP findings are consistent with an established theory in epilepsy pathology that hyperexcitable cortex underlies the ictal-onset zone and this promotes epileptogenic neuronal activity. Cortical excitability refers to the readiness of a neuron to generate an action potential when triggered by an excitatory post-synaptic potential. Hyperexcitability refers to a lower threshold for neuron activation [20]. Hyperexcitability in epilepsy may be due to a number of factors such as the pres-

ence of pathological tissue (e.g. lesions, cortical dysplasia) and down-regulation of local inhibitory circuits or up-regulation of excitatory circuits [142]. Other possible causes also include disruption of adenosine-mediated anti-convulsive mechanisms [33] and the effect of immune mediators which modulate excitability [165].

Cortical dysplasia was highly prevalent in the study cohort. Cortical dysplasia is a congenital abnormality affecting neuronal migration *in utero*, resulting in abnormal appearance of grey matter. Four of seven subjects (subject 1, 2, 4 and 6) had type IIb focal cortical dysplasia [30]. In these subjects the cortical dysplastic tissue was located in approximately the same brain region as the ictal-onset electrodes, although exact anatomical localisation of cortical dysplastic tissue was not performed. Focal type IIb cortical dysplasia is associated with cytomegalic dysmorphic neurons and balloon cells, distortion of the laminar structure of the cortical grey matter, and reduction in myelin of the underlying white matter [30]. Such pathology is known to generate abnormal neural tissue that may be hyperexcitable [314]. One study found more rapid propagation of seizure activity in paediatric epilepsy patients with dysplastic lesions than those with non-dysplastic lesions. In addition, the EEG onset characteristics differed between dysplastic and non-dysplastic cortex: the majority of patients with focal cortical dysplasia had fast frequencies at seizure onset compared to patients who did not have cortical dysplasia. The latter had more repetitive spiking at seizure onset [314]. There is a possibility that cortical dysplastic tissue resulted in higher amplitude of CCEPs. Therefore, further work is needed to differentiate between the contribution of the pathological finding of cortical dysplasia and the hyperexcitability of the cortex per se.

6.4.3 Non-Contiguous Seizure Spread

Contiguous seizure spread is more commonly observed than non-contiguous seizure spread and the mechanisms of contiguous spread are suspected to be through horizontal cortical layer V [302]. However, the mechanisms of non-contiguous seizure spread are unclear. This study found a higher prevalence of non-contiguous CCEP connections from onset to early and onset to late seizure spread sites than that expected. In addition, structural connections from onset to early, onset to late, and

early to later propagative sites were all more highly prevalent than expected. Therefore, both effective and structural connections provide highly plausible routes for non-contiguous seizure spread (Fig. 6.6 and 6.8). The high prevalence of both structural and effective connections supports the idea that the seizure spread mechanism is likely via a direct functional cortico-cortical connection, as opposed to indirect cortico-subcortico-cortical connection.

A trend for higher amplitude of CCEPs from onset to early and early to late sites, but not onset to late seizure spread sites was observed. As higher amplitude CCEP may reflect a stronger effective connection between those sites, this finding suggests that seizure spread can occur via early propagative sites which act as intermediates site for seizure propagation. However, the high prevalence of onset to late CCEP connections suggests that the primary route for seizure spread to late sites is directly from ictal-onset. Interestingly, despite high prevalence of all seizure spread routes in the structural networks, there is a trend for lower streamline density for onset to late and early to late connections.

This is the first study to examine mechanisms of non-contiguous seizure spread using CCEPs. Recently, Lega et al. [198] acquired CCEPs in thirty-seven focal epilepsy patients implanted with depth electrodes. The group studied the root-mean-squared (RMS) and gamma band activity in the response period at early and late seizure spread sites. They found an increase in both the RMS and low frequency gamma band activity at early compared to late sites, which was also present when matching the recordings by distance between early and late sites. The study also found that the low frequency gamma activity at early seizure spread sites was coherent with the ictal-onset zone, while lower frequency activity was not. They hypothesise that low inhibitory input at the early seizure spread sites lead to higher low frequency gamma band activity. These findings of high connectivity at early seizure spread sites agrees with our findings of both higher structural and effective connectivity between onset to early sites and provides further support for the notion that this seizure spread is via direct effective connection from the ictal-onset zone.

A key difference between this study and Lega et al. [198] is that this study only

examined plausible direct seizure spread routes (those from earlier to later propagative sites), whereas Lega et al. [198] examined all CCEPs connecting to early and late sites regardless of their origin. This means that our findings are more specific in relation to seizure spread whereas their findings are more useful for looking at the connectional architecture of seizure spread sites in relation to the rest of the electrode network. In addition, Lega et al. [198] studied epilepsy patients with only depth electrodes implanted, whereas this study includes patients with both grid and depth electrodes, which extends the finding of strongly connected seizure spread sites to cortical as well as sub-cortical sites. A limitation of both of these studies is that the criteria for early and late seizure spread sites is not clear- Lega et al. [198] defined early sites as those with seizure activity up to three seconds following seizure onset, and late sites as those with activity greater than three seconds. In our study we used thresholds of less than one second and greater than one second for early and late sites, respectively. Finally, as mentioned by Lega and colleagues, the process of identifying seizure electrodes is qualitative, and quantitative measures, such as the epileptogenicity index may be less biased and have lower intra-subject variation, which may lead to more accurate assessments of seizure spread [13].

6.4.4 Methodological Considerations

In this study CCEPs with latency greater than 250 ms were removed. This threshold was chosen in order to balance sensitivity to CCEPs relating to ictal-onset connectivity and to direct connections of short latency. Some CCEP studies have differentiated between early and late negative potentials with latencies of <100 ms and >100 ms [87, 125]. However, many CCEP studies have found that evoked potentials do not conform to this model of negative potentials, and that evoked potentials may have either negative or positive polarity [178, 116, 32]. Furthermore, there is some uncertainty about whether the early and late negative potentials reflect direct and indirect connections, or that both reflect direct excitatory potentials followed by inhibitory feedback circuits [116]. In addition, many studies examining connectivity of the ictal-onset zone have demonstrated increased prevalence of responses occurring from 100-1000 ms. We found that in the majority of subjects the distribu-

tion of CCEP peaks was bimodal with a second peak of the distribution occurring after 100ms, and that depth electrodes (possibly due to greater anatomical distance) had some skewing of latencies towards those greater than 100 ms (Fig. 6.9). In view of these discrepancies, we chose the threshold of 250 ms and examined only the first peaks of evoked potentials in order to give maximum sensitivity to direct connections which may reflect altered connectivity of ictal-onset zones. Despite this, ictal-onset connectivity and non-contiguous seizure spread results were also calculated using a 100 ms latency threshold and similar results were found (not shown).

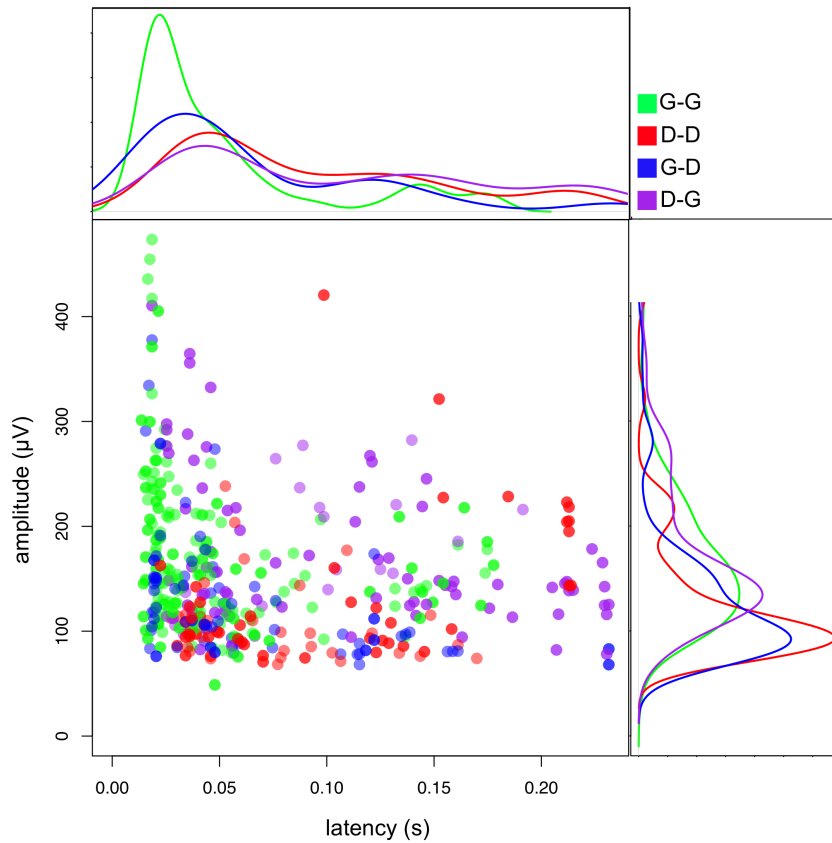


Figure 6.9: Marginal density histogram showing the amplitude and latency of peaks in the effective network of subject 1. The majority of early latency peaks are between grid electrodes (green line). At later latencies a higher proportion of peaks involve depth electrodes (red, blue and purple lines).

6.5 Summary

This was the first study to examine both structural and effective networks at a large-scale across in the human cortex. A high overlap but low correlation was found between structural and effective networks. This may have been due to the methodological limitations of both modalities and the large-scale nature of the analysis. Altered baseline and effective connectivity was found at ictal-onset electrodes, suggesting a hyperexcitable state of cortex at the epileptogenic focus. A high number of outgoing effective connections was found at ictal-onset sites and a high prevalence of structural and effective connections towards sites of non-contiguous seizure spread was observed. Together, these results suggest that the ictal-onset zone is highly excitable, highly outwardly connected, particularly with respect to early and late seizure spread sites, while structural networks also show a high degree of connections to seizure spread sites. CCEPs may be more useful for localising the ictal-onset zone given more widespread disturbances in connection features than in structural networks.

Chapter 7

Conclusions

Reconstructing and quantifying human brain connectivity using neuroimaging methods holds great promise for understanding healthy brain function and its pathological deviation. In this thesis, we assessed the reproducibility of structural networks and their consensus across pipelines, described methods to reconstruct large-scale structural and effective networks between implanted intracranial electrodes, quantified the correlation between structural and effective networks, and examined structural and effective connectivity of the ictal-onset zone and non-contiguous seizure spread in frontal and parietal lobe epilepsy patients. We showed that structural network connections are highly reproducible and highly similar across pipelines and that alterations in epileptogenic networks were observed in effective and structural inter-electrode networks. The following paragraphs will summarise the conclusions presented in chapter 4, 5 and 6 and discuss their implications in view of the wider literature, suggest future research and possible research trends, and acknowledge limitations of the analyses.

7.1 Reproducibility and Consensus in Structural Brain Networks

Reproducibility of structural network connections was high and increased with decreasing network density. This finding, together with other recently published reproducibility studies [320, 16, 71, 56, 108, 367, 36], demonstrates that despite some dependence of reproducibility on the reconstruction method, reproducibility

of structural network weights is reasonable. Therefore, both topology and connection weights of structural networks are suitable candidates for biomarkers of neurological diseases involving disconnection. Researchers applying network analysis to disease cohorts should be aware of the trade off between decreased sensitivity to suspected connectivity changes and increased reproducibility with decreasing network density. In particular, neurological diseases involving compensative or re-organisational changes in connectivity may be easier to detect than those involving reductions in connection strength.

A high convergence between independent pipelines was observed across all network densities. Although this does increase confidence in comparing studies employing the same atlas but different contemporary methods of similar capability, one should also consider that the network density also plays a dominant role in determining network topology and studies employing networks of different density should not be directly compared. As confirmed in Zhong et al. [368], networks reconstructed using more fundamentally different techniques have lower agreement. The trend for requiring data availability to accompany publications (as with the PLOS ONE journal [257]) may facilitate cross-study comparisons of structural networks. Future studies can test cross-study similarity in networks employing the same atlases but different pipelines as a possible pre-requisite for combining information across studies.

Core connections occurring robustly across structural network reconstruction pipelines were identified, termed ‘consensus networks’. These are the suspected set of connections corresponding most highly to the true structural network. As mentioned, it may be useful for future studies to apply multiple pipelines to their diffusion-weighted data in order to identify these connections. With increasing availability of software tools to combine neuroimaging post-processing methods, such as Nipype [147] and PANDA [85], it may become more common to apply multiple pipelines when reconstructing structural networks. As connections may become missing in disease populations, an interesting question for future research is how to extract and compare consensus networks between different subject popu-

lations who may have a different compliment of cortical connections.

In the general field of structural brain networks, I suspect there will be a move towards increasingly more accurate and detailed cortical parcellations. This will be likely due to continuing improvements in anatomical and functional criteria defining cortical areas, which may arise through improvements in image quality, parcellation algorithms and cohort sizes, among other factors. Interestingly, Besson et al. [25] demonstrated high reproducibility of high resolution structural networks (even with 500,000 nodes!), which provides some promise to counter the established reduction in reproducibility with increasing node scale [56] confirmed in this report. In fact, Glasser et al. [140] recently introduced a semi-automated multi-modal parcellation of the cerebral cortex using functional, cytoarchitectural and connectivity information derived from the Human Connectome Project. The atlas distinguishes 180 cortical regions per hemisphere, which is a relatively high estimate compared to other cortical atlases.

7.2 Reconstructing Structural and Effective Networks

In Chapter 5 an automated epoching procedure was described which can epoch CCEP data in the absence of time-locked stimulation or stimulation-tagged time-points. Although this may be useful with older CCEP systems, it is suspected that the majority of newly purchased CCEP equipment will have automatic ways of determining stimulation onset. The automated ICA-based artefact reduction technique implemented in this thesis reduced but did not eliminate artefactual waveforms in the evoked response. Therefore, acquisition-based solutions, such as acquiring CCEPs using an alternating monophasic pulse, should also be considered in future CCEP studies. If automated artefact reduction is desired, the artefact reduction method described here may produce more effective attenuation if the method for determining the number of ICs and IC selection technique can be improved. This may be facilitated by a deeper understanding of the shape of evoked waveforms of interest, over which there is still controversy.

Nevertheless, in CCEP data that was not acquired using an alternating pulses and that lacks automatic stimulation tags (as is the case in this study), the automated pipeline described in this thesis may be useful in future clinical studies on CCEPs in epilepsy clinics at the NHNN and beyond. With the increasing popularity of connectomics-based research, large-scale effective network analysis may become more common and therefore automated pipelines to extract effective networks from the raw CCEP data will be valuable, as they can be applied to retrospective data. Development of a graphical user interface for the R scripts currently used for epoching, artefact reduction, peak finding, and effective network reconstruction, would enable more widespread use in epilepsy clinics.

The electrode localisation method for determining electrode positions in diffusion space was reasonably accurate, and is theoretically more convincing than techniques based on surface projection, Talairach coordinate extraction or other methods, such as using the post-implantation MRI signal void. This is because the co-registration technique does not use assumptions about patient neuroanatomy and brain shift displacement. However, the co-registration method does depend on the availability of the pre- and post-implantation anatomical images. Better understanding and modelling of the effect of brain shift may enable adequate localisation of electrodes to pre-implantation images without the need for acquiring pre- and post-implantation anatomical images. As neuroimaging is becoming increasingly valuable in pre-surgical evaluation of epilepsy [160], the co-registration method may become the standard and most principled way to localise electrodes to pre-implantation spaces. Therefore, it may be beneficial to routinely acquire these anatomical images in order to best interpret findings from other neuroimaging modalities such as diffusion-weighted and functional images, with respect to the intracranial EEG electrode positions.

In the field of effective networks and CCEPs, a better understanding of the physiological basis of CCEPs is necessary. For example, there remains controversy over whether the N1 and N2 represent excitatory or inhibitory volleys, direct or indirect connections, or if other measures such as the A1 and A2 should be used instead,

in addition to the variability in presentation of the evoked responses across brain locations and subjects. Understanding how evoked potentials relate to the underlying neurophysiology of connections is essential for interpretation and study design. Resolving this may require further research to examine the shape of the evoked response in electrophysiological recordings of excitatory and inhibitory networks *in vitro*, or the use of more sophisticated computational models which examine the effect of different populations of excitatory and inhibitory neurons, their orientations, and how voltage fields propagate through the brain, on the evoked response. An interesting question is whether natural variations in cortical state (i.e. cortical excitability) underlie the heterogeneity in evoked responses observed across brain locations and subjects. This could be tested by correlating the evoked response amplitude to the paired functional correlation between the resting-state brain activity of regions underlying implanted electrodes. Overall, a better understanding of the evoked potential is essential and will lead to creation of a more accurate and interpretable effective connectivity networks.

7.3 Inter-Modal Comparison and Connectivity in Epilepsy

In contrary to theoretical expectations of agreement between structural and effective networks, a high overlap but low correlation was observed when assessing agreement in connectivity between all sites underlying implanted electrodes. This may be due to inherent methodological limitations in applying contemporary state-of-the-art structural network reconstruction pipelines to reconstruct connectivity between smaller regions of interest with shorter distances, as compared to macroscopic brain regions in cortical atlases. Therefore, while it cannot be excluded that there is no true correlation between the modalities, it is unlikely that current reconstruction methods for effective and structural networks will yield correlated connection weights suitable for combined analysis on a large scale. However, as demonstrated in Conner et al. [78], a moderate correlation may be observed for stronger connections selected *a priori*. A future trend may be that higher resolution imaging and

specialised tractography algorithms will enable accurate characterisation of short inter-electrode fibers and lead to a better characterisation of the correlation between structural and effective networks. Initially, it may be useful to assess the reproducibility and/or anatomical accuracy of structural connections with respect to the distance of connections. Subsequently, effort should be made to make custom algorithms suitable for short-range structural connections.

Our findings extend the notion of previously reported altered effective connectivity of the prescribed ictal-onset zone in delayed responses [324, 326, 125] to early responses. Together, these findings of altered effective connectivity of the ictal-onset zone are in agreement with existing models of epileptogenic networks which suggest seizure activity is promoted by hyperexcitable cortex [8]. This study suggests that seizures are likely to occur due to both spontaneous hyperexcitability following normal brain function and high outward connectivity which propagates seizure activity to other brain areas. Structural networks did not exhibit widespread alterations in ictal-onset connectivity which suggests that future studies should instead focus on effective connectivity when examining potential connective changes in epilepsy. Meanwhile, aforementioned assessment and improvement of short distance tractography may lead to better characterisation of ictal-onset zone structural connectivity.

Future research, potentially using the same data as in this study, could assess the ability of effective connectivity amplitude and baseline standard deviation to blindly discriminate ictal-onset zone from non ictal-onset zone. Subsequently, correlations can be made with areas classified as ictal-onset by CCEPs and those resected, to determine if higher outcome is observed when the CCEP-suggested ictal-onset zone is removed, as compared those not suggested by CCEPs. This would support previous studies suggesting favourable outcome in patients who had brain regions with abnormal delayed responses removed [326, 125]. Finally, this study demonstrates more explicitly than a previous study [198] that effective and structural connections are likely to support mechanisms of non-contiguous seizure spread. It is expected that, following further clarification of the interpretation of

CCEP evoked responses, effective connectivity markers, as gained through CCEPs, may aid identification of ictal-onset zone in future studies and lead to CCEPs playing a more prominent role in ictal-onset zone identification clinically.

7.4 Summary of Conclusions

In this thesis, reproducibility and agreement in state-of-the-art structural network reconstruction pipelines was quantified in healthy individuals. Findings reported here provide further support for reasonable to high reproducibility of connections and therefore advocate the use of network connection weights and derived topological measures as potential biomarkers for neurological disease, or in relating individual network fingerprints to neurological phenotype. Findings of correlation between connection strength and reproducibility indicate that neurological conditions involving reorganisational changes as opposed to connection degradation are well suited for network analysis, while pooling results across structural network studies that employ similar capability pipelines is feasible and may improve power in detection of suitable biomarkers.

An automated pipeline for reconstructing effective networks was evaluated and evidence of alterations in effective connectivity of the prescribed ictal-onset zone was found, in agreement with previous reports of alterations in delayed evoked responses. Low correlation between structural and effective connectivity may be due to lack of plausible short-range fibers reconstructed between smaller and closer regions underlying intracranial electrodes, compared to those demonstrated as highly reproducible between regions in cortical atlases. Accuracy in reconstructing such higher resolution structural networks is likely improve with continuing advances in tractography algorithms, structural image resolution and understanding of cortical areas.

On the other hand, the field of CCEP research would greatly benefit from a deeper understanding of the mechanisms that shape the evoked response, which may arise through further *in vitro* electrophysiology or computational modelling of neuronal populations. Nevertheless, effective connectivity reconstructed using CCEPs

suggest that the seizure onset zone is highly excitable and outwardly connected, particularly to sites of non-contiguous seizure spread. Future work should determine whether these effective connectivity properties blindly identify ictal-onset zone, in which case this may lead to improved seizure onset detection and seizure freedom following resective surgery in epilepsy.

Appendix A

Abbreviations

AAL	Automated Anatomical Labelling
ADC	Apparent diffusion coefficient
BEDPOST	Bayesian Estimation of Diffusion Parameters Obtained using Sampling Techniques
CCEP	Cortico-cortical Evoked Potential
CSD	Constrained Spherical Deconvolution
CSF	Cerebrospinal Fluid
CT	Computed Tomography
CV	Coefficient of Variation
DC	Dice Coefficient
DSI	Diffusion Spectrum Imaging
DWI	Diffusion-Weighted Imaging
EEG	Electroencephalography
EPI	Echo Planar Imaging
FA	Fractional Anisotropy
FID	Free Induction Decay
FLE	Frontal Lobe Epilepsy
FOD	Fiber Orientation Distribution
HARDI	High Angular Resolution Diffusion Imaging

IC	Independent Component
ICC	Intra-class Correlation Coefficient
MD	Mean Diffusivity
MRI	Magnetic Resonance Imaging
NHNN	National Hospital for Neurology and Neurosurgery
NMR	Nuclear Magnetic Resonance
NODDI	Neurite Orientation Dispersion and Density Imaging
ODF	Orientation Distribution Function
PDF	Probability Density Function
PFG	Pulsed-field Gradient
rIFG	right Inferior Frontal Gyrus
RGB	Reg Blue Green
RMS	Root Mean Squared
RF	Radiofrequency
SMA	Supplementary Motor Area
SPES	Singe Pulse Electrical Stimulation
SWI	Small-World Index
TE	Echo Time
TR	Repetition Time

Appendix B

Electrolyte *In Vitro* Stimulation Experiment

B.1 Introduction

In CCEP studies stimulation artefact may contaminate or obscure early responses to cortical stimulation, particularly at sites near to the stimulation electrodes. Therefore, we attempted to characterise the shape of the artefact waveform at various distances from the stimulation electrodes using an *in vitro* stimulation experiment.

B.2 Methods

One 6 x 8 platinum electrode grid (7.5 mm spacing, 4 mm diameter, 2.3 mm exposed surface area, Ad-tech), and one depth electrode (10 mm spacing, 1.12 mm diameter, 2.41 mm length) were placed firmly in EEG electrode gel (Elefix, Nihon Kohden, Tokyo, Japan) that had been spread on to a 10 cm diameter petri dish (Fig. B.1) on a work bench in an unshielded room at the NHNN and connected to the Nicolet LTM system, as described previously. An additional 2 x 8 grid was also placed on the gel but not analysed in this report. The Nicolet LTM system was configured to deliver an identical stimulus to that delivered to the epilepsy subjects in this thesis. All bipolar stimulations were performed at ~ 0.2 Hz and repeated 20 times for each electrode pair. Saline drops were applied to the top of the electrode grid every 10 minutes. The current applied varied between 1 - 4 mA. Firstly, 4 mA was used to stimulate all possible adjacent electrodes in rows 1-4. Then, 3 mA was then

applied to rows 1-2, and 2 mA to row 1. Only results from the 4 mA stimulation are presented here.



Figure B.1: Photograph of *in vitro* stimulation experiment. Electrode grids and a depth electrode were placed in EEG electrode gel and stimulations were performed as described for the epilepsy subjects. The central electrode grid was used for analysis of stimulation artefact waveform. The second and third depth electrode contacts (from left to right) were used as an average reference and the fourth and fifth were used as ground. A second electrode grid was placed on the left but was not used in this analysis.

The EEG data underwent exactly the same stimulation onset detection and epoching process as described in section 5.2.2. Experiment data was analysed by plotting the maximum absolute amplitude of mean early period waveforms (12-90 ms) with respect to distance from the stimulation site, and by visual inspection of the mean response across all electrodes.

B.3 Results

The experimental stimulation artefact had a duration between $\sim 100 - 300$ ms and contaminated the early waveform periods which may be used to search for CCEP peaks in subject data (Fig. B.3). Unfortunately, a number of other experimental artefacts prevented a robust analysis of the artefact waveform. All recordings were contaminated with 50 Hz noise of approximately $500 \mu\text{V}$ amplitude, arising from the AC power supply to nearby electronic equipment. Power line noise was reduced by applying a notch filter (Butterworth, phase-shift free, 10 Hz bandwidth with 3 dB reduction [70%], edge rise 24 dB/octave). However, while this reduced the 50 Hz component of the signal, it also created unwanted ripples surrounding the stimulation artefact (Fig. B.2). Other filters were tested (Fourier domain, Gaussian filter, infinite impulse response notch filters, low-pass filter) without sufficient reduction of 50 Hz noise and ripple. In addition, three channels exhibited a large and reproducible voltage surge of ~ 1000 μV following stimulation. When these highly responsive electrodes were themselves stimulated, large voltage surges in all other electrodes were recorded. The stimulation artefact waveform showed some dependence on the electrode row-pair, with the three adjacent row pairs having different amplitudes of response to the stimulation. As such, the CCEP amplitude did not show any clear effect with distance that could be used to normalise *in vivo* responses (Fig. B.3). The artefacts found in our experimental data and the corrections required to repeat the experiment effectively are shown in Figure B.5.

B.4 Discussion

Accurate estimation of the stimulus artefact and the relationship of the artefact shape with respect to distance may allow more robust analysis of early evoked responses. We attempted to characterise the stimulation artefact using an *in vitro* experiment. Unfortunately, a number of other artefacts prevented useful exploration of this data (see Fig. B.5). However, measures can be taken to obtain a useful estimation of stimulation artefact and its relation with distance. Power line interference can be reduced or eliminated by plating electrode wires to cancel lo-

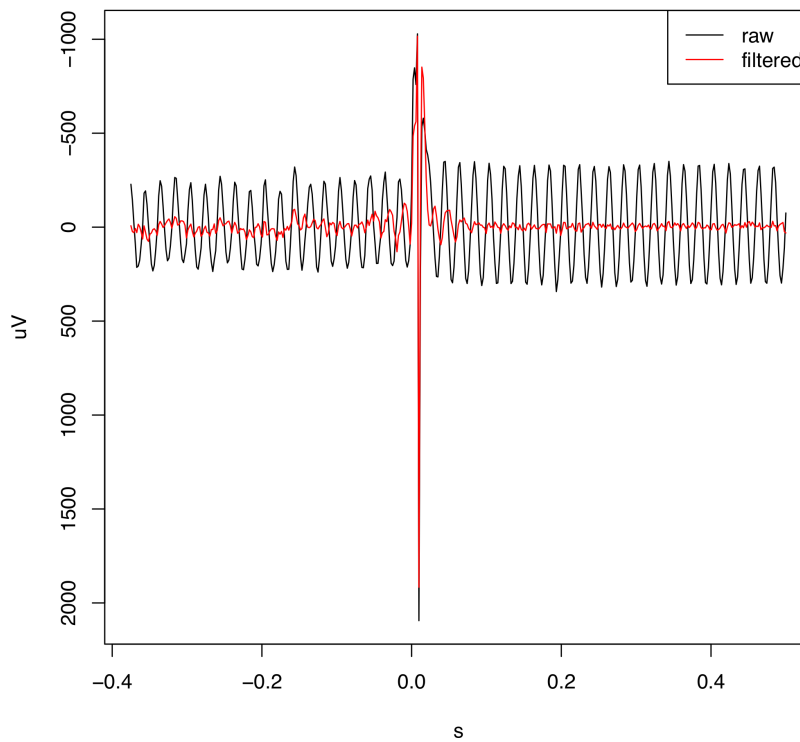


Figure B.2: *in vitro* experiment signal filtering. The raw response data (black) contains 50 Hz noise which was reduced using a notch filter (red).

cal electromagnetic fields and by shielding the experiment using a metallic mesh. Differential row-pair responses and outlying response electrodes may indicate inhomogeneous electrode-interface impedances. This may be reduced by avoiding the periodic application of saline drops and by ensuring homogeneous pressure across all electrodes when fixing the grid to the EEG electrode gel. Furthermore, a higher temporal resolution is desired to determine the artefact waveform and this can be achieved using an oscilloscope. Finally, other referential montages may be preferred for studying distance-related effects- reference electrodes may be placed in EEG electrode gel that is unconnected from the stimulation medium, preventing interference of the artefact with the reference electrode.

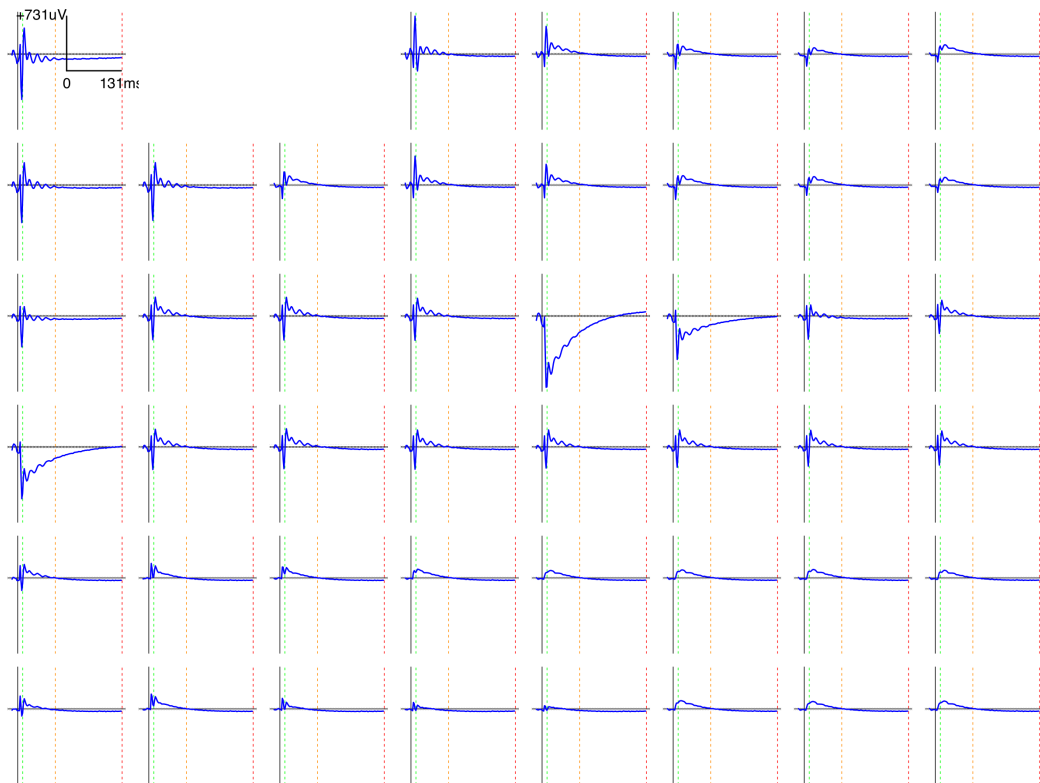


Figure B.3: *in vitro* experiment mean responses. Mean responses acquired following stimulation of electrodes in the upper-left corner of the central grid are shown.

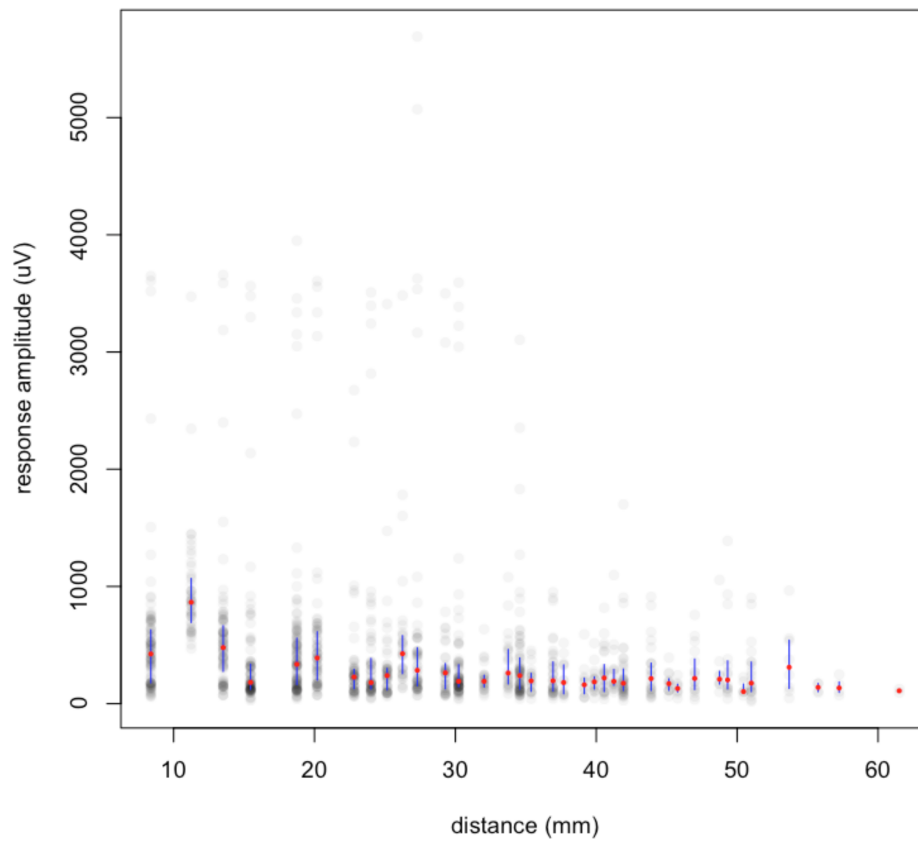


Figure B.4: Relation between distance and early period maximum absolute amplitude from the *in vitro* stimulation experiment. Maximum absolute value of the mean response is plotted against distance from the stimulation pair. Red dots and blue lines denote the median and inter-quartile range, respectively.


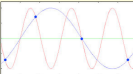


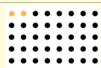

Artefact	Cause	Appearance	Prevalence experiment / humans	Correction(s)
Stimulus volume conduction	electromagnetism + capacitance, ringing		★★★★★ ★★★☆☆	-1/d ² theoretically, observe using better experiment
Under sampling vol. cond. effect	sampling frequency << stimulation pulse length		★★★★★ ★★★★★	- oscilloscope has >> sampling frequency
Recording channel voltage surge	high impedance electrode interface due to e.g. CSF/saline		★★★★★ ★★★★★	- ensure homogenous electrode contact - avoid saline drops - exclude channels
50Hz power cable noise	looping wires from nearby electronic equipment		★★★★★ ★★★★★	- plat wires - use metal shield - avoid elec. equipment - notch filter
data interpretation w.r.t distance	reference electrode distance ~ recording electrode distance		★★★★★ ★★★★★	- reference electrode distance >> recording electrode distance
different grid row-pair responses	-different row-pair impedances -defective electrode grid -unknown		★★★★★ ★★★★★	- ensure homogenous grid placement - normalise all data to nearest electrode to stim - replace electrode grid

Figure B.5: Summary of stimulation experiment artefacts and corrections required to re-perform the experiment effectively.

Appendix C

Summary of Publications

Journal papers

- C.S. Parker, F. Deligianni, M.J. Cardoso, P. Daga, M. Modat, M. Dayan, C.A. Clark, S. Ourselin, and J. Clayden. Consensus between Pipelines in Structural Brain Networks. *PloS one*, 9(10):e111262, 2014

Conference abstracts

- C.S. Parker, F. Deligianni, M.J. Cardoso, P. Daga, M. Modat, M. Dayan, C.A. Clark, S. Ourselin, and J. Clayden. Consensus between Pipelines in Structural Brain Networks. *Presentation in Proceedings of the ISMRM, Milan, Italy*, 2014
- C.S. Parker, F. Deligianni, M.J. Cardoso, P. Daga, M. Modat, M. Dayan, C.A. Clark, S. Ourselin, and J. Clayden. Consensus between Pipelines in Structural Brain Networks. *Proceedings of the ISMRM British Chapter, Edinburgh, UK*, 2014
- C.S. Parker, C.A. Clark, S. Ourselin, and J. Clayden. Agreement in Reproducibility of Whole-brain Structural Connectivity Networks with Alternative Pipelines. *Proceedings of the 22nd ISMRM British Chapter Symposium, UCL, UK*, 2013
- C.S. Parker, J. Clayden, and S. Ourselin. Effect of reconstruction pipeline on reproducibility of whole-brain structural networks. *Proceedings of the*

Annual Meeting of the ISMRM British Chapter, Cambridge, UK, 2012

- C.S. Parker, C.A. Clark, and J. Clayden. Reproducibility of whole-brain structural connectivity networks. *Proceedings of the Annual Meeting of the ISMRM British Chapter, Manchester, UK, 2011*

Bibliography

- [1] G. Alarcon, C. Binnie, R. Elwes, and C. Polkey. Power spectrum and intracranial eeg patterns at seizure onset in partial epilepsy. *Electroencephalography and clinical neurophysiology*, 94(5):326–337, 1995.
- [2] G. Alarcón, J. Martinez, S. V. Kerai, M. E. Lacruz, R. Q. Quiroga, R. P. Selway, M. P. Richardson, J. J. García Seoane, and A. Valentín. In vivo neuronal firing patterns during human epileptiform discharges replicated by electrical stimulation. *Clinical Neurophysiology*, 123(9):1736–1744, 2012.
- [3] B. Albowitz and U. Kuhnt. The contribution of intracortical connections to horizontal spread of activity in the neocortex as revealed by voltage sensitive dyes and a fast optical recording method. *European Journal of Neuroscience*, 5(10):1349–1359, 1993.
- [4] P. Allisy-Roberts and J. R. Williams. *Farr’s physics for medical imaging*. Elsevier Health Sciences, 2007.
- [5] K. Araki, K. Terada, K. Usui, N. Usui, Y. Araki, K. Baba, K. Matsuda, T. Tottori, and Y. Inoue. Bidirectional neural connectivity between basal temporal and posterior language areas in humans. *Clinical Neurophysiology*, 126(4):682–688, 2015.
- [6] H. Asanuma, A. Arnold, and P. Zarzecki. Further study on the excitation of pyramidal tract cells by intracortical microstimulation. *Experimental brain research*, 26(5):443–461, 1976.

- [7] F. A. Azevedo, L. R. Carvalho, L. T. Grinberg, J. M. Farfel, R. E. Ferretti, R. E. Leite, R. Lent, S. Herculano-Houzel, et al. Equal numbers of neuronal and nonneuronal cells make the human brain an isometrically scaled-up primate brain. *Journal of Comparative Neurology*, 513(5):532–541, 2009.
- [8] R. A. Badawy, A. S. Harvey, and R. A. Macdonell. Cortical hyperexcitability and epileptogenesis: understanding the mechanisms of epilepsy—part 1. *Journal of Clinical Neuroscience*, 16(3):355–365, 2009.
- [9] F. Bai, N. Shu, Y. Yuan, Y. Shi, H. Yu, D. Wu, J. Wang, M. Xia, Y. He, and Z. Zhang. Topologically convergent and divergent structural connectivity patterns between patients with remitted geriatric depression and amnesic mild cognitive impairment. *J. Neurosci.*, 32(12):4307–4318, 2012.
- [10] F. Bai, N. Shu, Y. Yuan, Y. Shi, H. Yu, D. Wu, J. Wang, M. Xia, Y. He, and Z. Zhang. Topologically convergent and divergent structural connectivity patterns between patients with remitted geriatric depression and amnesic mild cognitive impairment. *The Journal of Neuroscience*, 32(12):4307–4318, 2012.
- [11] D. S. Barron, N. Tandon, J. L. Lancaster, and P. T. Fox. Thalamic structural connectivity in medial temporal lobe epilepsy. *Epilepsia*, 55(6):e50–e55, 2014.
- [12] F. Barry, M. Walter, and C. Gallistel. On the optimal pulse duration in electrical stimulation of the brain. *Physiology & behavior*, 12(5):749–754, 1974.
- [13] F. Bartolomei, P. Chauvel, and F. Wendling. Epileptogenicity of brain structures in human temporal lobe epilepsy: a quantified study from intracerebral eeg. *Brain*, 131(7):1818–1830, 2008.
- [14] P. J. Basser. Relationships between diffusion tensor and q-space mri. *Magnetic resonance in medicine*, 47(2):392–397, 2002.

- [15] P. J. Basser, J. Mattiello, and D. LeBihan. Estimation of the effective self-diffusion tensor from the NMR spin echo. *J. Magn. Reson.. Series B*, 103(3): 247–54, Mar. 1994. ISSN 1064-1866.
- [16] D. S. Bassett, J. A. Brown, V. Deshpande, J. M. Carlson, and S. T. Grafton. Conserved and variable architecture of human white matter connectivity. *Neuroimage*, 54(2):1262–1279, 2011.
- [17] M. Bastiani, N. J. Shah, R. Goebel, and A. Roebroeck. Human cortical connectome reconstruction from diffusion weighted mri: the effect of tractography algorithm. *NeuroImage*, 62(3):1732–1749, 2012.
- [18] D. Batalle, E. Eixarch, F. Figueras, E. Muñoz-Moreno, N. Bargallo, M. Illa, R. Acosta-Rojas, I. Amat-Roldan, and E. Gratacos. Altered small-world topology of structural brain networks in infants with intrauterine growth restriction and its association with later neurodevelopmental outcome. *Neuroimage*, 60(2):1352–1366, 2012.
- [19] D. Bates, M. Maechler, and B. Bolker. R programming language: lme4 package, June 2013.
- [20] P. R. Bauer, S. Kalitzin, M. Zijlmans, J. W. Sander, and G. H. Visser. Cortical excitability as a potential clinical marker of epilepsy: a review of the clinical application of transcranial magnetic stimulation. *International journal of neural systems*, 24(02):1430001, 2014.
- [21] C. Baumgartner, R. Flint, I. Tuxhorn, P. Van Ness, J. Kosalko, A. Olbrich, G. Almer, K. Novak, and H. Luders. Supplementary motor area seizures propagation pathways as studied with invasive recordings. *Neurology*, 46(2): 508–511, 1996.
- [22] T. Behrens, M. Woolrich, M. Jenkinson, H. Johansen-Berg, R. Nunes, S. Clare, P. Matthews, J. Brady, and S. Smith. Characterization and propagation of uncertainty in diffusion-weighted MR imaging. *Magn. Reson. Med.*, 50(5):1077–1088, 2003.

- [23] T. Behrens, H. J. Berg, S. Jbabdi, M. Rushworth, and M. Woolrich. Probabilistic diffusion tractography with multiple fibre orientations: What can we gain? *Neuroimage*, 34(1):144–155, 2007.
- [24] R. M. Besseling, J. F. Jansen, G. M. Overvliet, S. J. van der Kruijs, S. C. Ebus, A. J. de Louw, P. A. Hofman, A. P. Aldenkamp, and W. H. Backes. Delayed convergence between brain network structure and function in rolandic epilepsy. *Frontiers in human neuroscience*, 8, 2014.
- [25] P. Besson, R. Lopes, X. Leclerc, P. Derambure, and L. Tyvaert. Intra-subject reliability of the high-resolution whole-brain structural connectome. *NeuroImage*, 102:283–293, 2014.
- [26] N. Biggs, E. K. Lloyd, and R. J. Wilson. *Graph Theory, 1736-1936*. Oxford University Press, 1976.
- [27] T. Bitan, J. R. Booth, J. Choy, D. D. Burman, D. R. Gitelman, and M.-M. Mesulam. Shifts of effective connectivity within a language network during rhyming and spelling. *The Journal of neuroscience*, 25(22):5397–5403, 2005.
- [28] G. G. Blasdel, J. S. Lund, and D. Fitzpatrick. Intrinsic connections of macaque striate cortex: axonal projections of cells outside lamina 4c. *The Journal of neuroscience*, 5(12):3350–3369, 1985.
- [29] F. Bloch. Nuclear induction. *Physical review*, 70(7-8):460, 1946.
- [30] I. Blümcke, M. Thom, E. Aronica, D. D. Armstrong, H. V. Vinters, A. Palmini, T. S. Jacques, G. Avanzini, A. J. Barkovich, G. Battaglia, et al. The clinicopathologic spectrum of focal cortical dysplasias: A consensus classification proposed by an ad hoc task force of the ilae diagnostic methods commission1. *Epilepsia*, 52(1):158–174, 2011.
- [31] W. T. Blume, D. Ociepa, and V. Kander. Frontal lobe seizure propagation: scalp and subdural eeg studies. *Epilepsia*, 42(4):491–503, 2001.

- [32] D. Boido, D. Kapetis, V. Gnatkovsky, C. Pastori, B. Galbardi, I. Sartori, L. Tassi, F. Cardinale, S. Francione, and M. Curtis. Stimulus-evoked potentials contribute to map the epileptogenic zone during stereo-eeG presurgical monitoring. *Human brain mapping*, 2014.
- [33] D. Boison. Adenosinergic signaling in epilepsy. *Neuropharmacology*, 2015.
- [34] L. Bonilha, T. Nesland, G. U. Martz, J. E. Joseph, M. V. Spampinato, J. C. Edwards, and A. Tabesh. Medial temporal lobe epilepsy is associated with neuronal fibre loss and paradoxical increase in structural connectivity of limbic structures. *Journal of Neurology, Neurosurgery & Psychiatry*, pages jnnp-2012, 2012.
- [35] L. Bonilha, T. Nesland, C. Rorden, and J. Fridriksson. Asymmetry of the structural brain connectome in healthy older adults. *Frontiers in psychiatry*, 4, 2013.
- [36] L. Bonilha, E. Gleichgerricht, J. Fridriksson, C. Rorden, J. L. Breedlove, T. Nesland, W. Paulus, G. Helms, and N. K. Focke. Reproducibility of the structural brain connectome derived from diffusion tensor imaging. *PloS one*, 10(9):e0135247, 2015.
- [37] W. H. Bosking, Y. Zhang, B. Schofield, and D. Fitzpatrick. Orientation selectivity and the arrangement of horizontal connections in tree shrew striate cortex. *The Journal of neuroscience*, 17(6):2112–2127, 1997.
- [38] S. Boulogne, P. Ryvlin, and S. Rheims. Single and paired-pulse electrical stimulation during invasive eeg recordings. *Revue neurologique*, 172(3):174–181, 2016.
- [39] R. Bracewell and P. B. Kahn. The fourier transform and its applications. *American Journal of Physics*, 34(8):712–712, 1966.
- [40] H. Braendgaard, S. Evans, C. Howard, and H. Gundersen. The total num-

- ber of neurons in the human neocortex unbiasedly estimated using optical disectors. *Journal of Microscopy*, 157(3):285–304, 1990.
- [41] U. Brandes. A faster algorithm for betweenness centrality*. *Journal of mathematical sociology*, 25(2):163–177, 2001.
- [42] J. Brill and J. R. Huguenard. Robust short-latency perisomatic inhibition onto neocortical pyramidal cells detected by laser-scanning photostimulation. *The Journal of Neuroscience*, 29(23):7413–7423, 2009.
- [43] K. Brodmann. Localisation in the cerebral cortex. *London: Smith-Gordon*, 998, 1909.
- [44] K. Brodmann. *Vergleichende Lokalisationslehre der Grosshirnrinde in ihren Prinzipien dargestellt auf Grund des Zellenbaues*. Barth, 1909.
- [45] D. N. Bub, M. Arguin, and A. R. Lecours. Jules dejerine and his interpretation of pure alexia. *Brain and language*, 45(4):531–559, 1993.
- [46] E. R. Buch, A. M. Shanechi, A. D. Fourkas, C. Weber, N. Birbaumer, and L. G. Cohen. Parietofrontal integrity determines neural modulation associated with grasping imagery after stroke. *Brain*, 135(2):596–614, 2012.
- [47] C. R. Buchanan, C. R. Pernet, K. J. Gorgolewski, A. J. Storkey, and M. E. Bastin. Test–retest reliability of structural brain networks from diffusion mri. *Neuroimage*, 86:231–243, 2014.
- [48] E. Bullmore and O. Sporns. Complex brain networks: graph theoretical analysis of structural and functional systems. *Nat. Rev. Neurosci.*, 10(3):186–198, 2009.
- [49] K. F. Burdach. *Vom Baue und Leben des Gehirns*, volume 3. Dyk, 1826.
- [50] A. Burkhalter. Intrinsic connections of rat primary visual cortex: laminar organization of axonal projections. *Journal of Comparative Neurology*, 279(2):171–186, 1989.

- [51] A. Burkhalter and K. L. Bernardo. Organization of corticocortical connections in human visual cortex. *Proceedings of the National Academy of Sciences*, 86(3):1071–1075, 1989.
- [52] D. P. Buxhoeveden and M. F. Casanova. The minicolumn hypothesis in neuroscience. *Brain*, 125(5):935–951, 2002.
- [53] G. Buzsáki, C. A. Anastassiou, and C. Koch. The origin of extracellular fields and currentseeg, ecog, lfp and spikes. *Nature Reviews Neuroscience*, 13(6):407–420, 2012.
- [54] K. Caeyenberghs, A. Leemans, I. Leunissen, K. Michiels, and S. P. Swinnen. Topological correlations of structural and functional networks in patients with traumatic brain injury. *Frontiers in human neuroscience*, 7, 2013.
- [55] W. Calvin. Competing for consciousness: how subconscious thoughts cook on the back burner, 1998.
- [56] L. Cammoun, X. Gigandet, D. Meskaldji, J. P. Thiran, O. Sporns, K. Q. Do, P. Maeder, R. Meuli, and P. Hagmann. Mapping the human connectome at multiple scales with diffusion spectrum MRI. *J. Neurosci. Methods*, 203(2):386–397, 2012.
- [57] A. W. Campbell. *Histological studies on the localisation of cerebral function*. University Press, 1905.
- [58] B. M. Campos, A. C. Coan, G. C. Beltramini, M. Liu, C. L. Yassuda, E. Ghizoni, C. Beaulieu, D. W. Gross, and F. Cendes. White matter abnormalities associate with type and localization of focal epileptogenic lesions. *Epilepsia*, 56(1):125–132, 2015.
- [59] J. M. Cardoso, K. Leung, M. Modat, S. Keihaninejad, D. Cash, J. Barnes, N. C. Fox, and S. Ourselin. STEPS: Similarity and Truth Estimation for Propagated Segmentations and its application to hippocampal segmentation

- and brain parcellation. *Med. Image Anal.*, 17(6):671–84, Mar. 2013. ISSN 1361-8423.
- [60] M. J. Cardoso, M. J. Clarkson, G. R. Ridgway, M. Modat, N. C. Fox, and S. Ourselin. Load: A locally adaptive cortical segmentation algorithm. *NeuroImage*, 56(3):1386–1397, 2011.
- [61] M. Catani and M. T. De Schotten. A diffusion tensor imaging tractography atlas for virtual in vivo dissections. *Cortex*, 44(8):1105–1132, 2008.
- [62] M. Catani and M. Thiebaut de Schotten. A diffusion tensor imaging tractography atlas for virtual in vivo dissections. *Cortex*, 44(8):1105–1132, 2008.
- [63] M. Catani, R. J. Howard, S. Pajevic, and D. K. Jones. Virtual in vivo interactive dissection of white matter fasciculi in the human brain. *Neuroimage*, 17(1):77–94, 2002.
- [64] M. Catani, D. K. Jones, et al. Perisylvian language networks of the human brain. *Annals of neurology*, 57(1):8–16, 2005.
- [65] M. Catani et al. Beyond localization: from hodology to function. *Philosophical Transactions of the Royal Society of London B: Biological Sciences*, 360(1456):767–779, 2005.
- [66] M. Catani et al. The rises and falls of disconnection syndromes. *Brain*, 128(10):2224–2239, 2005.
- [67] H. Catenoix, M. Magnin, M. Guenot, J. Isnard, F. Mauguiere, and P. Ryvlin. Hippocampal-orbitofrontal connectivity in human: an electrical stimulation study. *Clinical neurophysiology*, 116(8):1779–1784, 2005.
- [68] H. Catenoix, M. Magnin, F. Mauguiere, and P. Ryvlin. Evoked potential study of hippocampal efferent projections in the human brain. *Clinical Neurophysiology*, 122(12):2488–2497, 2011.

- [69] H. Chen, T. Liu, Y. Zhao, T. Zhang, Y. Li, M. Li, H. Zhang, H. Kuang, L. Guo, J. Z. Tsien, et al. Optimization of large-scale mouse brain connectome via joint evaluation of dti and neuron tracing data. *NeuroImage*, 115: 202–213, 2015.
- [70] T. Chenevert, J. Brunberg, and J. Pipe. Anisotropic diffusion within human white matter. In *Seventy sixth scientific assembly and annual meeting of the Radiological Society of North America*, 1990.
- [71] H. Cheng, Y. Wang, J. Sheng, W. G. Kronenberger, V. P. Mathews, T. A. Hummer, and A. J. Saykin. Characteristics and variability of structural networks derived from diffusion tensor imaging. *NeuroImage*, 61(4):1153–64, July 2012. ISSN 1095-9572.
- [72] H. Cheng, Y. Wang, J. Sheng, O. Sporns, W. G. Kronenberger, V. P. Mathews, T. A. Hummer, and A. J. Saykin. Optimization of seed density in DTI tractography for structural networks. *J. Neurosci. Methods*, 203(1):264–272, 2012.
- [73] J. D. Clayden, A. J. Storkey, S. M. Maniega, and M. E. Bastin. Reproducibility of tract segmentation between sessions using an unsupervised modelling-based approach. *NeuroImage*, 45(2):377–385, 2009.
- [74] J. D. Clayden, S. M. Maniega, A. J. Storkey, M. D. King, M. E. Bastin, and C. A. Clark. Tractor: Magnetic resonance imaging and tractography with r. *J. Statistical Software*, 44(8):1–18, 2011.
- [75] J. D. Clayden, M. Dayan, and C. A. Clark. Principal networks. *PloS one*, 8(4):e60997, 2013.
- [76] G. Cleveland, D. Chang, C. Hazlewood, and H. Rorschach. Nuclear magnetic resonance measurement of skeletal muscle: anisotropy of the diffusion coefficient of the intracellular water. *Biophysical journal*, 16(9):1043, 1976.

- [77] L. L. Cloutman and M. A. Lambon Ralph. Connectivity-based structural and functional parcellation of the human cortex using diffusion imaging and tractography. *Front. Neuroanat.*, 6:34, Jan. 2012. ISSN 1662-5129.
- [78] C. R. Conner, T. M. Ellmore, M. A. DiSano, T. A. Pieters, A. W. Potter, and N. Tandon. Anatomic and electro-physiologic connectivity of the language system: a combined dti-ccep study. *Computers in biology and medicine*, 41(12):1100–1109, 2011.
- [79] T. E. Conturo, R. C. McKinstry, E. Akbudak, and B. H. Robinson. Encoding of anisotropic diffusion with tetrahedral gradients: a general mathematical diffusion formalism and experimental results. *Magnetic Resonance in Medicine*, 35(3):399–412, 1996.
- [80] P. A. Cook, M. Symms, P. A. Boulby, and D. C. Alexander. Optimal acquisition orders of diffusion-weighted mri measurements. *Journal of magnetic resonance imaging*, 25(5):1051–1058, 2007.
- [81] R. L. Cooper, D. B. Chang, A. C. Young, C. J. Martin, and B. Ancker-Johnson. Restricted diffusion in biophysical systems: experiment. *Biophysical journal*, 14(3):161–177, 1974.
- [82] O. D. Creutzfeldt, S. Watanabe, and H. D. Lux. Relations between eeg phenomena and potentials of single cortical cells. i. evoked responses after thalamic and epicortical stimulation. *Electroencephalography and clinical neurophysiology*, 20(1):1–18, 1966.
- [83] J. Crofts, D. Higham, R. Bosnell, S. Jbabdi, P. Matthews, T. Behrens, and H. Johansen-Berg. Network analysis detects changes in the contralesional hemisphere following stroke. *Neuroimage*, 54(1):161–169, 2011.
- [84] G. Csardi and T. Nepusz. The igraph software package for complex network research. *InterJournal, Complex Systems*:1695, 2006. URL <http://igraph.org>.

- [85] Z. Cui, S. Zhong, P. Xu, Y. He, and G. Gong. Panda: a pipeline toolbox for analyzing brain diffusion images. 2013.
- [86] H. Damasio, D. Tranel, T. Grabowski, R. Adolphs, and A. Damasio. Neural systems behind word and concept retrieval. *Cognition*, 92(1):179–229, 2004.
- [87] O. David, A.-S. Job, L. De Palma, D. Hoffmann, L. Minotti, and P. Kahane. Probabilistic functional tractography of the human cortex. *NeuroImage*, 80:307–317, 2013.
- [88] M. A. de Reus and M. P. van den Heuvel. Estimating false positives and negatives in brain networks. *NeuroImage*, 70:402–409, 2013.
- [89] J. DeFelipe, S. Hendry, and E. Jones. A correlative electron microscopic study of basket cells and large gabaergic neurons in the monkey sensory-motor cortex. *Neuroscience*, 17(4):991–1009, 1986.
- [90] J. DeFelipe, S. Hendry, T. Hashikawa, M. Molinari, and E. Jones. A microcolumnar structure of monkey cerebral cortex revealed by immunocytochemical studies of double bouquet cell axons. *Neuroscience*, 37(3):655–673, 1990.
- [91] J. J. Dejerine. Contribution à l’étude anatomo-pathologique et clinique des différentes variétés de cécité verbale. 1892.
- [92] J. J. Dejerine. *Anatomie des centres nerveux*, volume 1. Rueff, 1895.
- [93] J. J. Dejerine and A. Dejerine. *Anatomie des centres nerveux, vol. 1*. Rueff et Cie, 1895.
- [94] J. M. Delgado. Depth stimulation of the brain. *Electrical Stimulation Research Techniques*, 1981.
- [95] A. Delorme and S. Makeig. Eeglab: an open source toolbox for analysis of single-trial eeg dynamics including independent component analysis. *Journal of neuroscience methods*, 134(1):9–21, 2004.

- [96] A. Delorme, T. Sejnowski, and S. Makeig. Enhanced detection of artifacts in eeg data using higher-order statistics and independent component analysis. *Neuroimage*, 34(4):1443–1449, 2007.
- [97] E. L. Dennis, N. Jahanshad, K. L. McMahon, G. I. de Zubicaray, N. G. Martin, I. B. Hickie, A. W. Toga, M. J. Wright, and P. M. Thompson. Development of brain structural connectivity between ages 12 and 30: A 4-tesla diffusion imaging study in 439 adolescents and adults. *NeuroImage*, 2012.
- [98] M. N. DeSalvo, L. Douw, N. Tanaka, C. Reinsberger, and S. M. Stuffelbeam. Altered structural connectome in temporal lobe epilepsy. *Radiology*, 270(3):842–848, 2013.
- [99] R. S. Desikan, F. Ségonne, B. Fischl, B. T. Quinn, B. C. Dickerson, D. Blacker, R. L. Buckner, A. M. Dale, R. P. Maguire, B. T. Hyman, M. S. Albert, and R. J. Killiany. An automated labeling system for subdividing the human cerebral cortex on MRI scans into gyral based regions of interest. *Neuroimage*, 31(3):968–980, 2006.
- [100] I. Diamond. The subdivisions of neocortex: a proposal to revise the traditional view of sensory, motor, and association areas. *Progress in psychobiology and physiological psychology*, 8:1–43, 1979.
- [101] B. Diehl, R. M. Busch, J. S. Duncan, Z. Piao, J. Tkach, and H. O. Lüders. Abnormalities in diffusion tensor imaging of the uncinate fasciculus relate to reduced memory in temporal lobe epilepsy. *Epilepsia*, 49(8):1409–1418, 2008.
- [102] B. Diehl, J. Tkach, Z. Piao, P. Ruggieri, E. LaPresto, P. Liu, E. Fisher, W. Bingaman, and I. Najm. Diffusion tensor imaging in patients with focal epilepsy due to cortical dysplasia in the temporo-occipital region: electro-clinico-pathological correlations. *Epilepsy research*, 90(3):178–187, 2010.
- [103] J.-R. Ding, D. An, W. Liao, J. Li, G.-R. Wu, Q. Xu, Z. Long, Q. Gong,

- D. Zhou, O. Sporns, et al. Altered functional and structural connectivity networks in psychogenic non-epileptic seizures. 2013.
- [104] M. Drakesmith, K. Caeyenberghs, A. Dutt, G. Lewis, A. David, and D. Jones. Overcoming the effects of false positives and threshold bias in graph theoretical analyses of neuroimaging data. *NeuroImage*, 2015.
- [105] J. M. Duarte-Carvajalino, N. Jahanshad, C. Lenglet, K. L. McMahon, G. I. de Zubicaray, N. G. Martin, M. J. Wright, P. M. Thompson, and G. Sapiro. Hierarchical topological network analysis of anatomical human brain connectivity and differences related to sex and kinship. *Neuroimage*, 59(4): 3784–3804, 2012.
- [106] J. M. Duarte-Carvajalino, N. Jahanshad, C. Lenglet, K. L. McMahon, G. I. de Zubicaray, N. G. Martin, M. J. Wright, P. M. Thompson, and G. Sapiro. Hierarchical topological network analysis of anatomical human brain connectivity and differences related to sex and kinship. *Neuroimage*, 59(4): 3784–3804, 2012.
- [107] M. Duchowny, P. Jayakar, and B. Levin. Aberrant neural circuits in malformations of cortical development and focal epilepsy. *Neurology*, 55(3): 423–428, 2000.
- [108] J. T. Duda, P. A. Cook, and J. C. Gee. Reproducibility of graph metrics of human brain structural networks. *Frontiers in neuroinformatics*, 8, 2014.
- [109] C. Echtermeyer, C. E. Han, A. Rotarska-Jagiela, H. Mohr, P. J. Uhlhaas, and M. Kaiser. Integrating temporal and spatial scales: human structural network motifs across age and region of interest size. *Front. Neuroinformatics*, 5:10, Jan. 2011. ISSN 1662-5196.
- [110] A. Einstein. *Investigations on the Theory of the Brownian Movement*. Courier Corporation, 1956.

- [111] T. M. Ellmore, M. S. Beauchamp, T. J. O'Neill, S. Dreyer, and N. Tandon. Relationships between essential cortical language sites and subcortical pathways: Clinical article. *Journal of neurosurgery*, 111(4):755–766, 2009.
- [112] R. Enatsu, Z. Piao, T. O'Connor, K. Horning, J. Mosher, R. Burgess, W. Bingaman, and D. Nair. Cortical excitability varies upon ictal onset patterns in neocortical epilepsy: a cortico-cortical evoked potential study. *Clinical Neurophysiology*, 123(2):252–260, 2012.
- [113] R. Enatsu, J. Bulacio, D. R. Nair, W. Bingaman, I. Najm, and J. Gonzalez-Martinez. Posterior cingulate epilepsy: clinical and neurophysiological analysis. *Journal of Neurology, Neurosurgery & Psychiatry*, pages jnnp–2013, 2013.
- [114] R. Enatsu, R. Matsumoto, Z. Piao, T. O'Connor, K. Horning, R. C. Burgess, J. Bulacio, W. Bingaman, and D. R. Nair. Cortical negative motor network in comparison with sensorimotor network: A cortico-cortical evoked potential study. *Cortex*, 49(8):2080–2096, 2013.
- [115] R. Enatsu, J. Gonzalez-Martinez, J. Bulacio, J. C. Mosher, R. C. Burgess, I. Najm, and D. R. Nair. Connectivity of the frontal and anterior insular network: a cortico-cortical evoked potential study. *Journal of neurosurgery*, pages 1–12, 2015.
- [116] L. Entz, E. Tóth, C. J. Keller, S. Bickel, D. M. Groppe, D. Fabó, L. R. Kozák, L. Erőss, I. Ulbert, and A. D. Mehta. Evoked effective connectivity of the human neocortex. *Human brain mapping*, 35(12):5736–5753, 2014.
- [117] S. Epelbaum, P. Pinel, R. Gaillard, C. Delmaire, M. Perrin, S. Dupont, S. Dehaene, and L. Cohen. Pure alexia as a disconnection syndrome: new diffusion imaging evidence for an old concept. *Cortex*, 44(8):962–974, 2008.
- [118] A. C. Evans, D. L. Collins, S. Mills, E. Brown, R. Kelly, and T. M. Peters. 3d statistical neuroanatomical models from 305 mri volumes. In *Nuclear Sci-*

- ence Symposium and Medical Imaging Conference, 1993., 1993 IEEE Conference Record.*, pages 1813–1817. IEEE, 1993.
- [119] O. V. Favorov and D. G. Kelly. Minicolumnar organization within somatosensory cortical segregates: I. development of afferent connections. *Cerebral Cortex*, 4(4):408–427, 1994.
- [120] D. J. Felleman and D. C. Van Essen. Distributed hierarchical processing in the primate cerebral cortex. *Cerebral cortex*, 1(1):1–47, 1991.
- [121] F. U. Fischer, D. Wolf, A. Scheurich, and A. Fellgiebel. Association of structural global brain network properties with intelligence in normal aging. *PloS one*, 9(1):e86258, 2014.
- [122] B. Fischl, A. van der Kouwe, C. Destrieux, E. Halgren, F. Ségonne, D. H. Salat, E. Busa, L. J. Seidman, J. Goldstein, D. Kennedy, V. Caviness, N. Makris, B. Rosen, and A. M. Dale. Automatically parcellating the human cerebral cortex. *Cereb. Cortex*, 14(1):11–22, 2004.
- [123] R. A. Fiskien, L. Garey, and T. Powell. The intrinsic, association and commissural connections of area 17 of the visual cortex. *Philosophical Transactions of the Royal Society of London. Series B, Biological Sciences*, pages 487–536, 1975.
- [124] D. Fitzpatrick, J. S. Lund, and G. G. Blasdel. Intrinsic connections of macaque striate cortex: afferent and efferent connections of lamina 4c. *J Neurosci*, 5(12):3329–3349, 1985.
- [125] D. Flanagan, A. Valentín, J. J. García Seoane, G. Alarcon, and S. G. Boyd. Single-pulse electrical stimulation helps to identify epileptogenic cortex in children. *Epilepsia*, 50(7):1793–1803, 2009.
- [126] P. Flechsig. Neue untersuchungen über die markbildung in den menschlichen gehirnlappen. *Neurol. Zentralbl.*, page 977, 1889.

- [127] S. J. Forkel, M. T. De Schotten, J. M. Kawadler, F. Dell'Acqua, A. Danek, and M. Catani. The anatomy of fronto-occipital connections from early blunt dissections to contemporary tractography. *Cortex*, 56:73–84, 2014.
- [128] L. R. Frank. Anisotropy in high angular resolution diffusion-weighted mri. *Magnetic Resonance in Medicine*, 45(6):935–939, 2001.
- [129] W. Franks, I. Schenker, P. Schmutz, and A. Hierlemann. Impedance characterization and modeling of electrodes for biomedical applications. *Biomedical Engineering, IEEE Transactions on*, 52(7):1295–1302, 2005.
- [130] L. C. Freeman. A set of measures of centrality based on betweenness. *Sociometry*, pages 35–41, 1977.
- [131] E. J. Friedman, A. S. Landsberg, J. P. Owen, Y.-O. Li, and P. Mukherjee. Stochastic geometric network models for groups of functional and structural connectomes. *NeuroImage*, 101:473–484, 2014.
- [132] R. D. Frostig. What does in vivo optical imaging tell us about the primary visual cortex in primates? In *Primary Visual Cortex in Primates*, pages 331–358. Springer, 1994.
- [133] T. Fumuro, R. Matsumoto, A. Shimotake, M. Matsushashi, M. Inouchi, S.-i. Urayama, N. Sawamoto, H. Fukuyama, R. Takahashi, and A. Ikeda. Network hyperexcitability in a patient with partial reading epilepsy: Converging evidence from magnetoencephalography, diffusion tractography, and functional magnetic resonance imaging. *Clinical Neurophysiology*, 126(4):675–681, 2015.
- [134] P. Gabbott, K. Martin, and D. Whitteridge. Connections between pyramidal neurons in layer 5 of cat visual cortex (area 17). *Journal of Comparative Neurology*, 259(3):364–381, 1987.
- [135] N. Geschwind. The paradoxical position of kurt goldstein in the history of aphasia. *Cortex*, 1(2):214–224, 1964.

- [136] N. Geschwind. *Disconnexion syndromes in animals and man*. Springer, 1974.
- [137] C. D. Gilbert and T. N. Wiesel. Morphology and intracortical projections of functionally characterised neurones in the cat visual cortex. *Nature*, 280 (5718):120–125, 1979.
- [138] C. D. Gilbert and T. N. Wiesel. Clustered intrinsic connections in cat visual cortex. *The Journal of Neuroscience*, 3(5):1116–1133, 1983.
- [139] C. D. Gilbert and T. N. Wiesel. Columnar specificity of intrinsic horizontal and corticocortical connections in cat visual cortex. *The Journal of Neuroscience*, 9(7):2432–2442, 1989.
- [140] M. Glasser, T. Coalson, E. Robinson, C. Hacker, J. Harwell, E. Yacoub, K. Ugurbil, J. Anderson, C. Beckmann, M. Jenkinson, et al. A multi-modal parcellation of human cerebral cortex. *Nature*, 2015.
- [141] M. F. Glasser, S. N. Sotiropoulos, J. A. Wilson, T. S. Coalson, B. Fischl, J. L. Andersson, J. Xu, S. Jbabdi, M. Webster, J. R. Polimeni, et al. The minimal preprocessing pipelines for the human connectome project. *Neuroimage*, 80: 105–124, 2013.
- [142] E. M. Goldberg and D. A. Coulter. Mechanisms of epileptogenesis: a convergence on neural circuit dysfunction. *Nature Reviews Neuroscience*, 14(5): 337–349, 2013.
- [143] G. Gong, Y. He, L. Concha, C. Lebel, D. W. Gross, A. C. Evans, and C. Beaulieu. Mapping anatomical connectivity patterns of human cerebral cortex using in vivo diffusion tensor imaging tractography. *Cereb. Cortex*, 19(3):524–536, 2009.
- [144] G. Gong, P. Rosa-Neto, F. Carbonell, Z. J. Chen, Y. He, and A. C. Evans. Age-and gender-related differences in the cortical anatomical network. *J. Neurosci.*, 29(50):15684–15693, 2009.

- [145] G. Gong, Y. He, Z. J. Chen, and A. C. Evans. Convergence and divergence of thickness correlations with diffusion connections across the human cerebral cortex. *Neuroimage*, 59(2):1239–1248, 2012.
- [146] G. González-Burgos, G. Barrionuevo, and D. A. Lewis. Horizontal synaptic connections in monkey prefrontal cortex: an in vitro electrophysiological study. *Cerebral Cortex*, 10(1):82–92, 2000.
- [147] K. Gorgolewski, C. D. Burns, C. Madison, D. Clark, Y. O. Halchenko, M. L. Waskom, and S. S. Ghosh. Nipype: a flexible, lightweight and extensible neuroimaging data processing framework in python. *Front Neuroinform*, 5(3), 2011.
- [148] R. Guerrini, F. Sicca, and L. Parmeggiani. Epilepsy and malformations of the cerebral cortex. *Epileptic disorders*, 5(2):9–26, 2003.
- [149] M. Guye, G. J. Parker, M. Symms, P. Boulby, C. A. Wheeler-Kingshott, A. Salek-Haddadi, G. J. Barker, and J. S. Duncan. Combined functional mri and tractography to demonstrate the connectivity of the human primary motor cortex in vivo. *Neuroimage*, 19(4):1349–1360, 2003.
- [150] A. C. Guyton and J. Hall. Textbook of physiology. *Philadelphia: WB Saunders*, 1, 1996.
- [151] P. Hagmann, M. Kurant, X. Gigandet, P. Thiran, V. J. Wedeen, R. Meuli, and J.-P. Thiran. Mapping human whole-brain structural networks with diffusion MRI. *PloS One*, 2(7):e597, 2007.
- [152] P. Hagmann, M. Kurant, X. Gigandet, P. Thiran, V. J. Wedeen, R. Meuli, and J.-P. Thiran. Mapping human whole-brain structural networks with diffusion mri. *PloS one*, 2(7):e597, 2007.
- [153] P. Hagmann, L. Cammoun, X. Gigandet, R. Meuli, C. J. Honey, V. J. Wedeen, and O. Sporns. Mapping the structural core of human cerebral cortex. *PLoS Biol.*, 6(7):e159, 2008.

- [154] P. Hagmann, O. Sporns, N. Madan, L. Cammoun, R. Pienaar, V. J. Wedeen, R. Meuli, J.-P. Thiran, and P. Grant. White matter maturation reshapes structural connectivity in the late developing human brain. *Proc. Natl. Acad. Sci.*, 107(44):19067–19072, 2010.
- [155] P. Hagmann, O. Sporns, N. Madan, L. Cammoun, R. Pienaar, V. J. Wedeen, R. Meuli, J.-P. Thiran, and P. Grant. White matter maturation reshapes structural connectivity in the late developing human brain. *Proc. Natl. Acad. Sci.*, 107(44):19067–19072, 2010.
- [156] A. Hammers, R. Allom, M. J. Koepp, S. L. Free, R. Myers, L. Lemieux, T. N. Mitchell, D. J. Brooks, and J. S. Duncan. Three-dimensional maximum probability atlas of the human brain, with particular reference to the temporal lobe. *Hum. Brain Mapp.*, 19(4):224–247, 2003.
- [157] N. Herschkowitz, J. Kagan, and K. Zilles. Neurobiological bases of behavioral development in the second year. *Neuropediatrics*, 30(5):221–230, 1999.
- [158] J. A. Hirsch and C. D. Gilbert. Synaptic physiology of horizontal connections in the cat’s visual cortex. *The Journal of Neuroscience*, 11(6):1800–1809, 1991.
- [159] C. Honey, O. Sporns, L. Cammoun, X. Gigandet, J.-P. Thiran, R. Meuli, and P. Hagmann. Predicting human resting-state functional connectivity from structural connectivity. *Proc. Natl. Acad. Sci.*, 106(6):2035–2040, 2009.
- [160] P. G. Hosking. Surgery for frontal lobe epilepsy. *Seizure*, 12(3):160–166, 2003.
- [161] M. D. Humphries, K. Gurney, and T. J. Prescott. The brainstem reticular formation is a small-world, not scale-free, network. *Proceedings of the Royal Society of London B: Biological Sciences*, 273(1585):503–511, 2006.
- [162] G. W. Huntley and E. G. Jones. Relationship of intrinsic connections to forelimb movement representations in monkey motor cortex: a correlative

- anatomic and physiological study. *Journal of neurophysiology*, 66(2):390–413, 1991.
- [163] A. Hyvärinen and E. Oja. Independent component analysis: algorithms and applications. *Neural networks*, 13(4):411–430, 2000.
- [164] M. Ingalhalikar, A. Smith, D. Parker, T. D. Satterthwaite, M. A. Elliott, K. Ruparel, H. Hakonarson, R. E. Gur, R. C. Gur, and R. Verma. Sex differences in the structural connectome of the human brain. *Proceedings of the National Academy of Sciences*, 111(2):823–828, 2014.
- [165] V. Iori, F. Frigerio, and A. Vezzani. Modulation of neuronal excitability by immune mediators in epilepsy. *Current opinion in pharmacology*, 26:118–123, 2016.
- [166] Y. Iturria-Medina, E. Canales-Rodriguez, L. Melie-Garcia, P. Valdes-Hernandez, E. Martinez-Montes, Y. Aleman-Gomez, and J. Sánchez-Bornot. Characterizing brain anatomical connections using diffusion weighted mri and graph theory. *Neuroimage*, 36(3):645–660, 2007.
- [167] Y. Iturria-Medina, A. P. Fernández, D. M. Morris, E. J. Canales-Rodríguez, H. A. Haroon, L. G. Pentón, M. Augath, L. G. García, N. Logothetis, G. J. Parker, et al. Brain hemispheric structural efficiency and interconnectivity rightward asymmetry in human and nonhuman primates. *Cereb. Cortex*, 21(1):56–67, 2011.
- [168] M. Iwasaki, R. Enatsu, R. Matsumoto, E. Novak, B. Thankappen, Z. Piao, K. Horning, W. Bingaman, D. Nair, et al. Accentuated cortico-cortical evoked potentials in neocortical epilepsy in areas of ictal onset. *Epileptic disorders*, 12(4):292–302, 2010.
- [169] M. Jenkinson and S. Smith. A global optimisation method for robust affine registration of brain images. *Med. Image Anal.*, 5(2):143–156, 2001.

- [170] E. Jones and H. Burton. Cytoarchitecture and somatic sensory connectivity of thalamic nuclei other than the ventrobasal complex in the cat. *Journal of Comparative Neurology*, 154(4):395–432, 1974.
- [171] E. Jones, J. Coulter, and S. Hendry. Intracortical connectivity of architectonic fields in the somatic sensory, motor and parietal cortex of monkeys. *Journal of Comparative Neurology*, 181(2):291–347, 1978.
- [172] E. G. Jones. Laminar distribution of cortical efferent cells. *Cerebral cortex*, 1:521–553, 1984.
- [173] W. Jost. Diffusion in solids, liquids, gases. 1960.
- [174] S. L. Juliano, D. P. Friedman, and D. E. Eslin. Corticocortical connections predict patches of stimulus-evoked metabolic activity in monkey somatosensory cortex. *Journal of Comparative Neurology*, 298(1):23–39, 1990.
- [175] S. L. Juliano, S. L. Palmer, R. V. Sonty, S. Noctor, and G. F. Hill. Development of local connections in ferret somatosensory cortex. *Journal of Comparative Neurology*, 374(2):259–277, 1996.
- [176] A. Keller and H. Asanuma. Synaptic relationships involving local axon collaterals of pyramidal neurons in the cat motor cortex. *Journal of Comparative Neurology*, 336(2):229–242, 1993.
- [177] C. J. Keller, S. Bickel, L. Entz, I. Ulbert, M. P. Milham, C. Kelly, and A. D. Mehta. Intrinsic functional architecture predicts electrically evoked responses in the human brain. *Proceedings of the National Academy of Sciences*, 108(25):10308–10313, 2011.
- [178] C. J. Keller, C. J. Honey, L. Entz, S. Bickel, D. M. Groppe, E. Toth, I. Ulbert, F. A. Lado, and A. D. Mehta. Corticocortical evoked potentials reveal projectors and integrators in human brain networks. *The Journal of Neuroscience*, 34(27):9152–9163, 2014.

- [179] C. J. Keller, C. J. Honey, P. Mégevand, L. Entz, I. Ulbert, and A. D. Mehta. Mapping human brain networks with cortico-cortical evoked potentials. *Philosophical Transactions of the Royal Society B: Biological Sciences*, 369(1653):20130528, 2014.
- [180] Z. Kisvarday, E. Toth, M. Rausch, and U. Eysel. Orientation-specific relationship between populations of excitatory and inhibitory lateral connections in the visual cortex of the cat. *Cerebral Cortex*, 7(7):605–618, 1997.
- [181] Z. F. Kisvárdy, D.-S. Kim, U. T. Eysel, and T. Bonhoeffer. Relationship between lateral inhibitory connections and the topography of the orientation map in cat visual cortex. *European Journal of Neuroscience*, 6(10):1619–1632, 1994.
- [182] J. Koester and S. Siegelbaum. Local signaling: passive electrical properties of the neuron. *Principles of neural science*, pages 140–149, 2000.
- [183] V. Kokkinos, G. Alarcón, R. P. Selway, and A. Valentín. Role of single pulse electrical stimulation (spes) to guide electrode implantation under general anaesthesia in presurgical assessment of epilepsy. *Seizure*, 22(3):198–204, 2013.
- [184] M. Z. Koubeissi and R. J. Maciunas. *Extratemporal lobe epilepsy surgery*, volume 10. John Libbey Eurotext, 2011.
- [185] M. Z. Koubeissi, R. P. Lesser, A. Sinai, W. D. Gaillard, P. J. Franaszczuk, and N. E. Crone. Connectivity between perisylvian and bilateral basal temporal cortices. *Cerebral Cortex*, 22(4):918–925, 2012.
- [186] S. Kovac, M. Deppe, S. Mohammadi, H. Schiffbauer, W. Schwindt, G. Möddel, M. Dogan, and S. Evers. Gelastic seizures: A case of lateral frontal lobe epilepsy and review of the literature. *Epilepsy & Behavior*, 15(2):249–253, 2009.

- [187] M. Kritzer, A. Cowey, and P. Somogyi. Patterns of inter-and intralaminar gabaergic connections distinguish striate (v1) and extrastriate (v2, v4) visual cortices and their functionally specialized subdivisions in the rhesus monkey. *The Journal of neuroscience*, 12(11):4545–4564, 1992.
- [188] Y. Kubota, R. Enatsu, J. Gonzalez-Martinez, J. Bulacio, J. Mosher, R. C. Burgess, and D. R. Nair. γ in vivo γ human hippocampal cingulate connectivity: A corticocortical evoked potentials (cceps) study. *Clinical Neurophysiology*, 124(8):1547–1556, 2013.
- [189] A. Kuceyeski, J. Maruta, S. N. Niogi, J. Ghajar, and A. Raj. The generation and validation of white matter connectivity importance maps. *NeuroImage*, 58(1):109–121, 2011.
- [190] A. Labate, A. Cherubini, G. Tripepi, L. Mumoli, E. Ferlazzo, U. Aguglia, A. Quattrone, and A. Gambardella. White matter abnormalities differentiate severe from benign temporal lobe epilepsy. *Epilepsia*, 56(7):1109–1116, 2015.
- [191] J. P. Lachaux, D. Rudrauf, and P. Kahane. Intracranial eeg and human brain mapping. *Journal of Physiology-Paris*, 97(4):613–628, 2003.
- [192] M. Lacruz, J. Garcia Seoane, A. Valentin, R. Selway, and G. Alarcon. Frontal and temporal functional connections of the living human brain. *European Journal of Neuroscience*, 26(5):1357–1370, 2007.
- [193] V. Latora and M. Marchiori. Efficient behavior of small-world networks. *Physical review letters*, 87(19):198701, 2001.
- [194] P. C. Lauterbur et al. Image formation by induced local interactions: examples employing nuclear magnetic resonance. *Nature*, 242(5394):190–191, 1973.
- [195] D. Le Bihan. Looking into the functional architecture of the brain with diffusion mri. *Nature Reviews Neuroscience*, 4(6):469–480, 2003.

- [196] D. Le Bihan, E. Breton, D. Lallemand, P. Grenier, E. Cabanis, and M. Laval-Jeantet. Imagerie de self-diffusion in vivo par résonance magnétique nucléaire. *Innovation et technologie en biologie et médecine*, 7(6):713–720, 1986.
- [197] D. Le Bihan, J.-F. Mangin, C. Poupon, C. A. Clark, S. Pappata, N. Molko, and H. Chabriat. Diffusion tensor imaging: concepts and applications. *Journal of magnetic resonance imaging*, 13(4):534–546, 2001.
- [198] B. Lega, S. Dionisio, P. Flanigan, W. Bingaman, I. Najm, D. Nair, and J. Gonzalez-Martinez. Cortico-cortical evoked potentials for sites of early versus late seizure spread in stereoelectroencephalography. *Epilepsy research*, 115:17–29, 2015.
- [199] A. Lemkaddem, A. Daducci, N. Kunz, F. Lazeyras, M. Seeck, J.-P. Thiran, and S. Vulliémoz. Connectivity and tissue microstructural alterations in right and left temporal lobe epilepsy revealed by diffusion spectrum imaging. *NeuroImage: Clinical*, 5:349–358, 2014.
- [200] J. B. Levitt, D. A. Lewis, T. Yoshioka, and J. S. Lund. Topography of pyramidal neuron intrinsic connections in macaque monkey prefrontal cortex (areas 9 and 46). *Journal of Comparative Neurology*, 338(3):360–376, 1993.
- [201] J. D. Lewis, R. J. Theilmann, J. Townsend, and A. C. Evans. Network efficiency in autism spectrum disorder and its relation to brain overgrowth. *Frontiers in human neuroscience*, 7, 2013.
- [202] L. Li, J. K. Rilling, T. M. Preuss, M. F. Glasser, F. W. Damen, and X. Hu. Quantitative assessment of a framework for creating anatomical brain networks via global tractography. *NeuroImage*, 61(4):1017–30, July 2012. ISSN 1095-9572.
- [203] L. Li, J. K. Rilling, T. M. Preuss, M. F. Glasser, and X. Hu. The effects of connection reconstruction method on the interregional connectivity of brain

- networks via diffusion tractography. *Hum. Brain Mapp.*, 33(8):1894–1913, 2012.
- [204] Y. Li, Y. Liu, J. Li, W. Qin, K. Li, C. Yu, and T. Jiang. Brain anatomical network and intelligence. *PLoS Comput. Biol.*, 5(5):e1000395, 2009.
- [205] W. Liao, Z. Zhang, Z. Pan, D. Mantini, J. Ding, X. Duan, C. Luo, Z. Wang, Q. Tan, G. Lu, et al. Default mode network abnormalities in mesial temporal lobe epilepsy: a study combining fmri and dti. *Human brain mapping*, 32(6):883–895, 2011.
- [206] B. Libet. Electrical stimulation of cortex in human subjects, and conscious sensory aspects. In *Somatosensory system*, pages 743–790. Springer, 1973.
- [207] J. P. Lieb, K. Hoque, C. E. Skomer, and X.-W. Song. Inter-hemispheric propagation of human mesial temporal lobe seizures: a coherence/phase analysis. *Electroencephalography and clinical neurophysiology*, 67(2):101–119, 1987.
- [208] J. C. Lilly, J. R. Hughes, E. C. Alvord Jr, and T. W. Galkin. Brief, noninjurious electric waveform for stimulation of the brain. *Science*, 1955.
- [209] J. J. Lin, J. D. Riley, J. Juranek, and S. C. Cramer. Vulnerability of the frontal-temporal connections in temporal lobe epilepsy. *Epilepsy research*, 82(2):162–170, 2008.
- [210] M. Liu, Z. Chen, C. Beaulieu, and D. W. Gross. Disrupted anatomic white matter network in left mesial temporal lobe epilepsy. *Epilepsia*, 55(5):674–682, 2014.
- [211] C.-Y. Lo, P.-N. Wang, K.-H. Chou, J. Wang, Y. He, and C.-P. Lin. Diffusion tensor tractography reveals abnormal topological organization in structural cortical networks in alzheimer’s disease. *J. Neurosci.*, 30(50):16876–16885, 2010.

- [212] N. K. Logothetis, M. Augath, Y. Murayama, A. Rauch, F. Sultan, J. Goense, A. Oeltermann, and H. Merkle. The effects of electrical microstimulation on cortical signal propagation. *Nature neuroscience*, 13(10):1283–1291, 2010.
- [213] J. S. Lund. Organization of neurons in the visual cortex, area 17, of the monkey (macaca mulatta). *Journal of Comparative Neurology*, 147(4):455–495, 1973.
- [214] J. S. Lund and R. Boothe. Interlaminar connections and pyramidal neuron organisation in the visual cortex, area 17, of the macaque monkey. *Journal of Comparative Neurology*, 159(3):305–334, 1975.
- [215] R. Malach, Y. Amir, M. Harel, and A. Grinvald. Relationship between intrinsic connections and functional architecture revealed by optical imaging and in vivo targeted biocytin injections in primate striate cortex. *Proceedings of the National Academy of Sciences*, 90(22):10469–10473, 1993.
- [216] M. Malpighi. De cerebri cortice. *Bologna: Montius*, 1666, 1996.
- [217] P. Mansfield. Multi-planar image formation using nmr spin echoes. *Journal of Physics C: Solid State Physics*, 10(3):L55, 1977.
- [218] K. Martin and D. Whitteridge. Form, function and intracortical projections of spiny neurones in the striate visual cortex of the cat. *The Journal of physiology*, 353(1):463–504, 1984.
- [219] MATLAB. *version 7.10.0 (R2010a)*. The MathWorks Inc., Natick, Massachusetts, 2010.
- [220] J. Matsubara, M. Cynader, and N. Swindale. Anatomical properties and physiological correlates of the intrinsic connections in cat area 18. *The Journal of neuroscience*, 7(5):1428–1446, 1987.
- [221] R. Matsumoto, D. R. Nair, E. LaPresto, I. Najm, W. Bingaman, H. Shibasaki, and H. O. Lüders. Functional connectivity in the human language system: a cortico-cortical evoked potential study. *Brain*, 127(10):2316–2330, 2004.

- [222] R. Matsumoto, M. Kinoshita, J. Taki, T. Hitomi, N. Mikuni, H. Shibasaki, H. Fukuyama, N. Hashimoto, and A. Ikeda. In vivo epileptogenicity of focal cortical dysplasia: a direct cortical paired stimulation study. *Epilepsia*, 46(11):1744–1749, 2005.
- [223] R. Matsumoto, D. R. Nair, E. LaPresto, W. Bingaman, H. Shibasaki, and H. O. Lüders. Functional connectivity in human cortical motor system: a cortico-cortical evoked potential study. *Brain*, 130(1):181–197, 2007.
- [224] R. Matsumoto, D. R. Nair, A. Ikeda, T. Fumuro, E. LaPresto, N. Mikuni, W. Bingaman, S. Miyamoto, H. Fukuyama, R. Takahashi, et al. Parieto-frontal network in humans studied by cortico-cortical evoked potential. *Human brain mapping*, 33(12):2856–2872, 2012.
- [225] N. Matsuzaki, C. Juhász, and E. Asano. Cortico-cortical evoked potentials and stimulation-elicited gamma activity preferentially propagate from lower-to higher-order visual areas. *Clinical Neurophysiology*, 124(7):1290–1296, 2013.
- [226] J. Mattiello, P. J. Basser, and D. Le Bihan. The b matrix in diffusion tensor echo-planar imaging. *Magnetic Resonance in Medicine*, 37(2):292–300, 1997.
- [227] P. Mazzarello. *Golgi: A Biography of the Founder of Modern Neuroscience*. Oxford University Press, USA, 2010.
- [228] B. A. McGuire, C. D. Gilbert, P. K. Rivlin, and T. N. Wiesel. Targets of horizontal connections in macaque primary visual cortex. *Journal of Comparative Neurology*, 305(3):370–392, 1991.
- [229] D. S. Melchitzky, S. R. Sesack, M. L. Pucak, and D. A. Lewis. Synaptic targets of pyramidal neurons providing intrinsic horizontal connections in monkey prefrontal cortex. *Journal of Comparative Neurology*, 390(2):211–224, 1998.

- [230] D. R. Merrill, M. Bikson, and J. G. Jefferys. Electrical stimulation of excitable tissue: design of efficacious and safe protocols. *Journal of neuroscience methods*, 141(2):171–198, 2005.
- [231] D. E. Meskaldji, M.-C. Ottet, L. Cammoun, P. Hagmann, R. Meuli, S. Eliez, J. P. Thiran, and S. Morgenthaler. Adaptive strategy for the statistical analysis of connectomes. *PloS one*, 6(8):e23009, 2011.
- [232] M. M. Mesulam et al. Patterns in behavioral neuroanatomy: association areas, the limbic system, and hemispheric specialization. *Principles of behavioral neurology*, pages 1–70, 1985.
- [233] M.-M. Mesulam et al. From sensation to cognition. *Brain*, 121(6):1013–1052, 1998.
- [234] L. Mihailovic and J. M. Delgado. Electrical stimulation of monkey brain with various frequencies and pulse durations. *Journal of neurophysiology*, 19(1):21–36, 1956.
- [235] J. Miró, A. Gurtubay-Antolin, P. Ripollés, J. Sierpowska, M. Juncadella, L. Fuentemilla, V. Sánchez, M. Falip, and A. Rodríguez-Fornells. Inter-hemispheric microstructural connectivity in bitemporal lobe epilepsy with hippocampal sclerosis. *Cortex*, 67:106–121, 2015.
- [236] U. Mitzdorf and W. Singer. Prominent excitatory pathways in the cat visual cortex (a 17 and a 18): a current source density analysis of electrically evoked potentials. *Experimental Brain Research*, 33(3-4):371–394, 1978.
- [237] M. Modat, G. R. Ridgway, Z. A. Taylor, M. Lehmann, J. Barnes, D. J. Hawkes, N. C. Fox, and S. Ourselin. Fast free-form deformation using graphics processing units. *Comput. Methods Prog. Biomed.*, 98(3):278–284, 2010.
- [238] I. S. Mohamed, H. Otsubo, M. Shroff, E. Donner, J. Drake, and O. C. Snead. Magnetoencephalography and diffusion tensor imaging in gelastic seizures

- secondary to a cingulate gyrus lesion. *Clinical neurology and neurosurgery*, 109(2):182–187, 2007.
- [239] S. Mori, B. J. Crain, V. Chacko, and P. Van Zijl. Three-dimensional tracking of axonal projections in the brain by magnetic resonance imaging. *Annals of neurology*, 45(2):265–269, 1999.
- [240] V. B. Mountcastle. The columnar organization of the neocortex. *Brain*, 120(4):701–722, 1997.
- [241] B. C. Munsell, C.-Y. Wee, S. S. Keller, B. Weber, C. Elger, L. A. T. da Silva, T. Nesland, M. Styner, D. Shen, and L. Bonilha. Evaluation of machine learning algorithms for treatment outcome prediction in patients with epilepsy based on structural connectome data. *NeuroImage*, 118:219–230, 2015.
- [242] S. S. Nathan, S. R. Sinha, B. Gordon, R. P. Lesser, and N. V. Thakor. Determination of current density distributions generated by electrical stimulation of the human cerebral cortex. *Electroencephalography and clinical neurophysiology*, 86(3):183–192, 1993.
- [243] M. E. Newman. Assortative mixing in networks. *Physical review letters*, 89(20):208701, 2002.
- [244] M. E. Newman. The structure and function of complex networks. *SIAM review*, 45(2):167–256, 2003.
- [245] R. Nieuwenhuys, J. Voogd, and C. Huijzen. *The Human Central Nervous System- A Synopsis and Atlas*. Springer-Verlag, 1991.
- [246] E. H. Nijhuis, A.-M. v. C. van Walsum, and D. G. Norris. Topographic hub maps of the human structural neocortical network. *PloS one*, 8(6):e65511, 2013.
- [247] L. Nowak and J. Bullier. Axons, but not cell bodies, are activated by electrical stimulation in cortical gray matter i. evidence from chronaxie measurements. *Experimental Brain Research*, 118(4):477–488, 1998.

- [248] J. P. O'Connor. Thomas willis and the background to cerebri anatome. *Journal of the Royal Society of Medicine*, 96(3):139–143, 2003.
- [249] J. L. O'Leary. Structure of the area striata of the cat. *Journal of Comparative Neurology*, 75(1):131–164, 1941.
- [250] E. Panagiotaki, T. Schneider, B. Siow, M. G. Hall, M. F. Lythgoe, and D. C. Alexander. Compartment models of the diffusion mr signal in brain white matter: a taxonomy and comparison. *Neuroimage*, 59(3):2241–2254, 2012.
- [251] C. S. Parker, F. Deligianni, M. J. Cardoso, P. Daga, M. Modat, M. Dayan, C. A. Clark, S. Ourselin, and J. D. Clayden. Consensus between pipelines in structural brain networks. *PloS one*, 9(10):e111262, 2014.
- [252] G. J. Parker, H. A. Haroon, and C. A. Wheeler-Kingshott. A framework for a streamline-based probabilistic index of connectivity (pico) using a structural interpretation of MRI diffusion measurements. *J. Magn. Reson. Imaging*, 18(2):242–254, 2003.
- [253] P. Patrikelis, E. Angelakis, and S. Gatzonis. Neurocognitive and behavioral functioning in frontal lobe epilepsy: a review. *Epilepsy & Behavior*, 14(1):19–26, 2009.
- [254] A. Perry, W. Wen, A. Lord, A. Thalamuthu, G. Roberts, P. B. Mitchell, P. S. Sachdev, and M. Breakspear. The organisation of the elderly connectome. *NeuroImage*, 114:414–426, 2015.
- [255] A. Peters and C. Sethares. Myelinated axons and the pyramidal cell modules in monkey primary visual cortex. *Journal of Comparative Neurology*, 365(2):232–255, 1996.
- [256] A. Piccolomini. *Anatomicae Praelectiones, explicantes mirificam corporis humani fabricam*. . Bonfadini, 1586.

- [257] PLOS ONE. Data availability, 2016. URL <http://journals.plos.org/plosone/s/data-availability>. [Online; accessed 23-May-2016].
- [258] J. W. Prescott, A. Guidon, P. M. Doraiswamy, K. Roy Choudhury, C. Liu, and J. R. Petrella. The alzheimer structural connectome: Changes in cortical network topology with increased amyloid plaque burden. *Radiology*, 273(1):175–184, 2014.
- [259] T. H. C. Project. The human connectome project. <http://www.humanconnectomeproject.org/>.
- [260] M. L. Pucak, J. B. Levitt, J. S. Lund, and D. A. Lewis. Patterns of intrinsic and associational circuitry in monkey prefrontal cortex. *Journal of Comparative Neurology*, 376(4):614–630, 1996.
- [261] R Development Core Team. *R: A Language and Environment for Statistical Computing*. R Foundation for Statistical Computing, Vienna, Austria, 2008. URL <http://www.R-project.org>. ISBN 3-900051-07-0.
- [262] A. Radhakrishnan, J. S. James, C. Kesavadas, B. Thomas, B. Bahuleyan, M. Abraham, and K. Radhakrishnan. Utility of diffusion tensor imaging tractography in decision making for extratemporal resective epilepsy surgery. *Epilepsy research*, 97(1):52–63, 2011.
- [263] A. Raj and Y.-h. Chen. The wiring economy principle: connectivity determines anatomy in the human brain. *PloS one*, 6(9):e14832, 2011.
- [264] J. B. Ranck Jr. Which elements are excited in electrical stimulation of mammalian central nervous system: a review. *Brain research*, 98(3):417–440, 1975.
- [265] N. Ratnarajah, A. Rifkin-Graboi, M. V. Fortier, Y. S. Chong, K. Kwek, S.-M. Saw, K. M. Godfrey, P. D. Gluckman, M. J. Meaney, and A. Qiu. Struc-

- tural connectivity asymmetry in the neonatal brain. *Neuroimage*, 75:187–194, 2013.
- [266] R. A. Reale, J. F. Brugge, and J. Z. Feng. Geometry and orientation of neuronal processes in cat primary auditory cortex (ai) related to characteristic-frequency maps. *Proceedings of the National Academy of Sciences*, 80(17):5449–5453, 1983.
- [267] J. C. Reil. Untersuchungen über den bau des grossen gehirns im menschen. *Arch. Physiol.(Halle)*, 9:136–208, 1809.
- [268] J. C. Reil. Die sylvische grube oder das thal, das gestreifte grobe hirnganglium, dessen kapsel und die seitenteile des groben gehirns. *Arch. Physiol.*, 11:89–100, 1812.
- [269] J. C. Reil. Die verdure commissur im groben gehirn. *Arch. Physiol.*, 11:89–100, 1812.
- [270] M. Reuter, H. D. Rosas, and B. Fischl. Highly accurate inverse consistent registration: a robust approach. *NeuroImage*, 53(4):1181–96, Dec. 2010. ISSN 1095-9572. doi: 10.1016/j.neuroimage.2010.07.020.
- [271] J. D. Riley, B. W. Fling, S. C. Cramer, and J. J. Lin. Altered organization of face-processing networks in temporal lobe epilepsy. *Epilepsia*, 56(5):762–771, 2015.
- [272] E. C. Robinson, A. Hammers, A. Ericsson, A. D. Edwards, and D. Rueckert. Identifying population differences in whole-brain structural networks: a machine learning approach. *NeuroImage*, 50(3):910–919, 2010.
- [273] K. Rockland. Intrinsically projecting pyramidal neurons of monkey striate cortex: an em-hrp study. In *Soc Neurosci Abstr*, volume 11, page 17, 1985.
- [274] K. S. Rockland and J. S. Lund. Widespread periodic intrinsic connections in the tree shrew visual cortex. *Science*, 215(4539):1532–1534, 1982.

- [275] K. S. Rockland and J. S. Lund. Intrinsic laminar lattice connections in primate visual cortex. *Journal of Comparative Neurology*, 216(3):303–318, 1983.
- [276] S. Rodrigo, C. Oppenheim, F. Chassoux, J. Hodel, A. De Vanssay, S. Baudoin-Chial, B. Devaux, and J.-F. Meder. Language lateralization in temporal lobe epilepsy using functional mri and probabilistic tractography. *Epilepsia*, 49(8):1367–1376, 2008.
- [277] D. Rosenberg, F. Mauguiere, H. Catenoix, I. Faillenot, and M. Magnin. Reciprocal thalamocortical connectivity of the medial pulvinar: a depth stimulation and evoked potential study in human brain. *Cerebral Cortex*, 19(6):1462–1473, 2009.
- [278] F. Rosenow and H. Lüders. Presurgical evaluation of epilepsy. *Brain*, 124(9):1683–1700, 2001.
- [279] M. Rubinov and O. Sporns. Complex network measures of brain connectivity: uses and interpretations. *Neuroimage*, 52(3):1059–1069, 2010.
- [280] D. Rueckert, L. I. Sonoda, C. Hayes, D. L. Hill, M. O. Leach, and D. J. Hawkes. Nonrigid registration using free-form deformations: application to breast MR images. *IEEE Trans. Med. Imaging*, 18(8):712–21, Aug. 1999. ISSN 0278-0062.
- [281] C. Schroeder, A. Mehta, and S. Givre. A spatiotemporal profile of visual system activation revealed by current source density analysis in the awake macaque. *Cerebral Cortex*, 8(7):575–592, 1998.
- [282] A. Schüz and R. Miller. *Cortical areas: unity and diversity*. CRC Press, 2003.
- [283] Seven Bridges of Knigsberg. Seven bridges of knigsberg — Wikipedia, the free encyclopedia, 2016. URL https://en.wikipedia.org/wiki/Seven_Bridges_of_Konigsberg. [Online; accessed 4-May-2016].

- [284] J. Shao, N. Myers, Q. Yang, J. Feng, C. Plant, C. Böhm, H. Förstl, A. Kurz, C. Zimmer, C. Meng, V. Riedl, A. Wohlschläger, and C. Sorg. Prediction of alzheimer's disease using individual structural connectivity networks. *Neurobiol. Aging*, 33(12):2756–2765, 2012.
- [285] F. Shi, P.-T. Yap, W. Gao, W. Lin, J. H. Gilmore, and D. Shen. Altered structural connectivity in neonates at genetic risk for schizophrenia: A combined study using morphological and white matter networks. *Neuroimage*, 2012.
- [286] N. Shu, Y. Liu, J. Li, Y. Li, C. Yu, and T. Jiang. Altered anatomical network in early blindness revealed by diffusion tensor tractography. *PLoS One*, 4(9):e7228, 2009.
- [287] N. Shu, Y. Liu, K. Li, Y. Duan, J. Wang, C. Yu, H. Dong, J. Ye, and Y. He. Diffusion tensor tractography reveals disrupted topological efficiency in white matter structural networks in multiple sclerosis. *Cerebral Cortex*, 21(11):2565–2577, 2011.
- [288] S. L. Simpson, S. Hayasaka, and P. J. Laurienti. Exponential random graph modeling for complex brain networks. *PLoS One*, 6(5):e20039, 2011.
- [289] S. L. Simpson, M. N. Moussa, and P. J. Laurienti. An exponential random graph modeling approach to creating group-based representative whole-brain connectivity networks. *Neuroimage*, 60(2):1117–1126, 2012.
- [290] S. M. Smith. Fast robust automated brain extraction. *Hum. Brain Mapp.*, 17(3):143–155, 2002.
- [291] O. Sporns, C. J. Honey, and R. Kötter. Identification and classification of hubs in brain networks. *PloS one*, 2(10):e1049, 2007.
- [292] E. Stejskal. Use of spin echoes in a pulsed magnetic-field gradient to study anisotropic, restricted diffusion and flow. *The Journal of Chemical Physics*, 43(10):3597–3603, 1965.
- [293] N. Steno. Discours de monsieur stenon sur l'anatomie du cerveau, 1669.

- [294] S. Stoney Jr, W. Thompson, and H. Asanuma. Excitation of pyramidal tract cells by intracortical microstimulation: effective extent of stimulating current. *Journal of neurophysiology*, 31(5):659–669, 1968.
- [295] J. Stretton, G. Winston, M. Sidhu, S. Bonelli, M. Centeno, C. Vollmar, R. Cleary, E. Williams, M. Symms, M. Koepp, et al. Disrupted segregation of working memory networks in temporal lobe epilepsy. *NeuroImage: Clinical*, 2:273–281, 2013.
- [296] N. C. Swann, W. Cai, C. R. Conner, T. A. Pieters, M. P. Claffey, J. S. George, A. R. Aron, and N. Tandon. Roles for the pre-supplementary motor area and the right inferior frontal gyrus in stopping action: electrophysiological responses and functional and structural connectivity. *Neuroimage*, 59(3): 2860–2870, 2012.
- [297] J. Szentágothai. The modular architectonic principle of neural centers. In *Reviews of Physiology, Biochemistry and Pharmacology, Volume 98*, pages 11–61. Springer, 1983.
- [298] J. Talairach and P. Tournoux. Co-planar stereotaxic atlas of the human brain. 3-dimensional proportional system: an approach to cerebral imaging. 1988.
- [299] M. Tanifuji, T. Sugiyama, and K. Murase. Horizontal propagation of excitation in rat visual cortical slices revealed by optical imaging. *Science*, 266 (5187):1057–1059, 1994.
- [300] P. N. Taylor, C. E. Han, J.-C. Schoene-Bake, B. Weber, and M. Kaiser. Structural connectivity changes in temporal lobe epilepsy: Spatial features contribute more than topological measures. *NeuroImage: Clinical*, 8:322–328, 2015.
- [301] R. C. Team. R: a language and environment for statistical computing. vienna: R foundation for statistical computing; 2012, 2012. URL <http://www.R-project.org/>.

- [302] A. E. Telfeian and B. W. Connors. Layer-specific pathways for the horizontal propagation of epileptiform discharges in neocortex. *Epilepsia*, 39(7):700–708, 1998.
- [303] J. F. Téllez-Zenteno, R. Dhar, and S. Wiebe. Long-term seizure outcomes following epilepsy surgery: a systematic review and meta-analysis. *Brain*, 128(5):1188–1198, 2005.
- [304] K. Terada, S. Umeoka, N. Usui, K. Baba, K. Usui, S. Fujitani, K. Matsuda, T. Tottori, F. Nakamura, and Y. Inoue. Uneven interhemispheric connections between left and right primary sensori-motor areas. *Human brain mapping*, 33(1):14–26, 2012.
- [305] A. Thomson and D. West. Fluctuations in pyramid-pyramid excitatory post-synaptic potentials modified by presynaptic firing pattern and postsynaptic membrane potential using paired intracellular recordings in rat neocortex. *Neuroscience*, 54(2):329–346, 1993.
- [306] L. J. Toth, D. Kim, S. Rao, and M. Sur. Integration of local inputs in visual cortex. *Cerebral Cortex*, 7(8):703–710, 1997.
- [307] J. Tournier, F. Calamante, and A. Connelly. Mrtrix: Diffusion tractography in crossing fiber regions. *Int. J. Imaging Syst. Technol.*, 22(1):53–66, 2012.
- [308] J.-D. Tournier, F. Calamante, D. G. Gadian, and A. Connelly. Direct estimation of the fiber orientation density function from diffusion-weighted MRI data using spherical deconvolution. *NeuroImage*, 23(3):1176–1185, 2004.
- [309] J.-D. Tournier, F. Calamante, and A. Connelly. Robust determination of the fibre orientation distribution in diffusion MRI: non-negativity constrained super-resolved spherical deconvolution. *NeuroImage*, 35(4):1459–1472, 2007.
- [310] J.-D. Tournier, F. Calamante, A. Connelly, et al. Robust determination of the fibre orientation distribution in diffusion MRI: non-negativity con-

- strained super-resolved spherical deconvolution. *NeuroImage*, 35(4):1459–1472, 2007.
- [311] L. Trebaul, D. Rudrauf, A.-S. Job, M. D. Mlia, I. Popa, A. Barborica, L. Minotti, I. Mndru, P. Kahane, and O. David. Stimulation artifact correction method for estimation of early cortico-cortical evoked potentials. *Journal of Neuroscience Methods*, 264:94 – 102, 2016. ISSN 0165-0270. doi: <http://dx.doi.org/10.1016/j.jneumeth.2016.03.002>. URL <http://www.sciencedirect.com/science/article/pii/S0165027016300085>.
- [312] D. Y. Ts’o, C. D. Gilbert, and T. N. Wiesel. Relationships between horizontal interactions and functional architecture in cat striate cortex as revealed by cross-correlation analysis. *The Journal of Neuroscience*, 6(4):1160–1170, 1986.
- [313] D. S. Tuch. Q-ball imaging. *Magnetic Resonance in Medicine*, 52(6):1358–1372, 2004.
- [314] D. Turkdogan, M. Duchowny, T. Resnick, and P. Jayakar. Subdural eeg patterns in children with taylor-type cortical dysplasia: comparison with nondysplastic lesions. *Journal of clinical neurophysiology*, 22(1):37–42, 2005.
- [315] R. Turner and D. Le Bihan. Single-shot diffusion imaging at 2.0 tesla. *Journal of Magnetic Resonance (1969)*, 86(3):445–452, 1990.
- [316] C. Tyler, S. Dunlop, R. Lund, A. Harman, J. Dann, L. Beazley, and J. Lund. Anatomical comparison of the macaque and marsupial visual cortex: common features that may reflect retention of essential cortical elements. *Journal of Comparative Neurology*, 400(4):449–468, 1998.
- [317] O. Tymofiyeva, C. P. Hess, E. Ziv, N. Tian, S. L. Bonifacio, P. S. McQuillen, D. M. Ferriero, A. J. Barkovich, and D. Xu. Towards the baby connectome:

- mapping the structural connectivity of the newborn brain. *PloS One*, 7(2): e31029, 2012.
- [318] N. Tzourio-Mazoyer, B. Landeau, D. Papathanassiou, F. Crivello, O. Etard, N. Delcroix, B. Mazoyer, M. Joliot, et al. Automated anatomical labeling of activations in spm using a macroscopic anatomical parcellation of the MNI MRI single-subject brain. *Neuroimage*, 15(1):273–289, 2002.
- [319] S. Umeoka, K. Terada, K. Baba, K. Usui, K. Matsuda, T. Tottori, N. Usui, F. Nakamura, Y. Inoue, T. Fujiwara, et al. Neural connection between bilateral basal temporal regions: Cortico-cortical evoked potential analysis in patients with temporal lobe epilepsy. *Neurosurgery*, 64(5):847–855, 2009.
- [320] M. Vaessen, P. Hofman, H. Tijssen, A. Aldenkamp, J. Jansen, and W. Backes. The effect and reproducibility of different clinical DTI gradient sets on small world brain connectivity measures. *Neuroimage*, 51(3):1106, 2010.
- [321] M. J. Vaessen, J. F. Jansen, M. C. Vlooswijk, P. A. Hofman, H. M. Majoie, A. P. Aldenkamp, and W. H. Backes. White matter network abnormalities are associated with cognitive decline in chronic epilepsy. *Cerebral cortex*, page bhr298, 2011.
- [322] M. J. Vaessen, J. F. Jansen, M. C. Vlooswijk, P. A. Hofman, H. M. Majoie, A. P. Aldenkamp, and W. H. Backes. White matter network abnormalities are associated with cognitive decline in chronic epilepsy. *Cereb. Cortex*, 22(9):2139–2147, 2012.
- [323] M. J. Vaessen, J. Jansen, H. Braakman, P. Hofman, A. De Louw, A. P. Aldenkamp, and W. H. Backes. Functional and structural network impairment in childhood frontal lobe epilepsy. *PloS one*, 9(3):e90068, 2014.
- [324] A. Valentin, M. Anderson, G. Alarcon, J. G. Seoane, R. Selway, C. Binnie, and C. Polkey. Responses to single pulse electrical stimulation identify epileptogenesis in the human brain in vivo. *Brain*, 125(8):1709–1718, 2002.

- [325] A. Valentin, G. Alarcon, J. Garcia-Seoane, M. Lacruz, S. Nayak, M. Honavar, R. Selway, C. Binnie, and C. Polkey. Single-pulse electrical stimulation identifies epileptogenic frontal cortex in the human brain. *Neurology*, 65(3):426–435, 2005.
- [326] A. Valentín, G. Alarcón, M. Honavar, J. J. García Seoane, R. P. Selway, C. E. Polkey, and C. D. Binnie. Single pulse electrical stimulation for identification of structural abnormalities and prediction of seizure outcome after epilepsy surgery: a prospective study. *The Lancet Neurology*, 4(11):718–726, 2005.
- [327] M. P. van den Heuvel and O. Sporns. Rich-club organization of the human connectome. *J. Neurosci.*, 31(44):15775–15786, 2011.
- [328] M. P. van den Heuvel, R. C. Mandl, C. J. Stam, R. S. Kahn, and H. E. H. Pol. Aberrant frontal and temporal complex network structure in schizophrenia: a graph theoretical analysis. *J. Neurosci.*, 30(47):15915–15926, 2010.
- [329] M. P. van den Heuvel, M. A. de Reus, L. Feldman Barrett, L. H. Scholtens, F. M. Coopmans, R. Schmidt, T. M. Preuss, J. K. Rilling, and L. Li. Comparison of diffusion tractography and tract-tracing measures of connectivity strength in rhesus macaque connectome. *Human brain mapping*, 36(8):3064–3075, 2015.
- [330] B. C. van Wijk, C. J. Stam, and A. Daffertshofer. Comparing brain networks of different size and connectivity density using graph theory. *PLoS One*, 5(10):e13701, 2010.
- [331] N. L. Voets, R. A. Menke, S. Jbabdi, M. Husain, R. Stacey, K. Carpenter, and J. E. Adcock. Thalamo-cortical disruption contributes to short-term memory deficits in patients with medial temporal lobe damage. *Cerebral Cortex*, page bhv109, 2015.
- [332] C. F. von Economo and G. N. Koskinas. *Die cytoarchitektonik der hirnrinde des erwachsenen menschen*. J. Springer, 1925.

- [333] S. Vulliemoz, C. Vollmar, M. J. Koepp, M. Yogarajah, J. O'Muircheartaigh, D. W. Carmichael, J. Stretton, M. P. Richardson, M. R. Symms, and J. S. Duncan. Connectivity of the supplementary motor area in juvenile myoclonic epilepsy and frontal lobe epilepsy. *Epilepsia*, 52(3):507–514, 2011.
- [334] Q. Wang, T.-P. Su, Y. Zhou, K.-H. Chou, I.-Y. Chen, T. Jiang, and C.-P. Lin. Anatomical insights into disrupted small-world networks in schizophrenia. *Neuroimage*, 59(2):1085–1093, 2012.
- [335] D. J. Watts and S. H. Strogatz. Collective dynamics of ‘small-world’ networks. *Nat.*, 393(6684):440–442, 1998.
- [336] V. J. Wedeen, P. Hagmann, W.-Y. I. Tseng, T. G. Reese, and R. M. Weisskoff. Mapping complex tissue architecture with diffusion spectrum magnetic resonance imaging. *Magn. Reson. Med.*, 54(6):1377–1386, 2005.
- [337] V. J. Wedeen, P. Hagmann, W.-Y. I. Tseng, T. G. Reese, and R. M. Weisskoff. Mapping complex tissue architecture with diffusion spectrum magnetic resonance imaging. *Magnetic Resonance in Medicine*, 54(6):1377–1386, 2005.
- [338] C.-Y. Wee, P.-T. Yap, D. Zhang, K. Denny, J. N. Browndyke, G. G. Potter, K. A. Welsh-Bohmer, L. Wang, and D. Shen. Identification of mci individuals using structural and functional connectivity networks. *Neuroimage*, 59(3):2045–2056, 2012.
- [339] W. Wen, W. Zhu, Y. He, N. A. Kochan, S. Reppermund, M. J. Slavin, H. Brodaty, J. Crawford, A. Xia, and P. Sachdev. Discrete neuroanatomical networks are associated with specific cognitive abilities in old age. *J. Neurosci.*, 31(4):1204–1212, 2011.
- [340] C. Wernicke. *Lehrbuch der geirnkrankeiten für aerzte und studirende*, volume 2. Fischer, 1881.
- [341] K. Wernicke. The aphasia symptom-complex (vol. 4). *Amsterdam: John Benjaminns*, 1874.

- [342] J. White, E. Southgate, J. Thomson, and S. Brenner. The structure of the nervous system of the nematode *caenorhabditis elegans*: the mind of a worm. *Phil. Trans. R. Soc. Lond*, 314:1–340, 1986.
- [343] T. Willis. 1664. *cerebri anatome, cui accessit nervorum descriptio et usus*. London: Martin & Allestry by University College London on, 5(09):06, 1965.
- [344] C. Wilson, M. Isokawa, T. Babb, and P. Crandall. Functional connections in the human temporal lobe. *Experimental brain research*, 82(2):279–292, 1990.
- [345] G. P. Winston, J. Stretton, M. K. Sidhu, M. R. Symms, and J. S. Duncan. Progressive white matter changes following anterior temporal lobe resection for epilepsy. *NeuroImage: Clinical*, 4:190–200, 2014.
- [346] Y. Xu, S. Qiu, J. Wang, Z. Liu, R. Zhang, S. Li, L. Cheng, W. Wang, and R. Huang. Disrupted topological properties of brain white matter networks in left temporal lobe epilepsy: A diffusion tensor imaging study. *Neuroscience*, 279:155–167, 2014.
- [347] K. Xue, C. Luo, D. Zhang, T. Yang, J. Li, D. Gong, L. Chen, Y. I. Medina, J. Gotman, D. Zhou, et al. Diffusion tensor tractography reveals disrupted structural connectivity in childhood absence epilepsy. *Epilepsy research*, 108(1):125–138, 2014.
- [348] S. R. y Cajal. *Studien über die Sehrinde der Katze*. Johann Ambrosius Barth, 1922.
- [349] N. H. YABUTA and E. M. CALLAWAY. Cytochrome-oxidase blobs and intrinsic horizontal connections of layer 2/3 pyramidal neurons in primate v1. *Visual neuroscience*, 15(06):1007–1027, 1998.
- [350] Y. Yamao, R. Matsumoto, T. Kunieda, Y. Arakawa, K. Kobayashi, K. Usami, S. Shibata, T. Kikuchi, N. Sawamoto, N. Mikuni, et al. Intraoperative dor-

sal language network mapping by using single-pulse electrical stimulation. *Human brain mapping*, 2014.

- [351] C. Yan, G. Gong, J. Wang, D. Wang, D. Liu, C. Zhu, Z. J. Chen, A. Evans, Y. Zang, and Y. He. Sex-and brain size–related small-world structural cortical networks in young adults: a DTI tractography study. *Cereb. cortex*, 21(2): 449–458, 2011.
- [352] C. Yan, G. Gong, J. Wang, D. Wang, D. Liu, C. Zhu, Z. J. Chen, A. Evans, Y. Zang, and Y. He. Sex-and brain size–related small-world structural cortical networks in young adults: a dti tractography study. *Cerebral cortex*, 21(2): 449–458, 2011.
- [353] P.-T. Yap, Y. Fan, Y. Chen, J. H. Gilmore, W. Lin, and D. Shen. Development trends of white matter connectivity in the first years of life. *PloS one*, 6(9): e24678, 2011.
- [354] J. D. Yeatman, K. S. Weiner, F. Pestilli, A. Rokem, A. Mezer, and B. A. Wandell. The vertical occipital fasciculus: A century of controversy resolved by in vivo measurements. *Proceedings of the National Academy of Sciences*, 111(48):E5214–E5223, 2014.
- [355] M. Yogarajah, N. K. Focke, S. B. Bonelli, P. Thompson, C. Vollmar, A. W. McEvoy, D. C. Alexander, M. R. Symms, M. J. Koepp, and J. S. Duncan. The structural plasticity of white matter networks following anterior temporal lobe resection. *Brain*, 133(8):2348–2364, 2010.
- [356] T. Yoshioka, J. B. Levitt, and J. S. Lund. Independence and merger of thalamocortical channels within macaque monkey primary visual cortex: anatomy of interlaminar projections. *Visual neuroscience*, 11(03):467–489, 1994.
- [357] A. Zalesky, A. Fornito, and E. T. Bullmore. Network-based statistic: identifying differences in brain networks. *Neuroimage*, 53(4):1197–1207, 2010.

- [358] A. Zalesky, A. Fornito, I. H. Harding, L. Cocchi, M. Yücel, C. Pantelis, and E. T. Bullmore. Whole-brain anatomical networks: does the choice of nodes matter? *Neuroimage*, 50(3):970, 2010.
- [359] A. Zalesky, A. Fornito, I. H. Harding, L. Cocchi, M. Yücel, C. Pantelis, and E. T. Bullmore. Whole-brain anatomical networks: does the choice of nodes matter? *Neuroimage*, 50(3):970, 2010.
- [360] A. Zalesky, A. Fornito, M. L. Seal, L. Cocchi, C.-F. Westin, E. T. Bullmore, G. F. Egan, and C. Pantelis. Disrupted axonal fiber connectivity in schizophrenia. *Biol. Psychiatr.*, 69(1):80–89, 2011.
- [361] A. Zalesky, L. Cocchi, A. Fornito, M. M. Murray, and E. Bullmore. Connectivity differences in brain networks. *NeuroImage*, 60(2):1055–1062, 2012.
- [362] S. Zeki. Cerebral akinetopsia (visual motion blindness). *Brain*, 114(2):811–824, 1991.
- [363] H. Zhang, T. Schneider, C. A. Wheeler-Kingshott, and D. C. Alexander. Noddi: practical in vivo neurite orientation dispersion and density imaging of the human brain. *Neuroimage*, 61(4):1000–1016, 2012.
- [364] Y. Zhang, L. Lin, C.-P. Lin, Y. Zhou, K.-H. Chou, C.-Y. Lo, T.-P. Su, and T. Jiang. Abnormal topological organization of structural brain networks in schizophrenia. *Schizophrenia research*, 2012.
- [365] Z. Zhang, W. Liao, H. Chen, D. Mantini, J.-R. Ding, Q. Xu, Z. Wang, C. Yuan, G. Chen, Q. Jiao, and G. Lu. Altered functional-structural coupling of large-scale brain networks in idiopathic generalized epilepsy. *Brain*, 134(10):2912–2928, 2011.
- [366] Z. Zhang, W. Liao, H. Chen, D. Mantini, J.-R. Ding, Q. Xu, Z. Wang, C. Yuan, G. Chen, Q. Jiao, et al. Altered functional–structural coupling of large-scale brain networks in idiopathic generalized epilepsy. *Brain*, 134(10):2912–2928, 2011.

- [367] T. Zhao, F. Duan, X. Liao, Z. Dai, M. Cao, Y. He, and N. Shu. Test-retest reliability of white matter structural brain networks: a multiband diffusion mri study. *Frontiers in human neuroscience*, 9, 2015.
- [368] S. Zhong, Y. He, and G. Gong. Convergence and divergence across construction methods for human brain white matter networks: An assessment based on individual differences. *Human brain mapping*, 36(5):1995–2013, 2015.